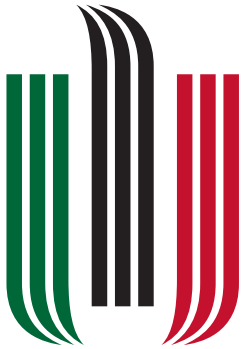

AGH UNIVERSITY OF SCIENCE AND TECHNOLOGY

FIELD OF SCIENCE: NATURAL SCIENCES

SCIENTIFIC DISCIPLINE: PHYSICAL SCIENCES

DOCTORAL THESIS

Diffraction study of deformation process for selected groups of grains and different phases in polycrystalline materials

Author: Przemysław Andrzej Kot

First supervisor: prof. dr hab. inż. Andrzej Baczmański
Assisting supervisor: dr inż. Marcin Wroński

Completed in: AGH-University of Science and Technology, Faculty of Physics and Applied Computer Sciences, Department of Condensed Matter Physics

Krakow, 2022

This PhD thesis has been completed in the framework of the Program POWER, project No. POWR.03.02.00-00-I004/16, co-financed by the European Union.

Declaration of the author of this dissertation

Aware of legal responsibility for making untrue statements I hereby declare that I have written this dissertation myself and all the contents of the dissertation have been obtained by legal means.

Declaration of the thesis Supervisor:

This dissertation is ready to be reviewed.

Abstract

In this work the stress measurement methodology for polycrystalline material using time-of-flight neutron diffraction technique was developed. The experiments were conducted mainly on the EPSILON-MSD diffractometer at the Join Institute for Nuclear Research in Dubna (Russia). This instrument allows to perform measurements of crystal lattice deformations simultaneously in 9 different directions of scattering vector. In order to efficiently process a large amount of measurement data, several programs for the analysis of the experimental results were prepared. Measurements were carried out *in situ* during mechanical and thermal loading of the samples. In order to minimize the systematic error, the stress increments were determined on the basis of the relative lattice strains. The research concerned two materials: Al/SiC_p composite obtained by powder sintering, where the volume fraction of silicon carbide was 17,8%, and hot-rolled magnesium alloy AZ31. The neutron diffraction time-of-flight technique enabled to determine the stresses in each phase of the composite and to apply the crystallite groups method in the case of a magnesium alloy samples. For the composite sample, *in situ* measurements were carried out during the compression test, and also the results of previous experiment performed at different temperatures were used and analysed. Measurements in magnesium alloy were made for the compression test in the rolling direction and the normal direction. The neutron diffraction measurements performed at Neutron Physics Laboratory (NPI, Řež near Prague, Czech Republic) during the tensile test in the rolling direction were also analysed in this work. An important achievement of the work is the development of a methodology for selective stress analysis for two phases and for different crystallite orientations based on measurements carried out in many directions and with the use of different hkl reflections.

The first part of the work concerns the analysis of the results of measurements carried out for the Al/SiC_p composite. The phenomenon of residual stress formation between the SiC grains and the Al alloy matrix during cooling, corresponding to the composite production conditions, was investigated. These stresses result from a significant difference in the thermal expansion coefficients of both phases. The thermal stresses in the phases were correctly predicted by the thermomechanical self-consistent model (TMSC). *In situ* measurements during the compression test of the Al/SiC_p composite allowed for the examination of stress changes in individual phases. It has been shown that in the elastic range, the deviatoric stresses localised on the SiC grains are much greater than theses localised in the aluminium matrix. The difference between the loading of the silicon carbide as compared to the loading of the Al matrix increased significantly when the aluminium was plastically deformed. There was also relaxation of thermal stresses during plastic deformation, the average values of which for each phase is hydrostatic. The stress

relaxation phenomenon was explained using a developed thermomechanical self-consistent model (DTMSC).

The second part of the work concerns the research performed in order to explain the strong anisotropy of the response of textured samples made of magnesium alloy (AZ31) to the applied external load. Despite the isotropic elasticity constants of the crystallites, the elastoplastic behaviour of the samples depended on the direction and nature of the applied load. The samples were cut from hot-rolled magnesium having a strong crystallographic texture with a dominant basal component (0001). The measurements showed a higher yield point and greater hardening of the material during compression in the normal direction compared to compression or tension in the rolling direction. Moreover, during the compression test in the rolling direction, a twinning phenomenon occurred leading to a characteristic plateau range on the macroscopic stress-strain relationship.

To explain such a characteristic behaviour of magnesium samples, the measurement method of crystallite groups was used, which allowed to investigate the stresses localised at grains with different crystal lattice orientations. The different loadings of the sample in combination with the strong texture resulted in very different behaviour of the crystallites. There are 4 groups of grains: hard, intermediate, soft and grains for which twinning occurs. For these groups, there are different sequences of activity of the slip and twinning systems. The evolutions of stress tensor components for individual groups of grains, depending on their orientations, were measured using *in situ* diffraction measurements during compression and tensile tests. The knowledge of the stress tensor allowed for the determination of the shear resolved stresses (RSS) on all slip systems and the twinning system, along with their uncertainties. On the basis of changes in these stresses during the tests, the critical resolved shear stresses (CRSS) needed to activate the slip and twinning systems were determined. The uncertainty analysis of the determined values was also carried out.

The measured CRSS values were used as input to the elastoplastic self-consistent (EPSC) model. This reduced the number of parameters that must be optimized to fit the model results to the experimentally determined lattice strains. As a result, the calculations became more unambiguous and allowed to verify the assumptions concerning the process of twins formation and the interaction between the grains. The model parameters determined in this study were also verified for a set of samples subjected to compression in various directions. In this work, for the first time, an analysis was carried out to determine all CRSS values, together with uncertainties, directly from the experiment and without model assumptions.

Streszczenie

W niniejszej pracy rozwinięto eksperymentalną metodologię wyznaczania naprężeń w materiałach polikrystalicznych przy pomocy dyfrakcji neutronów z zastosowaniem techniki pomiaru czasu przelotu. Badania prowadzone były głównie na dyfraktometrze EPSILON-MSD w Zjednoczonym Instytucie Badań Jądrowych w Dubnej (Rosja). Przyrząd ten pozwolił wykonać pomiary odkształceń sieci krystalicznej jednocześnie w 9 różnych kierunkach wektora rozpraszania. Aby efektywnie opracować dużą ilość danych pomiarowych, przygotowane zostało kilka programów umożliwiających analizę wyników. Pomiary prowadzone były *in situ* podczas mechanicznego i termicznego obciążania próbek. W celu zminimalizowania błędu systematycznego przyrosty naprężeń obliczane były na podstawie względnych odkształceń sieci krystalicznej. Badania dotyczyły dwóch materiałów: kompozytu Al/SiC_p uzyskanego metodą spiekania proszków, gdzie domieszka węglika krzemu wynosiła 17,8% oraz walcowanego na gorąco stopu magnezu AZ31. Dyfrakcyjna technika czasu przelotu neutronów umożliwiła wyznaczenie naprężeń w każdej z faz kompozytu oraz zastosowanie metody grup krystalitów w przypadku próbki ze stopu magnezu. Dla próbki kompozytowej pomiary *in situ* przeprowadzone zostały podczas próby ściskania, a w pracy wykorzystano również wyniki poprzednich pomiarów przeprowadzonych w różnych temperaturach. Pomiary dotyczące magnezu przeprowadzone zostały dla testu ściskania w kierunku walcowania i kierunku normalnym. Wykorzystano i przeanalizowano również pomiary wykonane w Laboratorium Fizyki Neutronowej (NPI, Řež koło Pragi, Czechy) podczas testu rozciągania w kierunku walcowania. Ważnym osiągnięciem pracy jest opracowanie metodologii selektywnej analizy naprężeń w dwóch fazach oraz dla różnych orientacji krystalitów na podstawie pomiarów przeprowadzonych w wielu kierunkach i za pomocą różnych refleksów hkl. Wyniki analizy danych pochodzących bezpośrednio z eksperymentów zostały skonfrontowane z wynikami modelu samouzgodnionego, w wyniku czego uzyskano dobrą zgodność modelu z pomiarami.

Pierwsza część pracy dotyczy analizy wyników pomiarów przeprowadzonych dla kompozytu Al/SiC_p. Zbadano zjawisko powstawania naprężeń własnych między ziarnami SiC i matrycą ze stopu Al podczas chłodzenia odpowiadającego warunkom produkcji kompozytu. Zjawisko to wynika ze znaczącej różnicy współczynników rozszerzalności temperaturowej obu faz. Naprężenia termiczne w fazach poprawnie przewidziane zostały przez termomechaniczny model samouzgodniony (TMSC). Pomiary *in situ* podczas próby ściskania kompozytu Al/SiC_p pozwoliły na zbadanie zmian naprężeń w poszczególnych

fazach. Pokazano, że w zakresie sprężystym naprężenia dewiatoryczne zlokalizowane na ziarnach SiC są znacznie większe niż w aluminiowej matrycy. Różnica między obciążeniem węglika krzemu w porównaniu z obciążeniem matrycy znacząco rosła, gdy aluminium odkształcało się plastycznie. W zakresie tym nastąpiła również relaksacja naprężeń termicznych, których średnie wartości dla obu faz mają charakter hydrostatyczny. Zachowanie to zostało wytłumaczone przy pomocy zmodyfikowanego samouzgodnionego modelu termomechanicznego (DTMSC).

Drugą część pracy stanowią wyniki badań przeprowadzonych w celu wyjaśnienia silnej anizotropii odpowiedzi steksturowanych próbek ze stopu magnezu (AZ31) na przyłożone siły zewnętrze. Pomimo izotropowych stałych sprężystości krystalitów, zachowanie elastoplastyczne próbek zależało od kierunku i charakteru przyłożonego obciążenia. Badane próbki wycięte z walcowanej na gorąco blachy posiadały silną teksturę z dominującą składową bazalną (0001). Pomiary wykazały wyższą granicę plastyczności i większe umacnianie się materiału podczas ściskania w kierunku normalnym w porównaniu ze ściskaniem lub rozciąganiem w kierunku walcowania. Ponadto, podczas próby ściskania w kierunku walcowania, wystąpiło zjawisko bliźniakowania z charakterystycznym zakresem plateau na makroskopowej zależności naprężenia od odkształcenia.

By wytłumaczyć tak charakterystyczne zachowanie próbek magnezowych, wykorzystano pomiarową metodę grup krystalitów, która pozwoliła zbadać lokalizację naprężeń na ziarnach posiadających różne orientacje sieci krystalicznej. Różne obciążenia próbki w połączeniu z silną teksturą spowodowały bardzo różne zachowanie się krystalitów. Wyodrębnić można 4 grupy ziaren: twarde, pośrednie, miękkie oraz ziarna, dla których zachodzi bliźniakowanie. Dla grup tych występują różne sekwencje aktywności systemów poślizgu i bliźniakowania. Przy pomocy dyfrakcyjnych pomiarów *in situ*, podczas prób ściskania i rozciągania, zmierzono ewolucję składowych naprężeń dla poszczególnych grup ziaren różniących się orientacjami. Znajomość tensora naprężeń pozwoliła również na wyznaczenie wartości naprężeń ścinających (RSS) na wszystkich systemach poślizgu i systemie bliźniakowania wraz z ich niepewnościami. Na podstawie zmian tych naprężeń, podczas przeprowadzonych testów, wyznaczone zostały krytyczne wartości naprężeń ścinających (CRSS) potrzebnych do uruchomienia systemów poślizgów i bliźniakowania. Przeprowadzono również analizę niepewności wyznaczonych wartości.

Zmierzone wartości CRSS zostały użyte jako dane wejściowe modelu samouzgodnionego deformacji elastoplastycznej (EPSC). Zmniejszyło to liczbę parametrów, które muszą być zoptymalizowane, aby dopasować wyniki modelu do eksperymentalnie wyznaczonych odkształceń sieci krystalicznej. Obliczenia stały się przez to bardziej jednoznaczne i pozwoliły miedzy innymi zweryfikować założenia dotyczące procesu tworzenia bliźniaków oraz oddziaływania miedzy ziarnami. Wyznaczone w tej

pracy parametry modelu zweryfikowane zostały również dla zestawu próbek poddanych ściskaniu w różnych kierunkach. W niniejszej pracy po raz pierwszy została przeprowadzona analiza pozwalająca na wyznaczenie wszystkich wartości CRSS, wraz z niepewnościami, bezpośrednio z eksperymentu i bez założeń modelowych.

Acknowledgements

At the very beginning I would like to thank my first supervisor Professor Andrzej Baczmański, without whom I would not have made it to where I am now. Starting from the stage of writing an BSc thesis, throughout the years of master's and doctorate studies, he devoted a huge amount of his time to me, providing valuable comments, constructive criticism, support both with scientific knowledge and with his many years of experience on many levels. Working with him was not only a valuable scientific experience, but also a pleasure.

I would also like to thank my assistant supervisor Doctor Marcin Wroński, who also gave me a lot of helpful comments and passed on a lot of experience. His often different approach to the currently analysed problem allowed for a creative solution.

At this point, I would also like to thank all the people with whom I worked during my doctorate for their kind attitude and a helping hand: Doctor Sebastian Wroński, Doctor Christian Scheffzük, Doctor Gizo Bokuchava and Professor Krzysztof Wierzbanowski.

Last but not least, I would like to thank my family for their understanding and continued support during my PhD.

Author of this thesis received the NCN scholarship in research project No. UMO-2017/25/B/ST8/00134 and was partially founded by the National Science Centre, Poland. The work was also partially supported by the project UMO-2021/41/N/ST5/00394 founded by the National Science Centre, directed by the author of this thesis.

The author also participated in the program “Excellence initiative – research university“ for the AGH University of Science and Technology

The neutron diffraction experiments used in this work were performed during the period 2017-2019 at JINR in Dubna (Russia) and the purchase of samples/reagents/ancillary equipment was partly financed by the joint JINR/AGH projects nr PWB/389-24/2017, PWB/254_24/2018 and PWB/129-23/2019.

Table of Contents

1. Introduction

The study of deformation processes in polycrystalline materials using diffraction methods has a long tradition. The use of neutron radiation [1–19] and high-energy synchrotron radiation [20–25] has proved to be particularly useful for this purpose. Due to the low absorption in most of the studied materials, these radiations allow for the measurements of the elastic lattice strains inside the sample, and the evolution of the lattice strains can be investigated *in situ* during deformation of the material. In this way, the mechanisms of plastic deformation in the polycrystalline grains, i.e. the phenomenon of slip on the crystalline planes and twinning, were studied. Interpretation of the results has typically been based on crystallographic models such as e.g. elastoplastic self-consistent (EPSC [4,8–12,16,17,19,23]) or elastic visco-plastic self-consistent (EVPSC [15,18]) models. The results of these models are usually compared with the lattice strains measured in the direction of the load applied to the sample and in the direction perpendicular to this load. This methodology, however, introduces ambiguities related to the assumptions of a specific model and the parameters used in it [26]. Therefore, attempts were made to directly determine the evolution of the stress tensor components for individual polycrystalline grains using synchrotron radiation and then to determine the variation of shear stresses on the slip or twinning systems [22]. The measurement method used for single crystallites is more direct and unambiguous, but its disadvantage is a small number of analysed grains which would give unrepresentative results. The task undertaken in this thesis is to use the selective feature of neutron diffraction to determine the evolution of the stress tensor for groups of grains belonging to different phases or having different grain orientations. In the conducted experiments, measurements are carried out for large sample volumes, containing a lot of crystallites, which ensures that the information is representative. Moreover, deformation measurements are made in many directions (not only in two), which allows estimating the variation of the stress tensor components and to directly investigate the deformation mechanisms at the level of the polycrystalline grains, without using the model. Moreover, the data obtained in this way allows to verify the assumptions of the models on the basis of the stresses at grain groups determined directly from the experiment. In this

work, two examples of materials described below are selected for the study, which are of practical importance and for which it is possible to separate stresses for groups of grains (AZ31 textured magnesium alloy) and for individual phases (Al/SiC_p composite).

1.1. Choice of materials and experimental methods

Among the many solid-state materials, metals are still the most widely used both in industry and in everyday life, especially due to their very good mechanical properties. In terms of crystal structure or composition, polycrystalline metallic materials can be divided into two groups: single-phase and multiphase (or composite) materials. A characteristic feature of polycrystals is their crystallographic texture depending on the specific material and the treatment used. As shown in many works, texture has a significant influence on the physical properties of a material [27–30]. One of the characteristics of highly textured materials is their anisotropic response to external conditions such as temperature and applied loads. For example, the anisotropy caused by texture can be very pronounced during plastic deformation, as shown in this work.

An example of a textured polycrystalline metal is the hot-rolled magnesium alloy AZ31 investigated in this work. This material has a hexagonal closed-packed (HCP) structure and isotropic crystal elastic constants. It shows a strong texture, with the dominant (0001) basal component, and its response to mechanical stress varies depending on the direction and type of load applied [31]. The high strength and low density of magnesium alloys make them attractive for industrial applications. Owing to their properties, they are often used in the aviation, automotive, electronics and medical industries [32–39]. In order to describe the plastic deformation of AZ31 alloy, many studies were carried out using various measurement techniques and analytical methods [14,16,19,29,40,41]. In previous works based on neutron diffraction experiments, (with the exception of paper [40]) the plastic properties of magnesium were studied mainly by fitting the results of the crystallographic model to the lattice strains measured *in situ* during mechanical tests. The disadvantage of such a methodology, however, is that it is difficult to eliminate the ambiguity of a large number of parameters used in the model [26]. In addition, assumptions such as the type of interaction between polycrystalline grains should be introduced into the model. The work undertaken in [40] was an attempt to determine the parameters of plastic strain and stress evolution for a polycrystalline grain directly from the diffraction experiment, and then to compare them with the model. This avoids ambiguity in determining parameters such as critical resolved shear stress (CRSS) for slip and twinning systems, and additional model assumptions are not necessary when describing plastic

deformation mechanisms. What is more, having information about the evolution of stresses for individual grains, it is possible to verify the type of intergranular interaction assumed in different models. This thesis is based on the first results presented in [40] and its aim is to develop a methodology based on direct diffraction measurements, allowing for a full description of the plastic deformation of AZ31 alloy at grain scale. To do this the diffraction crystallite group method (CGM) [42–46] in which the grain stresses are determined selectively for groups of grains having different lattice orientations should be significantly developed.

The Al/SiC_p composite is another example of a polycrystalline material for which a diffraction selective feature was used in this work. In this case, the stresses can be measured separately for Al and SiC due to the different diffraction patterns obtained for each component (phase). Multiphase materials, including composites, have physical properties that differ from those of each phase and result from their interaction. The composition of composite materials can be modified in order to obtain materials with desirable physical properties. One example of such composites are metal matrix composites (MMCs). In MMC, the metal matrix is doped with a stiffer and harder phase (reinforcement), which is most often a ceramic material. Ceramic materials are characterized by high stiffness, strength, resistance to high temperatures and abrasion resistance at a relatively low density, but they are brittle and not resistant to cracking [47,48]. Metals, in turn, are softer, more ductile, have lower strength, stiffness and are less heat resistant, deteriorating their mechanical properties at temperatures close to the melting point. The combination of the ceramic metallic phase with an addition of ceramics increases strength, stiffness, creep resistance in relation to metals as well as toughness and ductility in relation to ceramics [49–51]. Like magnesium alloys, MMCs are usually low-density and high-strength materials that are widely used in railways, aviation, maritime transport, construction and electronics [52–58].

There are several types of MMCs due to the nature of the reinforcement distribution. The most common and the simplest to create is the particle reinforcement leading to the isotropic properties of the composite material [59,60]. The phases present in such a material interact with each other through stress transfer or by the interaction of dislocations in the metal matrix with the reinforcement [50,61,62]. In MMCs the residual stresses can arise in individual phases of the composite material as a result of the production process. These stresses can be modified by changing external conditions, in particular by applying a load. The greatest change in stresses is observed when one of the phases deforms plastically [4,5,63]. An example of the composite studied in this work is the Al/SiC_p composite, in which the Al2124 aluminium matrix (83,2% by volume) is reinforced with SiC particles (17,8% by volume). The neutron diffraction study on the Al/SiC_p composite to date concerned mainly mechanical or thermal loading [1,6,64–66], however, the relaxation

during plastic deformation of the phase stresses resulting from the production of the material was not thoroughly investigated and explained. This is one of the goals of this thesis that can be achieved thanks to the selective feature of diffraction method.

1.2. The aims of the work

The first aim of the work is to develop diffraction methods for determining stresses and their interpretation in terms of using their selective feature that enables measurements for different phases or grain orientation. For this purpose, measurements should be made for many directions of the scattering vector and for different reflections hkl, which is possible e.g. in the case of a diffractometer at the EPSILON-MSD diffractometer used at the Frank Laboratory for Neutron Physic in Joint Institute for Nuclear Research in Dubna, Russia. This diffractometer is equipped with 9 detectors measuring the lattice strains in different directions, by using the TOF (time of flight) technique. Due to the possibility of collecting a lot of information about lattice deformation at the same time, this instrument enables the application of the crystallite group method with the use of neutron diffraction measurements. However, software should be developed that enables the preparation of the experiment and the interpretation of a large number of data.

The second goal is to study the stress evolution in both constituents of the thermally treated Al/SiC_p composite during the compression test. It is expected that the relaxation of the thermally induced phase stresses can be observed simultaneously with the evolution of the phase stresses induced by elastoplastic deformation. Then, the thermo-mechanical self-consistent model should be developed to explain the observed evolution of the two types of phase stresses during the compression test.

Another aim of the research is to verify the crystallite groups method (CGM) as a method that allows for the determination of stresses localized at various groups of crystallites, including those which are not dominant in the sample (it concerns the textured AZ31 alloy). Then, the stresses localized at groups of grains having different lattice orientations will be determined and the analysis of these data will show which groups of grains are the most responsible for the macroscopic behaviour of the sample subjected to different types of loading (the anisotropy of the plastic behaviour of the sample will be explained on the basis of plastic deformation mechanics occurring at the scale of polycrystalline grain).

Finally, the EPSC model will be verified on the basis of the experimental data obtained from the experiment performed with the AZ31 sample, i.e. experimental CRSS values can be entered into the model. Therefore, the type of intergranular interaction will be

determined by comparing the stress evolution determined for grain groups with the stresses predicted by the model for the corresponding grain orientations. In addition, the hardening process for slip systems will be described from the measured RSS evolutions and those predicted by the model.

It should be emphasized that the wide scope of this work concerns the development of experimental methodology, the study of material properties and theoretical modelling of the observed processes.

2. Elastic behaviour of crystals and polycrystalline materials

Each solid body subjected to external loads is deformed. Depending on the material from which the solid body is made, this deformation will proceed in different ways. Ceramic materials are hard, brittle materials that only deform elastically and break when the critical stress is exceeded. Metallic materials, which are the main topic of this work, belong to the group of materials in which the elastic behaviour occurs up to a certain critical stress, called the yield point. Then they undergo plastic deformation with strain hardening up to the ultimate strength, followed by necking and final fracture (plastic deformation will be described in next chapter). The nature of both behaviours is shown in Fig. 2.1

It is noteworthy that stiff ceramic materials generally undergo much less deformation at the same applied stress compared to metals. Therefore combination of the ductile metal and stiff ceramic materials in the composites leads to significant improvement of the mechanical properties (as in the case Al/SiC_p composite studied in this work).

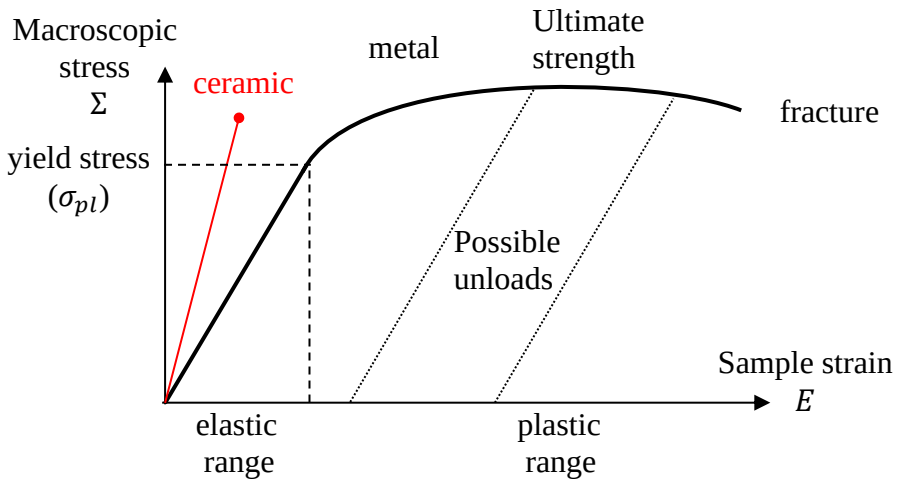

Fig. 2.1 Example macroscopic behaviour of material determined using tensile test. The relation between macroscopic stress (Σ) and sample strain (E) is presented.

This chapter presents the basic theoretical information on the elastic behaviour of solid body below the yield point, especially concerning crystals and polycrystalline materials. Moreover, the most important definitions and basic mathematical conventions are introduced. Therefore, the physical quantities (stress, strain and elastic tensors) used to describe the mechanical state of the material under an applied load are presented.

It should be emphasized that during the deformation of the polycrystalline material, various stresses are localised at the grains, hence their characteristic is very important. Depending on the local stress state, elastic or plastic deformation, and even damage process, occur at the grain scale. The relationship between the elastic deformation of the solid body and stresses are described by the macroscopic elastic constants defined in this chapter. To describe the mechanical behaviour of the polycrystalline material under applied load the stresses and strains at the microscopic and macroscopic scales, as well as elastic constants of crystallites and the intergranular interactions are considered.

2.1. Elasticity of solid body under applied load

The mathematical description of stresses requires the use of a second order tensor. To define the stress tensor components, one should divide the solid body into many infinitesimal cubes and determine the values of normal and tangential forces' components acting on an unit area of rectangular surfaces, as illustrated in Fig. 2.2. The components of a stress tensor and are defined as:

$$\sigma_{ij} = \lim_{\Delta S_j \to 0} \left(\frac{F_i}{\Delta S_j} \right) = \frac{\partial F_i}{\partial S_j} \tag{2.1}$$

where F_i is a force component acting on the surface ΔS_j (cf. Fig. 2.2).

If $i=j$, the values of σ_{11}, σ_{22} , σ_{33} are called normal stress components, while for $i \neq j$ the values of σ_{12}, σ_{21}, σ_{13}, σ_{31}, σ_{23}, σ_{32} are called the shear components. The equality between the symmetrical components of the stress tensor ($\sigma_{ij} = \sigma_{ji}$), occurring due to the static equilibrium of force moments, reduces the number of independent components from 9 to 6. This allows us to write the stress tensor in one of two forms, i.e. as a 3 x 3 matrix or according to Voigt notation in the form of a vector with 6 components. The relations between components defined using these conventions is given by equation (2.2) [43,67].

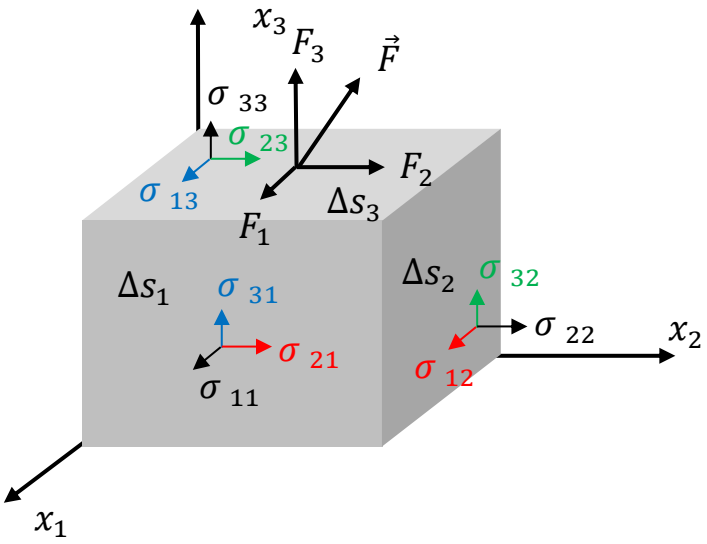

Fig. 2.2 The stress components defined for an infinitesimal cube (force acting on the surface S_3 is decomposed into normal and tangential components) [3].

$$\sigma_{ij} = \begin{bmatrix} \sigma_{11} & \sigma_{12} & \sigma_{13} \\ \sigma_{21} & \sigma_{22} & \sigma_{23} \\ \sigma_{31} & \sigma_{32} & \sigma_{33} \end{bmatrix} = \begin{bmatrix} \sigma_1 & \sigma_6 & \sigma_5 \\ \sigma_6 & \sigma_2 & \sigma_4 \\ \sigma_5 & \sigma_4 & \sigma_3 \end{bmatrix} \quad \text{and} \quad \sigma_i = \begin{bmatrix} \sigma_{11} \\ \sigma_{22} \\ \sigma_{33} \\ \sigma_{23} \\ \sigma_{13} \\ \sigma_{12} \end{bmatrix} = \begin{bmatrix} \sigma_1 \\ \sigma_2 \\ \sigma_3 \\ \sigma_4 \\ \sigma_5 \\ \sigma_6 \end{bmatrix} \tag{2.2}$$

The possible criterion for the classification of stresses is the form of a stress tensor. Taking this criterion into account, we can distinguish uniaxial, hydrostatic and deviatoric stresses, which correspond to simplest forms of the stress tensor.

Uniaxial stress is when the force acts in one direction only and it is perpendicular to given plane, for example cross section of a sample during tensile/compression test. A mathematical description of this stress state is given by a tensor with one non-zero diagonal component and all other components are equal to zero (equation (2.3)). Depending on the direction of the applied force, we say that the stress is tensile ($\sigma > 0$) or compressive ($\sigma < 0$).

In a state of hydrostatic stress, the solid body is compressed (or stretched) on all sides with the equal stress, i.e. the stress tensor consist of non-zero diagonal components equal to each other and all zero off-diagonal components (this stress causes the solid body volume to change due to elastic deformation, while the plastic deformation cannot occur). On contrary the deviatoric stress tensor is traceless and it can be transformed to the form which contains non-zero off-diagonal components, while the diagonal ones are equal to zero

(equation (2.3)). Such a state of stress forces a change in the shape of the solid body caused by elastic or plastic deformation.

$$\sigma_{ij}^{uniaxial} = \begin{bmatrix} 0 & 0 & 0 \\ 0 & 0 & 0 \\ 0 & 0 & \sigma \end{bmatrix},\ \sigma_{ij}^{hydrostatic} = \begin{bmatrix} p & 0 & 0 \\ 0 & p & 0 \\ 0 & 0 & p \end{bmatrix}, \sigma_{ij}^{deviatoric} = \begin{bmatrix} 0 & u & v \\ u & 0 & w \\ v & w & 0 \end{bmatrix} \quad (2.3)$$

Each stress tensor can be represented as a combination of hydrostatic and deviatoric tensors components. To do this, first the stress tensor should be presented in the system of principal axes (diagonalization of the tensor, described by equations (2.4))

$$\begin{aligned} \sigma_{ij} = \begin{bmatrix} \sigma_{11} & \sigma_{12} & \sigma_{13} \\ \sigma_{21} & \sigma_{22} & \sigma_{23} \\ \sigma_{31} & \sigma_{32} & \sigma_{33} \end{bmatrix} \xrightarrow{diagonalisation} \sigma'_{ij} = \begin{bmatrix} a & 0 & 0 \\ 0 & b & 0 \\ 0 & 0 & c \end{bmatrix} \\ = \begin{bmatrix} p & 0 & 0 \\ 0 & p & 0 \\ 0 & 0 & p \end{bmatrix} + \begin{bmatrix} q & 0 & 0 \\ 0 & r & 0 \\ 0 & 0 & s \end{bmatrix} \end{aligned} \quad (2.4)$$

where $p = \frac{a+b+c}{3}$, $q = a - p$, $r = b - p$, $s = c - p$ and $q + r + p = 0$.

Then, so obtained diagonal tensor can be presented as a sum of a hydrostatic tensor and an additional tensor, which, after appropriate rotations of the coordinate system, will change into a purely deviatoric form (equations (2.4) and (2.5)). It is worth noting that the rotation does not affect the hydrostatic tensor.

$$\begin{bmatrix} p & 0 & 0 \\ 0 & p & 0 \\ 0 & 0 & p \end{bmatrix} + \begin{bmatrix} q & 0 & 0 \\ 0 & r & 0 \\ 0 & 0 & s \end{bmatrix} \xrightarrow{rotations} \begin{bmatrix} p & 0 & 0 \\ 0 & p & 0 \\ 0 & 0 & p \end{bmatrix} + \begin{bmatrix} 0 & \sqrt{-\frac{qs}{2}} & \sqrt{-\frac{qs}{2}} \\ \sqrt{-\frac{qs}{2}} & 0 & -r \\ \sqrt{-\frac{qs}{2}} & -r & 0 \end{bmatrix} \quad (2.5)$$

The forces acting on the material cause a change in shape and volume of the solid body, which can be described by a displacement gradient (expressed by a second order tensor, cf. (2.2)), composed of a symmetric deformation tensor and an antisymmetric rotation tensor. Therefore, the definition of the deformation tensor is given by the formula:

$$\varepsilon_{ij} = \frac{1}{2}\left(\lim_{\delta x_i \to 0} \frac{\delta w_j}{\delta x_i} + \lim_{\delta x_j \to 0} \frac{\delta w_i}{\delta x_j} \right), \quad (2.6)$$

where: $\left(\frac{\delta w_i}{\delta x_i}, \frac{\delta w_i}{\delta x_j}, \frac{\delta w_i}{\delta x_k} \right)$ is a gradient of the displacement w_i occurring in direction i.

The antisymmetric rotation tensor is defined as:

$$\omega_{ij} = \frac{1}{2}\left(\lim_{\delta x_i \to 0} \frac{\delta w_j}{\delta x_i} - \lim_{\delta x_j \to 0} \frac{\delta w_i}{\delta x_j}\right) \tag{2.7}$$

The displacements of the square vertices for a two-dimensional example are shown in Fig. 2.3.

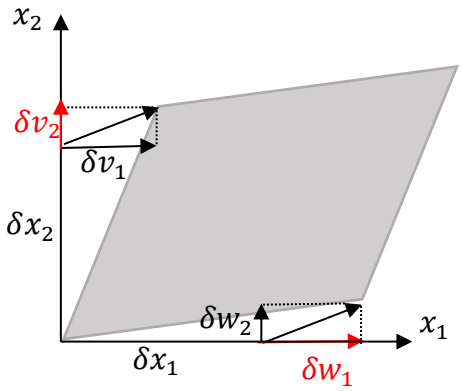

Fig. 2.3 Illustration of deformation of the 2D body with displacements of the square vertices. For better visualisation, the displacements related to the line sectors δx_1 and δx_2 are denoted by δw_i and δv_i, respectively (note that in the formulas (2.6) and (2.7) all displacements are expressed by δw_i).

Due to the fact that the strain tensor is a symmetrical tensor of the second order, we can also express it by means of a strain matrix or a vector (Voigt notation) [67]:

$$\varepsilon_{ij} = \begin{bmatrix} \varepsilon_{11} & \varepsilon_{12} & \varepsilon_{13} \\ \varepsilon_{21} & \varepsilon_{22} & \varepsilon_{23} \\ \varepsilon_{31} & \varepsilon_{32} & \varepsilon_{33} \end{bmatrix} = \begin{bmatrix} \varepsilon_1 & \frac{1}{2}\varepsilon_6 & \frac{1}{2}\varepsilon_5 \\ \frac{1}{2}\varepsilon_6 & \varepsilon_2 & \frac{1}{2}\varepsilon_4 \\ \frac{1}{2}\varepsilon_5 & \frac{1}{2}\varepsilon_4 & \varepsilon_3 \end{bmatrix} \quad \text{and} \quad \varepsilon_i = \begin{bmatrix} \varepsilon_1 \\ \varepsilon_2 \\ \varepsilon_3 \\ \varepsilon_4 \\ \varepsilon_5 \\ \varepsilon_6 \end{bmatrix} = \begin{bmatrix} \varepsilon_{11} \\ \varepsilon_{22} \\ \varepsilon_{33} \\ 2\varepsilon_{23} \\ 2\varepsilon_{13} \\ 2\varepsilon_{12} \end{bmatrix} \tag{2.8}$$

As stresses and strains have already been defined, so now it is necessary to define the relations between them occurring in the case of elastic deformation. Considering an isotropic material and uniaxial stress, this relation is given by two constants called the Young modulus (E) and Poisson ratio (v). In this case the Hooke's law is given by the equations:

$$\sigma_{11} = E\,\varepsilon_{11} \quad \text{or} \quad \varepsilon_{11} = \frac{\sigma_{11}}{E}$$
$$\text{and } \varepsilon_{22} = \varepsilon_{33} = -v\varepsilon_{11}, \tag{2.9}$$

In general, for the 3D case, Hooke's law is written in tensor form using the elastic constants c_{ijkl} and s_{ijkl}:

$$\sigma_{ij} = c_{ijkl}\varepsilon_{kl} \quad \text{and} \quad \varepsilon_{ij} = s_{ijkl}\sigma_{kl} \tag{2.10}$$

where c_{ijkl} and s_{ijkl} are the components of fourth-rank stiffness and compliance tensors, respectively.

Equation (2.10) can also be written in the Voigt convention, which uses 6x6 stiffness and compliance matrices:

$$\sigma_i = c_{ij}\varepsilon_j \quad \text{and} \quad \varepsilon_i = s_{ij}\sigma_j, \tag{2.11}$$

where the relations between indices used in the two conventions are given by (2.2) and(2.8). The relationships between the elastic constants in the four-order tensor convention and the Voigt convention are given below:

$$c_{ij} = c_{mnkl} \quad \text{and} \quad s_{ij} = p_{ij}s_{mnkl}$$
$$\text{where} \quad p_{ij} = \begin{pmatrix} 1 & 1 & 1 & 2 & 2 & 2 \\ 1 & 1 & 1 & 2 & 2 & 2 \\ 1 & 1 & 1 & 2 & 2 & 2 \\ 2 & 2 & 2 & 4 & 4 & 4 \\ 2 & 2 & 2 & 4 & 4 & 4 \\ 2 & 2 & 2 & 4 & 4 & 4 \end{pmatrix} \tag{2.12}$$

and the pairs of indices (*mn* and *kl*) are replaced with single indices (*i* and *j*) according to the rule: 11 → 1, 22 → 2, 33 → 3, 23 or 32 → 4, 13 or 31 → 5, 12 or 21 → 6.

The symmetry of the matrices of elastic constants results from the fact that the stress and strain tensors are symmetrical, i.e.:

$$s_{ij} = s_{ji} \quad \text{and} \quad c_{ij} = c_{ji} \tag{2.13}$$

2.2. Elastic behaviour of crystals

The elastic constants depend on the chemical composition of the material as well as its crystal structure. In general, the matrix of elastic constants may contain 21 independent non-zero components (this is the case of triclinic cell), however the crystal symmetries reduces their number. In the case of most popular metals' crystallographic structures the number of independent components is equal: 5 for hexagonal close packed lattice HCP (2.14), 3 for face centred cubic FCC and body centred cubic BCC lattices (2.15) while only 2 components are needed to describe properties of isotropic material (2.16).

The matrix of elastic constants for HCP lattice has the following structure [68]:

$$a_{ij}^{HCP} = \begin{pmatrix} a_{11} & a_{12} & a_{13} & & & \\ & a_{11} & a_{13} & & & \\ & & a_{33} & & & \\ & & & a_{44} & & \\ & & & & a_{44} & \\ & & & & & a_{66} \end{pmatrix}, \tag{2.14}$$

where $a_{66} = \begin{cases} 2(a_{11} - a_{12}) \text{ for compliance matrix, i. e. for } a_{ij} = s_{ij} \\ \frac{1}{2}(a_{11} - a_{12}) \text{ for stiffness matrix, i. e. for } a_{ij} = c_{ij} \end{cases}$

In the case of cubic lattices (FCC and BCC) we have [68]:

$$a_{ij}^{cubic} = \begin{pmatrix} a_{11} & a_{12} & a_{12} & & & \\ & a_{11} & a_{12} & & & \\ & & a_{11} & & & \\ & & & a_{44} & & \\ & & & & a_{44} & \\ & & & & & a_{44} \end{pmatrix}, \tag{2.15}$$

both for compliance and stiffness matrices.

These tensors for isotropic material have the form [68]:

$$a_{ij}^{isotropic} = \begin{pmatrix} a_{11} & a_{12} & a_{12} & & & \\ & a_{11} & a_{12} & & & \\ & & a_{11} & & & \\ & & & a_{66} & & \\ & & & & a_{66} & \\ & & & & & a_{66} \end{pmatrix}, \tag{2.16}$$

where $a_{66} = \begin{cases} 2(a_{11} - a_{12}) \text{ for compliance matrix, i. e. for } a_{ij} = s_{ij} \\ \frac{1}{2}(a_{11} - a_{12}) \text{ for stiffness matrix, i. e. for } a_{ij} = c_{ij} \end{cases}$

2.3. Polycrystalline materials and their elastic deformation

2.3.1. Orientation distribution function

When measuring and modelling the mechanical properties of polycrystalline materials, it is important to know the orientation distribution of grain lattice. It is a material property that significantly affects the mechanical properties of the material, such as a different mechanical behaviour depending on the direction of the applied external force. Forming a material, such as rolling, forging, drawing or extruding, allows the directions of the coordinate system to be defined. For example, in rolling, the coordinate system can be clearly defined as shown in Fig. 2.4.

To describe the orientation of the grain crystal lattice in relation to the sample the Miller indices can be used, i.e. the lattice orientation is given by the notation $\{hkl\} < uvw >$. In this convention the crystallographic plane parallel to the sample surface $\{hkl\}$ and the direction $< uvw >$ parallel to the x_1 axis of the sample system are indicated (x_1 is the direction characteristic for this process, e.g. x_1 || RD - rolling direction, cf. Fig. 2.4)

This notation may be used to indicate preferred texture orientations, but is not sufficient to describe a statistical distribution of the crystallite orientation. Therefore a more convenient method for description of grain orientations is the usage of Euler angles [67], which define rotations about the sample coordinates system (x_1, x_2, x_3) to bring it to the crystallite system (x_1^c, x_2^c, x_3^c), as shown in Fig. 2.5. The system (x_1^c, x_2^c, x_3^c) is defined by the principal crystallographic directions: [100], [010] and [001]. The first rotation is done about the x_3' axis by angle φ_1 and the next rotation is done about new x_1' axis by angle Φ. As a result of these rotations the x_3'' axis coincides with x_3^c axis of crystal system. The last rotation φ_2 , about x_3'' ‖ x_3^c axis brings the x_1''' and x_2''' axes to the x_1^c and x_2^c axes, respectively. The so defined three rotations unambiguously define orientation of the grain lattice with respect to the sample.

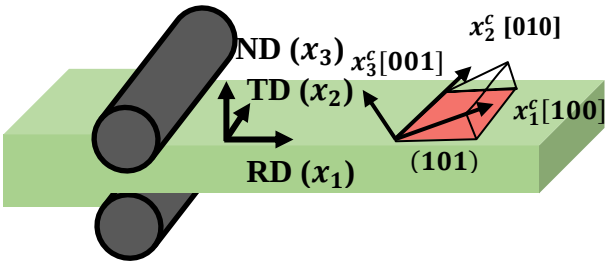

Fig. 2.4 Definition of sample coordinate system defined in the case of a rolled material and orientation of a crystallite described by Miller indices $(101)[10\bar{1}]$.

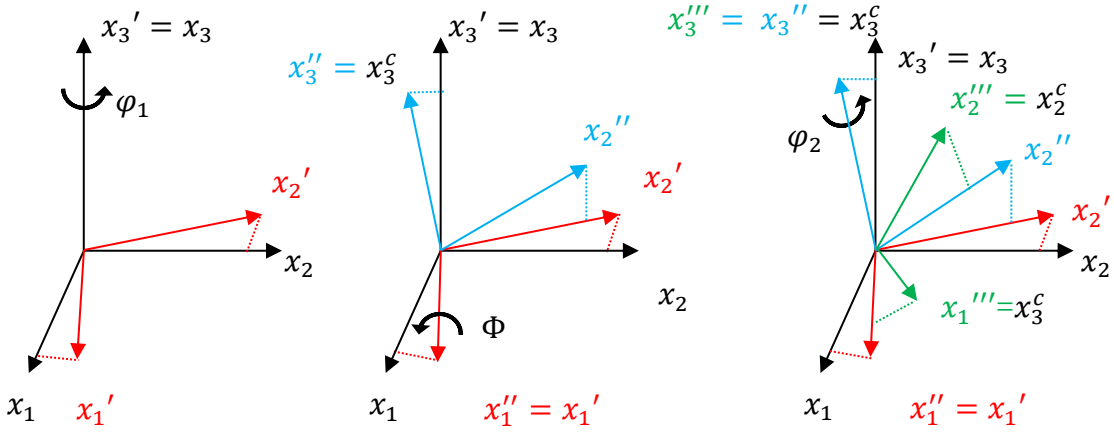

Fig. 2.5 Rotations by Euler angles in the X3-X1-X3 convention. [67]

To define the function describing grains orientation the Euler space is introduced, in which three angles $\varphi_1, \Phi, \varphi_2$ are the coordinates of a Cartesian system. Then, the so-called orientation distribution function (ODF) is introduced in the Euler space. It is a density function defining a volume fraction of the crystallites in the polycrystalline material having orientation within infinitesimal cube $\mathrm{d}\varphi_1\mathrm{d}\Phi\mathrm{d}\varphi_2$ surrounding orientation $\varphi_1, \Phi, \varphi_2$ in the Euler space [30].

$$\frac{dV_g}{V} = f(g)\mathrm{d}g = f(\varphi_1, \Phi, \varphi_2)\frac{\sin\Phi}{8\pi^2}\mathrm{d}\varphi_1\mathrm{d}\Phi\mathrm{d}\varphi_2 \tag{2.17}$$

where $dg = \frac{\sin\Phi}{8\pi^2}\varphi_1\mathrm{d}\Phi\mathrm{d}\varphi_2$ is an elementary volume of the orientation space.

The dimension of the entire Euler space is determined by the range of Euler angles $\varphi_1 \in [0°, 360°]$, $\Phi \in [0°, 180°]$, $\varphi_2 \in [0°, 360°]$. In case of a sample with a orthorhombic symmetry (determined by e.g. rolling process) and cubic lattice of grains, the basic range is reduced to $\varphi_1 \in [0\,°, 90\,°]$, $\Phi \in [0°, 90°]$, $\varphi_2 \in [0°, 90°]$; and for the same sample symmetry and hexagonal lattice $\varphi_1 \in [0°, 90°]$, $\Phi \in [0°, 90°]$, $\varphi_2 \in [0°, 60°]$.

The most common way of presenting ODF is a set of several two-dimensional maps, which are the sections through Euler space shifted by a constant step 5° along the φ_1 (or φ_2) axis. The values of the $f(g)$ function are presented on these maps using contour lines filled with shades of grey or with colours (Fig. 2.6).

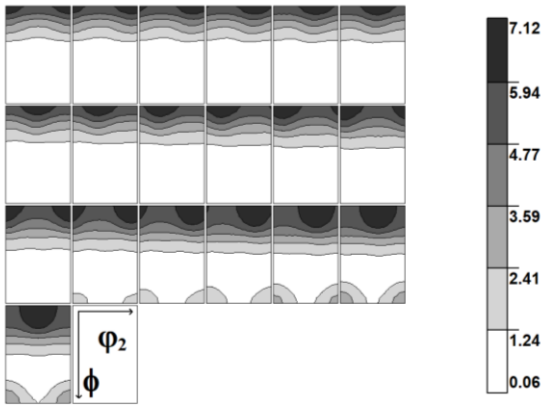

Fig. 2.6 Example of orientation distribution function (ODF) for hot rolled AZ31 magnesium alloy after compression test up to strain 2% in rolling direction. The sections through Euler space displaced with a constant step of 5° along the φ_1 axis ($\varphi_1 \in [0°, 90°]$, $\Phi \in [0°, 90°]$, $\varphi_2 \in [0°, 60°]$).

The orientation distribution function gives full information about the orientation distribution in a given material and it can be to obtained using two experimental techniques, i.e. Electron Back-Scattered Diffraction (EBSD) measurement and diffraction measurements of pole figures.

The measurements using EBSD technique are based on the diffraction of back scattered electrons on the lattice of near surface grain, resulting in a diffraction pattern in the form of Kikuchi lines registered on 2D detector. Using basic information about the crystal structure of the material, it is possible to identify the orientation of this grain from the Kikuchi pattern. The measurement is performed using scanning electron microscope and the map of orientations can be obtained with the resolution of a fraction of micrometre (the information for each point is available). The results are presented as the inverse pole figure map showing the crystallographic direction normal to the surface and visualizing the microstructure and size of the grains (Fig. 2.7). The important advantage of the EBSD measurement is that the misorientations between grains can be determined, which is very useful for twin studies. Moreover, the ODF function can be determined when the statistic of orientations for all map points is analysed. The disadvantage of this method that is that the measurements are performed for a very thin layer below the surface (from a few to several tenths of nm) due to small penetration depth of electrons in the studied materials.

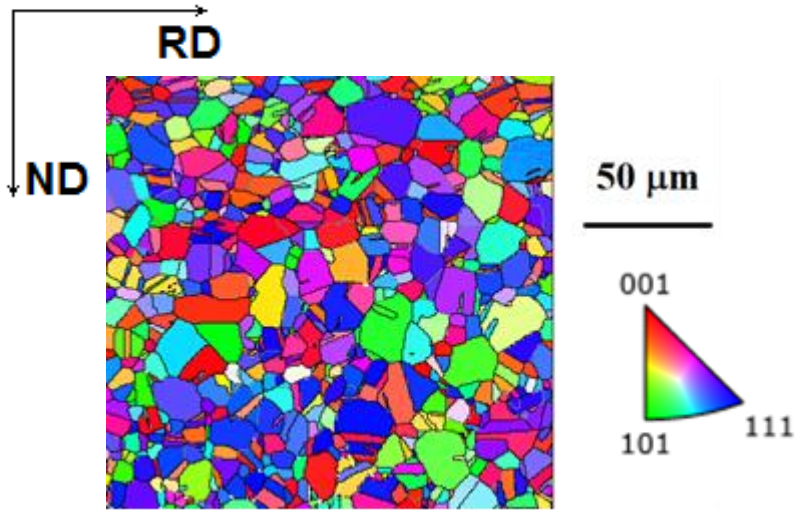

Fig. 2.7 Example of EBSD map for hot rolled austenitic steel.

The second method of ODF determination is based on the diffraction measurement of a set of direction distribution functions $P(\alpha,\beta)_{\{hkl\}}$, determined using different hkl reflections. The two-dimensional $P(\alpha,\beta)_{\{hkl\}}$ function depends on the polar coordinates α and β characterizing the orientation of given direction with respect to the sample system (Fig. 2.8a). This orientation is represented by a point in the stereographic projection (Fig. 2.8b). The $P(\alpha,\beta)_{\{hkl\}}$ is a density function defining a volume fraction of the crystallites $\frac{dV_{\{hkl\}}}{V}$ for which one of the poles of the $\{hkl\}$ type (i.e. directions normal to the $\{hkl\}$ planes) has the orientation within the solid angle $d\omega$:

$$\frac{dV_{\{hkl\}}}{V} = P_{\{hkl\}}(\alpha,\beta)d\omega \tag{2.18}$$

where: $d\omega = \frac{1}{4\pi} sin\,\alpha \;\; d\alpha \; d\beta$ is a solid angle corresponding to infinitely small intervals $(\alpha, \alpha + d\alpha)$ and $(\beta, \beta + d\beta)$.

The mathematical relationship between the pole figure and the orientation distribution function $f(\alpha,\beta,\gamma)$ is as follows:

$$P(\alpha,\beta)_{\{hkl\}} = \int_0^{2\pi} f(\alpha,\beta,\gamma)\,\mathrm{d}\gamma \tag{2.19}$$

where γ is a rotation angle about hkl-pole and the $f(\alpha,\beta,\gamma)$ values should be determined for the Euler angles $\varphi_1, \Phi, \varphi_2$ corresponding to the angles α,β,γ

The pole density function $P(\alpha,\beta)_{\{hkl\}}$ is shown as the map on stereographical projections plane (Fig. 2.8c). To calculate the ODF from a set of pole figures measured for different $\{hkl\}$ plane families appropriate algorithms were developed [30,69,70].

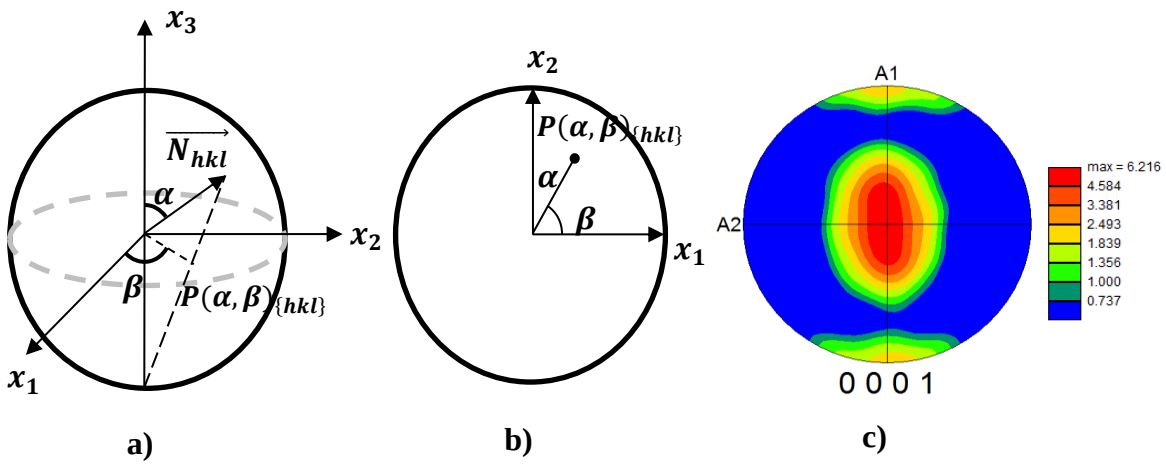

Fig. 2.8 The principle of a stereographic projection (a and b) and pole figure (0001) measured for hot rolled AZ31 magnesium alloy sample (c).

The advantage of the diffraction method is that the texture can be measured using different radiations. Due to high absorption in the materials the texture in the subsurface layer (of a several or dozen μm) is measured using X- rays. On the contrary, the average texture for a large sample volume can be determined with neutrons due to their low absorption in many materials.

It should be emphasized that the ODF is treated as the weighting function when the mean properties of polycrystalline material are calculated, as it is shown in this work. In the presented here methodologies for stress measurements the stereographic projection and pole figures are used to select the preferred grain orientations.

2.3.2. Stresses in polycrystalline material

The stress field in polycrystalline materials can be heterogeneous and anisotropic at the scale of grain groups or individual grains. The stress at a given point in these materials can be described in terms of first order stresses, second order stresses, and third order stresses. Each of stress types has a different extent and cause for its occurrence [71–73].

The first-order stresses are the overall stresses occurring for the relatively large volumes containing many polycrystalline grains, mainly due to external forces applied to the sample or internal inhomogeneity of plastic deformations resulting from mechanical or thermal processing [72]. This type of stress can be defined for the entire sample volume

or for a certain volume selected in the sample (for example, the volume from which the stress is measured by diffraction). First order stresses occur e.g. in the surface layer of a mechanically / thermally treated sample and the stress varies with depth leading to a balance of forces and moments of forces through the sample. They can also be generated due to the difference in thermal expansion of two different materials bonded together, such as coatings deposited on a substrate. The first-order stress is defined as the mean value (see Fig. 2.9a and Fig. 2.10a):

$$\sigma_{ij}^{I} = \frac{1}{V}\int_{V} \sigma_{ij}(\vec{r})\ \mathrm{dV} = \sum_{g}^{N} f^{g}\sigma_{ij}^{g}, \tag{2.20}$$

where: V – polycrystalline volume for which the stress is defined, g – grain number, N – number of grains in the volume V, f^{g} – grain volume fraction, $\sigma_{ij}(\vec{r})$ – local stress at $\vec{r}$ position, σ_{ij}^{g} – grains stresses.

Different stresses can arise in multiphase materials that are subjected to tensile / compression tests or thermal processes in different phases due to different physical properties. Therefore, it is convenient to distinguish between these phases and introduce the concept of phase stresses σ_{ij}^{ph}, which can be defined analogously to the first-order stresses, i.e . (see Fig. 2.10b):

$$\sigma_{ij}^{ph} = \frac{1}{V_{ph}}\int_{V_{ph}} \sigma_{ij}(\vec{r})\ \mathrm{dV_{ph}} = \sum_{g}^{N_{ph}} f^{g}\sigma_{ij}^{g}, \tag{2.21}$$

where: V_{ph} – considered phase volume, N_{ph} – number of grains of belonging to *ph*-phase having volume V_{ph} , $f^{g} = \frac{V_g}{V_{ph}}$ – grain volume fraction relatively to V_{ph}.

Stresses defined in this way for individual phases allow to introduce a relationship between them and the first order stress, i.e. (see Fig. 2.9 and Fig. 2.10)::

$$\sigma_{ij}^{I} = \sum_{ph} f^{ph}\sigma_{ij}^{ph}, \tag{2.22}$$

where f^{ph} is the volume fraction of the ph phase in the entire considered sample volume, and σ_{ij}^{ph} is the average stress for *ph* phase.

Second order stresses are the stresses occurring between grains in the sample. They are caused by different orientations of the lattice in relation to the sample, which is the reason for the different behaviour of the crystallites [72] . When external forces are applied to the material, the elastic response ($\sigma^{g,ER}$) of the grain will depend on its orientation since the elastic constants of a single crystal are often anisotropic. Another reason for second order stresses is mechanical machining. During the plastic deformation of a polycrystalline material, the differences between the plastic deformations of grains having different orientations cause their mismatch in the boundary areas. This leads to the so-called incompatibility stresses ($\sigma^{g,IC}$). Second order stresses may also arise during the cooling or heating process due to the anisotropy of the thermal expansion coefficients of the phases or

crystallites, which leads to different grain contractions or stretching in different directions relative to the sample. The second order stresses can be defined as the difference between the averaged stresses for the grain and the first order stresses (for a single-phase material) or the stresses in a given phase (for a multi-phase material); (c.f. Fig. 2.9 and Fig. 2.10):

$$\sigma_{ij}^{II} = \sigma_{ij}^{g} - \sigma_{ij}^{I} \quad \text{or} \quad \sigma_{ij}^{II} = \sigma_{ij}^{g} - \sigma_{ij}^{ph}, \tag{2.23}$$

An important property of such defined second-order stresses is that they equilibrate in the entire volume of the sample, i.e. their sum is zero.

Finally, third order stresses, called local stresses, change inside the grain. They are the result of the accumulation of dislocations or the presence of other structural defects. Their mathematical definition can be presented using the formula (see Fig. 2.9a and Fig. 2.10a):

$$\sigma_{ij}^{III}(\vec{r}) = \sigma_{ij}(\vec{r}) - \sigma_{ij}^{g} \tag{2.24}$$

where $\sigma_{ij}(\vec{r})$ is the actual value of the stress at the point, and σ_{ij}^{g} is the average value of the stress in the grain. This definition implies that their sums inside the grain is equal to zero.

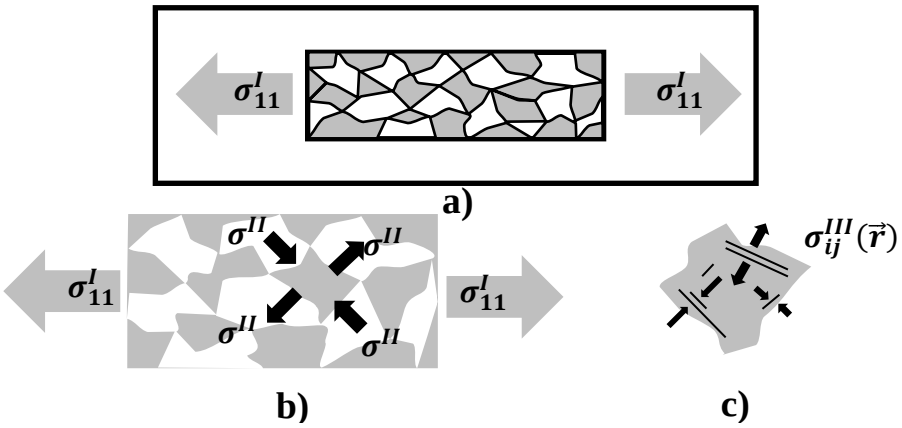

Fig. 2.9 Scheme of stresses in polycrystalline material: a) first order stress, b) second order stress, c) third order stress.

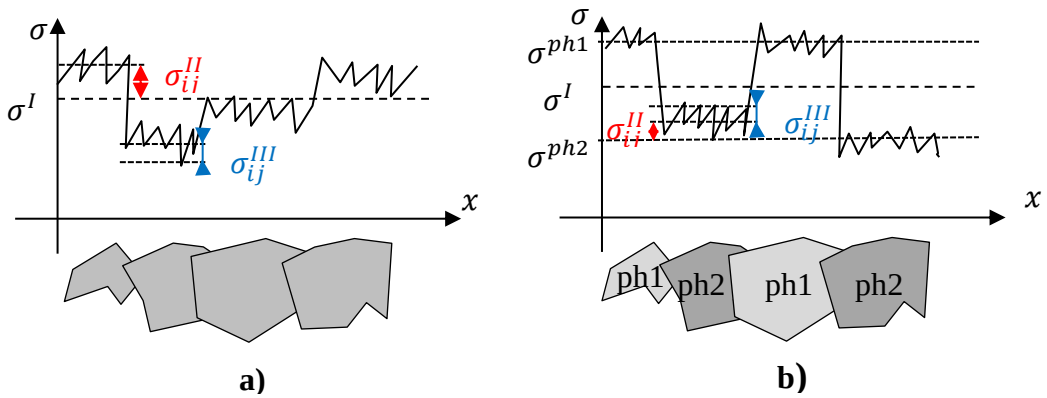

Fig. 2.10 Scheme of stress different types of stresses in polycrystalline material: a) single phase and b) multiphase [65].

2.3.3. Macroscopic elastic constants of polycrystalline materials

To calculate the first order stresses and macroscopic elastic constants the transformation between crystallite frame and sample frame are very useful. For example when shear stresses on slip or twinning systems or overall elastic constants for polycrystalline material are computed. To find out these transformations the rotation matrices are defined as shown below for the rotations by angle Φ about axis x_1 and by φ angle about axis x_3, respectively, i.e:

$$R_1(\Phi) = \begin{bmatrix} 1 & 0 & 0 \\ 0 & \cos\Phi & \sin\Phi \\ 0 & -\sin\Phi & \cos\Phi \end{bmatrix}, \quad R_3(\varphi) = \begin{bmatrix} \cos\varphi & \sin\varphi & 0 \\ -\sin\varphi & \cos\varphi & 0 \\ 0 & 0 & 1 \end{bmatrix} \tag{2.25}$$

Thus, for subsequent rotations of the sample frame about x_3 by the angle φ_1, about $x_1{}'$ by the angle Φ and about $x_3{}''$ axis by the angle φ_2 we obtain the following rotation matrix:

$$g_{ij}(\varphi_1, \Phi, \varphi_2) = \begin{bmatrix} c_1c_2 - s_1s_2C & s_1c_2 + c_1s_2C & s_2S \\ -c_1s_2 - s_1c_2C & -s_1s_2 + c_1c_2C & c_2S \\ s_1S & -c_1S & C \end{bmatrix} \tag{2.26}$$

where $s_i = \sin\varphi_i$, $c_i = \cos\varphi_i$, $S = \sin\Phi$, $C = \cos\Phi$.

The transformations of the stress and strain tensors from sample strain to crystallite frame are given by:

$$\sigma_{ij}^{new} = g_{ik}g_{jl}\sigma_{kl}^{old}, \ \varepsilon_{ij}^{new} = g_{ik}g_{jl}\varepsilon_{kl}^{old}, \tag{2.27}$$

while the single crystal elastic tensors are transformed as follows:

$$\begin{aligned} s_{ijkl} &= g_{im}g_{jn}g_{ko}g_{lp}s_{mnop}\,, \\ c_{ijkl} &= g_{im}g_{jn}g_{ko}g_{lp}c_{mnop} \end{aligned} \tag{2.28}$$

Having defined stresses and strains for all grains with respect to the sample coordinate system, macroscopic stress (Σ_{ij}) and strain (E_{ij}) tensors can be calculated analogously to equation (2.20):

$$\Sigma_{ij} = \frac{1}{V_s}\int_{V_s}\sigma_{ij}(\vec{r})\,\mathrm{dV} = \sum_g^N f^g\sigma_{ij}^g, \qquad E_{ij} = \frac{1}{V_s}\int_{V_s}\varepsilon_{ij}(\vec{r})\,\mathrm{dV} = \sum_g^N f^g\varepsilon_{ij}^g, \tag{2.29}$$

where the averages are calculated over all grains (N) withing entire volume of the sample V_s .

Different methods were used to calculate overall elastic constants of polycrystalline material. In general we can postulate existence of macroscopic elastic constants C_{ijkl} and S_{ijkl} which fulfil the following relations:

$$\Sigma_{ij} = C_{ijkl}\, E_{kl}\,, \quad E_{ij} = S_{ijkl}\, \Sigma_{kl} \quad \text{and} \quad C_{ijkl} = S_{ijkl}^{-1} \tag{2.30}$$

According to the simplest assumptions of homogenous stress (introduced by Reuss[74]) the effective compliance tensor S_{ijkl} can be calculated:

$$\sigma_{ij}^{g} = \Sigma_{ij} \quad \Rightarrow \quad S_{ijkl}^{R} = \left\{ \sum_{g}^{N} f^{g} s_{ijmn}^{g} \right\} \tag{2.31}$$

and this definition can be easy proved:

$$\begin{aligned} E_{ij} &= \sum_{g}^{N} f^{g} \varepsilon_{ij}^{g} = \sum_{g}^{N} f^{g} s_{ijmn}^{g} \sigma_{mn}^{g} = \sum_{g}^{N} f^{g} s_{ijmn}^{g} \Sigma_{mn} \\ &= \left\{ \sum_{g}^{N} f^{g} s_{ijmn}^{g} \right\} \Sigma_{mn}\,. \end{aligned} \tag{2.32}$$

On the other hand, when homogenous strain is assumed (according to Voigt [75]) the effective stiffness tensor C_{ijkl} can be computed:

$$\varepsilon_{ij}^{g} = E_{ij} \quad \Rightarrow \quad C_{ijkl}^{V} = \left\{ \sum_{g}^{N} f^{g} c_{ijmn}^{g} \right\}, \tag{2.33}$$

because:

$$\begin{aligned} \Sigma_{ij} &= \sum_{g}^{N} f^{g} \sigma_{ij}^{g} = \sum_{g}^{N} f^{g} c_{ijmn}^{g} \varepsilon_{mn}^{g} = \sum_{g}^{N} f^{g} c_{ijmn}^{g} E_{mn} \\ &= \left\{ \sum_{g}^{N} f^{g} c_{ijmn}^{g} \right\} E_{mn} \end{aligned} \tag{2.34}$$

However, for such defined macroscopic elastic constants, the reciprocal relationship between the macroscopic stiffness and the compliance tensor is not satisfied, i.e.:

$$S_{ijkl}^{R} \neq (C^{V})_{ijkl}^{-1} \tag{2.35}$$

This relationship is also not fulfilled for the Hill approach[76]:

$$S_{ijkl}^{H} = \frac{1}{2}\left\{ S_{ijkl}^{R} + (C^{V})_{ijkl}^{-1} \right\} \quad \text{and} \quad C_{ijkl}^{H} = \frac{1}{2}\left\{ C_{ijkl}^{V} + (S^{R})_{ijkl}^{-1} \right\} \tag{2.36}$$

To satisfy reciprocal relationship for the macroscopic stiffness and compliance tensors different methods were proposed, for example the use of geometric mean as proposed by Morawiec [77] or the self-consistent calculations based on interaction of the grain with homogenous continuous medium (matrix) approximated by Eshelby [78] inclusion as proposed by Kroner [79] in the case of isotropic matrix.

In the present work the self-consistent model based on the Eshelby approach was used to predict elasto-plastic deformation of polycrystalline material, as described in subsection 3.3.3. The calculation of macroscopic mechanical properties was done according to Lipinski-Berveiller model [80] enabling calculation of so-called localisation (concentration) tensors. These tensors A^g_{ijkl} and B^g_{ijkl} relate the macroscopic strain and stress tensors with those localised on the grain g:

$$\varepsilon^g_{ij} = A^g_{ijkl} E_{kl} \quad \text{and} \quad \sigma^g_{ij} = B^g_{ijkl} \Sigma_{kl} \tag{2.37}$$

where

$$(A^g)^{-1}_{ijkl} = I_{ijkl} - T^{gg}_{ijnm}\left(c^g_{mnkl} - C_{mnkl}\right) \tag{2.38}$$

and T^{gg}_{ijnm} is the interaction tensor calculated on the basis of interaction of the Eshelby-type ellipsoidal inclusion within anisotropic homogenous medium characterized by the stiffness tensor C_{ijkl}.

This method enables to calculate effective overall elastic tensors (and also elastoplastic tensors, cf. chapter 3) for textured polycrystalline material using the following formula:

$$C^{eff}_{ijkl} = \sum_g^N f^g \, c^g_{ijmn} A^{\ g}_{mnkl} \tag{2.39}$$

The formula for calculation of the C^{eff}_{ijkl} tensor can be easily justified:

$$\begin{aligned} \Sigma_{ij} = C^{eff}_{ijkl} E_{kl} &= \left\{ \sum_g^N f^g c^g_{ijmn} A^{\ g}_{mnkl} \right\} E_{kl} = \sum_g^N f^g c^g_{ijmn} \left\{ A^{\ g}_{mnkl} E_{kl} \right\} \\ &= \sum_g^N f^g c^g_{ijmn} \varepsilon^g_{mn} = \sum_g^N f^g \sigma^g_{ij} = \Sigma_{ij} \end{aligned} \tag{2.40}$$

The strain localisation tensor $A^{\ g}_{ijkl}$ is calculated using the self-consistent procedure in which $C^{eff}_{ijkl} \to C_{ijkl}$ is substituted into equation (2.38) in the iterative procedure until the difference between C^{eff}_{ijkl} in subsequent iteration steps is larger than the assumed criterion.

If the convergence is achieved, the so obtained stiffness tensor C_{ijkl} fulfils strictly relation between macroscopic stress Σ_{ij} and strain E_{ij} tensors, therefore the compliance tensor is given as $S_{ijkl} = C^{-1}_{ijkl}$.

3. Plastic deformation

3.1. Macroscopic description of plastic deformation

As mentioned in chapter 2, the force applied to a solid body causes its deformation and creates stress. When increasing the load applied to the solid, the stress increases. The deformation is elastic if the body returns to its original shape after unloading and the deformation is proportional to the stress. The elasticity of solids is relatively simple to describe - the relationship between stresses and strains is described by Hooke law which in the case of a three-dimensional is given by the equation (2.10).

When the stress in the solid exceeds a critical value called yield point, plastic deformation occurs [67]. During plastic deformation, the relationship between the macroscopic stress and the deformation of a solid is no longer linear and significantly depends on the material, the method of its processing and the type of the stress tensor. A characteristic feature of plastic deformation is a much greater increase in deformation compared to the case of elasticity (for the same increase in the applied stress) and permanent deformation, i.e. after unloading the solid does not return to its original dimensions or shape (the deformation does not return to zero value, cf. dotted lines in Fig. 2.1). Usually it is difficult to define exactly the yield stress, therefore the offset yield point is arbitrarily defined and the value of proof stress at 0,1% or 0,2% plastic strain is given. However, in this work, the yield stress is defined as the stress at the point where the proportional range of elasticity ends and the permanent component of plastic strain occurs. In ductile materials, plastic deformation leads to large deformations, up to fracture of the material (see Fig. 2.1).

To define the stress state for which a solid in the elastic range goes into the plastic range, one can use the Tresca criterion or the von Mises criterion. These criteria can be represented by a five-dimensional surface built in a six-dimensional space defined by the

components of the stress tensor. This surface is called the yield stress and it separates the space for which the stress state corresponds to elastic deformation (inside the surface) from the space where the stress state causes plastic deformation (outside the surface).

Tresca criterion is the simplest criterion describing the yield stress. According to this criterion the plastic deformation begins when the maximum shear stress, i.e. half of the difference between the maximum and minimum principal stress components, is greater than $\frac{1}{2}\sigma_{pl}$:

$$\frac{1}{2}\max(|\sigma_{11}-\sigma_{22}|,|\sigma_{11}-\sigma_{33}|,|\sigma_{22}-\sigma_{33}|)=\frac{1}{2}\sigma_{pl} \tag{3.1}$$

where $\sigma_{11},\sigma_{22},\sigma_{33}$ are the stress tensor components in principal axis system and σ_{pl} is the yield stress for an uniaxial test.

To illustrate the yield surface built according to the Tresca criterion, it can be assumed that one of the stress components in the principal axis system is equal to zero (e.g. $\sigma_{33}=0$ MPa). In such a case the yield surface is reduced to two-dimensional polygon shown in Fig. 3.1). For the general state of stresses, there are three non-zero stress components, and the plasticity surface takes the form of a hexagonal prism.

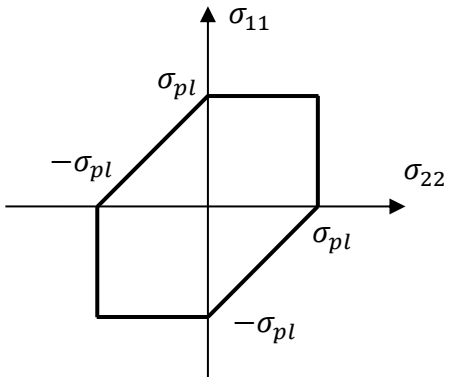

Fig. 3.1 Tresca criterion for two-dimensional stress state with σ_{11} and σ_{22} nonzero stress components and $\sigma_{33}=0$ MPa. The yield condition is fulfilled for edge of the polygon.

The second criterion describing the yield stress is the von Mises criterion. In this case, plastic deformation begins when the von Mises stress value exceeds the yield stress σ_{pl} defined for the uniaxial test, i.e.:

$$\sigma_{vM}=\sigma_{pl}$$

$$\sqrt{\frac{1}{2}[(\sigma_{11}-\sigma_{22})^2+(\sigma_{11}-\sigma_{33})^2+(\sigma_{22}-\sigma_{33})^2]+3(\sigma_{12}^2+\sigma_{13}^2+\sigma_{23}^2)}=\sigma_{pl} \tag{3.2}$$

The advantage of the von Mises stress formula is that it is based on a full stress tensor and is independent of the coordinate system, so it is not necessary to convert the stress tensor to the principal axis system. To illustrate the yield stress condition, it can be assumed that one of the components of the stress tensor is zero. As shown in Fig. 3.2, the von Mises criterion is fulfilled for the ellipse edge. For comparison, in this figure also the polygon showing the yield condition according to the Tresca criterion. It can be observed that, the von Mises criterion gives a smoother yield line and the elastic region is larger compared to that obtained for the Tresca criterion is shown. In general, when all stress components are present, the yield surface built according to the von Mises criterion takes the shape of an elliptical cylinder.

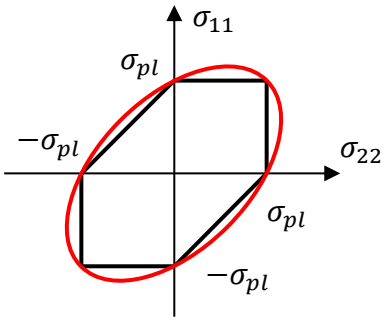

Fig. 3.2 Von Mises yield surface criterion (red) compared with Tresca criterion (black) for yield surface. The nonzero stress tensor components are σ_{11} and σ_{22}.

3.2. Plastic deformation mechanisms of single crystal

During elastic deformation, the displacement of atoms does not change their relative arrangement in the crystal lattice. In the case of plastic deformation, the relative arrangement of atoms changes due to the so-called crystallographic slips, during which a part of the crystallite moves with respect to the rest. This slip occurs on a given crystal plane in a strictly defined direction. The slip plane and slip direction form the so-called slip system. The slips can take place on one plane or on several parallel planes adjacent to each other, which form so called slip band (cf. Fig. 3.3). It should be noted that the shear band is relatively thin and in models it can be assumed that the slip occurs on a single plane. It should be emphasized that slips are significantly facilitated by dislocations movement on the slip planes, if the density of deformation is small. However, when the dislocation density increases during plastic deformation, they begin to intersect, which in turn makes slips difficult.

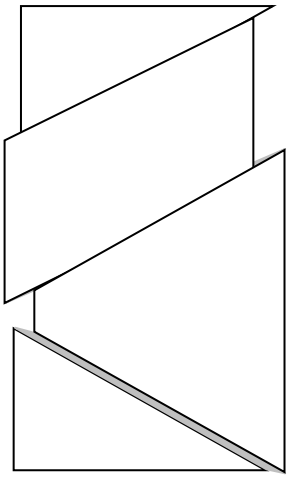

Fig. 3.3 Example of a slip system with a single slip plane and a slip band marked with grey.

Crystallographic slip is described by the slip system which defines the slip plane (hkl) and the slip direction $[uvw]$. There are symmetrically equivalent slip systems in each crystallite, denoted by $\{hkl\}\langle uvw\rangle$ (in the case of hexagonal structure the four-index Miller-Bravais notation is used). Slip systems are generally the close packed (most densely packed) planes and directions, however, when they do not allow the required deformation, less packed systems and twinning process are also activated (as in the case of hexagonal structure). Exaples of slip system for cubic and hexagonal structures are shown in Fig. 3.4 and Fig. 3.5. The potentially active slip systems in different crystal structures are given in Table 3.1.

Table 3.1 Families of slip systems available for different crystallographic structures (they are shown in Fig. 3.5).

Structure	Direction	Plane	Name
FCC	$\langle 1\bar{1}0\rangle$	$\{111\}$	
BCC	$\langle 1\bar{1}1\rangle$	$\{110\}$	Pencil glide
	$\langle 11\bar{1}\rangle$	$\{112\}$	
	$\langle 11\bar{1}\rangle$	$\{123\}$	
HCP	$\langle 11\bar{2}0\rangle$	$\{0001\}$	Basal
	$\langle 11\bar{2}0\rangle$	$\{1\bar{1}00\}$	Prismatic
	$\langle 11\bar{2}0\rangle$	$\{1\bar{1}01\}$	Pyramidal <a>
	$\langle \bar{1}2\bar{1}3\rangle$	$\{1\bar{1}01\}$	First order pyramidal <c+a>
	$\langle \bar{1}2\bar{1}3\rangle$	$\{1\bar{2}12\}$	Second order pyramidal <c+a>

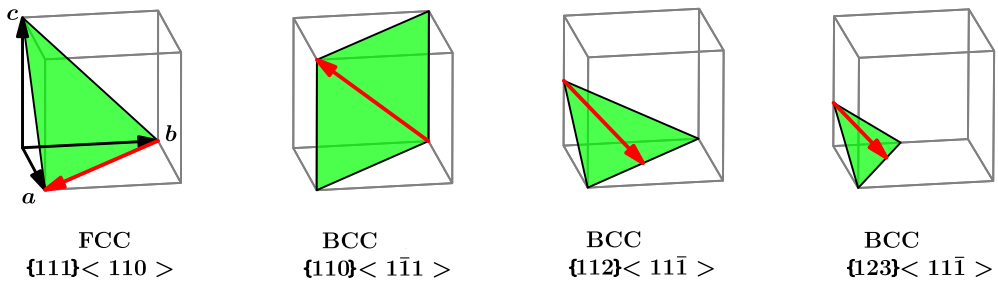

Fig. 3.4 Possible slip systems for face centred cubic and body centred cubic structures.

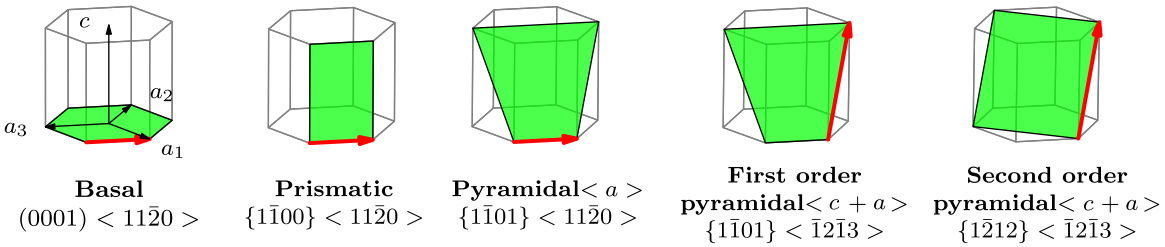

Fig. 3.5 Possible slip systems for hexagonal closed package (HCP) structure.

Crystallographic slips are the main causes of plastic deformation. The variety of slip systems allows the crystal to activate slips in different directions on different planes. During plastic deformation, only some of the slip systems are activated. The activation criterion for the slip system s in a grain g is that the value of the resolved shear stress (RSS) $\tau^{g,s} = \sigma_{13}^{g,s}$ reaches a certain critical value $\tau_{cr}^{g,s}$ (CRSS), depending on the material and the slip system state (Schmid criterion):

$$\sigma_{13}^{g,s} = \tau^{g,s} = \tau_{cr}^{g,s} \tag{3.3}$$

where $\sigma_{13}^{g,s}$ is defined with respect to the slip system coordinates determined by the slip direction vector $\vec{m}$ and vector normal to the plane on which the slip occurs $\vec{n}$ (cf. Fig. 3.6).

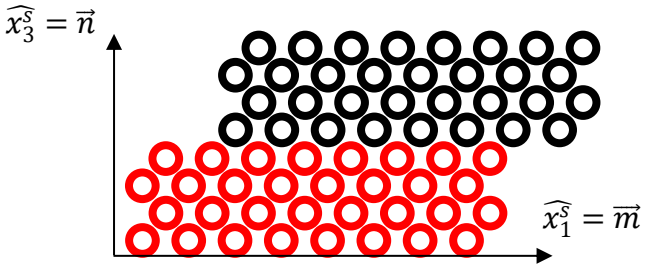

Fig. 3.6 Definition of a coordinate system based on a slip system: $\vec{m}$- normalized slip direction vector, $\vec{n}$ - normalized vector normal to the slip plane. The same definition is used for the twin system.

In the coordinate system related to the slip system (defined in Fig. 3.6), the increment of the displacement gradient caused by a single slip is expressed by one independent shear component:

$$\Delta\gamma^{g,s} = \Delta e_{13}^{g,s} \tag{3.4}$$

Thus, the increment of the displacement gradient $\Delta e_{ij}^{g,s(pl)}$ corresponding to the contribution of *s* slip system in plastic deformation of a grain g are given by the equation:

$$\Delta e_{ij}^{g,s(pl)} = m_i^{g,s}\, n_j^{g,s}\, \Delta\gamma^{g,s} \tag{3.5}$$

where $\Delta e_{ij}^{g,s(pl)}$ is expressed in the sample system and $m_i^{g,s}$ and $n_i^{g,s}$ are the components of the unit vectors $\vec{m}$ and $\vec{n}$ (cf. Fig. 3.6) defined with respect to the sample system.

Having the displacement gradient tensor defined on the basis of equation (2.6) and (2.7), the strain $\Delta\varepsilon_{ij}^{g,s(pl)}$ and rotation $\Delta\omega_{ij}^{g,s(pl)}$ increments for *s* system in g grain can be found:

$$\begin{aligned} \Delta\varepsilon_{ij}^{g,s(pl)} &= R_{ij}^{g,s}\, \Delta\gamma^{g,s}, \\ \Delta\omega_{ij}^{g,s(pl)} &= Q_{ij}^{g,s} \Delta\gamma^{g,s}, \end{aligned} \tag{3.6}$$

where:

$$\begin{aligned} R_{ij}^{g,s} &= \tfrac{1}{2}\left(m_i^{g,s} n_j^{g,s} + m_j^{g,s} n_i^{g,s}\right), \\ Q_{ij}^{g,s} &= \frac{1}{2}\left(m_i^s n_j^s - m_j^s n_i^s\right). \end{aligned} \tag{3.7}$$

and $\Delta\varepsilon_{ij}^{g,s(pl)}$ and $\Delta\omega_{ij}^{g,s(pl)}$ are expressed with respect to the sample coordinate system.

Finally, to obtain the total strain and rotation increments for g grain the contributions from all active slip systems *s* should be summed up:

$$\Delta\varepsilon_{ij}^{g(pl)} = \sum_s \Delta\varepsilon_{ij}^{g,s(pl)}, \qquad \Delta\omega_{ij}^{g(pl)} = \sum_s \Delta\omega_{ij}^{g,s(pl)} \tag{3.8}$$

If we assume that the grain is surrounded by a non-rotating matrix the plastic rotation tensor $\Delta\omega_{ij}^{g(pl)}$ is compensated by the rotation of the crystal lattice $\Delta\omega_{ij}^{g(cr)}$ (see Fig. 3.7) [72], i.e.:

$$\Delta\omega_{ij}^{g(pl)} = -\Delta\omega_{ij}^{g(cr)}. \tag{3.9}$$

It should be emphasised that the $\Delta\omega_{ij}^{g(cr)}$ rotation leads to formation of crystallographic texture.

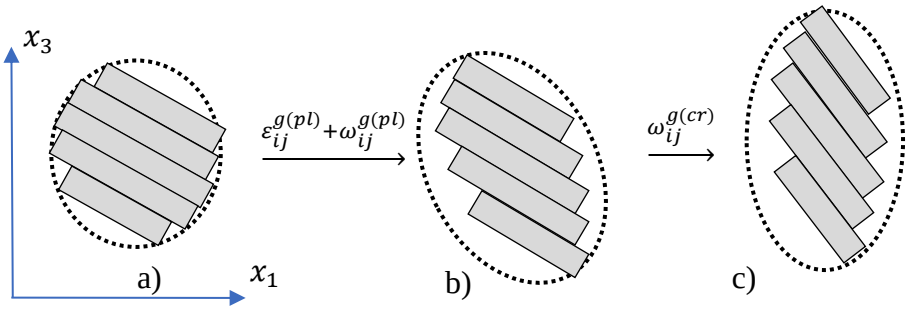

Fig. 3.7 Plastic deformation of a grain during compression along the $\mathbf{x_1}$ axis: a) before slip, b) after slip on one of the systems, c) and crystal rotation of the lattice to accommodate the grain to the non-rotating matrix.

To calculate the resolved shear stress $\tau^{g,s}$ (RSS) at the *s* system the following equation can be used:

$$\tau^{g,s} = R_{ij}^{g,s}\sigma_{ij}^{g} \tag{3.10}$$

where σ_{ij}^{g} is the stress tensor at the grain g defined with respect to the sample system.

When the Schmid condition (3.3) is satisfied for a given slip system, i.e. $\tau^{g,s}$ reaches critical value (CRSS – critical resolved stress $\tau_{cr}^{g,s}$) the crystal begins to slip on that system [67]. Along with it, the number of dislocations multiplies. At some point, there are so many of them that they start to block each other and make the slip difficult. It manifests itself in increasing the critical shear stress (τ_{cr}) with an increase in the shear strain on a given system. This phenomenon is described by the so-called H^{st} work hardening matrix relating increase in CRSS ($\Delta\tau_{cr}^{t}$) with different slip systems active in a given crystallite:

$$\Delta\tau_{cr}^{g,t} = \sum_{s} H^{ts}\Delta\gamma^{g,s} \tag{3.11}$$

where the index t applies to all potentially active systems in a given grain, and the sum is determined over all currently active systems s.

The H^{ts} matrix describes the hardening relation and interaction between two slip systems t and s which depends on their relative geometrical orientation. In general, H^{ts} terms can be divided into two groups – weak hardening (h_w) and strong hardening (h_s) [81]. This allows to compose the matrix using only 2 terms - h_w and $\alpha = \frac{h_s}{h_w}$. The simplest assumption of constant h_w and α parameters leads to linear hardening law. The most common way to obtain H^{ts} matrix is by using the Voce law. To introduce this law the total shear strain Γ^{g} on all active slip systems in a grain g is calculated [82–84]:

$$\Gamma^{g} = \sum_{s} \gamma^{g,s}, \tag{3.12}$$

where $\gamma^{g,s}$ is the total shear strain on active slip system s in grain g.

On the basis of the Γ^g value, the critical stress for each slip system s in the grain g can be determined [83]:

$$\tau_{cr}^{g,s} = \tau_0^{g,s} + (\tau_1^s + \theta_1^s \Gamma^g)\left(1 - e^{-\frac{\theta_0^s}{\tau_1^s}\Gamma^g}\right), \tag{3.13}$$

where: τ_0^s is a current value of initial critical resolved shear stress (CRSS) on slip system s in grain g, while τ_1^s, θ_0^s and θ_1^s are phenological hardening parameters for given slip system s (equal for all grains) which must be found out from evaluable experimental results (e.g. macroscopic stress-strain plot, lattice strains, grain stresses or/and evolutions of CRSS during plastic deformation) compared to given crystallographic model.

The interpretation of the adjustable parameters in Voce's law is as follows: $\tau_0^{g,s}$ is the initial value of CRSS for $\Gamma^g = 0$, θ_0^s and θ_1^s are respectively initial and final values of the rate of hardening, and $\tau_0^{s,g} + \tau_1^s$ is the intersection of the $\tau_{cr}^{g,s}$ axis with the tangent line to the end of the hardening curve (see Fig. 3.8).

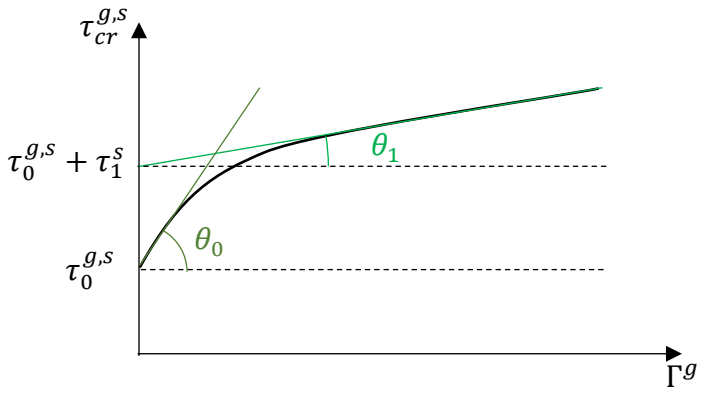

Fig. 3.8 Geometrical interpretation of Voce law.

Usually, the hardening matrix relating different slip systems H^{st} is calculated:

$$H^{st} = \frac{\mathrm{d}\tau^{g,s}}{\mathrm{d}\Gamma^g} h_{st}, \tag{3.14}$$

where h_{st} is a matrix depending on geometrical relations between slip systems [81].

In the case of HCP structure a large difference occurs between CRSS values and hardening parameters for different slip systems and introduction of h_{st} leads to additional sets of parameters which are not well defined and potentially can be fitted. This is why in this work the simplified method to calculate the H^{st} values assuming $h_{st} = 1$ was used. In this case the values of self-hardening (H^{ss} hardening of s system by the same system) the $\frac{\mathrm{d}\tau^{gs}}{\mathrm{d}\Gamma^g}$ is directly determined from equation (3.13), while in the case of $s \neq t$, the arithmetic mean is calculated, i.e.:

$$H^{st} = \frac{1}{2}\left(\frac{\mathrm{d}\tau^{gs}}{\mathrm{d}\Gamma^g} + \frac{\mathrm{d}\tau^{gt}}{\mathrm{d}\Gamma^g}\right). \tag{3.15}$$

The second most important mechanism of plastic deformation is twinning. It is a kind of complement to the slip systems in order to increase number of directions in which the displacements will take place. The twinning process itself is based on the movement of successive atomic layers in one direction, so that with each step more and more layers are shifted. As a result, a new twin-grain is created from the so called parent-grain (see Fig. 3.9). Similarly as in the case of the crystallographic slip, the formation of the twin orientation is related to the twinning system, which is defined by the $\{hkl\}$ plane and the $\langle uvw \rangle$ direction vector. Unlike the slip systems in twin systems, the sign of the direction vector is important, i.e. the slips can occur in two opposite directions, while in the case of twin only one direction of twinning is possible.

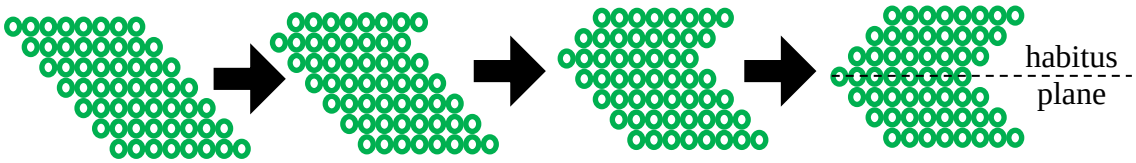

Fig. 3.9 Scheme of the formation of twin orientation.

The orientation of the twin lattice with respect to the parent lattice is strictly defined. In general there are 4 different relation between the lattices of the parent and twin, however in the case of cento-symmetric crystals (as hexagonal lattice) they reduce to two independent relations. Therefore two types of twins can be created using two symmetry operations, i.e. the lattice of type 1 twin is obtained from rotation about normal to twinning plane by 180º, as shown in Fig. 3.10a (the same twin orientation can be obtained as mirror image in twinning plane) and the lattice of the type 2 twin is obtained from the rotation by 180º about the twinning direction, shown in Fig. 3.10b (or equally through mirror reflection in the plane normal to twinning direction). There is also a third type of twins, the so-called compound twins for which lattice orientation can be obtained by any of the above operations. As shown in Fig. 3.10 c and d, both rotations by 180º, i.e. about normal to twining plane or about twinning direction lead to the same orientation of twin lattice.

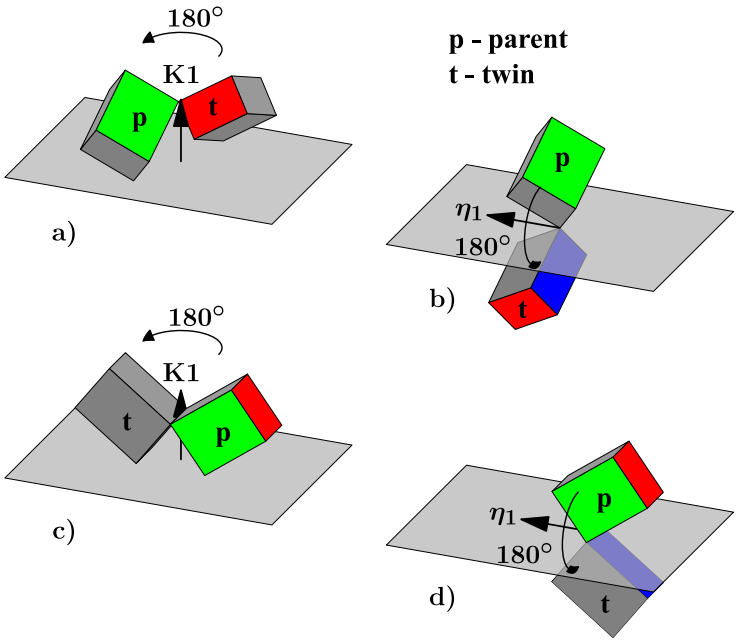

Fig. 3.10 Different types of twins for orthorhombic lattice with: a) type 1 twin after rotation by 180º about $\boldsymbol{K_1}$ || normal to twining plane {111}, b) type 2 twin after rotation by 180º about $\boldsymbol{\eta_1}$ || twinning direction $< 1\bar{1}0 >$; and compound twin obtained either through c) rotation by 180º about $\boldsymbol{K_1}$ - normal to twining plane || {101} or (b) rotation by 180º about $\boldsymbol{\eta_1}$ - twinning direction $< 10\bar{1} >$, cf. [85].

There well-defined orientation relationships between the crystal lattices of the parent and twin variants are typically known from experiment or can be determined from theoretical calculations [86]. The orientation of the twin can be calculated using the rotation represented by the following rotation [67]:

$$\begin{bmatrix} u_t \\ v_t \\ w_t \end{bmatrix} = \begin{bmatrix} (2t_1^2 - 1) & 2t_1t_2 & 2t_1t_3 \\ 2t_2t_1 & (2t_2^2 - 1) & 2t_2t_3 \\ 2t_3t_1 & 2t_3t_2 & (2t_3^2 - 1) \end{bmatrix} \begin{bmatrix} u_p \\ v_p \\ w_p \end{bmatrix} \tag{3.16}$$

where $\begin{bmatrix} u_t \\ v_t \\ w_t \end{bmatrix}$ and $\begin{bmatrix} u_p \\ v_p \\ w_p \end{bmatrix}$ are vectors expressed in the twin and the parent reference frames, respectively and t_i are the components unit vector perpendicular to twinning plane for the type 1 twin or components of unit vector along twinning direction for the type 2 twin.

The twinning systems occurring for the crystallite with the HCP structure are given in Table 3.2 and shown in Fig. 3.11. It should be emphasised that twins represented by these systems are the compound twins, therefore both rotations defined by equation (3.16) can be used to calculate the orientations of twin lattice. In this work, the rotation given by equation (3.16) is used in calculation of lattice orientation for the first order tensile twins (t_i is chosen as unit vector perpendicular to twinning plane $\{1\bar{1}02\}$).

Table 3.2 Families of twin systems potentially active in HCP structure
(see also Fig. 3.11)

First order tensile twin TT1	$\langle\bar{1}101\rangle$	$\{1\bar{1}02\}$
Second order tensile twin TT2	$\langle\bar{1}2\bar{1}6\rangle$	$\{1\bar{2}11\}$
First order compression twin CT1	$\langle\bar{1}102\rangle$	$\{1\bar{1}01\}$
Second order compression twin CT2	$\langle1\bar{2}1\bar{3}\rangle$	$\{1\bar{2}12\}$

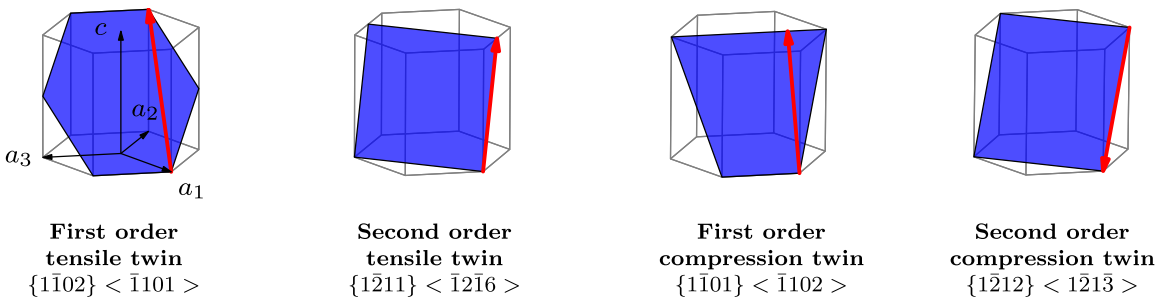

Fig. 3.11 Possible twinning systems for HCP structure.

The increment of the volume fraction $\delta w^{g,t}$ of the twin is related to the increment of shear strain $\delta\gamma^t$ occurring on the twin system t in the grain g and it is given by the well-known equation [16]:

$$\delta w^{g,t} = \delta\gamma^{g,t}/S \tag{3.17}$$

where characteristic total shear strain $S = 0{,}13$ [87] for tensile twins in Mg.

In the same time the change in the volume of the parent p is equal to:

$$\delta w^{g,p} = -\delta w^{g,t} \tag{3.18}$$

The evolution of the grain properties can be done using the same procedures as for the slip systems, as describes above by the equations (3.3) - (3.13) and taking into account the change of the volume fraction of the twin and parent [16]. It should be however emphasised that the twinning process is not well understanded and more difficult to predict comparing to crystallographic slip phenomena. It is known, that propagation of the twins occurs easily under small stress, but the process of twinning requires a large stress to be activated. Therefore, in addition to the "continuous approximation" in which a twin is born when the CRSS of a twin is exceeded, preliminary or threshold assumptions concerning twin nucleation have also been proposed. For example in the "finite initial fraction" (FIF) approach the initial size of the twin "at birth" is assumed, which corresponds to the initial

shear strain on twin system [16]. This initial plastic deformation leads to the back-stress localised in the parent and twin, originated from interaction with the surrounding matrix. In the FIF approach significant relaxation of the load at the "just born" twin was predicted by EPSC model and this result was confirmed by neutron diffraction experiment. However, the further evolution of the model stress at the twin is rather far from the experimental result [16].

Another method of implementing the twinning mechanism to calculation is the PTR "predominant twin reorientation" scheme used especially in the viscoplastic self-consistent VPSC models [18,88–90]. In this method the orientation of the grain is not changed until the volume fraction $w^{g,t}$ (related to the shear strain on t system in grain g by equation (3.17)) reaches the threshold defined below. The volume fraction which is supposed to be twinned due to the activity of the *t* system is calculated as the sum over all deformation steps:

$$w^{g,t} = \sum_{steps} \delta w^{g,t} \tag{3.19}$$

Then the volume fractions F_R of twins in the polycrystalline material is determined for all systems t and over all grains g having f^g the volume fractions in the sample:

$$F_R = \sum_g f^g \sum_t w^{g,t} \tag{3.20}$$

Moreover, the fraction of the grains reoriented due to twinning is calculated:

$$F_E = \sum_{g(twin)} f^{g(twin)} \tag{3.21}$$

Finally, the threshold value determining the creation of a twin is defined:

$$F_T = A_1 + A_2 \frac{F_E}{F_R} \tag{3.22}$$

In the PTR method the orientation of a given grain is fully changed to the orientation of the twin when $w^{g,t}$ volume fraction exceeds threshold value F_T (i.e. $w^{g,t} > F_T$). This happens for the twin system which is the most active in the grain and exhibits the highest value of shear strain. The self-consistent feature of the threshold F_T defined in this way is that a too rapidly increasing ratio F_E / F_R leads to an increase in the threshold F_T and consequently a decrease in the number of reorienting grains. The values of constants A_1 and A_2 can be adjusted in order to obtain the rate of twins increase close to experimental one, e.g. $A_1 = A_2 = 0{,}25$ was proposed in [88].

3.3. Crystallographic elastic-plastic self-consistent model

3.3.1. Model approach

When describing elastic and plastic deformation of polycrystalline material at a microscopic scale, one should consider the interactions occurring at this scale, e.g. intergranular interactions. For this purpose, various types of models are used, the common feature of which is the assumption of certain initial material parameters, such as the elastic constants of individual crystallites, crystallographic texture and certainly the initial CRSS values for potentially active slip and twin systems. Then in the calculations the scale transition model taking into account the grain interaction as well as the hardening parameters for slip and twin systems and rotations of the grains must be taken into account.

A commonly used model used to predict the elastic-plastic behaviour of a material is the finite element method (FEM). However, this method is mainly suitable for predicting complex loading conditions of a material without taking into account its crystallographic structure. FEM calculations in which crystallites are taken into account are time consuming and give poor statistical information. Therefore, crystallographic models in which interactions between grains are approximated by e.g. Eshelby-type interactions of an ellipsoidal inclusion with the surrounding homogeneous matrix [78]. Certainly, the results of the calculations have to be experimentally verified, and the model parameters, such as the parameters of Voce law, are adjusted in order to obtain agreement of the model calculations with the experimental results.

The first and simplest models of elastic deformation are those proposed by Voigt [75] and Reuss [74]. They are based on the assumption of homogeneity of strains (Voigt) or homogeneity of stresses over all grains of polycrystalline material (Reuss). Analogous assumptions, i.e. homogeneity of total strain and homogeneity of stress, were applied to plastic deformation by Taylor [91] and Sachs [92]. The Taylor model was also modified assuming relaxation of some components of the stress or strain tensor by Van Houtte [93] and Canova et al. [83]. Then, Kröner [94] introduced an idea of self-consistent modelling for elastic properties of a heterogeneous material, which was extended by Hill [95] for elastoplasticity. The elastoplastic self-consistent (EPSC) models are based on the Eshelby approach [78] in which the polycrystalline grains are approximated by ellipsoidal inclusions embedded in a homogeneous matrix, which shows the average properties of polycrystalline materials at a macroscopic scale.

To predict the elastoplastic nature of macroscopic and local deformation for one or two-phase polycrystalline materials, different types of modelling have been developed. For example the Hill idea of EPSC model was applied by Turner and Tomé [21,96] and then developed by e.g. [82,97–100]. These algorithms were applied to interpret results of diffraction experiments by [11,12,14,82]. Alternative methodology, used in this work was elaborated by Lipinski and Berveiller [80] and developed by [21,101–104]. The latter method was also used to analyse the results of diffraction experiments in order to study mechanical behaviour of solids at different scales [21,65,66,105–107].

3.3.2. Micro- and macroscopic description of elastoplastic deformation

The main goal of EPSC calculation is to predict influence of the external loading such as applied force or temperature change on microscopic behaviour of individual grains.

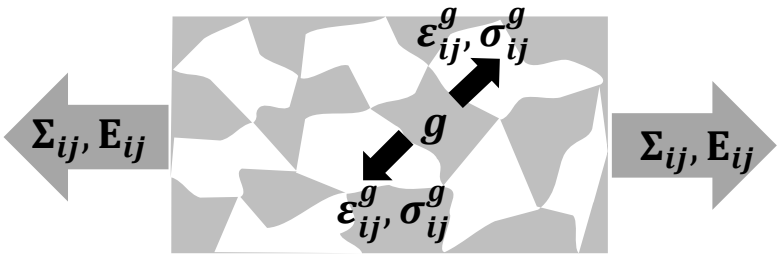

Fig. 3.12 Example of polycrystal material under applied load leading to the response to the macroscopic stress Σ_{ij}: macroscopic elastoplastic strain E_{ij}, microstress σ_{ij}^{g} and elastoplastic microstrain ε_{ij}^{g} appearing at grain g.

The relationships between macroscopic strain and stress in the elastic range of loading is described in subsection 2.3.3 by the formula (2.30). It should be noted that the Hooke law relates the stress and elastic strain at the macroscopic and microscopic scale, i.e.:

$$\begin{aligned} \sigma_{ij}^{g} &= c_{ijkl}\varepsilon_{kl}^{g(el)} = c_{ijkl}\left(\varepsilon_{kl}^{g} - \varepsilon_{kl}^{g(pl)}\right) \quad \text{or} \quad \varepsilon_{ij}^{g} - \varepsilon_{ij}^{g(pl)} = s_{ijkl}\sigma_{kl}^{g} \\ \Sigma_{ij} &= C_{ijkl}E_{kl}^{(el)} = C_{ijkl}\left(E_{kl} - E_{kl}^{(pl)}\right) \quad \text{or} \quad E_{ij} - E_{ij}^{(pl)} = S_{ijkl}\Sigma_{kl} \end{aligned} \tag{3.23}$$

where c_{ijkl} and s_{ijkl} are the microscopic stiffness and the compliance tensors, $\varepsilon_{ij}^{g(el)}$, $\varepsilon_{ij}^{g(pl)}$ and ε_{ij}^{g} are the elastic, plastic and total microstrains, and σ_{kl}^{g} is the microstress. Capital letters are used for analogous macroscopic quantities.

It is worth noting, that plastic deformation causes an additional increase in strain, which is not directly related to the stress value. However, it is possible to describe the elastoplastic deformation by determining the increase in the strain value for a given increase in the stress. In this way, the relationship between the stress $\Delta\Sigma_{ij}$ and the strain ΔE_{ij} increments can be given using a tangent modulus tensor L_{ijkl}, i.e.:

$$\Delta\Sigma_{ij} = L_{ijkl}\Delta E_{kl} \quad \text{or} \quad \Delta E_{ij} = L^{-1}_{ijkl}\Delta\Sigma_{kl} \tag{3.24}$$

The graphical interpretation of the tangent modulus is shown in Fig. 3.13.

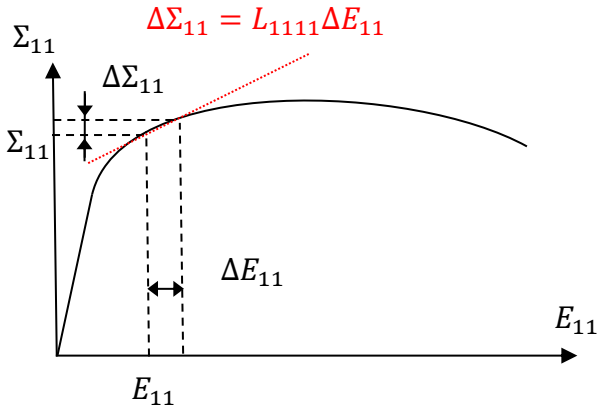

Fig. 3.13 Relation between strain increment ΔE_{11} and stress increment $\Delta\Sigma_{11}$ defines component L_{1111} of macroscopic tangent modulus tensor.

The L_{ijkl} tensor, defined in this way generally depends not only on the value of macroscopic strain, but also on the rate of strain increase. However, the rate independent EPSC model predicts the mechanical behaviour of the sample for infinitely slow strain rate, therefore the tensor L_{ijkl} depends solely on the macroscopic sample strain.

To calculate the macroscopic L_{ijkl} tensor at first the local tangent modulus tensor l^g_{ijkl}, defined for a grain g, should be determined, i.e. [80,103]:

$$\Delta\sigma^g_{ij} = l^g_{ijkl}\Delta\varepsilon^g_{kl} \tag{3.25}$$

where $\Delta\sigma^g_{ij}$ and $\Delta\varepsilon^g_{kl}$ are the increments of stress and strain at grain g, respectively.

Rewriting equation (3.23) the following relation can be obtained:

$$\Delta\sigma^g_{ij} = c^g_{ijkl}\Delta\varepsilon^{g(el)}_{kl} = c_{ijkl}\left(\Delta\varepsilon^g_{kl} - \Delta\varepsilon^{g(pl)}_{kl}\right) \tag{3.26}$$

where c^g_{ijkl} are the single crystal stiffnesses.

By using equation (3.6) and equation (3.8) the plastic strain increment can be expressed by the shear strain increments $\Delta\gamma_{kl}^{g,s}$ at different active slip systems s:

$$\Delta\sigma_{ij}^{g} = c_{ijkl}^{g}\left(\Delta\varepsilon_{kl}^{g} - \sum_{s} R_{kl}^{g,s}\Delta\gamma_{kl}^{g,s}\right) \tag{3.27}$$

where summation should be done over all active system s.

Assuming the resolve shear stress increment equal to the increment of its critical value and using equation (3.10) the increment of critical shear stress at the active slip system t can be found:

$$\Delta\tau_{cr}^{g,t} = R_{ij}^{g,t}\Delta\sigma_{ij}^{g} = R_{ij}^{t}c_{ijkl}^{g}\left(\Delta\varepsilon_{kl}^{g} - \sum_{s} R_{kl}^{g,s}\Delta\gamma_{kl}^{g,s}\right) \tag{3.28}$$

Comparing the obtained equation (3.28) with equation (3.11) it can be written:

$$\sum_{s} H^{ts}\Delta\gamma_{kl}^{g,s} = R_{ij}^{t}c_{ijkl}^{g}\left(\Delta\varepsilon_{kl}^{g} - \sum_{s} R_{kl}^{g,s}\Delta\gamma_{kl}^{g,s}\right) \tag{3.29}$$

After grouping the slip increment terms:

$$\begin{aligned}\sum_{s}(M^{-1})^{g,ts}\Delta\gamma_{kl}^{g,s} &= \sum_{s}\left(H^{ts} + R_{ij}^{g,t}c_{ijkl}^{g}R_{kl}^{g,s}\right)\Delta\gamma_{kl}^{g,s} \\ &= R_{ij}^{g,t}c_{ijkl}^{g}\Delta\varepsilon_{kl}^{g}\end{aligned} \tag{3.30}$$

where $(M^{-1})^{g,ts} = H^{ts} + R_{ij}^{g,t}c_{ijkl}^{g}R_{kl}^{g,s}$

The slip increment on slip system s is given by the formula [80,108,109]:

$$\Delta\gamma_{kl}^{g,s} = \sum_{t} M^{g,st}R_{ij}^{g,t}c_{ijkl}^{g}\Delta\varepsilon_{kl}^{g} \tag{3.31}$$

where summation is done over all active slip systems t.

Finally, after substituting the equation (3.31) to equation (3.27) and simple transformations:

$$\Delta\sigma_{ij}^{g} = \left(c_{ijkl}^{g} - \sum_{s,t} c_{ijmn}^{g}R_{mn}^{g,s}M^{g,st}R_{ij}^{g,t}c_{ijkl}^{g}\right)\Delta\varepsilon_{kl}^{g} \tag{3.32}$$

and comparing this equation with equation (3.25), the relation between microscopic strain increment and stress increment can be written using local tangent modulus tensor l_{ijkl}^{g} for a grain g:

$$\Delta\sigma_{ij}^{g} = l_{ijkl}^{g}\Delta\varepsilon_{kl}^{g}$$

$$l_{ijkl}^{g} = c_{ijkl}^{g} - \sum_{s,t} c_{ijmn}^{g} R_{mn}^{g,s} M^{g,st} R_{ij}^{g,t} c_{ijkl}^{g} \tag{3.33}$$

The relation between microscopic and macroscopic stress increment and strain increment as well as local and macroscopic tangent modulus tensor must be established. This relation is proposed by different models, such as EPSC model described below.

3.3.3. Elastoplastic self-consistent model

In the case of plastic deformation, the strain and stress localisation laws defined for elastic deformation (equation (2.37)) must be modified. Due to nonlinear character of stress-strain relations these relation should be written for infinitesimal increments of stress and strain, i.e.:

$$\Delta\varepsilon_{ij}^{g} = A_{ijkl}^{g}\Delta E_{kl} \qquad \text{and} \qquad \Delta\sigma_{ij}^{g} = B_{ijkl}^{g}\Delta\Sigma_{kl}\,, \tag{3.34}$$

where A_{ijkl}^{g} and B_{ijkl}^{g} localisation tensors which depend on the sample strain.

Then, an analogues expression to equation (2.38) can be written on the basis of tangent moduli defined by expressions (3.24) and (3.25):

$$(A^{g})^{-1}_{ijkl} = I_{ijkl} - T_{ijnm}^{gg}\left(l_{mnkl}^{g} - L_{mnkl}\right). \tag{3.35}$$

and

$$B_{ijkl}^{g} = l_{ijop}^{g} A_{opmn}^{g} L_{mnkl}^{-1}, \tag{3.36}$$

where the interaction T_{ijnm}^{gg} tensor is calculated similarly as in equation (2.38) assuming the Eshelby-type ellipsoidal inclusion and using method of calculations developed by Lipinski and Berveiller [80], based on continuum mechanics theory.

The macroscopic values of stress and strain increments can be expressed as weighted mean values calculated over all grains (cf. equation (2.29)):

$$\Delta\Sigma_{ij} = \sum_{g}^{N} f^{g}\Delta\sigma_{ij}^{g} \qquad \text{and} \qquad \Delta E_{ij} = \sum_{g}^{N} f^{g}\Delta\varepsilon_{ij}^{g} \tag{3.37}$$

where f^{g} is the volume fraction of grain g.

The macroscopic effective tangent modulus tensor can be expressed as:

$$L_{ijkl}^{eff} = \sum_{g} f^{g} l_{ijmn}^{g} A_{mnkl}^{g} \tag{3.38}$$

This formula can be proven in similar way as its counterpart in elastic range (see (2.40)).

In the above equation, the tensor A_{mnkl}^{g} is used to compute L_{ijkl}^{eff}, but to compute A_{mnkl}^{g} first the tensor L_{ijkl} must be known. At this point, the self-consistent calculations are introduced in which the tangent modulus tensor L_{ijkl}^{eff} is calculated and substituted as L_{ijkl} in equation (3.35), and the calculations are repeated (similarly as presented in the subsection 2.3.3 in the case of elasticity). This self-consistent calculations are performed until the change in effective macroscopic tangent modulus in subsequent iteration steps fulfils the following criterium:

$$\frac{\sum_{ijkl}\left(L_{ijkl} - L_{ijkl}^{eff}\right)^{2}}{\sum_{ijkl} L_{ijkl}^{2}} < \delta^{2} \tag{3.39}$$

where δ is an assumed value (in this work $\delta = 0{,}05$).

The above criterion is also used in the self-consistent procedure for calculation within elastic range, for which $L_{ijkl} = C_{ijkl}$ and $l_{ijkl}^{g} = c_{ijkl}^{g}$.

In this work, calculations using the EPSC model are first performed for the elastic deformation (i.e. when no slip or twin system is active), and then for the nonlinear elastic-plastic deformation. In the latter case, the calculations are conducted iteratively, increasing the macrostress Σ_{11} (or Σ_{33}) successively by an assumed step $\Delta\Sigma_{11}$ (or $\Delta\Sigma_{33}$) in a given direction (e.q. $\Delta\Sigma_{11} = 1$ MPa, during tensile test). After each step, the strains and stresses at the grains, the grain orientations and the CRSS values for slip and twin systems are updated. The effective tensor L_{ijkl}^{eff} obtained from the previous step is the starting one for the current step, in which the self-consistent calculations are performed until the criterion (3.39) is fulfilled. It should be emphasized that during the self-consistent calculations, tensor l_{ijkl}^{g} is determined for the set of the active slip systems which must be updated. For this purpose, a combination of active systems is selected that corresponds to the most loaded systems, i.e. those for which the RSS values most exceed the CRSS values (according to Schmid law). The number of active slip systems is limited to a maximum of 5 linearly independent systems in a given grain, see [80] for details.

Finally, it is worth noting that the grain interactions represented by the tensor T_{ijkl}^{gg} (obtained from the self-consistent model and Eshelby approximation) do not always agree with the experimental results. In this case, the model can be modified as it was done e.g. in [21] adjusting the model results to the experimental data. The assumed in model grains interaction should be described by localization tensors which is between simplest extreme models of elastoplastic deformations are those based on the assumptions of Taylor/Voigt and Sachs/Reuss:

- the homogenous stress assumption - Sachs model [92] for plasticity and Reuss model (see section 4.3) for elastic deformation, i.e.

$$B_{ijkl}^{g} = I_{ijkl}, \tag{3.40}$$

- the homogenous strain assumption - Taylor model [91] for plasticity and Voigt model (see section 4.3) for elastic deformation), i.e.

$$A_{ijkl}^{g} = I_{ijkl}. \tag{3.41}$$

4. Diffraction methods of stress analysis and their development

4.1. Diffraction measurements of lattice strain

The study of the stress state and mechanical properties of polycrystalline materials requires the use of experimental techniques allowing for measurements at the macroscopic scale but also at the microscopic scale, i.e. at the level of the polycrystalline grain. To measure the stresses at different scales diffraction methods are often used, because they are sensitive to small elastic deformations of the crystal lattice caused by local stresses. Methods based on X-ray diffraction as well as neutron diffraction are now widely used to measure the elastic strains of the lattice.

In Fig. 4.1 example X-ray spectrum and spectrum of thermal neutrons are shown. In the case of the Angle-Dispersive (AD) method, the monochromatic characteristic X-rays are used, while the monochromatic neutron radiation is obtained with the use of a monochromator. The Energy-Dispersive (ED) technique uses a continuous spectrum of white synchrotron or neutron radiation.

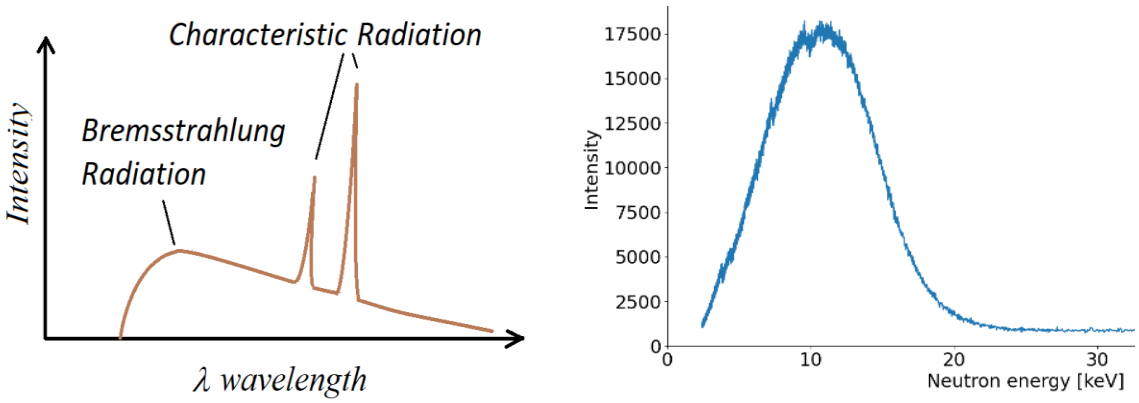

a) **b)**

Fig. 4.1 Typical X-ray spectrum (a) [110] and thermal neutrons spectrum measured using TOF method on EPSILON-MSD diffractometer at JINR in Dubna (b).

There are two methods of generating neutron radiation that can be used to measure lattice strains in polycrystalline materials. The first is nuclear fission reaction in a nuclear reactor, the second is the proton bombardment of a target made of heavy elements (e.g. uranium or tungsten) leading to a spallation process in which the emission of neutrons, protons, alpha particles and light atoms nuclei occurs. The spectrum of neutrons obtained this way contains a large number of fast neutrons. In the first stage, their energy should be reduced to fractions of eV (so-called thermalization), which corresponds to a wavelength of the order of the interplanar spacing in the tested crystals/polycrystals. The second step in neutron beam preparation depends on the experimental method. In the case of the AD method, the beam is monochromatized and a triaxial spectrometer (TSA) with an implemented Euler cradle is used to change the scattering angle and the orientation of the sample [40,111] However, in the Time of Flight (TOF) method, which is an ED-type technique, a white beam (with a given range of wavelength) in the form of shorts pulses separated by pauses is needed. When a beam from a continuously operating reactor is used, the pulses can be obtained with the help of the so-called chopper. In the case of pulse neutron reactors choppers are used to modify the temporal structure of the beam. Such a beam is produced by the IBR-2 pulse reactor at the Joint Institute for Nuclear Research (JINR) in Dubna, Russia [112]. In Fig. 4.1 the energy spectrum of thermalized neutrons coming from the IBR-2 reactor is compared with the spectrum of X-ray radiation.

Having a radiation source, it is possible to conduct a diffraction experiment on the crystal and measure the lattice strain ε_{hkl}, which is defined as:

$$\varepsilon_{hkl} = \frac{d_{hkl} - d^0_{hkl}}{d^0_{hkl}} \tag{4.1}$$

where the d^0_{hkl} and d_{hkl} are the interplanar spacing for the stress-free (i.e. strain-free) crystal and for the same crystal under applied stress, respectively. The interplanar spacings are measured using hkl reflection.

In the case of AD methods the interplanar spacings d_{hkl} can be determined from measured scattering angle 2θ using the well-known Bragg law (see Fig. 4.2):

$$n\lambda = 2d_{hkl}\sin\theta, \tag{4.2}$$

where: λ is the wavelength, n is a natural number representing the order of the diffraction peak, d_{hkl} is the interplanar spacings for the planes (hkl).

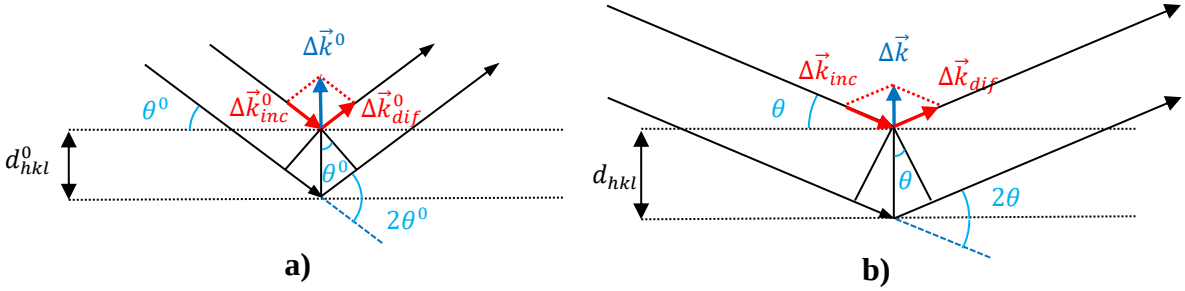

Fig. 4.2 Diffraction of monochromatic radiation on stress-free crystal (a) and crystal under load (b). The increase in interplanar spacing $d^0_{hkl} \rightarrow d_{hkl}$ corresponds to decrease of the scattering angle $2\theta^0 \rightarrow 2\theta$ and decrease of the length of scattering vector $\left|\overrightarrow{\Delta k^0}\right| \rightarrow \left|\overrightarrow{\Delta k}\right|$.

The diffraction conditions equivalent to Bragg law can be expressed using the wave vectors $\vec{k}_{inc}$ and $\vec{k}_{dif}$ for the incident and diffracted waves ($\left|\vec{k}\right| = \frac{2\pi}{\lambda}$), respectively [113].

$$\left|\overrightarrow{\Delta k}\right| = \left|\vec{k}_{dif} - \vec{k}_{inc}\right| = \frac{4\pi\sin\theta}{\lambda} = \left|\overrightarrow{G_{hkl}}\right| \tag{4.3}$$

where $\overrightarrow{G_{hkl}}$ is reciprocal lattice vector and and $\left|\overrightarrow{\Delta k}\right|$ is the scattering vector normal to the (hkl) plane, defined in Fig. 4.2.

It should be emphasised that the lattice strain is always measured in the direction of the scattering vector $\overrightarrow{\Delta k}$ being normal to the diffracting plane. The vector $\overrightarrow{\Delta k}$ is defined in Fig. 4.2, where the change in the value of the interplanar spacing and the corresponding change in the scattering angle are also shown.

In the ED method, the 2θ scattering angle is constant, and the interplanar distances can be determined from the measured wavelength λ satisfying Bragg law (equation (4.2)). As mentioned above this can be done by using the TOF neutron diffraction method. The principles of the TOF method are presented in Fig. 4.3. The short neutron pulse formed by the chopper travels along the path to the sample (L_0) where it is scattered and travels along the path (L_1) to the detector. The total path of the neutrons from the chopper to the detector (L) is travelled by the neutrons at different times T, depending on their velocity v, which in turn depends on their momentum p. Then, according de Broglie wavelength associated with a moving neutron λ can be expressed through the time of flight T:

$$\lambda = \frac{h}{p} = \frac{hT}{m_n L} \tag{4.4}$$

where $p = m_n v = m_n \frac{L}{T}$, h - Planck constant, m_n is neutron mass.

Finally, the interplanar spacing d_{hkl} can be related to time T using Bragg law (equation (4.2)):

$$d_{hkl} = \frac{nh}{2p \sin\theta} = \frac{nhT}{2\mathrm{m_n} L \sin\theta} \,. \tag{4.5}$$

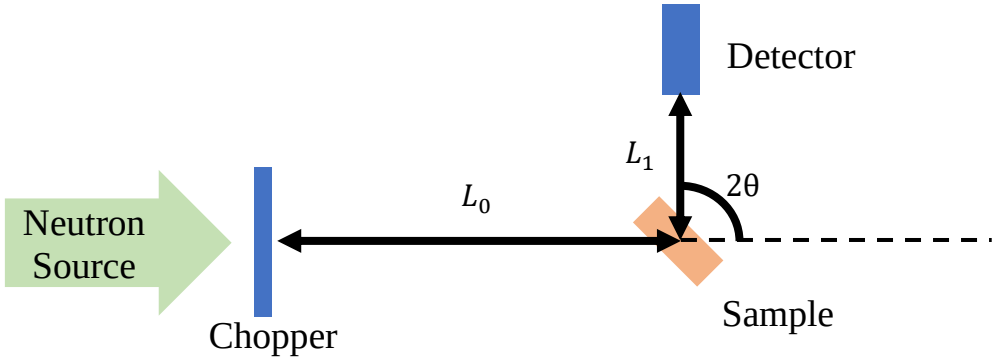

Fig. 4.3 Scheme of the TOF method.

The formula derived above allows the measurement of interplanar distances by measuring the time of flight of neutrons. This is done by counting the number of neutrons captured by the detector over a specific time interval called a channel. Each channel has a constant time span Δt which, when multiplied by the channel number N, gives the travel time of the particle from the source, through sample to detector. In this way, the dependence of the number of registered neutrons on the channel number is obtained, which can be easily transformed into a diffractogram depending on the interplanar spacing d_{hkl}.

Due to high absorption in most of the materials, the X-ray characteristic radiation (produced using X-ray tube) is applied to measure stress state in the near surface volume

of the sample (order of dozen μm). On the other hand, the high energy synchrotron radiation and neutrons penetrate the materials much deeper (up to cm), see Fig. 4.4. The latter techniques are convenient for stress analysis in transmission mode or inside the material.

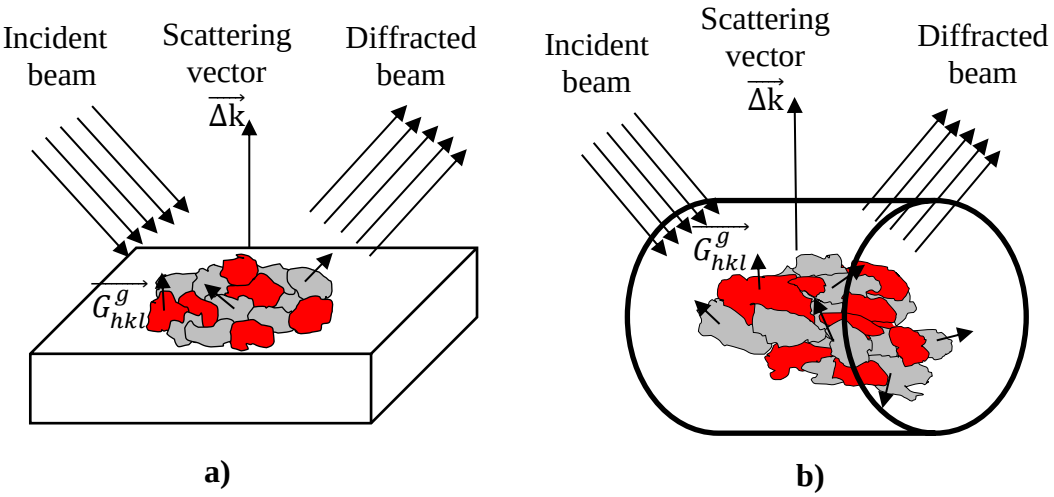

Fig. 4.4 The measurement of interplanar spacings for the grains close to the surface using X-ray diffraction (a) and inside the sample volume by using neutron diffraction (b). The diffracting grains (red) are determined by condition that scattering vector $\overrightarrow{\Delta k}$ is normal to the reflecting planes $\{hkl\}$ of grain g described by vector $\overrightarrow{G^g_{hkl}}$.

As a result of the experiment, one obtains a diffraction peak showing the dependence of the scattered radiation intensity on the 2θ scattering angle for the AD method or on the neutron flight time T (or directly d_{hkl} - spacings, see equation (4.5)) for the TOF method. It is worth noting that to determine the crystal structure, the entire patterns obtained from diffraction are analysed, e.g. by the Rietveld method. [114,115]. However, for strain analysis, the peak positions have to be independently and accurately determined, therefore the peak profiles have to be analysed separately Fig. 4.5.

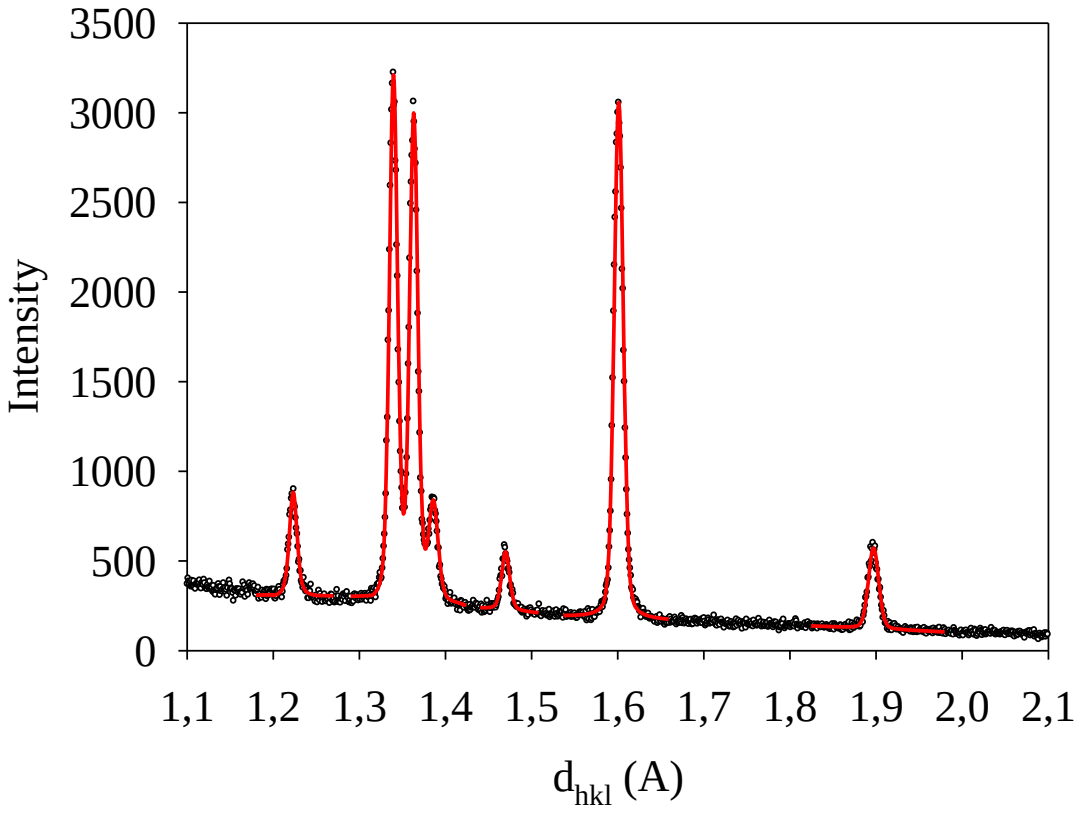

Fig. 4.5 Diffraction peaks for a stress-free magnesium AZ31 sample obtained using TOF method on EPSILON-MSD diffractometer. The pseudo-Voigt function is separately fitted to the experimental points. Peaks in range 1,3Å-1,4Å are fitted as a sum of three independent peaks.

In order to determine the parameters of a diffraction peak, such as its position and half-width, the theoretical function describing the shape of this peak should be adjusted. Often used functions for peak matching are Gauss, Lorentz and pseudo-Voigt functions (the latter is a superposition of Gauss and Lorentz functions). These functions are compared in Fig. 4.6 and described by the following formulas [116]:

$$\text{Gauss function: } G(x) = Ae^{-\frac{(x-x_0)^2}{FWHM^2}\log 2},$$

$$\text{Lorentz function: } L(x) = A\frac{1}{1+\frac{(x-x_0)^2}{FWHM^2}} \text{ and} \tag{4.6}$$

$$\text{Pseudo-Voigt function: } PV(x) = \eta G(x) + (1-\eta)L(x)$$

where: A is a peak amplitude, x_0 is a peak position, $FWHM$ means peak full width at half of maximum and η is a Gauss fraction in the pseudo-Voigt function.

When describing the peak shape, the pseudo-Voigt function is the most often used, because the Gaussian function contained in it describes the effect of intra-grain (third order) stresses on the peak shape, leading to the broadening of the peak in its upper part. On the other hand, the Lorentz function well describes the interference phenomenon in the case of small crystallites. So the pseudo-Voigt function describes well the effect of lattice deformations inside the grains as well as the grain size[117,118].

The peak position and the resulting mean interplanar distance are determined by fitting the function to the experimental peak. Then, the mean elastic strain is calculated from the formula:

$$< \varepsilon >_{\{hkl\}} = \frac{< d >_{\{hkl\}} - d^0_{hkl}}{d^0_{hkl}} \tag{4.7}$$

where $< d >_{\{hkl\}}$ is the mean spacing between planes $\{hkl\}$ for the group of diffracting crystallites (the scattering vector is normal to these planes). The interplanar spacings are measured using hkl reflection.

The average lattice strains $< \varepsilon >_{\{hkl\}}$ measured for the groups of diffracting grains are the basis for determining the stresses in the polycrystalline material.

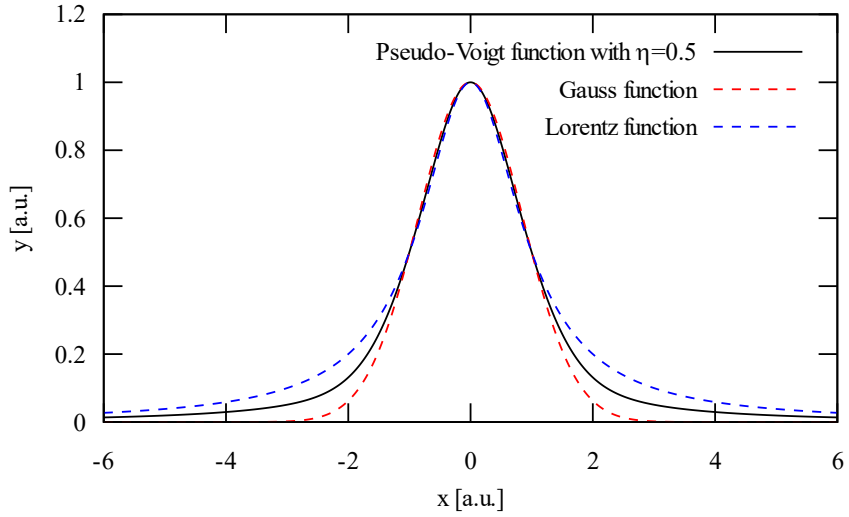

Fig. 4.6 Comparison of Gauss, Lorentz and Pseudo-Voigt functions with parameters: $A = 1, x_0 = 0, FWHM = 2$.

4.2. Determination of macroscopic stresses or phase stresses

The stress in the measured gauge volume can be defined with respect to the sample system (denoted by σ_{ij}, without prime) or in the "scattering vector" coordinate system (denoted by $\sigma_{ij}{}'$, with prime). Both systems are defined in Fig. 4.7 and the transformation between them can be done using a_{ij} matrix, i.e.:

$$\sigma_{ij}{}' = a_{ik}a_{jl}\sigma_{kl} \text{ and } \varepsilon_{ij}{}' = a_{ik}a_{jl}\varepsilon_{kl} \tag{4.8}$$

where $a_{ij} \coloneqq a_{ij}(\psi,\varphi)$ matrix is determined by the angles ψ and φ shown in Fig. 4.7:

$$a_{ij}(\psi,\varphi) = \begin{bmatrix} \cos\varphi\cos\psi & \sin\varphi\cos\psi & -\sin\psi \\ -\sin\varphi & \cos\varphi & 0 \\ \cos\varphi\sin\psi & \sin\varphi\sin\psi & \cos\psi \end{bmatrix} \tag{4.9}$$

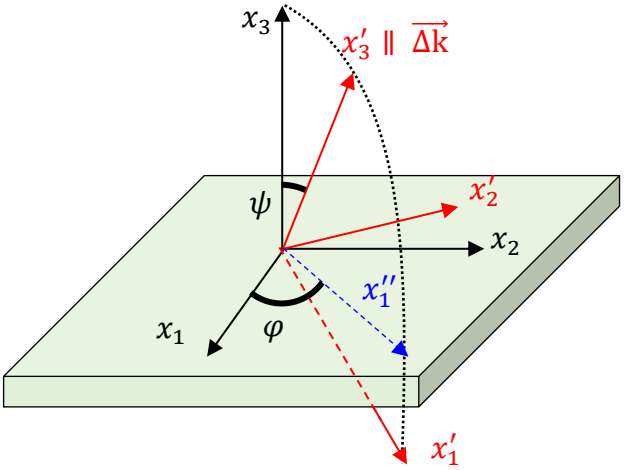

Fig. 4.7 Rotation of the sample coordinate $\boldsymbol{X}$ system to the scattering vector coordinate system $\boldsymbol{X}'$ (where x_3' is parallel to scattering vector $\overrightarrow{\Delta k}$) by the angles φ and ψ. The axis x_2' lies on the surface of the sample and x_1'' is a horizontal projection of x_1'.

Since one is able to measure the lattice strain by measuring the interplanar distances the first order stress (equation (2.20)) in single phase material or phase stress (equation (2.21)) in multiphase material can be determined. Hence, in order to obtain stress tensor the relation between this tensor and elastic lattice strains $< \varepsilon'(\psi,\varphi) >_{\{hkl\}}$ measured along scattering vector, parallel to x_3' axis and normal to planes $\{hkl\}$, must be found, i.e. [43,45,71,119]:

$$< \varepsilon'(\psi,\varphi) >_{\{hkl\}} = R_{ij}(hkl,\psi,\varphi)\,\sigma_{ij}'^{M} \quad \text{or} \tag{4.10}$$

$$< \varepsilon'(\psi,\varphi) >_{\{hkl\}} = F_{ij}(hkl,\psi,\varphi)\sigma_{ij}^{M} \tag{4.11}$$

where $< \varepsilon'(\psi,\varphi) >_{\{hkl\}}$ is the mean lattice strain calculated over the selected group of diffracting grains, while the stress σ_{ij}^{M} is the first order stress (for single phase material,

i.e. $\sigma_{ij}^{M} = \sigma_{ij}^{I}$) or phase stress (for multiphase material $\sigma_{ij}^{M} = \sigma_{ij}^{ph}$); and prim is used to distinguish the sample system $\boldsymbol{X}$ and scattering vector coordinate system $\boldsymbol{X}'$.

$$F_{ij}(hkl,\psi,\varphi) = R_{mn}(hkl,\psi,\varphi)a_{mi}a_{nj} \tag{4.12}$$

It should be emphasised that equation (4.11) can be significantly simplified in the case of the so called quasi-isotropic sample i.e. polycrystalline material with random texture, which is isotropic at the macroscopic scale but it can be anisotropic at the grain scale. In such case equation (4.11) can be rewritten with two independent X-ray elastic constants (XEC) s_1^{hkl} and s_2^{hkl}, which do not depend on the direction of measurement [43,71]:

$$\begin{aligned} &< \varepsilon'(\psi,\varphi) >_{\{hkl\}} = s_1^{hkl}(\sigma_{11}^{M} + \sigma_{22}^{M} + \sigma_{33}^{M}) \\ &+\frac{1}{2}s_2^{hkl}\,(\sigma_{11}^{M}\cos^2\varphi + \sigma_{22}^{M}\sin^2\varphi + \sigma_{12}^{M}\sin 2\varphi)\sin^2\psi \\ &+\frac{1}{2}s_2^{hkl}\sigma_{33}^{M}\cos^2\psi + \frac{1}{2}s_2^{hkl}(\sigma_{13}^{M}\cos^2\varphi + \sigma_{23}^{M}\sin^2\varphi) \end{aligned} \tag{4.13}$$

where $s_1^{hkl} = R_{11}(hkl) = R_{22}(hkl)$ and $\frac{1}{2}s_2^{hkl} = \big(R_{33}(hkl) - R_{11}(hkl)\big)$.

When the stresses σ_{ii}^{M} are defined with respect to principal directions (i.e. $\sigma_{13}^{M} = \sigma_{12}^{M} = \sigma_{23}^{M} = 0$) the above equation can be written in the following form:

$$\begin{aligned} &< \varepsilon'(\psi,\varphi) >_{\{hkl\}} = s_1^{hkl}(\sigma_{11}^{M} + \sigma_{22}^{M} + \sigma_{33}^{M}) \\ &+\frac{1}{2}s_2^{hkl}\,[(\sigma_{11}^{M}-\sigma_{33}^{M})\cos^2\varphi + (\sigma_{22}^{M}-\sigma_{33}^{M})\sin^2\varphi)]\sin^2\psi + \frac{1}{2}s_2^{hkl}\sigma_{33}^{M} \end{aligned} \tag{4.14}$$

The above equation is linear with respect to $\sin^2\psi$, which allows to apply linear regression to stress analysis. In the more general cases (i.e. using equations (4.11) and (4.12)) the stress tensor can be determined by diffraction measurement of the lattice strains for many independent directions of the scattering vector. Then the stresses tensor components are determined by least square fitting procedure in which the values of σ_{ij}^{M} are adjusted in equations (4.11), (4.13) or (4.14) in order to fit the calculated values of $< \varepsilon'(\psi,\varphi) >_{\{hkl\}}$ to the experimental ones, see e.g. [120]. However, the use of these equations requires the knowledge of the X-ray stress factors (XSFs), which can be directly measured [120–123] or calculated from the single crystal elastic constants (SECs) and the determined orientation distribution function (ODF), assuming an appropriate model of grain interaction. The most important model for calculation of XSFs are recalled below [45,73,124–127].

4.3. Prediction of diffraction elastic constants

The X-ray elastic constants are essential to calculate stress tensor using diffraction measurements. To calculate X-ray elastic constants $F_{ij}(hkl,\psi,\varphi)$, firstly $R_{ij}(hkl,\psi,\varphi)$ factors should be determined (cf. equation (4.12)). The determination of the $R_{ij}(hkl,\psi,\varphi)$ factors requires certain assumptions, the most popular of which are (see Fig. 4.8):

a) Reuss model assuming homogenous stress [45,74,124,125,127],
b) Voigt model assuming homogenous strain [45,75,126,127],
c) Eshelby-Kröner model based on ellipsoidal inclusion in homogenous medium [45,73,78,79,128].

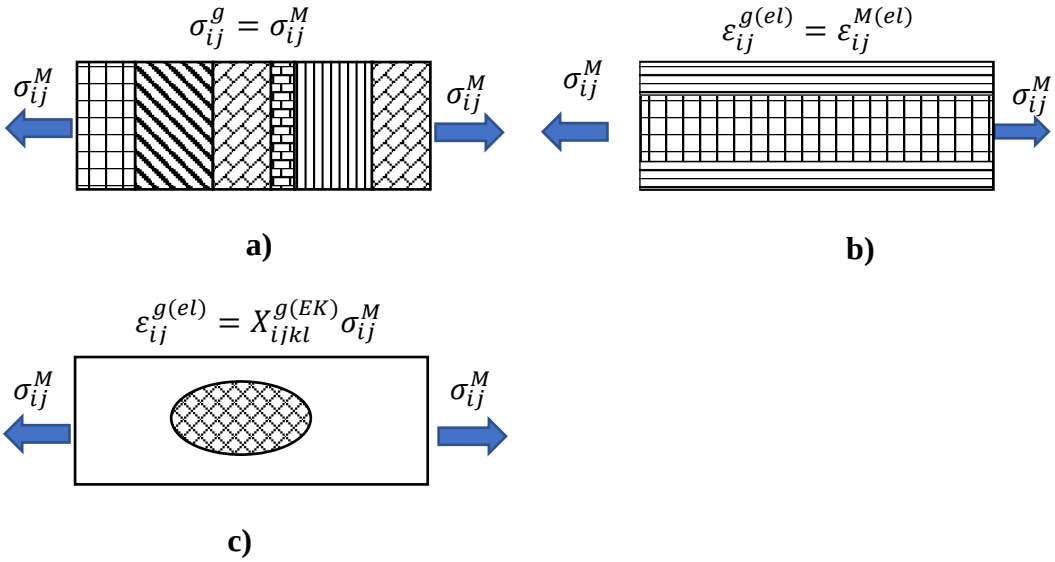

Fig. 4.8 Scheme of interactions between different grains for the mean stress σ_{ij}^{M}: a) Reuss model (homogenous stress), b) Voigt model (homogenous strain), c) Eshelby-Kröner model (ellipsoidal inclusion).

The Reuss model assumption ($\sigma'^{g}_{ij} = \sigma'^{M}_{ij}$) that the grains stress are equal to the mean stress (first order or phase stress) allows us to factor the constant values σ'^{M}_{ij} out of the average, defined over the diffraction grains, which leads to the following relation [72]:

$$< \varepsilon'(\psi,\varphi) >_{\{hkl\}} = < \varepsilon'_{33} >_{\{hkl\}} = < s'^{g}_{33ij}\sigma'^{g}_{ij} >_{\{hkl\}} = < s'^{g}_{33ij}\sigma'^{M}_{ij} >_{\{hkl\}} = < s'^{g}_{33ij} >_{\{hkl\}} \sigma'^{M}_{ij} \tag{4.15}$$

where σ'^{g}_{ij} and s'^{g}_{33ij} are the grain stress tensor and grain compliance tensor expressed in the scattering vector system of coordinates.

Comparing equations (4.10) and (4.15) the values of $R_{ij}^{R}(hkl,\psi,\varphi)$ can be calculated:

$$R_{ij}^{R}(hkl,\psi,\varphi) = < s'_{33ij}(\psi,\varphi) >_{\{hkl\}} = \frac{\sum_{\overrightarrow{\Delta k}\perp\{hkl\}} \int_0^{2\pi} s'^{\,g}_{33ij}\ f(g)\ d\gamma}{\sum_{\overrightarrow{\Delta k}\perp\{hkl\}} \int_0^{2\pi} f(g)\ d\gamma} \tag{4.16}$$

where summation $\sum_{\overrightarrow{\Delta k}\perp\{hkl\}}$ is carried out over all symmetrically equivalent diffracting plains $\{hkl\}$ being perpendicular to the scattering vector $\overrightarrow{\Delta k}$, γ is the rotation angle of grain lattice about scattering vector to obtain all orientations g for which $\overrightarrow{\Delta k} \perp \{hkl\}$ and $f(g)$ is the volume fraction of these orientations given by ODF.

Second mentioned assumption used to determine the $R_{ij}^{V}(\psi,\varphi)$ factors is based on Voigt model assumption $\varepsilon_{ij}^{\prime\, g\,(el)} = \varepsilon_{ij}^{\prime\, M(el)}$ applied to microscopic Hook law ($\sigma_{ij}^{\prime\, g} = c_{ijkl}^{\prime\, g}\varepsilon_{kl}^{\prime\, g\,(el)}$) , where $c_{ijkl}^{\prime\, g}$ is the grain stiffness tensor $\varepsilon_{ij}^{\prime\, g(el)}$ is the elastic strain of the grain, and $\varepsilon_{ij}^{\prime\, M(el)}$ is the average elastic strain for the gauge volume or given phase within this volume, defined in the scattering vector coordinate system. In this case, the mean elastic strain $\varepsilon_{kl}^{M(el)}$ can be factored out of the average calculated over <u>all grains in the gauge volume or all grains belonging to a given phase</u> [72].

$$\sigma_{ij}^{\prime\, M} = \left[c_{ijkl}^{\prime\, g}\varepsilon_{kl}^{\prime\, g\,(el)}\right] = \left[c_{ijkl}^{\prime\, g}\varepsilon_{kl}^{\prime\, M(el)}\right] = \left[c_{ijkl}^{\prime\, g}\right]\varepsilon_{kl}^{\prime\, M(el)}$$
$$\text{and } < \varepsilon'(\psi,\varphi) >_{\{hkl\}} = \varepsilon_{33}^{\prime\, M(el)} = [c'^{\,g}]_{33ij}^{-1}\sigma_{ij}^{\prime\, M} \tag{4.17}$$

where $[\ldots]$ bracket means average calculated over the whole considered volume:

$$\left[c_{ijkl}^{\prime\, g}\right] = \int_E c_{ijkl}^{\prime\, g}(g)\, f(g)\mathrm{dg}, \tag{4.18}$$

where E is the entire orientation space for which $f(g)$ is defined and dg is an elementary volume in Euler space (see subsection 2.3.2).

Comparing equations (4.10) and (4.17) the values of $R_{ij}^{V}(\psi,\varphi)$ can be calculated:

$$R_{ij}^{V}(\psi,\varphi) = [c'^{\,g}]_{33ij}^{-1} \tag{4.19}$$

It should be emphasised that the $R_{ij}^{V}(\psi,\varphi)$ and consequently $F_{ij}^{V}(\psi,\varphi)$ XSFs do not depend on the hkl reflection (i.e. $\{hkl\}$ planes) because $\left[c_{ijkl}^{\prime\, g}\right]$ average is calculated over all grains but not only diffracting grains.

Third assumption commonly used to determine the $R_{ij}^{EK}(hkl,\psi,\varphi)$ factors is self-consistent Eshelby-Kröner model based on an ellipsoidal inclusion inside a continuous homogenous medium. In this model elastic strain components ($\varepsilon_{ij}^{\prime\, g(el)}$) and stress ($\sigma_{ij}^{\prime\, g}$) for grain g and mean elastic strain ($\varepsilon_{ij}^{\prime\, M(el)}$) and stress ($\sigma_{ij}^{\prime\, M}$) are obtained using concentration tensors $A^{\prime\, g}$ and $B^{\prime\, g}$ respectively:

$$\varepsilon_{ij}^{\prime\, g(el)} = A_{ijkl}^{\prime\, g}\varepsilon_{kl}^{\prime\, M(el)} \text{ and } \sigma_{ij}^{\prime\, g} = B_{ijkl}^{\prime\, g}\sigma_{kl}^{\prime\, M} \tag{4.20}$$

where $A_{ijkl}^{\prime\, g}$ and $B_{ijkl}^{\prime\, g} = c_{ijop}^{\prime g} A_{opmn}^{\prime\, g} S_{mnkl}^{\prime\, eff}$ are concentration tensors calculated using purely elastic interaction in self-consistent method described in subsection 2.3.3 and section 3.3, $c_{ijkl}^{\prime g}$is the grain stiffnes tensor and $S_{ijkl}^{\prime\, eff}$ is the effective compliance tensor written in crystallite coordinate system, which can be calculated as inverted mean stiffness tensor $C_{ijkl}^{\prime\, eff}$ computed from formula (2.39). It should be emphasised that the effective values ($S_{mnkl}^{\prime\, eff}$and $C_{mnkl}^{\prime\, eff}$) characterising matrix properties in the self-consistent model are calculated over whole gauge volume in the case of single phase material, while for the multiphase material each phase is considered independently, i.e. the effective properties are the properties of separate phase but not of the whole material. This enables independent determination of the phase stresses in each phase as has been done in this work for the Al/SiC_p composite (cf. Chapter 5).

Combining macroscopic and microscopic Hooke law with the use of localisation tensors $A_{ijkl}^{\prime\, g}$ and $B_{ijkl}^{\prime\, g}$ one obtains the relation between the microscopic strain and the mean stress:

$$\varepsilon_{ij}^{\prime\, g(el)} = X_{ijkl}^{\prime\, g}\sigma_{kl}^{\prime\, M} \tag{4.21}$$

where: $X_{ijkl}^{\prime\, g} = A_{ijmn}^{\prime\, g} S_{mnkl}^{\prime\, eff} = s_{ijmn}^{\prime g} B_{mnkl}^{\prime\, g}$.

Having the above relation the diffraction elastic constants $R_{ij}^{EK}(hkl,\psi,\varphi)$ can be calculated similarly to equation (4.16):

$$R_{ij}^{EK}(hkl,\psi,\varphi) = \frac{\sum_{\overrightarrow{\Delta k}\perp\{hkl\}} \int_0^{2\pi} X_{33ij}^{\prime\, g}\ f(g)\, d\gamma}{\sum_{\overrightarrow{\Delta k}\perp\{hkl\}} \int_0^{2\pi} f(g)\, d\gamma} \tag{4.22}$$

where summation is carried out exactly in the same way as in equation (4.16).

4.4. Crystallite Group Method (CGM)

Apart from the interphase interactions, one of the main reasons for the differences between the grain stresses in polycrystalline materials is the difference in the orientation of the crystal lattice. The grain orientation effect is the greater, the stronger the crystallographic texture and the more anisotropic the polycrystalline grain. It should be emphasized that the above defined XSFs and the equations (4.10)-(4.14) are suitable when the first order σ_{ij}^{I} or phase stresses σ_{ij}^{ph} are determined, i.e. mean values of the stress over gauge volume (equation (2.17)) or given phase within this volume (equation (2.18)). However, using such approach the second order stresses σ_{ij}^{II} being deviations from such averages (equation (2.20)) cannot be determined. It can be done in two ways. The first one is to analyse the additional contribution of stresses σ_{ij}^{II} into equations (4.10)-(4.14) causing disagreement between fitted and measured lattice strains. In this case the interpretation must be based on crystallographic model predicting such disagreements for given mode of deformation. The disadvantages of this approach is its limitation to samples subjected to strictly defined types of deformation, e.g. cold rolling or uniaxial tests. The methodology of determination of the plastic incompatibilities σ_{ij}^{II} stresses, based on the equations (4.10)-(4.14) with additional term interpreted by EPSC model was developed by Baczmanski et al. [24,29,73,129–131]. Another method for determination of the σ_{ij}^{II} stresses or rather the stresses for groups of grains (crystallites) σ_{ij}^{CR} having similar lattice orientations is based on direct measurement based on the crystallite group method (CGM), used in this work. This approach was proposed for texture materials for which the preferred orientations are defined [40,42–46]. Alternatively, the grain stresses can be determined for specific grains using synchrotron radiation [22].

In order to determine the stresses for crystallite groups having selected orientations (CGM method) the diffraction measurements, especially with neutron or synchrotron radiations can be used. Due to the fact that diffraction allows for independent measurement of the interplanar spacings for selected $\{hkl\}$ planes it is possible to find out such poles $P(\psi,\phi)_{\{hkl\}}$ on pole figure (defined by the ψ and ϕ angles and hkl reflection in Fig. 4.9) for which the measured lattice strains are mostly affected by the grains having given orientation of the crystallite lattice.

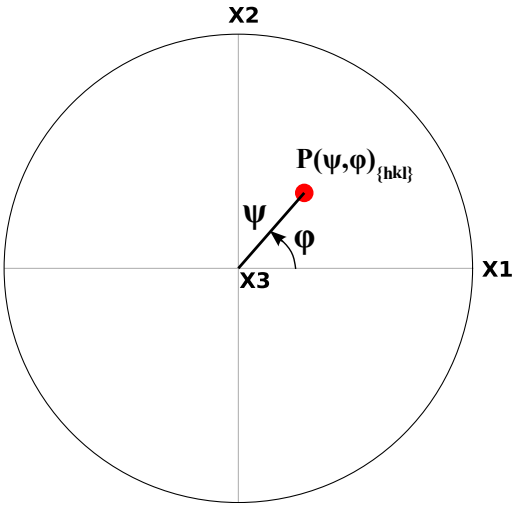

Fig. 4.9 Selected pole $P(\psi,\phi)_{\{hkl\}}$ in pole figure for which the lattice strain is measured in CGM (cf. Fig. 2.8 and note that due to literature conventions the α and β letters used in the case of texture characterisation were changes to ψ and φ used in the stress measurement methodology).

When the lattice strains are measured for a set of poles corresponding to given lattice orientation the stress tensor σ_{ij}^{CR} for a group of grains having approximately this orientation can be determined. This can be done using the least squares procedure in which the lattice strains are adjusted to the measured values according to the formula:

$$< \varepsilon(\varphi,\psi) >_{hkl} = a_{3k}a_{3l}s_{klij}\sigma_{ij}^{CR} \tag{4.23}$$

where: s_{klij} are the single crystal elastic constants (SECs) and a_{ij} transformation matrix is defined in equations (4.8) and (4.9).

In order to unequivocally determine the stresses for a given orientation, the selected reflections must mostly come from that orientation, which means that a given orientation should be the one preferred for a given crystallographic texture. As shown in chapter 6, for a simple texture, it is also possible to estimate stresses for particular non-preferred orientations. However, when choosing reflections for orientation corresponding to weak texture intensity a special attention should be paid to exclude reflections coming from the strong preferred orientations, to avoid their significant contribution to the selected poles.

It should be emphasized that in the case of CGM the single crystal elastic constants are usually used in the relation (4.23), however in this work the $F_{ij}^{R}(hkl,\varphi,\psi)$ calculated according to Reuss model were applied in stress analysis, i.e.:

$$< \varepsilon(hkl,\varphi,\psi) >_{hkl} = F_{ij}^{R}(hkl,\varphi,\psi)\ \sigma_{ij}^{CR} \tag{4.24}$$

In such a case instead of single grain the elastic properties are calculated for a group of grains selected by diffraction and crystallographic texture, assuming that for this group the stress is the same for each grain in this group. This assumption is valid for groups consisting of grain orientations being close to the preferred texture orientations [45]. It is worth to noting, that the crystallites of magnesium exhibit low elastic anisotropy, therefore the choice of different types of $F_{ij}(hkl, \varphi, \psi)$ factors (or use the SECs) does not change scientifically the obtained results.

In order to effectively search for the orientation of crystallites, a simple program was written, thanks to which it is possible to calculate the position and show the poles defined in Fig. 4.9. The program allows to draw:

- poles for selected crystallite having given orientation (by setting Eulerian angles or rotating around axes of sample coordinate system),
- lines showing reflections of preferred orientations for sample with fibre texture (0001),
- positions of scattering vector stereographic projection for detectors used during neutron measurements.

As an example, the poles for the orientation for which $[0001] \parallel$ RD and $[1\bar{2}\,10] \parallel$ *T*D) of a crystallite with the HCP structure and $\frac{c}{a} = 1{,}624$ [132] are presented in Fig. 4.10. It shows that the coloured points representing reflections from the preferred orientations of the (0001) fibre texture contain the poles corresponding to the crystallite with the initial orientation. Furthermore, it is clearly seen that the preferred orientations correspond to the original orientation rotated by any angle about the *c*-axis of the unit cell being parallel to normal direction ND.

Fig. 4.11 shows an example orientation tilted from the initial one through rotation about an axis $\boldsymbol{x_1}$ by angle of 43°. One can see here that, for example, the reflections $0\bar{1}3$ and $1\bar{1}3$ of the tilted orientation are close to the yellow line representing the positions of the reflections from the $\{1013\}$ family of preferred orientation (see Fig. 4.10). Due to the significant share of the preferred orientations in these reflections, they should be excluded from the analysis carried out for the tilted orientation, showing a lower intensity of the texture. Such analysis should be performed for all not preferred orientations.

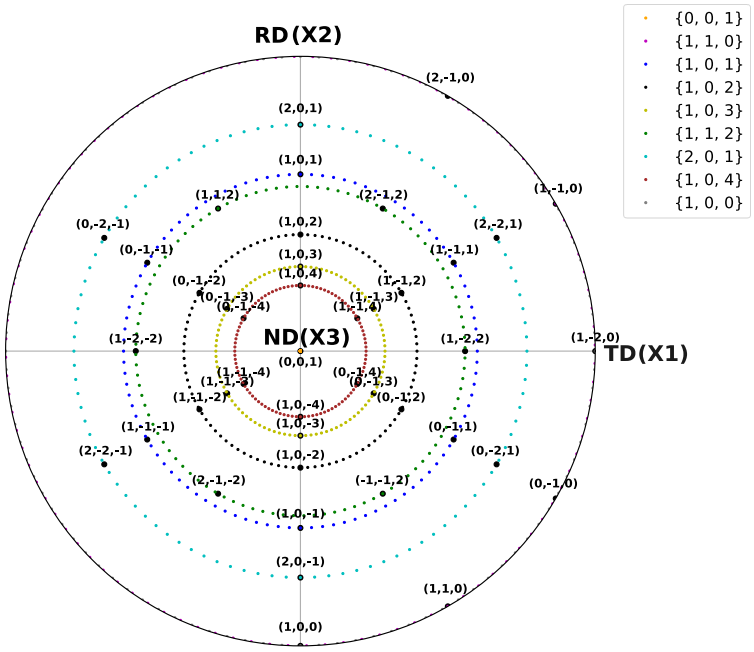

Fig. 4.10 An example of the initial orientation of a crystallite with HCP structure and $\frac{c}{a} = 1{,}624$ [132] (corresponding to Mg structure). The coloured points represent reflections from the preferred orientations in the (0001) fibre texture.

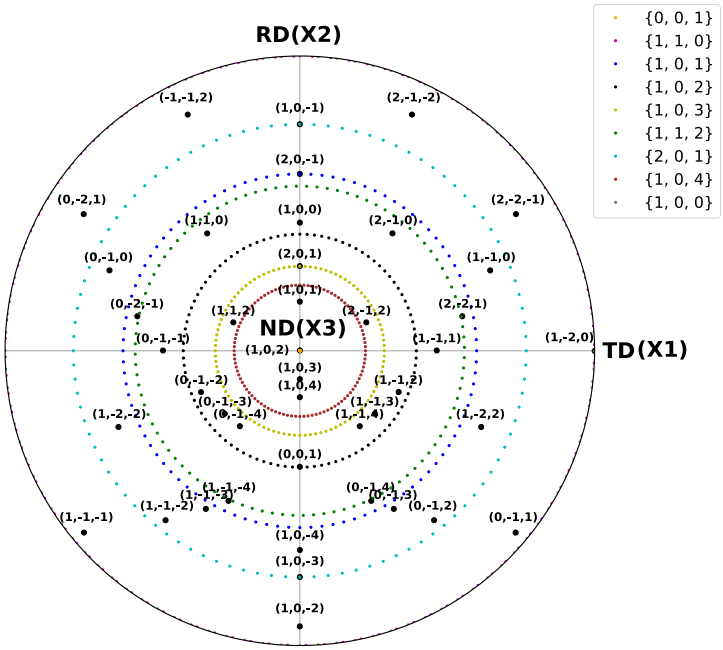

Fig. 4.11 An example of an orientation of a crystallite with HCP structure and $\frac{c}{a} = 1{,}624$ [132](corresponding to Mg structure) rotated in relation to the initial orientation by Euler angles $\phi_1 = 0°$, $\Phi = 43°$, $\phi_2 = 0°$. The coloured points represent reflections from the preferred orientations in the (0001) fibre texture.

4.5. Implementation of the stress analysis methods on the used equipment

In order to determine stresses using the above described methods the relative lattice strains (with respect to the stress free powder or initial sample) or simply the interplanar spacings in the case of surface measurements (with assumption of $\sigma_{33}^{I} = 0$) should be measured in different directions. These directions are determined by the scattering vector with respect to the sample system coordinates $\boldsymbol{X}$, as defined in Fig. 4.7. The $\boldsymbol{X}$ system can be constructed in any way, however, it is most convenient for both the calculation and further description of stresses to choose a right-handed system so that its axes are parallel to the main directions determined by the sample treatment (e.g. rolling) or determined by the applied load. One of the possible constructions of such a system (used in this work) is the choice the $\boldsymbol{x_3}$ axis parallel to the direction of the applied force.

The orientations of the scattering are changed in different ways depending on the experimental setup used for measurements. The stress analysis performed in this work was done on the basis of measurements carried out using two experimental techniques:

- angle dispersive (AD) method with the monochromatic neutron radiation with wavelength λ = 1,1580 Å on a TKSN 400 (HK9) diffractometer in the Nuclear Physics Institute in Řež (Czech Republic),
- energy dispersive (ED) method with polychromatic neutron radiation (TOF method) on EPSILON-MSD and FSD diffractometers at the Frank Laboratory of Neutron Physics in Joint Institute for Nuclear Research in Dubna (Russia).

The measurements on TKSN 400 (HK9) diffractometer were done previously [40] and the analysis of the results was significantly developed and used in this work. The lattice strains were measured for different poles which orientations (positions in pole figure) were changed using Eulerian cradle (cf. Fig. 4.12), while the hkl reflections were chosen by setting appropriate 2θ angle. The rotation angles ψ and φ and sample system coordinates $\boldsymbol{X}$ are defined in Fig. 4.12b (cf. also Fig. 4.7). Additionally, a tensile rig was mounted in the Eulerian cradle in order to apply load to the sample during *in situ* diffraction measurements.

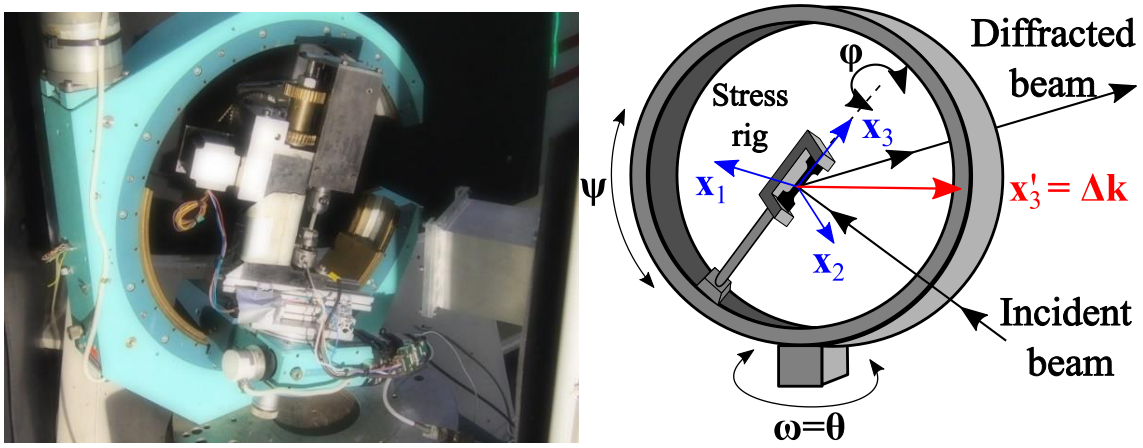

a) **b)**

Fig. 4.12 The picture of Eulerian cradle used on TKSN 400 (HK9) diffractometer (a). Sketch of Eulerian cradle (b) used to change the orientation of the sample with respect to the scattering vector $\overrightarrow{\Delta k}$ by changing angles ψ and φ, while reflection hkl is chosen by setting scattering angle 2θ (where $\boldsymbol{X'}$ is a laboratory system and for sample system: $\boldsymbol{x_1} \parallel$ TD, $\boldsymbol{x_2} \parallel$ ND, $\boldsymbol{x_3} \parallel$ RD).

The main experiments performed in the frame of this work were conducted on EPSILON-MSD diffractometer. The secondary optics of this diffractometer consists of 3 groups of detector banks (named L_1-L_9, cf. Fig. 4.13), arranged so that each of them is perpendicular to the incident neutron beam, i.e. $2\theta = 90°$ for each detector. The advantage of such an arrangement of detectors (L_i) is that the scattering vector $\overrightarrow{\Delta k_i} = (\vec{k}_i - \vec{k}_{inc})$ for each of them has a different direction with respect to the sample (see Fig. 4.14). Therefore the lattice strains can be measured in 9 different directions simultanously which have to be determined using the convention defined in Fig. 4.7, i.e. the ψ^i and φ^i have to be found for each i-*th* detector.

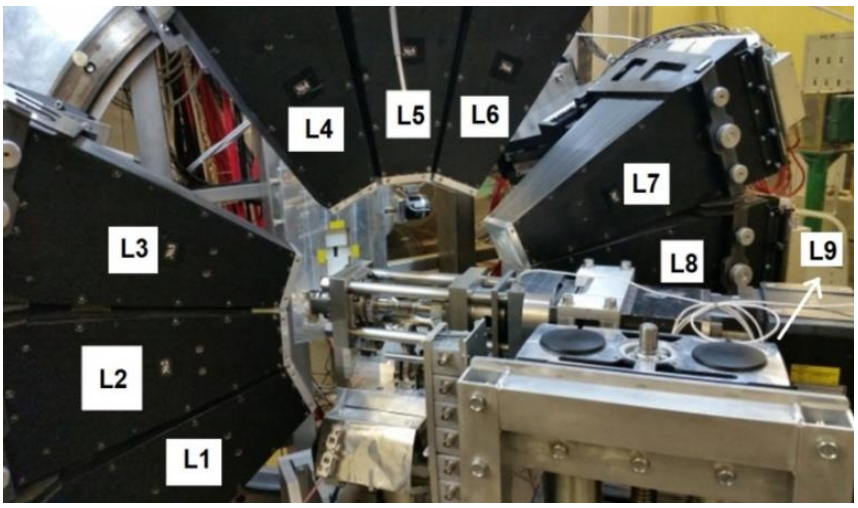

Fig. 4.13 Picture of EPSILON-MSD diffractometer.

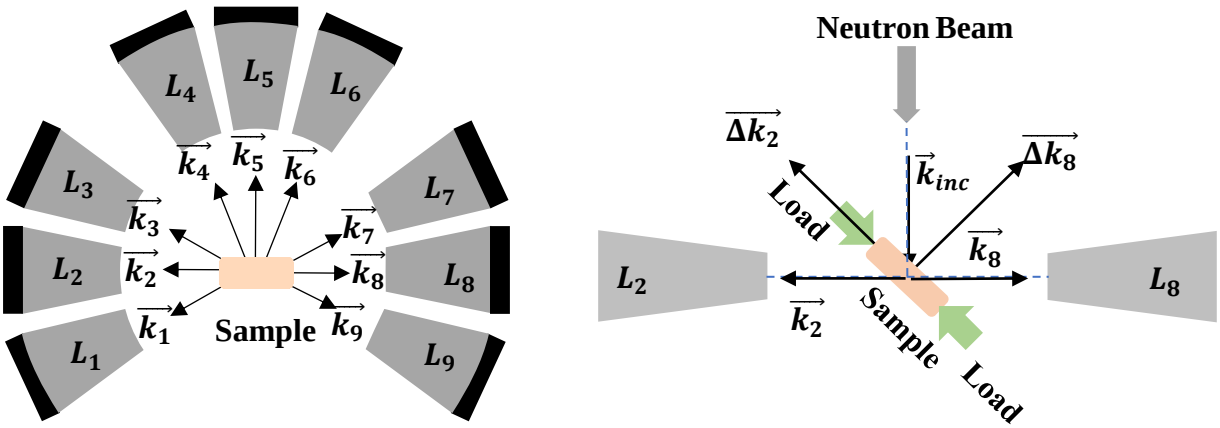

a) Front view **b) Top view**

Fig. 4.14 Schematic diagram of detector banks at the EPSILON-MSD diffractometer showing in figure (a) the directions of the diffracted beams (directions of wave vectors $\vec{k}_i$). Two example scattering vectors $\overrightarrow{\Delta k_2}$ and $\overrightarrow{\Delta k_8}$, shown in figure (b), are placed on the planes containing the incident wave vector $\vec{k}_{inc}$ and diffracted wave vectors $\overrightarrow{k_2}$ and $\overrightarrow{k_8}$, respectively. The same constructions can be drawn for all other detectors for which $2\theta = 90°$.

To determine the angles ψ and φ the sample system $\boldsymbol{X}$ can be defined through unite vectors $\widehat{x_3} = \frac{\overrightarrow{\Delta k_2}}{|\overrightarrow{\Delta k_2}|}$, $\widehat{x_1} = -\frac{\overrightarrow{\Delta k_8}}{|\overrightarrow{\Delta k_8}|}$, $\widehat{x_2} = \widehat{x_3} \times \widehat{x_1}$ (cf. Fig. 4.14 and Fig. 4.15). Therefore the direction x_3 of the sample system is parallel to the scattering vector ($\overrightarrow{\Delta k_2}$) of the detector L_2, direction x_1 is opposite to the scattering vector ($-\overrightarrow{\Delta k_8}$) of detector L_8 and direction x_2 points to the detector L_5, but it is not parallel to any scattering vector.

If we know the transformation matrix (4.9) between sample system $\boldsymbol{X}$ and scattering vector system $\boldsymbol{X'}$ the angles φ and ψ (defined in Fig. 4.7) can be determined from:

$$\begin{aligned} \cos\psi = a_{33} &\Longrightarrow \psi = \arccos a_{33} \\ \operatorname{tg}\varphi = \frac{a_{32}}{a_{31}} &\Longrightarrow \varphi = \operatorname{atan2}(a_{32}, a_{31}) \end{aligned} \tag{4.25}$$

where function $\operatorname{atan2}(y, x)$ defined for domain $[0,2\pi)$ takes form:

$$\operatorname{atan2}(x,y) = \begin{cases} arctg\left(\frac{y}{x}\right) + \pi & if\ x < 0 \\ arctg\left(\frac{y}{x}\right) & if\ x > 0\ and\ y \geq 0 \\ arctg\left(\frac{y}{x}\right) + 2\pi & if\ x > 0\ and\ y < 0 \\ \frac{\pi}{2} & if\ y > 0\ and\ x = 0 \\ \frac{3\pi}{2} & if\ y < 0\ and\ x = 0 \\ undefined & if\ x = y = 0 \end{cases}. \tag{4.26}$$

This allows us to calculate the angles φ and ψ for any orientations of the scattering vector particularly for these orientations which are seen by the detectors L_1 - L_8 at EPSILON-MSD. To do this, let us define intermediate laboratory system $\boldsymbol{X^{lab}}$ by rotation of the sample system $\boldsymbol{X}$ about axis x_2 by angle α (see Fig. 4.15). The orientations of the scattering vectors with respect to laboratory system $\boldsymbol{X^{lab}}$ can be easily found, i.e., they are given by angles:

$$\begin{aligned} \psi^{lab} &= \alpha, \\ \varphi^{lab,i} &= \omega^i \end{aligned} \tag{4.27}$$

where $\alpha = \theta = 45°$ and $\boldsymbol{\omega^i}$ is angle defining position of the i-th detector by rotation around $\boldsymbol{x_3^{lab}}$ parallel to the incident neutron beam, see Fig. 4.15 (the angles $\boldsymbol{\omega_i}$ are given in Table 4.1). Therefore the transformation matrix from $\boldsymbol{X^{lab}}$ system to $\boldsymbol{X'}$ is given by:

$$R_{kl}^{lab,i} = \begin{bmatrix} \cos\omega^i \cos\alpha & \sin\omega^i \cos\alpha & -\sin\alpha \\ -\sin\omega^i & \cos\omega^i & 0 \\ \cos\omega^i \sin\alpha & \sin\omega^i \sin\alpha & \cos\alpha \end{bmatrix} \tag{4.28}$$

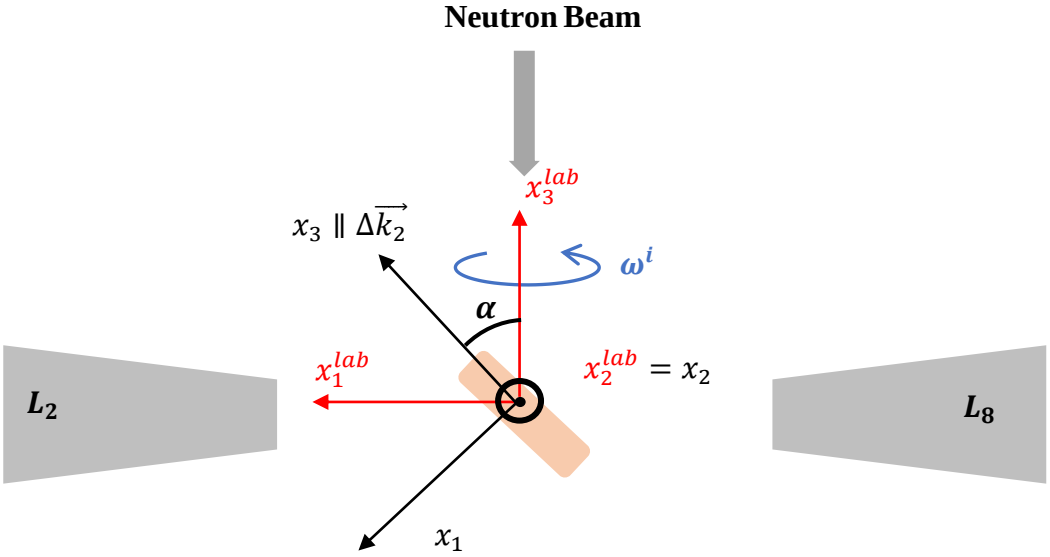

Fig. 4.15 Orientation of the laboratory system $\boldsymbol{X^{lab}}$ with respect to the sample coordinate system $\boldsymbol{X}$.

The transformation from the sample coordinate system $\boldsymbol{X}$ to the laboratory system $\boldsymbol{X^{lab}}$ can be determined (see Fig. 4.15):

$$R_{mn}^{\alpha} = \begin{bmatrix} \cos\alpha & 0 & \sin\alpha \\ 0 & 1 & 0 \\ -\sin\alpha & 0 & \cos\alpha \end{bmatrix}. \tag{4.29}$$

Therefore, taking into account both transformations (4.28) and (4.29) the transformation from the sample coordinate system $\boldsymbol{X}$ to the scattering vector system $\boldsymbol{X'}$ can be found:

$$R_{kl}^{i} = R_{km}^{lab,i} R_{ml}^{\alpha} = \begin{bmatrix} \cos^2\alpha\cos\omega^i + \sin^2\alpha & \sin\omega^i\cos\alpha & \cos\alpha\sin\alpha\left(\sin\alpha\cos\omega^i - 1\right) \\ -\cos\alpha\sin\omega^i & \cos\omega^i & -\sin\alpha\sin\omega^i \\ \sin\alpha\cos\alpha\left(\cos\omega^i - 1\right) & \sin\omega^i\sin\alpha & \cos^2\alpha + \sin^2\alpha\cos\omega^i \end{bmatrix} \tag{4.30}$$

Thus the formulas for the angles describing scattering vector orientations with respect to the sample coordinate system $\boldsymbol{X}$ can be written for *i-th* detector:

$$\begin{aligned} \psi^i &= \arccos R_{33}^i = \arccos(\cos^2\alpha + \sin^2\alpha\cos\omega^i) \\ \varphi^i &= \operatorname{atan2}\left(R_{31}^i, R_{32}^i\right) = \operatorname{atan2}\left(\sin\alpha\cos\alpha\left(\cos\omega^i - 1\right), \sin\omega^i\sin\alpha\right) \end{aligned} \tag{4.31}$$

These formulas were used to calculate the φ^i and ψ^i angles for the sample placed in the EPSILON-MSD diffractometer in such a way that the direction of the applied load is parallel to the scattering vector $\overrightarrow{\Delta k_2}$, which means that the angle α is equal to 45° (Fig. 4.15). The calculated values of φ^i and ψ^i angles are presented in Table 4.1 and the corresponding poles $P\left(\psi^i, \varphi^i\right)_{\{hkl\}}$ are drawn in the pole figure in Fig. 4.16. The advantage of TOF method is that the whole spectrum enabling to measure different hkl reflections is measured for each orientation φ^i and ψ^i.

Table 4.1 Orientations of the scattering vector for 9 diffractometers with respect to laboratory system $\boldsymbol{X^{lab}}$ and to sample system $\boldsymbol{X}$.

Detector		L_1	L_2	L_3	L_4	L_5	L_6	L_7	L_8	L_9
Laboratory system $\boldsymbol{X^{lab}}$	ω^i	339°	0°	21°	69°	90°	111°	159°	180°	201°
	α	45°								
Sample system $\boldsymbol{X}$	ψ^i	14,81°	0,00°	14,81°	47,22°	60,00°	71,28°	88,10°	90,00°	88,10°
	φ^i	262,53°	90,00°	97,46°	115,92°	125,26°	135,81°	165,31°	180,00°	194,69°

It is worth noting that the TOF method with 9 detectors allows for the simultaneous collection of a lot of information on the lattice strains, which can be used to determine the components of the stress tensor and their anisotropy, as well as to select grain groups using CGM for textured polycrystalline materials. This is a significant progress in research on the determination of the CRSS values and the phenomenon of stress partitioning between grains / phases. Such direct analysis is not possible without additional model prediction, when lattice strains are measured in only two directions, as is usually done on other instruments in the case of *in situ* measurements using the TOF method.

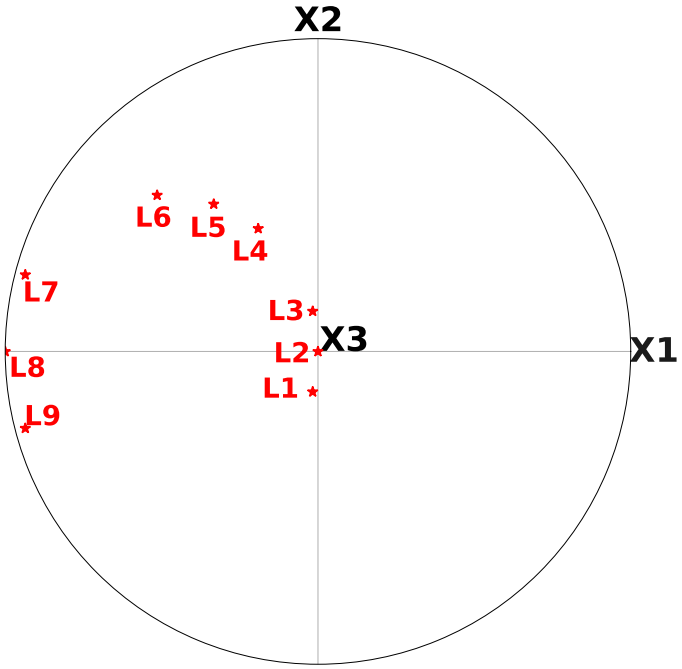

Fig. 4.16 Poles $P\left(\psi^i, \varphi^i\right)_{\{hkl\}}$ corresponding to orientations of the scattering vector for 9 detectors $L_1 - L_9$ defined with respect to sample coordinate system $\boldsymbol{X}$ (for each orientation different hkl reflections are available using TOF method).

4.6. Uncertainty analysis

Many factors influence the shape of the diffraction peak. In the AD method, the incident beam is never perfectly monochromatic, which affects the wavelength uncertainty in the Bragg law. Another factor influencing the uncertainty of the determined position and shape of the diffraction peak is the divergence of the radiation beam, which affects the uncertainty of the diffraction angle. During diffraction measurements, the lattice strain uncertainty related to the diffraction angle increases with the decrease of the diffraction angle, which is especially important in the case of X-ray diffraction [43,71].

In the case of using monochromatic X-ray radiation, the uncertainty of the determined interplanar spacing is influenced by setting the sample in the right position, collimation of the radiation beam and the value of the scattering value angle [43,71]. It should be emphasized that for neutron measurements, the position of the sample has a much smaller impact on the accuracy of the measurement (compared to the X-ray method), because the gauge volume for which the lattice strains are determined is usually inside the sample and its position is determined by the slits or collimators forming the beam [133]. The source of measurement uncertainty (mainly systematic) may be phenomena such as extinction and absorption of the neutron beam. In the case of AD neutron measurements conducted inside the sample, the cuboid-shaped reference volume obtained for $2\theta = 90\ ^\circ$ is the optimal. For this shape, the smallest changes in the gauge volume occur during a 2θ scan.

The neutron diffraction measurements presented in this work were done during *in situ* tensile, compression tests or during thermal treatment. In these cases the measurements of lattice strains were performed relatively to the interplanar spacings measured for the initial sample (except for deformation measured for twins which are born during deformation). From these data the change in the stress/strain with respect to the initial sample are determined. The advantage of this method is that the possible systematic errors are cancelled when the relative lattice strains are calculated. The only exception is the case of twins which appear during deformation and the grains with twin orientations are practically not present in the initial sample because of significant crystallographic texture. Therefore, the initial values of interplanar spacings for some of reflections from twin orientations must be extrapolated from other interplanar spacings measured in the undeformed sample. The method of extrapolation proposed by Clausen et al. [16] was applied in this work and the possible systematic uncertainty was estimated. This uncertainty is in the order of statistical errors and is discussed in section 6.3 and section 7.1, where the error corridor was drawn (cf. Fig. 7.6e, f) in order to compare systematic and statistic uncertainties. In the other presented results the systematic and statistic errors were added to show maximal error bar when the experimental results are compared with model (cf. Fig. 7.6a-d).

It should be noted that the uncertainties of the measured stresses cannot be calculated directly, especially for CGM in which the groups of grains can interfere leading to inconsistent results when the stress tensor is calculated using the least square procedure. This is the main cause of errors in the results presented in this paper, but the analysis should also take into account the statistical uncertainty related to the determined peak position, especially for low peak intensity. Since the stress uncertainties cannot be calculated directly, the most reasonable method of analysis is based on estimation of the convergence between the experimental lattice strains and those fitted by the least squares procedure [43].

In the work, the components of stress tensor were determined using the STRESS program [73,120,127,134], in which the least squares method is used to determine the stresses from the measured lattice strains on the basis of equation (4.11) or (4.24). In calculations the General Linear Least Squares (GLLS) procedure [135] is used and the fitting is based on minimisation of merit function:

$$\chi^2 = \frac{1}{N-M}\sum_{n=1}^{N}\left(\frac{\langle a(\varphi_n,\psi_n)\rangle_{\{hkl\}}^{exp} - \langle a(\varphi_n,\psi_n)\rangle_{\{hkl\}}^{cal}}{\delta_n}\right)^2 \qquad (4.32)$$

where the experimental and fitted lattice strains in the *n-th* measurement are denoted by $\langle \varepsilon'(\psi_n,\varphi_n)\rangle_{\{hkl\}}^{exp}$ and $\langle \varepsilon'(\psi_n,\varphi_n)\rangle_{\{hkl\}}^{cal}$, δ_n is the uncertainty of measured lattice strain determined from uncertainty of peak position, the sum is calculated for N measurements, and M is the number of determined components of the stress tensor (i.e. number of fitting parameters).

As the result the stress components σ_{ij}^{M} or σ_{ij}^{CR} and their uncertainties are calculated from the residuals $\langle a(\varphi_n,\psi_n)\rangle_{\{hkl\}}^{exp} - \langle a(\varphi_n,\psi_n)\rangle_{\{hkl\}}^{cal}$ which contribution is weighted by inverted strain uncertainties $1/\delta_n$. In the GLLS procedure the uncertainties of the adjusted stresses σ_{ij} are computed from equation $\delta\sigma_{ij} = \sqrt{Var(\sigma_{ij}) * \chi^2}$, where Var means variance and such uncertainties correspond to the assumption of a "good fit" for which $\chi^2 = 1$. Thus, the presented stress uncertainties originate from the disagreement between theoretical and experimental lattice strains but also the statistical error for particular measurements is taken into account.

5. Evolution of phase stresses in Al/SiC_p composite

5.1. State of art and previous studies

In this part of the thesis the stress evolution in metal constituents of matrix composite (MMC) during heat treatment and mechanical loading are studied. To do this the stress partitioning between Al matrix and SiC-particle reinforcement in Al/SiC_p is investigated. The theoretical study is carried out using the developed EPSC model considering generation and relaxation of the thermal origin stresses. The model results are compared with lattice strains determined using TOF diffraction measurements, carried out *in situ* during thermal treatment followed by compression test. The unquestionable advantage of the diffraction technique is that the measurements can be done independently in Al matrix and SiC_p reinforcement. This allowed the study of the stresses in both composite components during elastoplastic deformation [1,64], temperature variation [136], thermal and mechanical treatments [137,138] and damage process [2,139]. It was found that phase stresses of opposite signs are generated in the Al-matric and SiC_p reinforcement during cooling of the composite [137]. The so called thermal stresses arise due to difference in thermal expansion/contraction of the constituents and they can be relaxed by elastoplastic deformation [4,63] or thermo-mechanical process [5].

It should be noted that the MMC are the materials which exhibit better mechanical properties compared to the Al and SiC constituents. The stiffness, strength as well as wear resistance of the composite is superior compared to Al alloy [140,141]. The key question is: what is the cause of this improvement in mechanical properties? Generally, two main reasons for enhancing the MMC are considered:

- the matrix is hardened due to pining of dislocations on small reinforcement particles, which depends on the size and distribution of the particles [142],

- the load is transferred from the metal matrix to elastically deformed reinforcement, leading to higher strengths of composite comparing to the metal alloy [65].

The problem of stress partitioning between matrix and reinforcement was investigated using both the model prediction and the diffraction measurements. Among them the FEM method was used to find out the so called 'exact solution' for the macroscopic behaviour of the Al/SiC_p composite, which was then compared with self-consistent calculations and Mori-Tanaka model [143–145]. The latter models were based on the Eshelby type approximation of the ellipsoidal inclusion embedded in the homogeneous medium [78]. It was found that the self-consistent model gives too stiff response [146] which can be improved assuming isotropic tangent modulus in calculation [144,147,148]. On the other hand, the EPSC model used for the two-phase material (i.e. Al/SiC_p) was successfully verified by comparing the model results with lattice strains in Al and SiC components measured *in situ* with neutron diffraction during sample bending [64]. The agreement of the experimental and model results confirmed that the interaction between Al matrix and SiC particles was correctly calculated (for Al/SiC_p composite containing 17% volume fraction of SiC particles with diameter of $3\ \mu m$ and Al2124 alloy matrix).

The results of previous studies of the Al/SiC_p composite carried out with the participation of the author of this dissertation are briefly summarized in this section as an introduction to the main research conducted in this thesis. Recently the Al/SiC_p (17,8% volume fraction of SiC particles with mean diameter of $0{,}7\ \mu m$ and Al2124 alloy matrix) composite used in this work was studied comparing the EPSC calculations with mechanical tensile test [65,66,149]. The full characterisation of this material is given in section 5.2 As shown in Fig. 5.1 a good agreement of the macroscopic stress-strain curve for Al/SiC_p composite was obtained in the case of the anisotropic EPSC model. In calculations the same properties as obtained for the Al2124 alloy without reinforcement were assumed (cf. the measured and predicted curves for Al2124 alloy). Both Al2124 alloy and Al/SiC_p composite were subjected to the same treatment T6, cf. next section and [65].

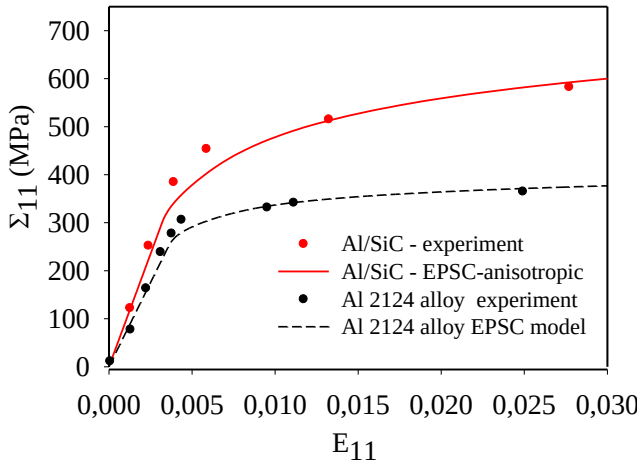

Fig. 5.1 Comparison of experimental tensile tests, obtained for the unreinforced Al2124 alloy and the Al/SiC_p composite, with EPSC model [65,66,149].

The study, concerning phase stresses (σ_{ij}^{ph} defined in subsection 2.3.2) in the Al matrix and SiC_p reinforcement, was performed using TOF neutron diffraction on EPSILON-MDS diffractometer (cf. section 4.5) [65]. The results show that the stress in both constituents significantly changed due to plastic deformation, suggesting relaxation of the initial mean phase stresses created previously by thermal treatment (this result agree with other papers concerning Al/SiC_p [4,5,63]). It was found that thermal stresses arise between the phases in the cooled sample due to the difference in thermal expansion coefficient (CTE) of components such as Al matrix and SiC_p reinforcement (see Table 5.3). As a result, the equilibrium between the stresses in the components leads to a zero macroscopic stress calculated as the average over the whole volume of the sample.

In another experiment, the TOF measurements were conducted *in situ* and the lattice strains along the applied tensile load were measured and compared with EPSC model prediction (EPSILON-MDS diffractometer) [65]. Two thermal treatments (T1 and T6) were applied before experiment to the initial (non-deformed) samples. In both cases the initial phase stresses (σ_{ij}^{ph}) having thermal origin were assumed and their relaxation was noticed by comparing the evolutions of lattice strains measured by diffraction with those predicted by the model (the model prediction did not take into account the phase stress relaxation), cf. Fig. 5.2.

The effect of thermal stresses relaxation is seen as the increase in lattice strains in the SiC_p reinforcement and simultaneous decrease in the strains in Al matrix, which was not predicted by the EPSC model starting from the state with initial thermal stress (dashed lines in Fig. 5.2). After this relaxation the experimental lattice strains are in agreement with model prediction in which zero initial stresses were assumed (continues lines in Fig. 5.2).

In both studied samples smaller lattice strains were found in the stiffer SiC_p reinforcement compared to the more compliant Al matrix (cf. Table 5.3). Also it was found, that T1 treatment leads to smaller value of the yield stress for the Al matrix compared to the T6 treatment. This was explained through precipitation hardening of the Al matrix due to the artificial aging applied during T6 treatment which leads to harder matrix comparing to this obtained after T1 treatment [65].

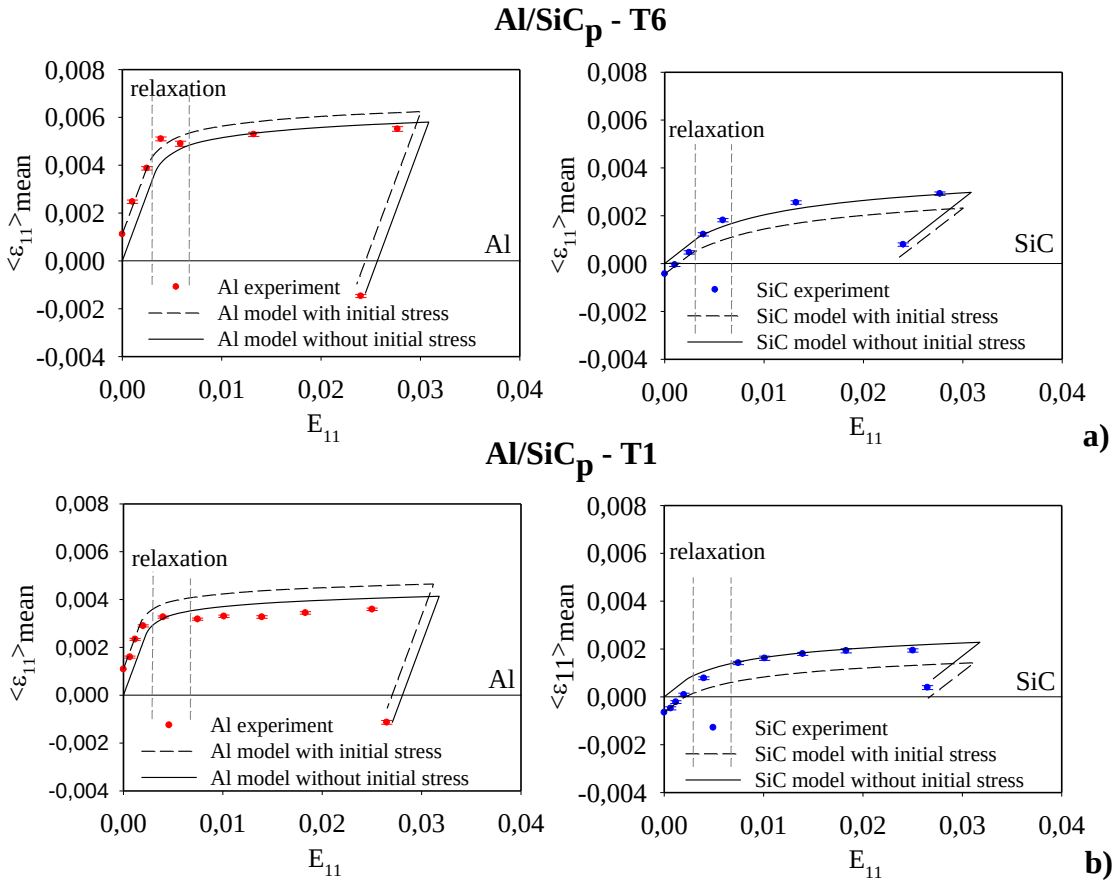

Fig. 5.2 Comparison of the predicted and measured arithmetic means of the lattice strains in the Al matrix (for reflections: 200, 111, 220, 311) and in SiC_p reinforcement (for reflections: 006/102, 108/110, 202/116) after heat treatments T6 (a) and T1 (b). In calculations the initial thermal origin stresses are used as the input data (dashed lines) or zero values of the initial stresses are introduced (continuous lines). Between the vertical dashed lines the phase stresses relax [65].

Then *in situ* diffraction experiment during thermal treatments was performed on the FSD diffractometer (cf. section 4.5)using the TOF neutron diffraction by Kot et al. [66]. The latter results were previously analysed in the MSc thesis of the author of this dissertation [150]. The Al/SiC_p composite, Al2124 alloy and SiC powder were independently subjected to heating followed by cooling using the mirror furnace with infrared radiation. Lattice strain caused by thermal expansion in Al2124 alloy (without

reinforcement) and a SiC powder versus temperature are shown in Fig. 5.3a, and compared with the lattice strains in both components of the Al/SiC_p composite in Fig. 5.3b.

The total lattice strain $\langle\varepsilon\rangle^{T}_{\{hkl\}}$ measured for planes $\{hkl\}$ at temperature T are defined by the equation:

$$\langle\varepsilon\rangle^{T}_{\{hkl\}} = \frac{\langle d\rangle^{\mathrm{T}}_{\{hkl\}} - \langle d\rangle^{0}_{\{hkl\}}}{\langle d\rangle^{0}_{\{hkl\}}} \tag{5.1}$$

where $\langle d\rangle^{\mathrm{T}}_{\{hkl\}}$ and $\langle d\rangle^{0}_{\{hkl\}}$ are the measured interplanar spacings at temperature T and at room temperature, respectively.

The influence of the elastic interaction between the composite constituents (Al matrix and SiC_p reinforcement) on the lattice strains obtained from neutron diffraction can be seen in Fig. 5.3b. For the Al matrix, the total lattice stain grows slower with the temperature compared to the Al2124 alloy without reinforcement, while the opposite effect occurs in SiC_p. The obtained results suggest that in addition to thermal expansion in the tested composite, the experimental lattice strains are influenced by the elastic interaction between the phases.

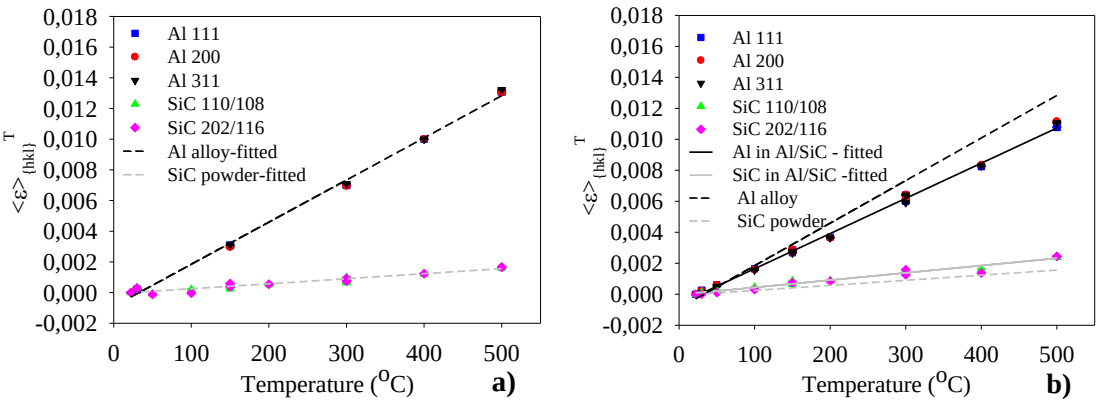

Fig. 5.3 (a) Lattice strain in a sample of Al2124 alloy (without reinforcement) and a SiC powder sample versus temperature. (b) Comparison of the lattice strain for individual phases in the composite (solid lines adjusted to the experimental data) with the straight lines adjusted to the strains in the Al2124 alloy without reinforcement and the SiC powder (dashed lines, also shown in figure a) [66].

The elastic lattice strains in the composite components $\langle\varepsilon\rangle_{\{hkl\}}^{Al,elast}$ and $\langle\varepsilon\rangle_{\{hkl\}}^{SiC,elast}$ related to interphase stresses in the composite (excluding thermal expansion) are defined through:

$$\langle\varepsilon\rangle_{\{hkl\}}^{Al,elast} = \frac{\langle d\rangle_{\{hkl\}}^{\text{Al\_comp.}} - \langle d\rangle_{\{hkl\}}^{\text{Al\_alloy}}}{\langle d\rangle_{\{hkl\}}^{\text{Al\_alloy}}} \quad \text{and} \quad \langle\varepsilon\rangle_{\{hkl\}}^{SiC,elast} = \frac{\langle d\rangle_{\{hkl\}}^{\text{SiC\_comp.}} - \langle d\rangle_{\{hkl\}}^{\text{SiC\_powd.}}}{\langle d\rangle_{\{hkl\}}^{\text{SiC\_powd.}}} \qquad (5.2)$$

where $\langle d\rangle_{\{hkl\}}^{\text{Al\_comp.}}$ and $\langle d\rangle_{\{hkl\}}^{\text{SiC\_comp.}}$ interplanar spacings are determined in the composite for Al matrix and in the SiC_p reinforcement, while $\langle d\rangle_{\{hkl\}}^{\text{Al\_alloy}}$ and $\langle d\rangle_{\{hkl\}}^{\text{SiC\_powd.}}$ are measured in the unreinforced Al2142 alloy and in the SiC powder.

For both components of composite, the elastic lattice strains were determined at different temperatures and from these strains the corresponding average phase stresses (hydrostatic stresses σ_H^{Al} and σ_H^{SiC}) in Al matrix and in the SiC_p reinforcement were computed from equations:

$$\sigma_H^{Al} = 3K^{Al}\langle\varepsilon\rangle_{mean}^{Al,elast} \quad \text{and} \quad \sigma_H^{SiC} = 3K^{SiC}\langle\varepsilon\rangle_{mean}^{SiC,elast} \qquad (5.3)$$

where the bulk moduli K^{Al} and K^{SiC} were computed from temperature dependent Young moduli and Poisson ratios taken from [151] and [152], respectively

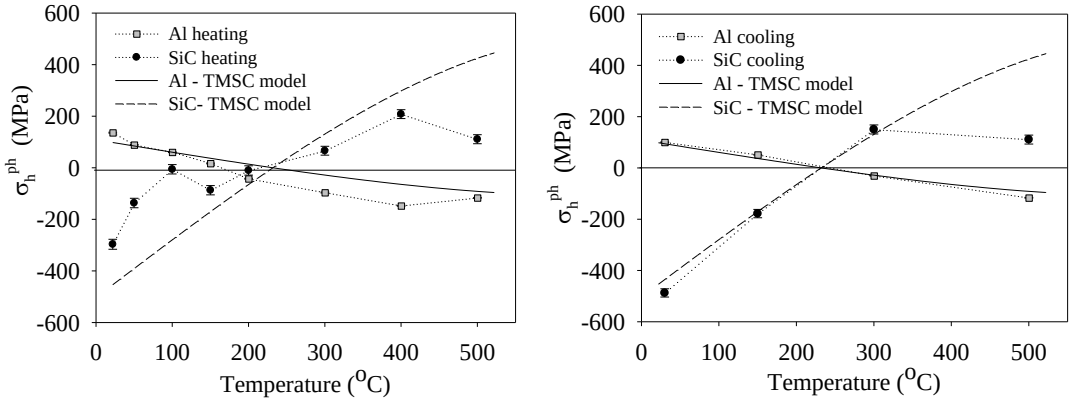

Fig. 5.4 Temperature dependence of mean hydrostatic stresses in Al matrix and SiC_p reinforcement. Comparison of the experimental results with thermo-mechanical self-consistent model (TMSC) [153,154], see also section 5.3 and [66].

The obtained results confirmed generation of the phase stresses during sample heating and cooling. As expected comparing the CTE for composite components (cf. Table 5.3) the compressive hydrostatic stress was created in SiC_p reinforcement and the tensile mean stress was generated in Al matrix, as the effect of relative volume change.

Summarizing the results of the previous measurements the following conclusions concerning studied in this thesis Al/SiC_p composite can be drawn:

- different lattice strains/stresses were observed in Al matrix and SiC_p reinforcement during tensile test,
- transfer of the stress from soft/compliance Al matrix to hard/stiff SiC_p reinforcement leads to the strengthening of Al/SiC_p composite, which is correctly predicted by the EPSC model,
- different values of the CTE factor for Al matrix and SiC_p reinforcement leads to generation of the phase stresses,
- relaxation of thermal origin phase stresses in plastically deformed Al/SiC_p composite is observed.

This is the starting point for the research carried out in this thesis, in which not only the evolutions of lattice strains are measured, but also the stresses for the cooled composite subjected to the compression test are determined. The evolution of theses stresses are compared with developed self-consistent model allowing possible explanation of the observed stress evolutions.

5.2. Characterisation of the material

Material used in this work was produced by powder metallurgy method called BP process (applied by Materion company, former name BP Metal Composites) in which the Al2124 (the composition is given in Table 5.1) and SiC powders are blended and compacted into an aluminium can. The volume fraction of SiC particles in the studied composite is 17,8%. The mixture is then subjected to vacuum degassing at 500°C. Finally the powder is pressed isostatically under a pressure of 100 MPa and a temperature of 500°C [155]. The so obtained material has undergone the T6 thermal treatment which consists of solution treatment at 491°C for 6h, water quenching and artificial aging for 4 hour at 191°C. This process is usually used to improve the mechanical strength of the material due to precipitation hardening of the Al2124 matrix. The fast cooling after solution heat treatment (at 491°C) leads to supersaturated by alloying elements solid state solution, from which the dispersed particles (Cu-Al-Mg) precipitate during aging treatment (at 191°C) [65,66,156].

The microstructure of the Al/SiC_p obtained using scanning electron microscope (SEM) is shown in Fig. 5.5. In this figure the particles of SiC separated from the Al2124 matrix during surface preparation are seen. The mean size of the SiC particles is equal to 0,7 μm

Table 5.1 The composition of Al2124 alloy (wt. %)

Cu	Mg	Mn	Fe	Zn	Si	Ti	Cr	Al
4,18	1,46	0,52	0,3	0,25	0,2	0,15	0,1	balance

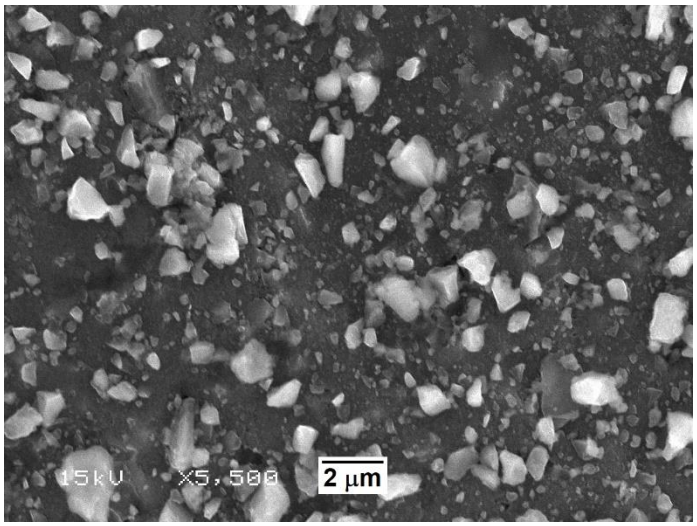

Fig. 5.5 The SEM image obtained for the Al/SiC_p composite, showing the SiC particles after removing of the Al2124 alloy.

The analysis of the crystal structure showed, that the hexagonal polytype 6H is 80% by volume of the powder used in the production of the composite [149]. The Al2124 alloy has a FCC crystallographic structure. In Fig. 5.6 the TOF diffraction patterns obtained separately for the SiC powder and Al2124 alloy (subjected to T6 treatment), as well for the composite at room temperature and at temperature of 300 ºC are presented. The most pronounced diffraction peaks potentially useful in the stress analysis are indexed (some of them however must be eliminated due to overlapping, i.e. SiC 109 and Al 220). It is worth noting that most of the SiC-peaks are composed from two undistinguishable reflections hkl having nearly the same positions, therefore they are treated as single peaks in the stress analysis. Moreover the positions of the peaks corresponding to 6H polytype are very close to those of 3C polytype, cf. Table 5.2. It means that different polytypes of SiC contribute into the analysed peaks but certainly the influence is of 6H polytype is dominating due to its volume fraction of about 80%.

Table 5.2 Chosen reflections of Al2124 alloy ($a = 4{,}0550$Å), SiC 3C polytype ($a = 4{,}3581$Å) and 6H polytype ($a = 3{,}081$Å and $c = 15{,}1248$ Å). The reflections used in stress analysis are underlined [149].

Al2124		SiC			
		Cubic 3C polytype		Hexagonal 6H polytype	
hkl	d [Å]	*hkl*	d [Å]	*hkl*	d [Å]
111	2,3412	111	2,5162	006	2,5208
				102	2,5162
200	2,0275	200	2,1790	104	2,1801
220	1,4337	220	1,5408	108	1,5426
				110	1,5405
311	1,2226	311	1,3140	116	1,3145
222	1,1706			202	1,3138

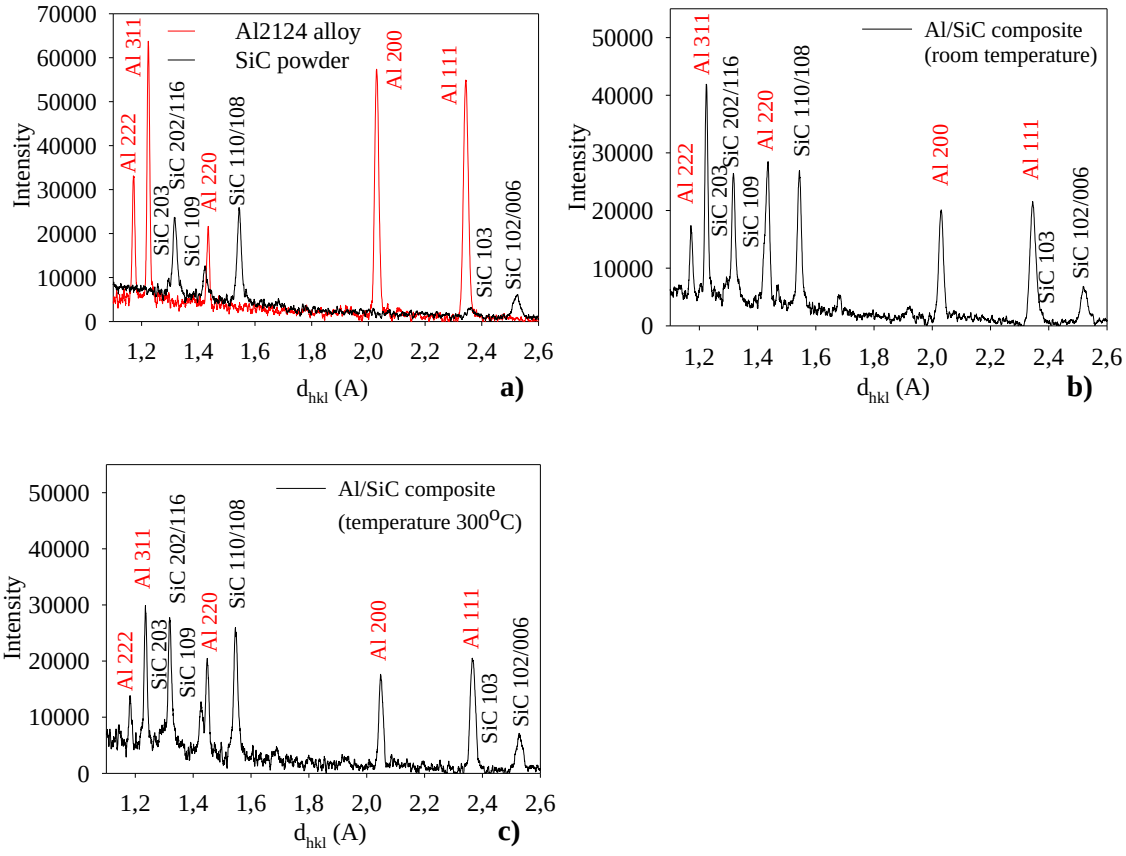

Fig. 5.6 The TOF diffraction patterns of: (a) Al2124 – alloy after T6 treatment (red line) and SiC powder (black line), (b) Al/SiC_p composite at room temperature and (c) the same composite at temperature of 300 ºC. The measurements were done using the FSD diffractometer.

As shown in Fig. 5.6b and Fig. 5.6c the peaks corresponding to SiC 109 and Al 220 reflections overlaps at room temperatures, while they are separated at 300 ºC, i.e. these peaks must be excluded from analysis. The reflections used to determine stresses in both constituents of Al/SiC_p composite are underlined in Table 5.2.

The elastic and thermal properties of both constituents of Al/SiC_p composite are given in Table 5.1 The single crystal elastic constants (SECs) of 6H-SiC polytype are presented. It should be emphasised that the SECs of 6H-SiC and 3C-SiC polytypes are similar. It was also checked that the stress determination as well as modelling of elastoplastic deformation performed with assumption of 6H-SiC or 3C-SiC polytype (with corresponding reflections shown in Table 5.2 and SECs presented in Table 5.3 give almost the same results [149,150]. This means that further analysis and stress modelling can be performed with the assumption that only polytype 6H-SiC is present in the powder (and in the composite), while the content of other polytypes does not lead to different results.

Table 5.3 Single crystal elastic constants (SEC) and coefficient of thermal expansion (CTE) of 6H-SiC [66,152] and Al2124 alloy [151,157].

Material	Young modulus (GPa)	Single crystal elastic constants at room temperature (GPa)					Mean CTE (K^{-1}) for the range: 22 ºC – 500ºC
		c_{11}	c_{33}	c_{44}	c_{12}	c_{13}	
6H-SiC	460	501	553	163	111	52	$3{,}3\ 10^{-6}$
Al	68	105,8	28,3	28,3	60,4	60,4	$27{,}5\ 10^{-6}$

To characterise crystallographic texture of the studied material the pole figures were independently measured for Al2124 matrix and SiC_p reinforcement using Cu radiation on X-Pert Panalytical X-ray diffractometer. As shown Fig. 5.7 the Al2124 matrix exhibits weak texture and almost random texture is observed for SiC_p reinforcement.

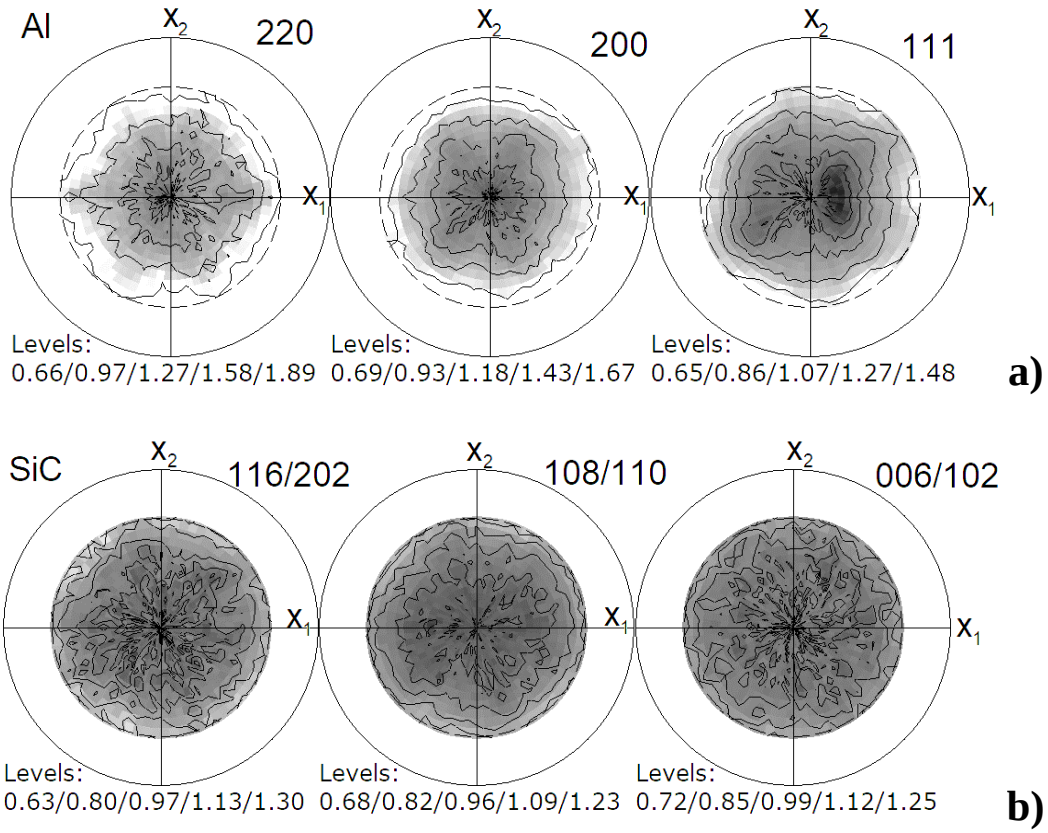

Fig. 5.7 Pole figures measured individually for the Al2124 matrix and SiC_p reinforcement [149].

Finally, it should be emphasised that the model calculations (EPSC model) already compared with tensile mechanical tests and diffraction measurements performed during tensile tests [65,66,149] allowed to determine the parameters of Voce law (equation (3.13)) for the Al2124 - alloy subjected to the T6 thermal treatment. The critical resolved shear stress (τ_0) and linear hardening parameter ($H = \theta_0 = \theta_1$) for the slip system $\langle 1\bar{1}0\rangle\{111\}$ are the same for the Al2124 alloy without reinforcement and for the composite matrix build of the same alloy, cf. Table 5.4.

Table 5.4 Critical resolved shear stress τ_0 (CRSS) and H (hardening parameter) for the $\langle 1\bar{1}0\rangle\{111\}$ slip systems in Al2124 alloy [149].

Material	τ_0 - CRSS (MPa)	$H = \theta_0 = \theta_1$ (MPa)
Al2124 – alloy (T6)	120	50
Al/SiC_p – composite (T6)	120	50

5.3. Development of self-consistent model

In this section the formulation of the self-consistent model enabling prediction both thermal and elasto-plastic deformations is presented and developed. The idea of the model is based on the work of Corvasce et al. [153,154].

If, during elastoplastic deformation, temperature changes the increment of total deformation $\Delta\varepsilon_{ij}^{g}$ for a grain g can be described by equation:

$$\Delta\varepsilon_{ij}^{g} = \Delta\varepsilon_{ij}^{g(el)} + \Delta\varepsilon_{kl}^{g(pl)} + \Delta\varepsilon_{ij}^{g(th)} \tag{5.4}$$

where $\Delta\varepsilon_{ij}^{g(el)}$, $\Delta\varepsilon_{kl}^{g(pl)}$ and $\Delta\varepsilon_{ij}^{g(th)}$ are the increments of elastic, plastic and thermal deformations, respectively.

Taking into account the thermal dilatation does not change the grain stress (for free grain which is not embedded into the matrix), the constitutive equation for a grain can be written (cf. equation (3.26)) :

$$\Delta\sigma_{ij}^{g} = l_{ijkl}^{g}(\Delta\varepsilon_{kl}^{g} - \Delta\varepsilon_{kl}^{g(th)}) = l_{ijkl}^{g}\Delta\varepsilon_{kl}^{g} - m_{ij}^{g}\,\Delta\theta \tag{5.5}$$

where $m_{ij}^{g} = l_{ijkl}^{g}\,\alpha_{kl}^{g}$, α_{kl}^{g} is the CTE tensor, $\Delta\theta$ is temperature increment and tangent modulus l_{ijkl}^{g} is defined in equation (3.25).

The increment of a grain deformation $\Delta\varepsilon_{ij}^{g}$ can be related to the increment of the macroscopic sample strain $\Delta\mathrm{E}_{kl}$ and temperature change $\Delta\theta$ (cf. equation (3.26)

$$\Delta\varepsilon_{ij}^{g} = A_{ijkl}^{g}\Delta\mathrm{E}_{kl} + a_{ij}^{g}\Delta\theta \tag{5.6}$$

where $a_{ij}^{g} = -A_{ijkl}^{g}T_{klnm}^{gg}\left(m_{mn}^{g} - M_{mn}\right)$ and $M_{ij} = \sum_{g} f^{g}(l_{ijkl}^{g}a_{kl}^{g} - m_{ij}^{g})$, while A_{ijkl}^{g} is defined by equation (3.35) using interaction tensor T_{klnm}^{gg}.

Equation (5.6) can be rewritten in more useful form which can be used to perform interaction of macrostress $\Delta\Sigma_{mn}$ (e.g. during mechanical loading) and temperature $\Delta\theta$:

$$\Delta\varepsilon_{ij}^{g} = A_{ijkl}^{g}L_{klmn}^{-1}\Delta\Sigma_{mn} + a_{ij}^{g}\Delta\theta \tag{5.7}$$

where macroscopic tangent modulus L_{ijkl} can be computed using equation (3.38).

The above equations are the basis of various thermo-mechanical or mechanical models. In this work three model versions given by equation (5.8) are used. The first one is the EPSC model (given by equations (5.8) and detailly described in subsection 3.3.3) in which

the temperature does not change, i.e. $\Delta\theta = 0$. The second one, i.e. thermo-mechanical self-consistent (TMSC defined by equations (5.8) and described by Corvasce et al. [153,154]) model is used to determine the phase stresses in the composite generated during temperature change due to difference in CTE between matrix and reinforcement. In this case elastic deformation was assumed for both components, i.e. $l^g_{ijkl} = c^g_{ijkl}$ and $L_{ijkl} = C_{ijkl}$. The TSCM model was successfully used in the works summarised in the previous section (cf. Fig. 5.4).

$$\begin{cases} \Delta\sigma^g_{ij} = l^g_{ijkl}\Delta\varepsilon^g_{kl} \\ \Delta\Sigma_{ij} = L_{ijkl}\Delta\mathrm{E}_{kl} \\ \Delta\varepsilon^g_{ij} = A^g_{ijkl}\Delta\mathrm{E}_{kl} \end{cases} \quad \begin{cases} \Delta\sigma^g_{ij} = c^g_{ijkl}\Delta\varepsilon^g_{kl} - m^g_{ij}\Delta\theta \\ \Delta\Sigma_{ij} = C_{ijkl}\Delta\mathrm{E}_{kl} - M_{ij}\Delta\theta \\ \Delta\varepsilon^g_{ij} = A^g_{ijkl}\Delta\mathrm{E}_{kl} + a^g_{ij}\Delta\theta \end{cases} \quad \begin{cases} \Delta\sigma^g_{ij} = l^g_{ijkl}\Delta\varepsilon^g_{kl} - \Delta m^g_{ij}\theta \\ \Delta\Sigma_{ij} = L_{ijkl}\Delta\mathrm{E}_{kl} - \Delta M_{ij}\theta \\ \Delta\varepsilon^g_{ij} = A^g_{ijkl}\Delta\mathrm{E}_{kl} + \Delta a^g_{ij}\theta \end{cases} \tag{5.8}$$

a) EPSC b) TMSC c) DTMSC

Finally, the third model version is proposed in this work in order to predict the variation in the residual phase stresses due to change in grains and matrix properties from the elastic to elastoplastic behaviour (i.e. $c^g_{ijkl} \rightarrow l^g_{ijkl}$ and $C_{ijkl} \rightarrow L_{ijkl}$). This change is additionally added to constitutive equations, as written in the formulas (5.8). The so defined developed thermo-mechanical self-consistent (DTMSC) model assumes elastoplastic properties of the composite in which the evolution of strains and stresses imposed by total temperature change of θ is considered.

In this work the self-consistent calculations were done using three versions of the model and in all cases the same input file consisting of 2000 spherical grains was used. The grains are divided between two phases, i.e. 356 (volume fraction of 17,8 %) of them are assigned to SiC particles and 1644 (volume fraction of 82,2 %) represent Al matrix. The elastic properties of the grains were defined using appropriate single crystal elastic constants given in Table 5.3 for both constituents of the composite. Due to insignificant crystallographic texture in both components (cf. Fig. 5.7) random lattice orientations were generated for all grains. It should be emphasized that during the deformation only the Al2124 matrix undergoes plastic deformation, while for SiC particles exclusively elastic deformation occurs. Therefore the potentially active $< 1\bar{1}0 > \{111\}$ slip systems were assumed in the aluminium alloy crystallites (FCC crystal structure).

5.4. Lattice strains measurements during *in situ* compression test

Previous investigation performed on the Al/SiC_p composite by author of this dissertation (in the frame of his MSc thesis) showed that important interphase stresses are generated between Al2124 matrix and SiC_p reinforcement during sample colling from temperature 500 ºC to room temperature [66]. As reported in neutron diffraction studies effect of relaxation of this stresses was observed in the samples for which the lattice strains were measured before and after plastic deformation [4,5,65]. However, a systematic study of the evolution of the stress tensor in both composite components during sample deformation has not yet been performed. This is the aim of this work in which the advantages of the EPSILON-MSD diffractometer were used to follow the evolution of stress tensor components in the Al2124 matrix and SiC_p reinforcement during compression test. Then the types and origins of this stresses as well as the reasons of their evolution are discusses on the basis of the thermomechanical models [66].

As mentioned above, the relative lattice spacings were determined during compression test by applying given loads to the cylindrical sample with diameter of 13,5 mm and length of 27 mm. Fig. 5.8 shows the values of macroscopic stress and strain for which the interplanar spacings were measured. It is worth noting that the diffraction measurements were performed at constant sample strains after stabilisation of the macrostress, which in the case of plastic deformation decreases in some extend during a few minutes up to about half hour after each step of sample loading (the relaxation time depends on the material and total sample strain).

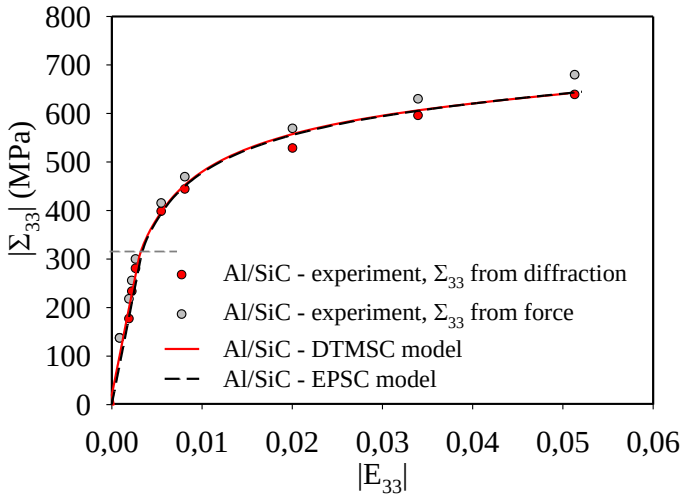

Fig. 5.8 Dependence of the macroscopic compressive stress (calculated from the load applied to the sample – grey symbols) versus macroscopic strain for the sample states for which the lattice strains were determined compared with the predictions obtained using EPSC and DTMSC model (the overlapping black and red lines). The macroscopic stress calculated from diffraction experiment is also shown (red symbols).

For each step of sample strain corresponding to chosen applied load, the interplanar spacings were measured using the TOF technique for different orientations of the scattering vector with respect to the sample. It was done thanks to the advantages of the EPSILON-MDS diffractometer equipped with nine detector systems collecting neutron beam diffracted in different directions (cf. section 4.5). At each orientation of the scattering vector marked by L1-L9 in Fig. 5.9 the TOF diffraction pattern shown in Fig. 5.10 was measured and the selected intense diffraction peaks were used to determine the relative lattice strains calculated according to formulas:

$$\langle\varepsilon\rangle_{\{hkl\}}^{Al} = \frac{\langle d\rangle_{\{hkl\}}^{\mathrm{Al},\Sigma} - \langle d\rangle_{\{hkl\}}^{\mathrm{Al},\Sigma=0}}{\langle d\rangle_{\{hkl\}}^{\mathrm{Al},\Sigma=0}} \quad \text{and} \quad \langle\varepsilon\rangle_{\{hkl\}}^{SiC} = \frac{\langle d\rangle_{\{hkl\}}^{\mathrm{SiC},\Sigma} - \langle d\rangle_{\{hkl\}}^{\mathrm{SiC},\Sigma}}{\langle d\rangle_{\{hkl\}}^{\mathrm{SiC},\Sigma=0}} \qquad (5.9)$$

where $\langle d\rangle_{\{hkl\}}^{\mathrm{Al},\Sigma}$ and $\langle d\rangle_{\{hkl\}}^{\mathrm{SiC},\Sigma}$ spacings are determined in the composite for Al matrix and in the SiC_p reinforcement under the load causing macroscopic stress Σ, while $\langle d\rangle_{\{hkl\}}^{\mathrm{Al},\Sigma=0}$ and $\langle d\rangle_{\{hkl\}}^{\mathrm{SiC},\Sigma=0}$ are measured in both constituents but for the initial sample without external load.

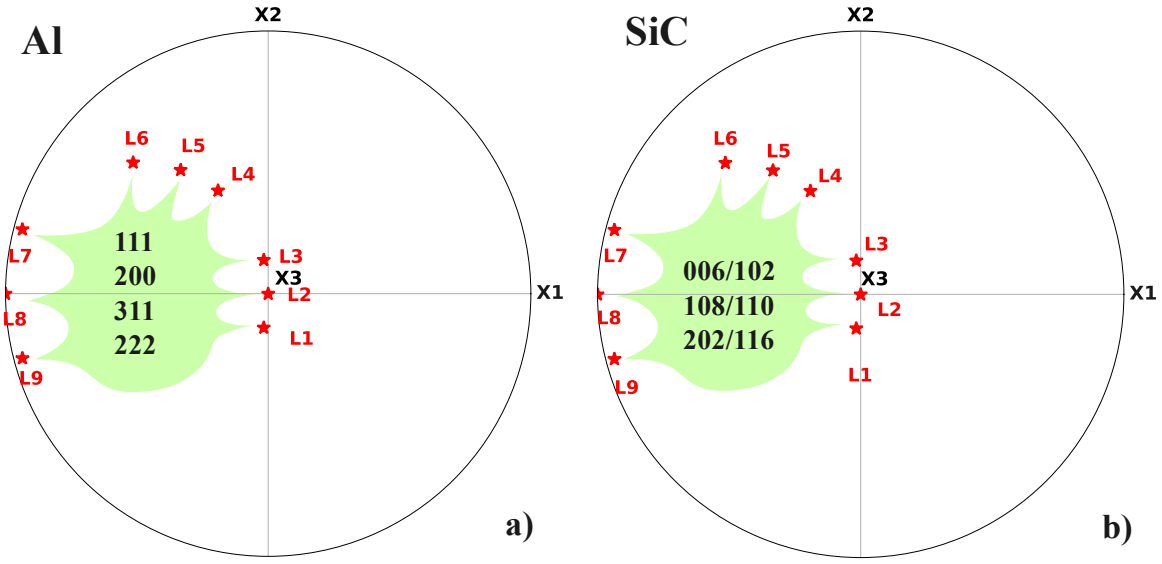

Fig. 5.9 Orientations of the scattering vector with respect to the sample coordinate system marked in pole figures and hkl reflections of Al matrix and SiC_p reinforcement chosen for stress analysis. The load is applied along x_3 axis.

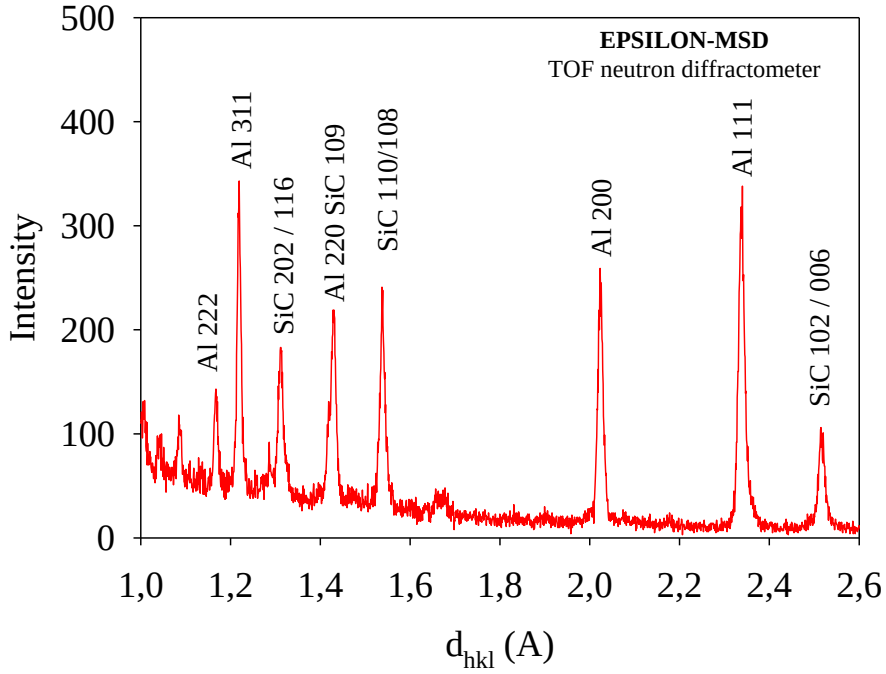

Fig. 5.10 TOF-diffraction pattern measured in both constituents of the Al/SiC_p composite. The indices of the reflections used in analysis are given.

The hkl reflections selected for stress analysis are marked in Fig. 5.10 and Fig. 5.9. The load was applied along the x_3 axis and a wide incident beam (width of 10 mm) was used in order for an acceptable counting statistic. Each data acquisition for a given load took about 22 h. The diffraction peaks were fitted using pseudo-Voigt function in order to find out their positions. The influence of small peaks observed at the peak tail (e.g. SiC $202/116$) was minimized by simultaneous fitting of superposition of two pseudo-Voigt functions. The peaks being superposition of the reflections from two constituents were excluded from analysis (e.g. Al 220 and SiC 109).

It is worth noting that the sets of lattice strains measured for each load in different directions and separately for Al2124 and SiC enabled determination of principal phase stresses (σ_{ii}^{ph} defined in subsection 2.3.2) for both constituents individually. The relative lattice strains (calculated according (5.9)) are plotted in Fig. 5.11 versus $sin^2\psi$ for three example loads (ψ is defined in Fig. 4.9). In this figure the experimental points measured for available reflections are shown together with lines obtained from stress analysis. The σ_{ii}^{ph} values were adjusted in the least square fitting procedure in order to fit the theoretical lines to the experimental points, simultaneously for all hkl reflection in given composite constituent (Al2124 or SiC). In stress analysis the Eshelby-Kröner model was used to calculate the X-ray stress factors (for details see section 4.3) from single crystal elastic

constants given in Table 5.3, assuming a quasi-isotropic sample with random distribution of grains orientations for both constituents. It is worth noting that a very good fitting of the lines to theoretical points was obtained and the lines are almost linear. This means that the stress state almost exhibits cylindrical (rotational) symmetry about the direction of the applied load (i.e. $\sigma_{11}^{ph} \approx \sigma_{22}^{ph}$) and therefore the strains do not depend significantly on the value of φ angle (defined in Fig. 4.9).

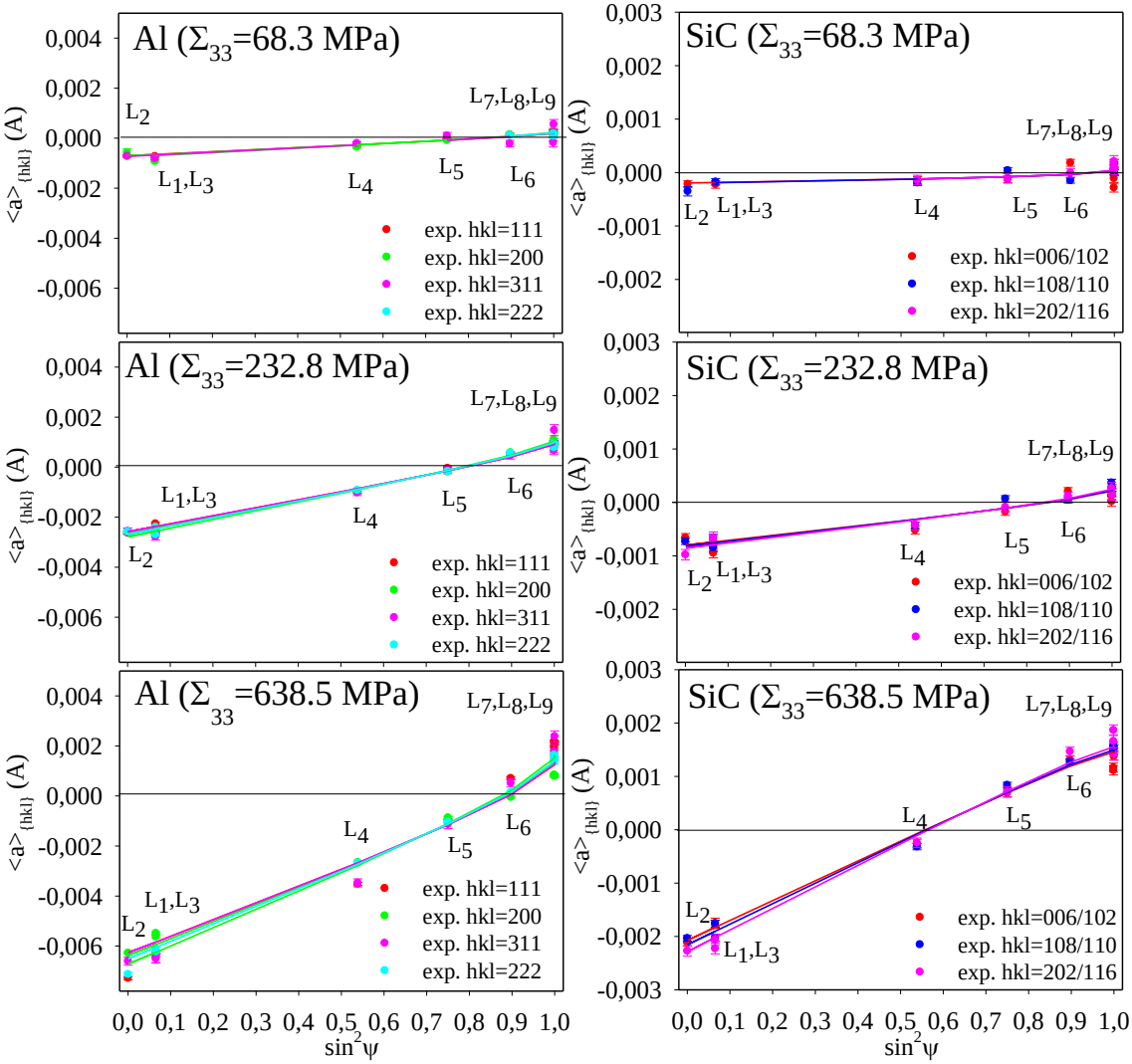

Fig. 5.11 Example $\langle\varepsilon\rangle_{\{hkl\}}^{ph}$ versus relative lattice strains versus $sin^2\psi$ determined in Al2124 and SiC for three applied loads. Note, that the values of the ψ angles for L1-L9 detector systems are given in Table 4.1, while the values of φ angle is not shown and they are different for each presented point.

The values of the σ_{ii}^{ph} were determined from fitting procedure for each applied load and after sample unloading. These results are discussed and compared with self-consistent model in next section.

5.5. Phase stress evolution during compression test

The phase stresses for the sample subjected to T6 treatment were determined from measured lattice strains. The lattice strains were calculated, as the relative difference between interplanar spacings in the constituents of composite and the corresponding interplanar spacings in the separate constituents, subjected to the same thermal treatment (cf. equation (5.3)). It was found that the mean compressive hydrostatic stress $\sigma_{11}^{SiC} \approx \sigma_{22}^{SiC} \approx \sigma_{33}^{SiC} \approx$ -614 ± 115 MPa and balancing tensile mean stress $\sigma_{11}^{Al} \approx \sigma_{22}^{Al} \approx \sigma_{33}^{Al} \approx$ 122 ± 18 MPa were generated during cooling of the composite for the sample after T6 treatment. It should be noted that the rule of mixture written for both phases of the composite should lead to equilibrium of the phase stresses (i.e. the macrostress should be equal to zero for the initial non-loaded sample):

$$f\sigma_{ii}^{SiC} + (1-f)\sigma_{ii}^{Al} \approx 0 \tag{5.10}$$

where $f = 0{,}178$ is the volume fraction of SiC and i=1,2,3).

The values of the stresses obtained from experiment nearly fulfil equation (5.10), i.e. the macrostress calculated from this equation is equal to -9 MPa. In order to ensure equilibrium conditions the thermal origin stresses were slightly modified (within the uncertainty range) and the values $\sigma_{11}^{SiC} = \sigma_{22}^{SiC} = \sigma_{33}^{SiC} =$ -615 MPa and tensile hydrostatic stress $\sigma_{11}^{Al} = \sigma_{22}^{Al} = \sigma_{33}^{Al} =$ 132 MPa were assumed as the initial stress state before compression test. These starting values are denoted as stage 1 in Fig. 5.12 and Fig. 5.15.

The changes in principal stresses in both constituents during compassion test were determined from equation (5.10) and there are shown in Fig. 5.12 versus applied stress $|\Sigma_{33}|$ as the stages 1-2. The macroscopic first order principal stresses σ_{ii}^{I} calculated from the rule of mixture:

$$\sigma_{ii}^{I} = f\sigma_{ii}^{SiC} + (1-f)\sigma_{ii}^{Al} \tag{5.11}$$

are approximately equal to the macrostress state: $\sigma_{33}^{I} \approx \Sigma_{33}$, $\sigma_{22}^{I} \approx \sigma_{33}^{I} \approx 0$, where Σ_{33} is the true stress calculated as the load divided by the current cross section of the sample (compare red and grey symbols in Fig. 5.8). This means that the macrostress determined from diffraction agree with the applied stress Σ_{33}.

Finally the sample was unloaded and the corresponding evolutions of the stresses in both constituents are shown in Fig. 5.12 (see stages 2→3).

Analysing the evolution of experimentally determined phase stresses (σ_{33}^{Al} and σ_{33}^{SiC}) in the direction parallel to the applied load (cf. Fig. 5.12) it can be concluded that these stresses change linearly in both constituents of composite up to $|\Sigma_{33}| \approx$ 310-320 MPa. In

this range of sample loading the stresses perpendicular to the load ($\sigma_{11}^{Al}, \sigma_{22}^{Al}, \sigma_{11}^{SiC}$ and σ_{22}^{SiC}) do not change significantly. Such range of compression test corresponds to elastic sample deformation confirmed by linear dependence of macroscopic stress Σ_{33} versus sample stain E_{33} (cf. Fig. 5.8). Then, over $|\Sigma_{33}| \approx$ 310-320 MPa significantly nonlinear behaviour of phase stresses (σ_{ii}^{Al} and σ_{ii}^{SiC}) occurs during elastoplastic deformation. Finally after sample unloading the phase stresses do not return to the values determined for the initial sample (i.e. the stress stages 1 and 3 are significantly different).

In Fig. 5.12 the experimental data are compared with the results of prediction performed by EPSC model starting from initial stresses (stage 1) assigned to the grains in the input file. In calculations the CRSS and H parameter of linear hardening given Table 5.4 were assumed for the slip system $< 1\bar{1}0 > \{111\}$ in the grains of Al2124 matrix. An excellent agreement between stresses localised in both phases (σ_{ii}^{Al} and σ_{ii}^{SiC}) was obtained for the range of elastic deformation occurring in Al2124-matrix and SiC_p reinforcement, i.e. up to $|\Sigma_{33}| \approx$ 310-320 MPa, however over this threshold a significant departure of the theoretical lines from experimental points is observed. What is more, as shown in Fig. 5.8, a very good agreement between experiment and model prediction was found for the macroscopic stress, and in this case the accordance is observed for full range of deformation.

The above results show that the disagreement between model and experiment is observed for the phase stresses (σ_{ii}^{Al} and σ_{ii}^{SiC}) in the plastic range of deformation (plasticity occurs for Al2124 alloy only). However, the model inconsistency is eliminated when calculating macroscopic stresses using the rule of mixture defined by equation (5.11) due to the self-equilibration of the thermally generated phase stresses. The further analysis should take into account the nature of phase stresses that arise both in the initial and deformed material. Therefore, the von Mises phase stresses ($\sigma_{von\ Mises}^{Al}$ and $\sigma_{von\ Mises}^{SiC}$ shown in Fig. 5.13) and hydrostatic mean phase stresses ($\sigma_{hydrostatic}^{Al}$ and $\sigma_{hydrostatic}^{SiC}$ shown in Fig. 5.14) are determined from the principal phase stresses and compared with model calculation. All these values represent semi-macroscopic behaviour of the considered constituents within composite. In Fig. 5.13 the evolution of the von Mises phase stresses versus the macroscopic stress is presented both for experimental data and model prediction. It is shown that the von Mises phase stresses predicted by the EPSC model perfectly agree with the experimental data for both the Al2124 matrix and the SiC_p reinforcement, i.e. the evolution of phase stresses responsible for elastic and plastic deformation is correctly predicted by the model.

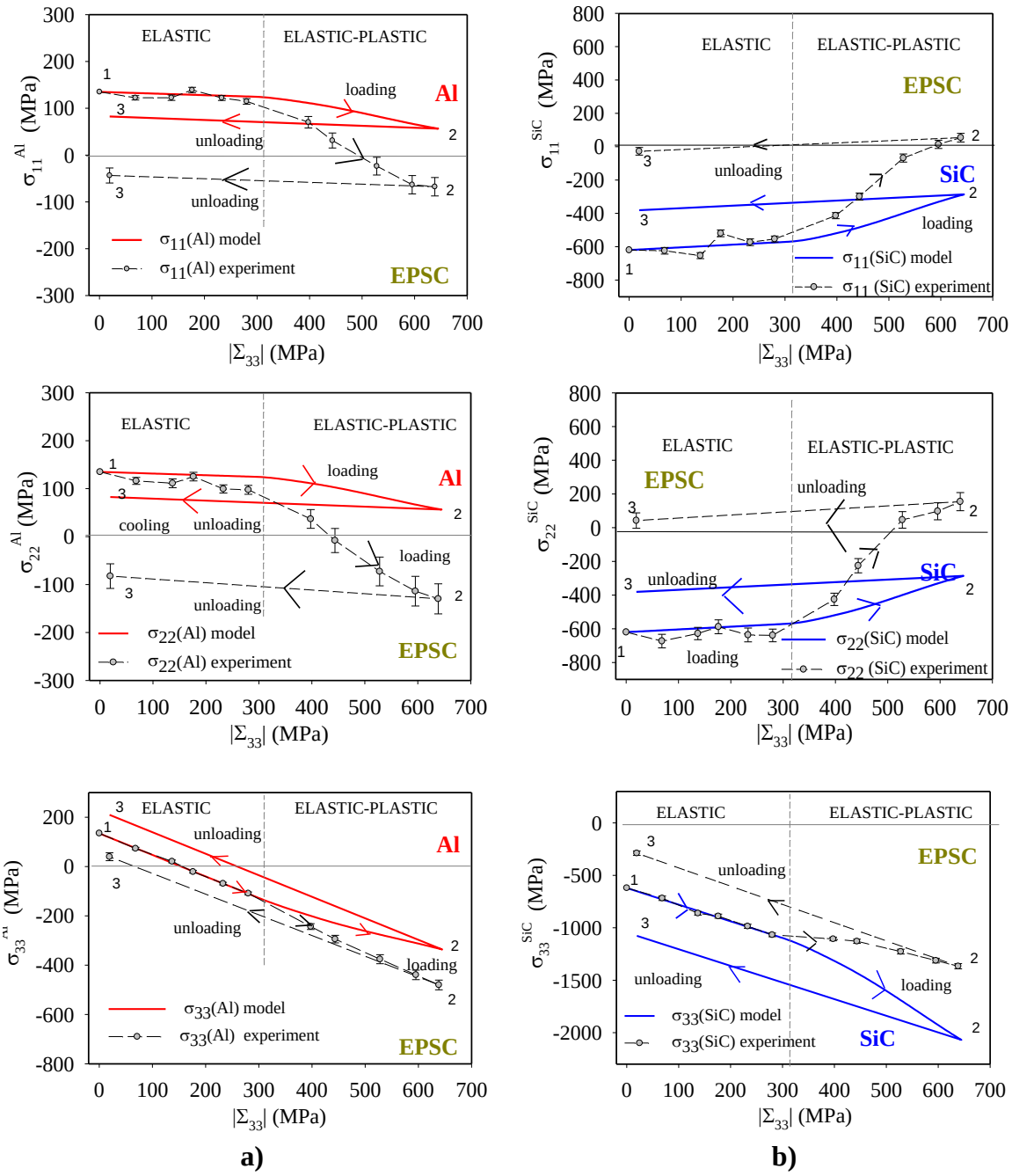

Fig. 5.12 Evolution of phase stresses in Al2124 matrix (a) and SiC_p reinforcement (b) versus compressive stress $|\Sigma_{33}|$ applied along x_3 axis during compression (stages 1-2) and unloading (stages 2-3). Experimental results are compared with EPSC prediction.

It is worth noting that the evolution of the phase von Mises stresses well illustrates partitioning of the load between matrix and reinforcement (cf. Fig. 5.13). During elastic deformation (up to $|\Sigma_{33}| \approx$ 310-320 MPa) larger stress is concentrated at the reinforcement due to much stiffer elastic behaviour of SiC comparing to Al2124 alloy (cf. Young modulus given for both components in Table 5.3). Moreover, this difference increases significantly faster during plastic deformation of Al2124 matrix (over $|\Sigma_{33}| \approx$ 310-320 MPa) and elastic

behaviour of SiC_p reinforcement. Note that over $|\Sigma_{33}| \approx 310$ MPa the plot of σ_{ii}^{Al} versus $|\Sigma_{33}|$ starts to saturate, while the plot of σ_{ii}^{SiC} versus $|\Sigma_{33}|$ grows faster. The transfer of the load from the more compliant and softer Al2124 matrix to stiff SiC_p reinforcement causses well-known composite strengthening effect.

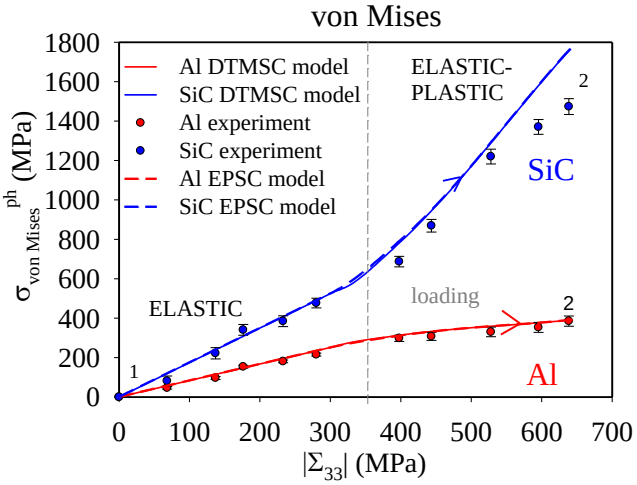

Fig. 5.13 Von Mises stresses in Al2124 matrix and SiC_p reinforcement versus compressive stress $|\Sigma_{33}|$ applied along x_3 axis (stages 1-2). Experimental results are compared with EPSC and DTMSC prediction.

In the next step of analysis the evolution of the mean hydrostatic phase stresses are compared with EPSC model ($\sigma_{hydrostatic}^{Al}$ and $\sigma_{hydrostatic}^{SiC}$ in Fig. 5.14 a). At first stages 0-1 the hydrostatic stresses ($\sigma_{ii}^{SiC} \approx$ -615 MPa and $\sigma_{ii}^{Al} \approx 132$ MPa) generated due to sample cooling are shown (approximately such stresses were measured in the sample after T6 thermal treatment [149]). The prediction of these stresses was done with TMSC model (see equation (5.8 b) for total temperature decrease $\theta = T - T_0 = -283\ K$, where T is the room temperature and T_0 is the temperature in which the phases stresses compensate. Then the evolution of the phase stresses during compression (elastic and elastoplastic deformation, stages 1-2) and elastic unloading (stages 2-3) are compared with EPSC model. A significant disagreement between theoretical and experimental results is observed. In model calculations the mean hydrostatic stresses in both constituents change linearly versus applied stress $|\Sigma_{33}|$ during compression test and unloading. After loading and unloading mean hydrostatic stresses returned to the initial values for both constituents of the composite, i.e. plastic deformation did not change the mean hydrostatic stress in the SiC particles and Al2124 alloy matrix. On the contrary, in the case of experiment data the nonlinear evolution of the phases stresses occurred during plastic deformation, and after sample unloading almost complete relaxation of the mean hydrostatic phase stresses was observed. It can be concluded that the EPSC model starting from the hydrostatic state of

stresses assumed for spherical inclusions in both components of the composite cannot predict the effect of thermal stresses relaxation.

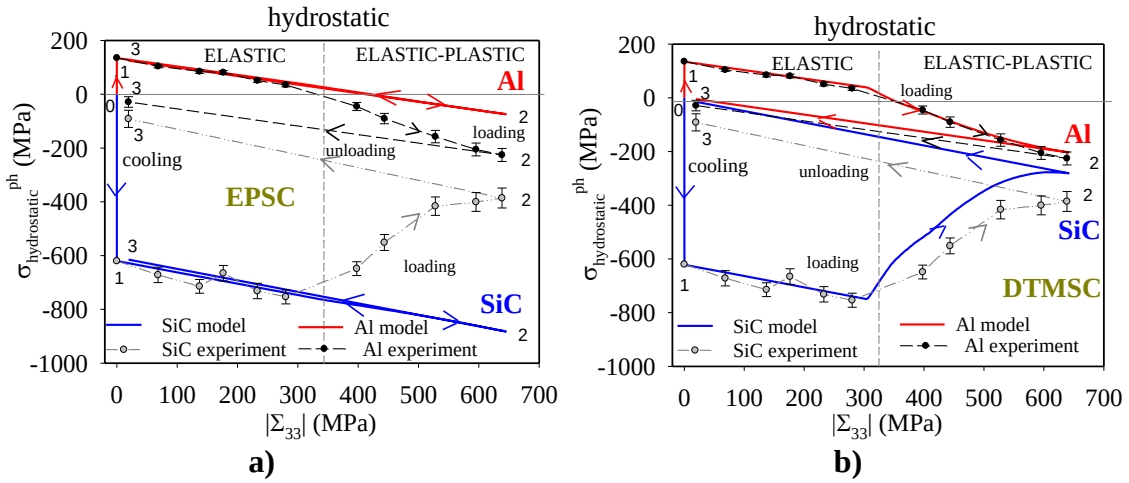

Fig. 5.14 Comparison of the EPSC (a) and DTMSC (b) models with measured mean hydrostatic stresses in Al2124 matrix and SiC_p reinforcement. Stages 0-1 show stresses generation during cooling, stages 1-2 correspond to compression test and stages 2-3 represent unloading.

It should be however emphasized that the mean hydrostatic stress in the Al2124 matrix determined from diffraction and used as the input for TMSC or EPSC model does not correspond to the real stress state that occurs in the composite. The stresses measured by diffraction and calculated by the self-consistent models are the average values for many grains in given phase and their spatial variation within the matrix is not taken into account. In real composite the stress in the Al2124 matrix is strongly heterogeneous especially around reinforcement particles [51]. To overcame the above problem the modified DTMSC model was developed and applied in this work. In this model the initial hydrostatic stresses produced during cooling are assigned to all grains in the Al2124 matrix, but then the correction of these stresses is performed in each interaction step (cf. using the temperature dependent term in equation (5.8 c) with $\theta = -283\ K$). This correction allows to calculate the thermal origin phase stresses generated for current state of the material using Eshelby approach, instead of prediction of initial hydrostatic stresses evolution leading to false result. It the DTMSC model the average thermal origin phase stresses are calculated for the homogenous medium described by current tangent moduli tensors l_{ijkl} and L_{ijkl} .

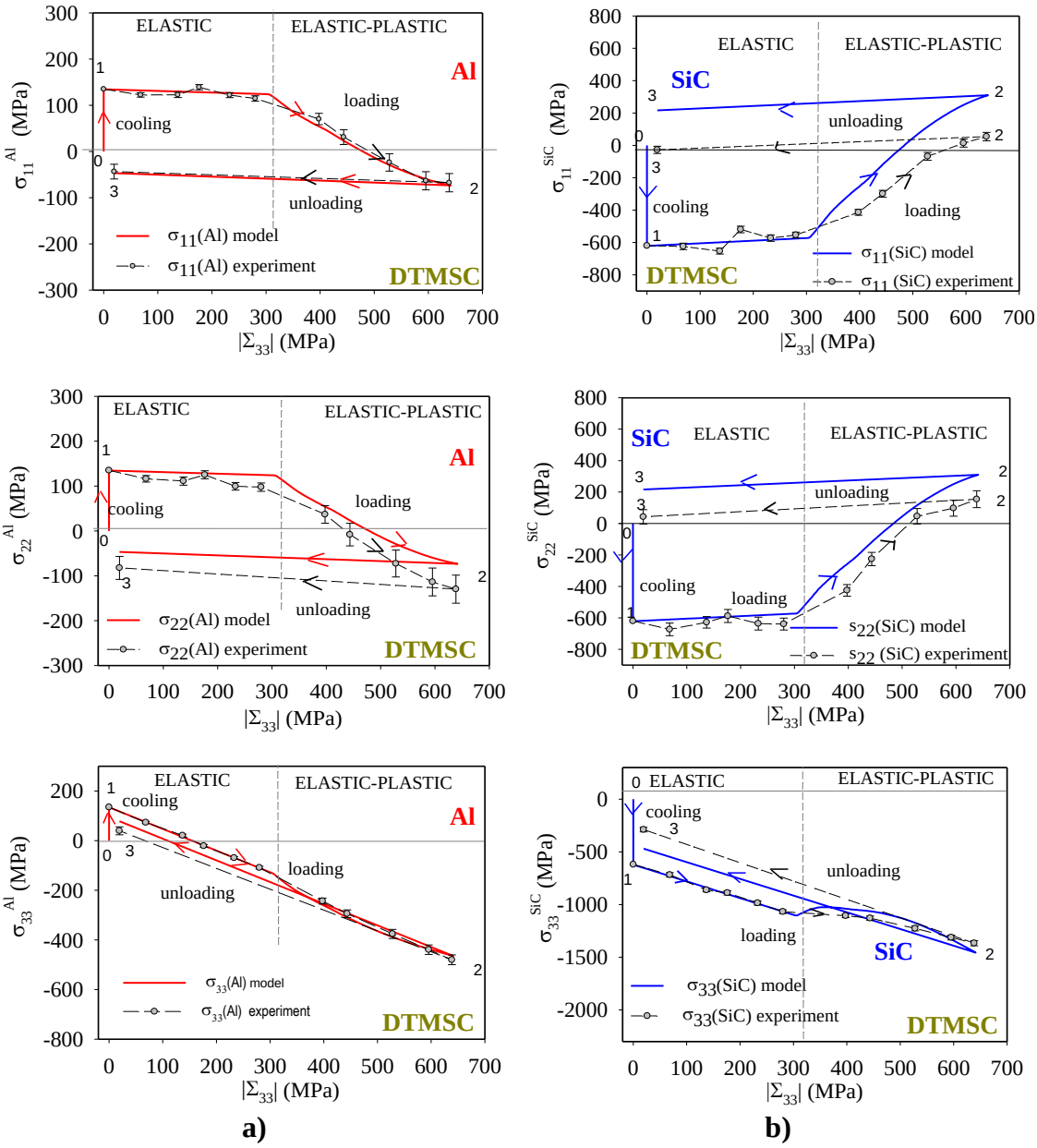

Fig. 5.15 Evolution of phase stresses in Al2124 matrix (a) and SiC_p reinforcement (b) versus compressive stress $|\Sigma_{33}|$ applied along x_3 axis during cooling (stages 0-1), compression (stages 1-2) and unloading (stages 2-3). Experimental results are compared with DTMSC prediction.

In Fig. 5.14b the experimental mean hydrostatic phase stresses were compared with the predictions of the DTMSC model and a very good agreement was found between the experiment and model prediction. The nonlinear evolution of the stresses $\sigma^{Al}_{hydrostatic}$ and $\sigma^{SiC}_{hydrostatic}$ during plastic deformation leading to relaxation of these stresses after unloading is well predicted by the DTMSC model. As shown in Fig. 5.13 and Fig. 5.8, also the von Mises phase stresses $\sigma^{Al}_{von\ Mises}$ and $\sigma^{SiC}_{von\ Mises}$ and the macroscopic stress are correctly predicted by the DTMSC model, in this cases the results of DTMSC

and EPSC models are almost identical. It means that the modification introduced into DTMSC model influence only the thermal origin stresses and the other results are the same as in the case of EPSC model. Finally the principal phase stresses are compared with model calculation (σ_{ii}^{Al} and σ_{ii}^{SiC} in Fig. 5.15). It was found that the DTMSC model, which takes into account the relaxation of the thermal stresses, predicts the evolution of phase stresses during plastic deformation much better compared to the EPSC model. It is worth noting that after unloading the residual phases stresses remain in the sample. However, according to model results these stresses should have mostly deviatoric character. It was found that tensile stress σ_{33}^{Al} and compressive stress σ_{33}^{SiC} are generated in the direction of sample compression, while compressive stresses σ_{11}^{Al}, σ_{22}^{Al} and tensile stresses $\sigma_{11}^{SiC}, \sigma_{22}^{SiC}$ were created in the directions perpendicular to the applied load, cf. stage 3 in Fig. 5.15. As showed in this figure the model result is confirmed by the experimental data obtained for Al2124 matrix and at least qualitatively for the SiC particles. As already discussed, the thermal phase stresses relaxed after plastic deformation and unloading of the sample, cf. stage 3 in Fig. 5.14 b.

The states of the residual phase stresses having different origins are illustrated in Fig. 5.16. In the case of sample colling the change of volume fraction causes generation of mean hydrostatic phase stresses, while in the case of plastic deformation (e.g. in compression mode) the mismatch of the grains shape leads to deviatoric type of phase stresses.

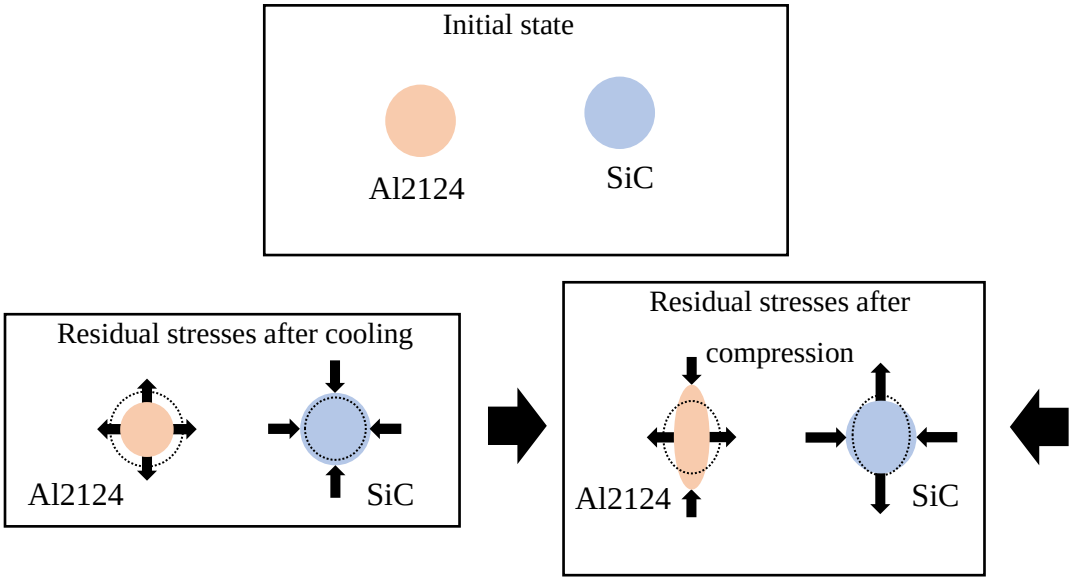

Fig. 5.16 Residual phase stresses generated due to cooling and plastic compression of Al/SiC_p composite.

5.6. Summary

This part of the work concerns determination of phase stress evolution in both constituents of Al/SiC_p composite during thermal treatment and elastoplastic compression test. The experimental study was performed using TOF neutron diffraction method which enables lattice strains measurement independently in different phases. Thanks to the advantages of EPSILON-EDS TOF diffractometer the measurements were done simultaneously in 9 directions and the principal components of stress tensor were determined for different loads applied to the sample. Moreover the EPSC model was developed in order to study different types of the stresses during cooling, compression and unloading.

It was found, that thermal origin phase stresses are generated in Al/SiC_p composite during sample cooling from high temperature due to difference in CTE of Al and SiC. The average values of these stresses show hydrostatic nature in each phase, however significant stress heterogeneities in the Al2124 matrix are expected around particles of SiC. The experimental values of compressive stress in SiC_p and tensile stress in Al2124 matrix are correctly predicted by the TMSC model assuming elastic behaviour of both composite components. The thermal origin phase stresses are self-equilibrated leading to a zero state of macroscopic stresses for an unloaded sample.

During purely elastic deformation of the composite, the stresses evolve linearly in both components and the stiff SiC_p reinforcement is more loaded compared to the more elastically compliant Al2124 matrix. This stress partitioning between phases, leading to strengthening of the composite, is well predicted by the EPSC model. However, when the plastic deformation begins in the Al2124 matrix, the EPSC prediction of phase stresses is incorrect if the hydrostatic stresses are assigned to all grains belonging to both phases.

Analysing the experimental data, it was found that during the plastic deformation of the Al2124 matrix, the phase stresses of thermal origin relax and they are replaced by residual stresses resulting from grain shape mismatch. This process was predicted by the DTMSC model in which thermal expansion of the both constituents were performed for the current state of the material subjected to plastic deformation. When this correction was applied to the EPSC model, thermal stresses relaxation was well predicted, leading to a correct simulation of the stress distribution between phases and residual stress after unloading of the sample. It was found that significantly higher von Mises stress is localized in the elastic SiC_p reinforcement, comparing to the plastic Al2124 matrix. This means that the reinforcement partially relieves the matrix, taking greater load and thus causes mechanical strengthening of the composite. It is worth noting that such a load partitioning

leads to a reduction of the von Mises stress at the matrix to the current value of yield stress of the Al2124 alloy (determined by work hardening of the of the Al2124).

Finally, it should be emphasized that the thermal stress relaxation process may be more complex than that predicted by the DTMSC model. This is due to possible discontinuities in the material resulting from the damage process taking place at the interface between the Al2124 matrix and the SiC particles. This may be an additional cause of phase stress relaxation, which is not included in the self-consistent models used in this work. Despite difficulties in full interpretation of the mechanisms of thermal stresses relaxation, an important achievement of this work is the experimental determination of mean phase stress tensors in both composite components during thermal treatment and mechanical loading. This allowed to describe and discuss the evolution of phase stresses having different nature and origin.

6. Diffraction study of grain stresses and activation of twin and slip systems in AZ31 magnesium alloy

6.1. State of art – introduction

Magnesium exhibits strongly anisotropic plastic properties, which are governed by slip and twinning modes with very different critical activation stresses. The slip systems, on which deformation is controlled by movement of dislocations, are the given in Table 3.1 and shown in Fig. 3.5. Their activation can be observed under different loading conditions [158]. Twinning can be also activated in magnesium. The twin systems are classified into two groups, depending on imposing of tensile or compressive strain along <c> axis (see Table 3.2, Fig. 3.11).

In numerous works concerning magnesium alloys, the CRSS for basic deformation modes were determined by fitting experimental data of mechanical tests (tension, compression) and/or lattice strains measured *in situ* using diffraction to theoretical deformation models (e.g., [13–15,17–19,22,23,158–164]). However, the estimated values of CRSS are often scattered in wide ranges. After elimination of extreme results these values are as follows: for basal slip systems 2-50 MPa, for prismatic systems 45-120 MPa, for pyramidal systems 40-160 MPa and for tension twins 15- 50 MPa (Suppl. Material in [23]). The value of 200 MPa for compression twins can be added to this revue [26]. Generally, it can be emphasised that CRSS of the deformation modes of magnesium alloys can be ordered from low to high values, as follows: basal slip, tensile twinning, prismatic slip, pyramidal slip, and compression twinning.

Accordingly, two easy deformation modes are basal slip and tensile twinning. However, the basal slip is predominant only for advantageous crystal orientations, when loading force is deviated from crystal <c> axis. It was also observed that the basal slip systems, having the lowest CRSS, show a non-negligible latent hardening. Therefore, also

other slip or twin systems must be activated to allow plastic deformation of the sample to occur. It was found that also the so called slip-induced twinning appears, which is mainly governed by the geometrical compatibility parameter [165]; this mechanism activates the tension twins. Another interesting result is presented in [163], where the visco-plastic model was developed. Different factors can influence the deformation pattern in magnesium and magnesium alloys. Besides temperature, it is also ageing [166]. It was found that in the initial range of deformation the aging promotes twinning over slip but the presence of precipitates leads to thinner twins. Upon unloading a further forward twinning as well as de-twinning are observed.

It should be noted that much of the data, discussed above, was obtained using deformation models (mostly visco-plastic model, based on Eshelby type interaction) to estimate CRSS values from different mechanical tests. However, in a real sample the interactions between grains can have more complex character, and they can be described by a spectrum of models between Sachs, Hill and Taylor/Lin [24]. Another problem concerns important number of parameters used in the models, which must be fitted with experimental data. Some progress in this aspect was proposed in [26], where a model with strongly reduced number of parameters was used.

Generally, the determined CRSS values basing on model assumptions are in rather wide ranges, as summarized in [23]. The results obtained from deformation models are not always. Moreover, only the initial values of CRSS are determined and its further variation is based on phenomenological laws (in most cases Voce law). In this aspect new arising methods of direct determination of CRSS from experimental data, are noteworthy. In order to directly determine CRSS from experiments, various techniques are used to measure the stresses in individual grains or groups of grains [22,42–44,46] and in individual phases of polycrystalline materials [107,130,167]. In [22] the resolved shear stresses (RSS) in titanium were directly determined using high energy X-ray diffraction microscopy. However, the study was done for individual grains and a some spread appeared in the obtained CRSS values. The first direct determination of RSS in AZ31 magnesium alloy for different slip systems was performed in [40]; *in situ* measurements for four selected crystal orientations were done. This kind of experiments seem to be very promising.

Another approach to the study of deformation mechanisms in magnesium was proposed using simulations based on molecular dynamics (MD) method [168,169]. The calculations developed using MD are directly comparable to experimental results on very small samples. Obviously, most of deformation experiments on magnesium are mechanical tests on macroscopic samples. It should be noted that a series of interesting observations were done performing compression tests on micro- and nanopillar magnesium samples [170–172]. In the case of compression along <c> axis of micropillar samples pyramidal slip was observed and next due to a misalignment of loading force a massive basal slip was

observed. Another behaviour was observed in nanopillar samples: a compression twinning was observed, followed by basal slip inside a formed twin. On the other hand, when tension strain was imposed along <c> axis - tensile twinning was activated [171]. Next, when crystal <c> axis was strongly tilted from the loading direction the basal slip was predominant. And finally, tension twinning was dominating when compressive stress was applied perpendicularly to the <c> axis [172]. The calculations done using MD confirm most of the above experimental results.

Another useful technique for testing the micromechanical properties of materials is acoustic emission [173–178]. This phenomenon occurs during sample deformation and may come from various sources that are difficult to distinguish. One of the first and most popular methods based on acoustic emission is the so-called hit-based method, which consists in setting parameters such as the amplitude or duration of the event for the recorded signal. A characteristic feature of the acoustic emission is the difference in the sound wave coming from different sources, which allows the spectral analysis to identify these sources. An example of a technique that uses this dependency is called adaptive sequential k-means (ASK). This method was used to test the magnesium alloy and allowed to demonstrate significant activity of the primary and twin systems during mechanical tests carried out in different directions for a sample with a significant texture [175,176]. It is worth noting that acoustic emission is a method complementary to diffraction studies, especially neutron diffraction. The combination of these methods allows to describe the mechanisms of plastic deformation and to study the dynamics of these processes.

The above discussion shows that activation of deformation modes in magnesium can depend on many factors, therefore the CRSS values estimated by fitting of experimental results with deformation models are not unique. The new method proposed in the present work is based on direct determination of CRSS from diffraction *in situ* experiments, without using deformation models. Such determined CRSS will constitute an important basic data.

Another important goal of this work is to determine experimentally the stresses localized at grains with different orientations in order to explain the huge difference in mechanical stress-strain plots obtained for different loading tests performed for strongly textured sample (cf. Fig. 6.4), shown in Fig. 6.6. Moreover, the measured partitioning of the load between the grains will allow us to verify the intergranular interactions in the elastoplastic self-consistent (EPSC) model. The verified and modified model will be used to determine the work hardening occurring on different slip systems. Finally, the role of twinning process in softening followed by strengthening of the sample subjected to compression test in rolling direction - RD (Fig. 6.6) will be explained.

6.2. Material characterization and experiments

The studied material was the hot rolled magnesium alloy AZ31. The chemical composition of this alloy is presented in Table 6.1. The alloy orientation map and texture, determined by EBSD technique, are presented in Fig. 6.1, where a strong basal texture component is visible. The average grain size of the alloy is 12,2μm with a standard deviation of 7,9μm.

In order to measure the stress components using neutron diffraction, three loading experiments were performed - tensile in rolling direction (later called RDT) [40], compression in normal direction (NDC) and compression in rolling direction (RDC). Example diffractogram of the initial undeformed material and the sample loaded with a stress of $\Sigma_{RD} = 247$ MPa in the rolling direction, obtained on an EPSILON - MSD diffractometer, are shown in Fig. 6.2. The appearance of a twin orientation can be noticed by significant increase in 002 reflection and changes in intensities of other peaks.

Table 6.1 Chemical composition of AZ31 magnesium alloy

Element	Al	Zn	Mn	Cu	Mg
Composition (wt., %)	2,5-3,5	0,7-1,3	0,2-1,0	0,05	94,15-96,55

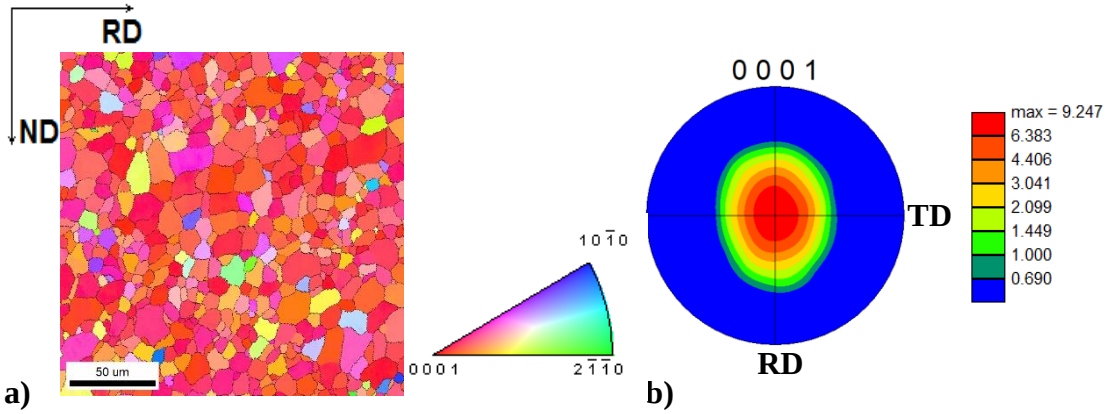

Fig. 6.1 EBSD orientation map (a) and (0001) pole figure for the initial undeformed sample (b).

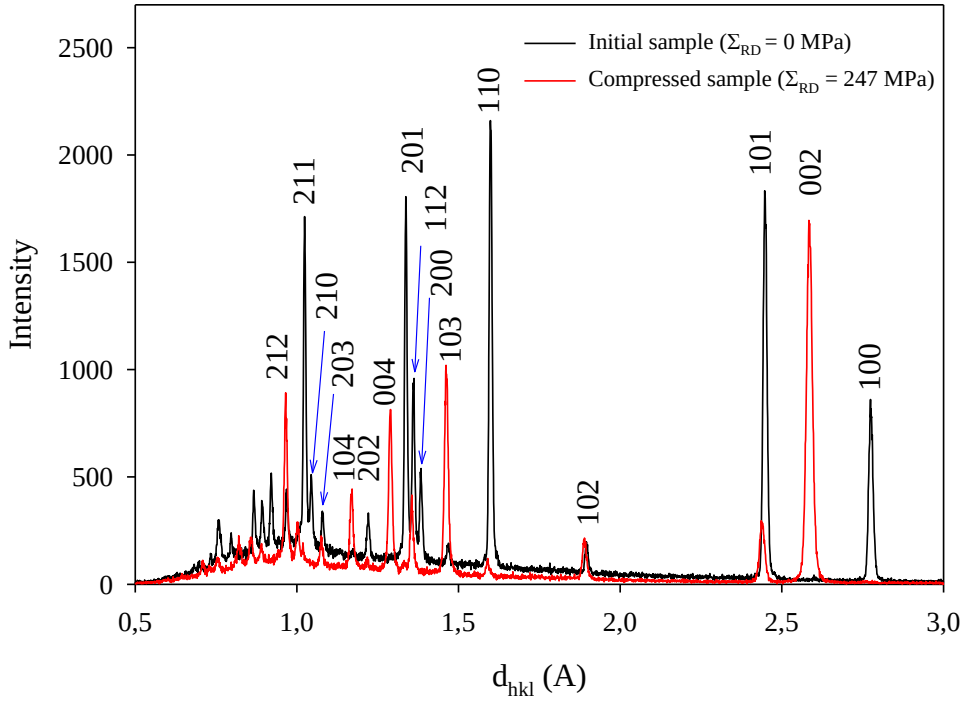

Fig. 6.2 Comparison of the diffractograms from L2 detector for the initial undeformed magnesium AZ31 sample and the sample under compressive load ($\Sigma_{RD} = 247$ MPa) in rolling direction (RD). A change in texture is visible, especially in the 002 reflection, resulting from the appearance of a tensile twin orientation.

The first experiment (RDT) was carried out on a TKSN 400 (HK9) diffractometer at the Nuclear Physics Institute in Řež (Czech Republic) using angle dispersive (AD) method (see section 4.5). To do measurements for the selected orientations: A, B, C and D (see Fig. 6.3 and Fig. 6.4) unique sets of poles were chosen, which are presented in Table A2.1 (Appendix 2). The sample used in this experiment was in the bar shape with a length of 2 cm and a 4 mm square cross-section. The results of this experiment have already been published [40] and in this work the data from this experiment are analysed and compared with next experiments (NDC and RDC).

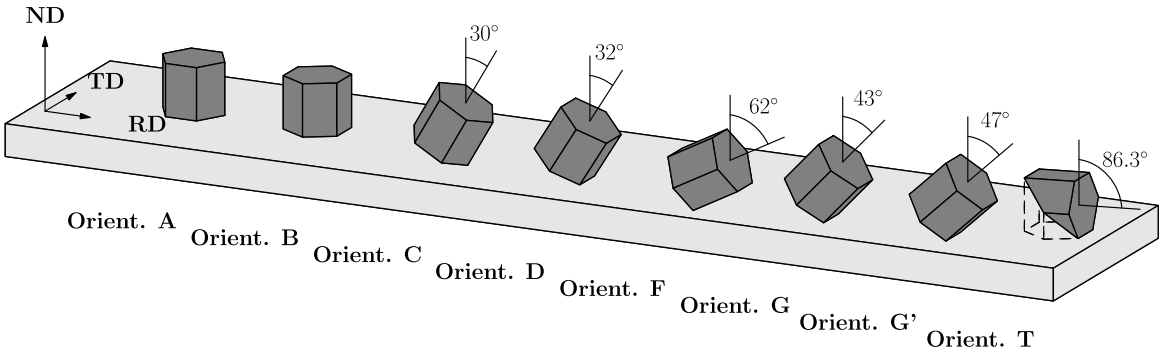

Fig. 6.3 Visualisation of orientations examined during experiments.

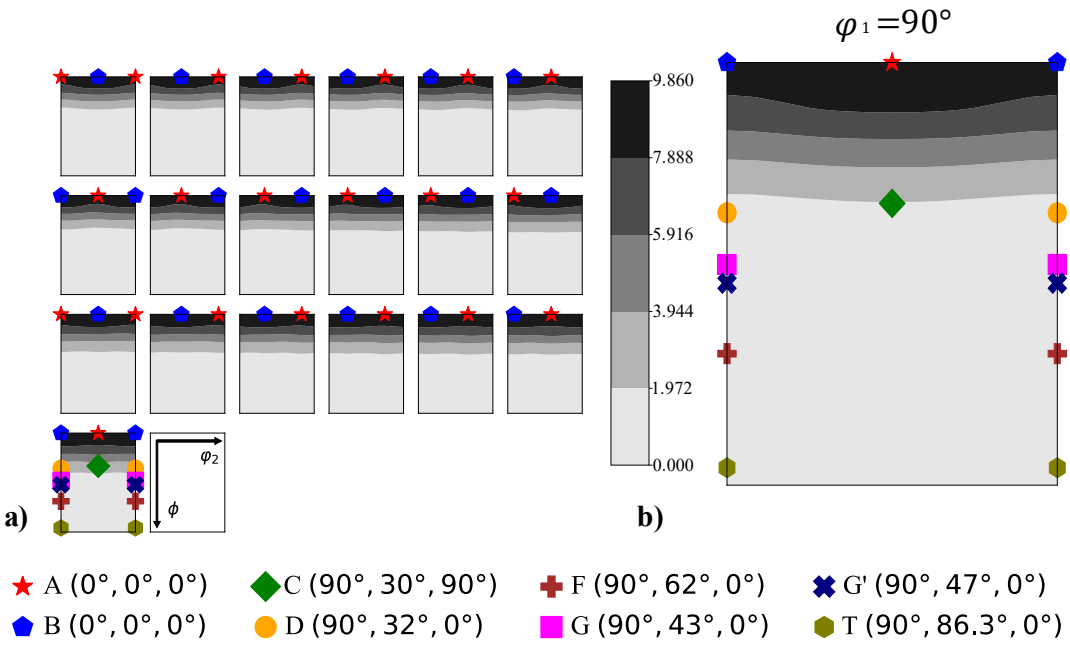

Fig. 6.4 Experimental ODF obtained from EBSD measurements for the initial undeformed sample.

The next two experiments (NDC and RDC) were performed on the EPSILON-MSD diffractometer at the Joint Institute for Nuclear Research (JINR) in Dubna (Russia), using the time-of-flight method (see section 4.5). Samples measured during *in situ* experiments had cylindrical shape and their initial dimensions were 24,04 mm length and 13,9 mm diameter in NDC experiment and 27,4 mm length and 13,9 mm diameter in RDC experiment. Measurements were made with an incoming beam width of 10 mm, and each data acquisition for a given load took about 10 hours. To avoid potential systematic errors the relative lattice strains were determined (cf. equation (6.1)).

The measurement geometry using nine detectors is presented in section 4.5. The compressing stress rig allowed the sample to be rotated by any angle about its axis, which allowed to increase the number of measured orientations. One turn of 90° was done during the RDC experiment and the measurement was performed before and after rotation increasing number of measurement directions. A conjunction of detector's geometry with symmetry of the samples (due to crystallographic texture) enabled measurements for many poles, which allowed to analyse many orientations after the experiment. In the NDC experiment the orientations measured are A, B, D, F and G, while in the RDC experiment - A, B, D, F and G'. These orientations are marked on the orientation distribution function (ODF, see Fig. 6.4) and their visualisation is showed in Fig. 6.3. Poles used for measurements of lattice strains in these experiments are listed in Table A2.1 (Appendix 2). Examples of orientations used in NDC and RDC experiments are also presented in pole figures (see Fig. 6.5), where the positions of scattering vector corresponding to the

detectors and their symmetrical positions are marked, considering the symmetries resulting from crystallographic texture of the sample (the load is in the centre of each pole figure).

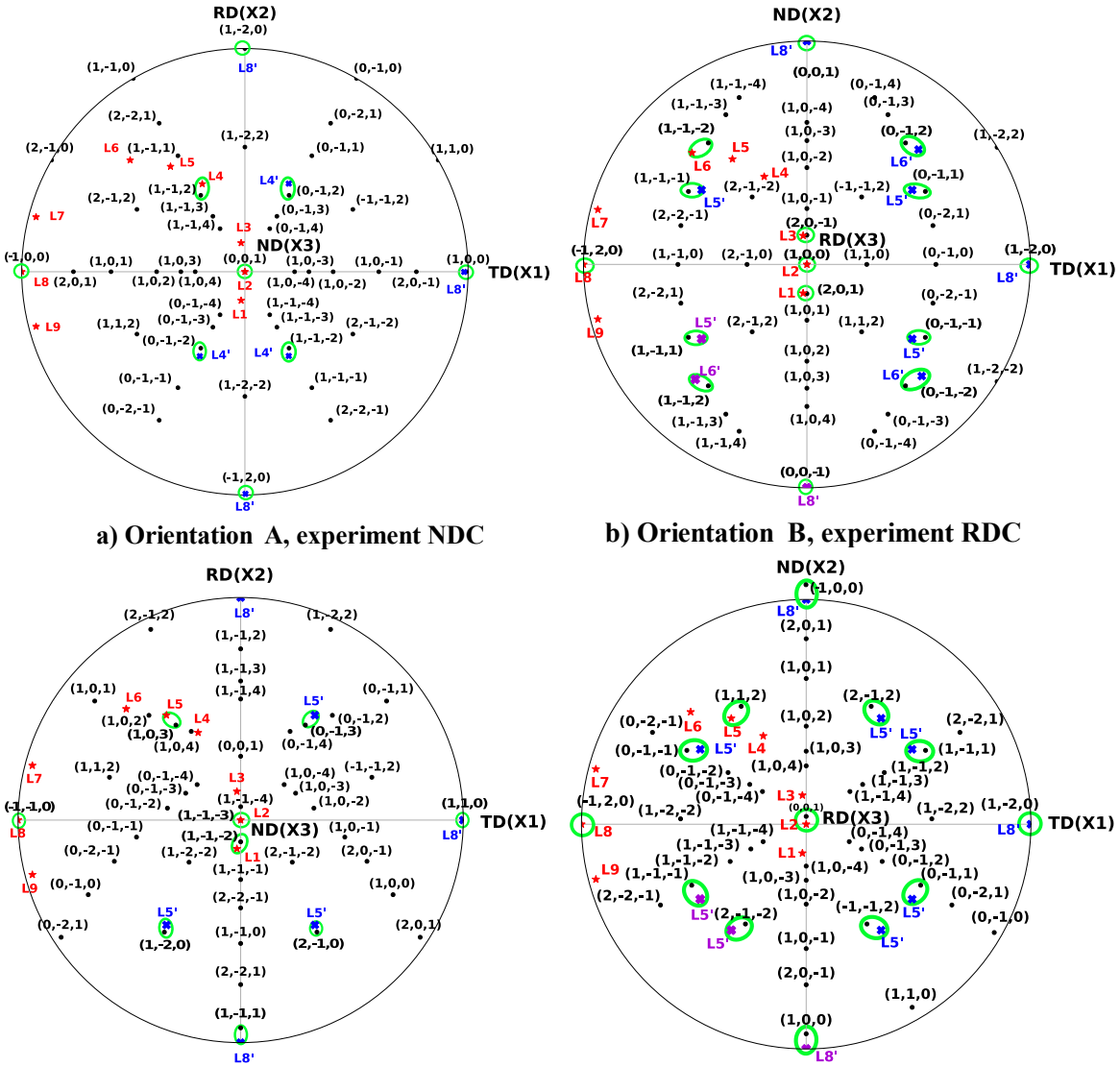

a) Orientation A, experiment NDC **b) Orientation B, experiment RDC**

c) Orientation D, experiment NDC **d) Orientation T, experiment RDC**

Fig. 6.5 Poles used for stress determination for different grain orientations and experiments performed on EPSILON-MSD instrument. Points L1-L9 (red stars) are the orientations of scattering vector for nine detector's before sample rotation, points L1'-L9' (purple "x") are the scattering vector orientations after rotation about cylinder axis by 90º and (blue "x") equivalent orientations find out using sample symmetries (due to crystallographic texture). The orientation of the applied load is always in the centre of pole figure.

Ex situ experiments (before neutron diffraction) were done first, using the same stress rig and the same conditions as during *in situ* neutron measurements to precisely plan the increments of measuring steps. In order to perform *in situ* neutron diffraction measurements, the force was increased until the predetermined stress (during elastic deformation) or strain (during plastic deformation) value, after which the stress rig was

stopped to maintain a constant sample strain. The diffraction measurements were performed for the so applied increments of the load, but above the yield point it was necessary to wait for stabilisation of the decreasing exponentially macroscopic stress. Therefore in the plastic deformation range the measurements were started about 30 min after each increment of the applied load. Macroscopic stress-strain curves obtained for each of the experiments after partial relaxation of macrostress (states for which the diffraction measurements were started) are presented in Fig. 6.6. It is worth noting that there is a large difference in the macroscopic stress response of the sample to a given macroscopic strain, depending on the nature (compressive or tensile) and direction (along RD or ND) of the applied load. As shown in Fig. 6.6, during the RDC experiment the extent of a plateau occurred during which the twins were created, while the strengthening of the sample is much more significant when the load is applied along ND direction comparing to RD direction. These differences in macroscopic behaviour of the sample should be explained by mechanisms of plastic deformation at the scale of polycrystalline grains.

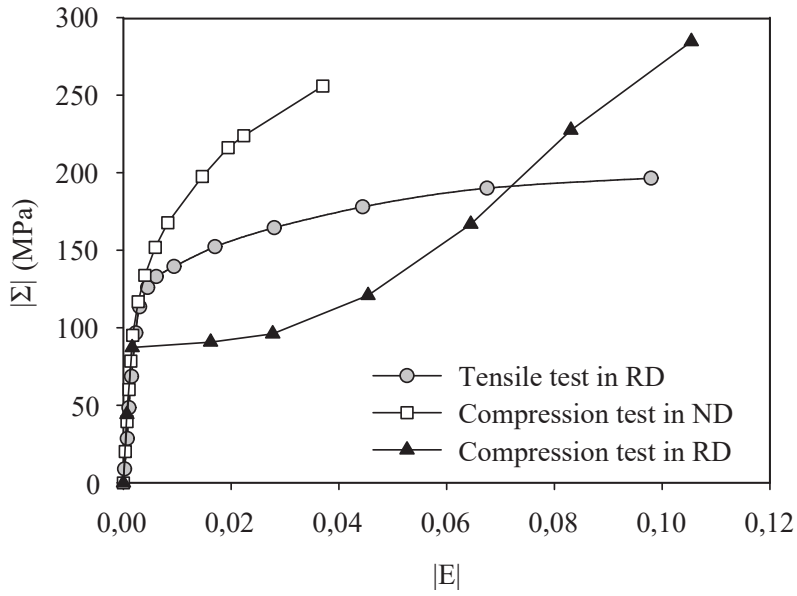

Fig. 6.6 The results of three different tests carried out for the tested AZ31 alloy. The presented stress values were determined for the imposed macrostrains after the initial relaxation of the macro-stresses. Diffraction measurements were performed at these points.

6.3. Direct determining of grain stresses and CRSS values

6.3.1. Determination of stresses for given orientations

The important goal of this work is to determine experimentally the stresses for selected groups of crystallites, both those which are very numerous due to crystallographic texture, but also those which are very few and do not play a significant role during the deformation process. The stress evolution for a given grain orientation was determined using crystallite group method (see section 4.4), i.e. from the set of lattice strains measured during tensile/compression test for appropriate hkl reflections and orientations of the scattering vector, which are closest to the poles corresponding to the tested grain (Table A2.1 in Appendix 2) were chosen.

The lattice strains were calculated from the formula:

$$< \varepsilon(hkl, \varphi, \psi) >_{hkl} = \frac{< d >_{hkl} - < d >^0_{hkl}}{< d >^0_{hkl}} \tag{6.1}$$

where $< d >_{hkl}$ and $< d >^0_{hkl}$ are the interplanar spacings measured for the sample under applied load and the initial non-loaded sample, respectively.

In the case of determining the lattice strain during twin formation, the initial value of $< d >^0_{hkl}$ could not be obtained directly from the measurement, because the twin orientation are not present in the initial sample (notice the absence of peak 002 for the initial sample in Fig. 6.2). To determine the missing $< d >^0_{hkl}$ values the available interplanar spacings from two detectors were compared and the $< d >^0_{hkl}$ values for missing reflections were determined from interpolation (this concerns especially missing 002 and 004 reflections in L2 detector). For details see Appendix 1. This approach was previously proposed by Clausen et al. in [16].

Having measured lattice strains for sets of poles corresponding to given grain orientations the components of stress tensor were calculated using the crystal group method (CGM) described in section 4.4 The $F^R_{ij}(hkl, \varphi, \psi)$ factors used in equation (4.24) were calculated from single crystal elastic constants: $c_{11} = 59{,}3$ GPa, $c_{33} = 61{,}5$ GPa, $c_{44} = 16{,}4$ GPa, $c_{12} = 25{,}7$ GPa, $c_{13} = 21{,}4$ GPa taking into account [157].

The first analysed experiment is the tensile test performed in the rolling direction (RD). In Fig. 6.7 the grain stresses for orientations A, B, C and D (defined in Fig. 6.3 and Fig. 6.4) versus the macroscopic stress corresponding to the applied load are shown. The sets of strains used for stress determination are shown in [40]. Because of the sample and crystals symmetry only the non-zero principal stresses σ^A_{ii} and σ^B_{ii} were chosen for the A and B orientations. In the case of orientation C the non-zero σ^C_{23} component is also shown. This

shear stress can be different from zero because the crystallite axis <c> is tilted from the X_3^S sample axis (normal to the surface of the sample, ND) toward the direction X_2^S (RD) along which the tensile force was applied. Therefore, these axes of the stress tensor defined with respect to the sample system may not coincide with the principal stress axes. Finally in the case of D orientation only the σ_{33}^D was determined because the strains were measured only in two directions. In Fig. 6.7 also the results of EPSC model are shown however, they will be discussed in the section 7.1.

Analysing the experimentally determined components of stress tensor it can be noticed that in the beginning of compression test (Σ_{RD} smaller than about 70-90 MPa) the grain stresses are practically equal to the applied load, i.e. $\sigma_{33}^{A,B,C,D} = \Sigma_{RD}$ and other stress component are equal to zero (see Fig. 6.7). This means that, due to a low elastic anisotropy of crystallites equal stresses are localized at all grains having different lattice orientations. However, when plastic deformation begins (Σ_{RD} between 70-90 MPa), the partitioning of stresses between grains changes. A higher compressive stress in the loading direction is localized at grains having orientation A and B (with <c> axis parallel to ND), i.e. $\sigma_{33}^{A,B} > \Sigma_{RD}$ (Fig. 6.7). Simultaneously, the value of $\sigma_{11}^{A,B}$ remains almost equal to zero, while a small compressive stress $\sigma_{22}^{A,B} < 0$ is generated. The deviation of the grain stress components from the macroscopic values increases with increasing applied load. The opposite behaviour is demonstrated by the tilted grains with orientations C and D, for which the tensile stress in the direction of the load decreases comparing to the macroscopic value ($\sigma_{33}^{C,D} < \Sigma_{RD}$). This means that the plastic deformation occurred for the grains D and C causing transfer of part of the load to other grains which remain elastic. Representatives of the still elastically deformed grains are those with the A and B orientations. For such grains the stress is greater than the macroscopic stress Σ_{RD}. The interaction between grains in the direction perpendicular to the load is more complex than in the loading direction and it could be explained by model.

Then, it can be noticed that for $\Sigma_{RD} > 125$ MPa the trend of the plots obtained for the orientations A and B again changes, i.e. the deviation of the grain stresses from the macroscopic values stabilizes and does not increase anymore. It can be interpreted as the beginning of plastic deformation for the grains A and B. At the same time, the change in the behaviour of stresses also takes place for the grains C and D, i.e. greater stress is transferred to these grains in response to the plastic deformation of the grains having orientations such as the A and B. It should be emphasised that the Σ_{RD} thresholds, where the trends of plots change, cannot be directly used in Schmid low to determine RSS values on activated slip systems because of intergranular stresses. Therefore in this work calculations of the RSS will be based on the stress tensor components determined for selected orientations using neutron diffraction.

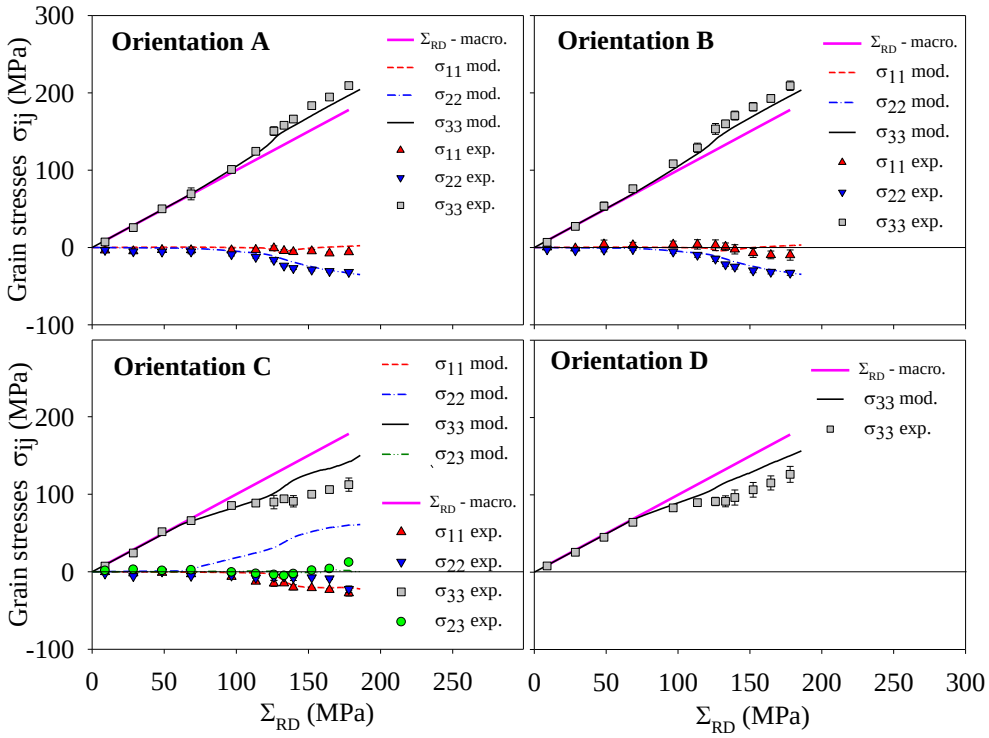

Fig. 6.7 Evolution of the grain stresses for orientations A, B, C and D versus macrostress Σ_{RD} during tensile test performed along RD compared with model using threshold assumption. The evolution of macroscopic stress Σ_{RD} is drawn with a pink line.

In the second and the third experiments the sample was compressed respectively in the ND and RD directions, and TOF method was used. The sets of reflection used in these experiments are shown in Fig. 6.5 and in Table A2.1 (Appendix 2).

Due to sample and crystal symmetries, in analysis of the data obtained in NDC experiment (compression in ND) only the non-zero principal stresses σ_{ii}^{A} were determined for the orientation A, while in the case of orientations D, F and G additionally non-zero $\sigma_{23}^{D,F,G}$ component was determined. Similarly, as in the previous experiment, this shear stress can be different from zero because the crystallite axis <c> is tilted from the X_3^S (ND) sample axis (along which the compressive force was applied) towards the direction X_2^S (RD). The results of stress components evolution during NDC experiment are presented in Fig. 6.8 for orientations A, D, F and G (the result for orientation B was almost identical with this for orientation A, due to texture and crystal symmetry). Also, in Fig. 6.8 the results of EPSC model are shown to analyse them in section 7.1.

Similarly, as in the previous experiment it can be noticed that the in the beginning of the test (for $|\Sigma_{ND}|$ less than about 70-90 MPa) the grain stresses are practically equal to the applied load, i.e. $\sigma_{33}^{A,B} = \Sigma_{ND}$ and the other stress components are equal to zero (cf. Fig. 6.8). This confirms that, the crystallites exhibit low crystal anisotropy leading to the same localised stress for every grains having different lattice orientations. However, when plastic deformation starts (at about $|\Sigma_{ND}| \approx$ 70 – 90 MPa), a greater compressive stress in the loading direction is localized at the grains having orientation A and B ($|\sigma_{33}^{A,B}| > |\Sigma_{ND}|$), and simultaneously nonzero tensile stress tensor components $\sigma_{11}^{A,B} \approx \sigma_{22}^{A,B} > 0$ are generated at the transverse directions. The deviation of the grain stress components from the macroscopic values increases with increasing load. The opposite behaviour is demonstrated by the "tilted grains" with orientations D, F and G, for which the compressive stress in the direction of the load decreases comparing to the macroscopic value ($|\sigma_{33}^{D,F,G}| < |\Sigma_{ND}|$). Also, for these grains the nonzero stresses are generated in the directions perpendicular to the load, but their behaviour is complex. Similarly, as in the previous experiment, transfer of the stress from plastically deformed grains (e.g. D, F and G orientations) to the elastically deformed ones (e.g. orientations A and B) occurred. Then, it can be noticed that for $|\Sigma_{ND}| > 180$ MPa the trend of the plots obtained for the orientations A and B again changes, and the deviation of the grain stresses from the macroscopic values does not increase. This means the beginning of plastic deformation for the grains A and B. The changes in the behaviours of stresses localized at grains D, F and G are not significant for $|\Sigma_{ND}| > 180$ MPa.

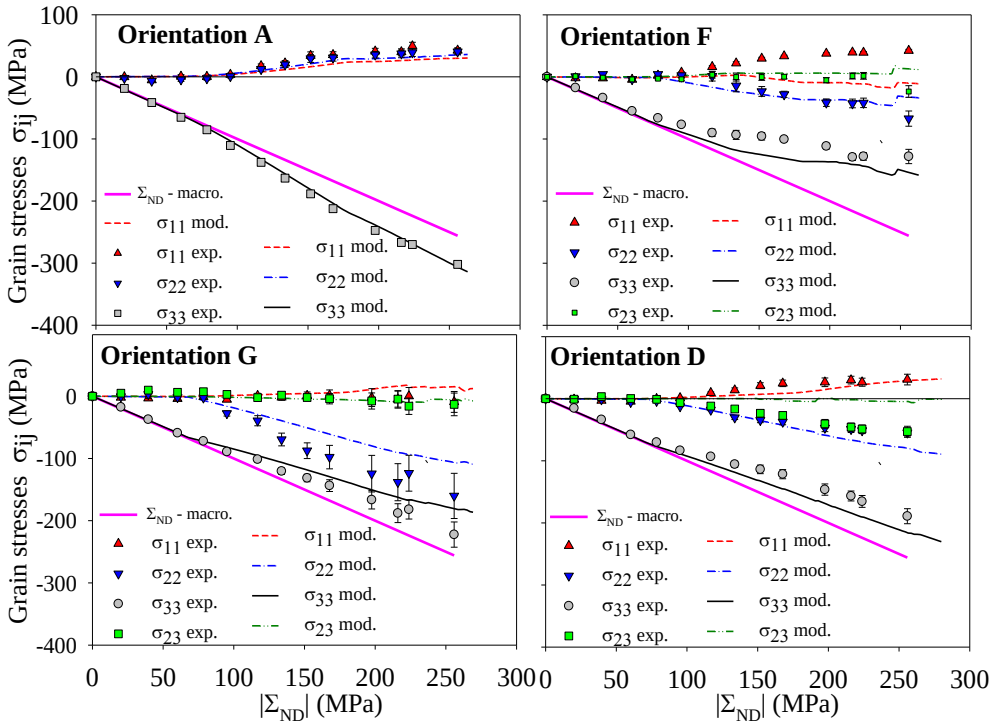

Fig. 6.8 Evolution of the grain stresses for orientations A, D, F and G versus macrostress $|\Sigma_{ND}|$ during compression test performed along ND compared with model using threshold assumption. The evolution of macroscopic stress $|\Sigma_{ND}|$ is drawn with a pink line.

In the third experiment (RDC), a compressive load in the direction of RD was applied, and in this case the twinning process took place at about $|\Sigma_{RD}| \approx 90$ MPa for a significant number of grain orientations. Before twinning insignificant deviations of the stresses from the macroscopic stress were observed for the studied orientations A, B and G' (cf. Fig. 6.9). During twinning occurring at approximately constant load, the twins (orientation T) are formed mostly from crystallites having B orientation, which completely disappeared. The new twins, when they born exhibit compressive stress $|\sigma_{33}^{T}|$ slightly smaller than the macrostress $|\Sigma_{RD}|$, but the stress $|\sigma_{33}^{T}|$ arises during increasing of the load and quickly exceeds the value $|\Sigma_{RD}|$. Then the deviation of the $|\sigma_{33}^{T}|$ from $|\Sigma_{RD}|$ value increases until the $|\Sigma_{RD}|$ reaches about 150 MPa, where the deviation stabilises. The transverse stresses $|\sigma_{11}^{T}|$ and $|\sigma_{22}^{T}|$ are tensile, they start from zero value and progressively arise until $|\Sigma_{RD}| \approx$ 150 MPa. This behaviour is characteristic for the elastically deformed grains (up to $|\Sigma_{RD}| \approx$ 150 MPa) in the plastically deformed material, i.e. elastic grains accumulate greater stresses as compared to macrostress. The A-oriented grains also transform into twins, but due to the lower Schmid coefficient (see next section) this transition is much slower and some of them remain in the sample much longer compared to the B-oriented grains. The stress $|\sigma_{33}^{A}|$ for the A-grains is higher than the macroscopic stress $|\Sigma_{RD}|$ at the beginning, but with increasing load, the stress $|\sigma_{33}^{A}|$ approaches the macroscopic stress value, while the stresses

in the direction perpendicular to the load are small and tensile or they are close to zero. The behaviour of the G'-oriented grains is similar to that which was observed in the previous experiment (compression in ND direction), i.e. the stress in the load direction $|\sigma_{33}^{G'}|$ arises slower than the macrostress $|\Sigma_{RD}|$ when plastic deformation begins. The behaviour of the transverse stresses and shear stress, for this grain orientation, are caused by interaction between grains, therefore their evolutions should be explained by the model.

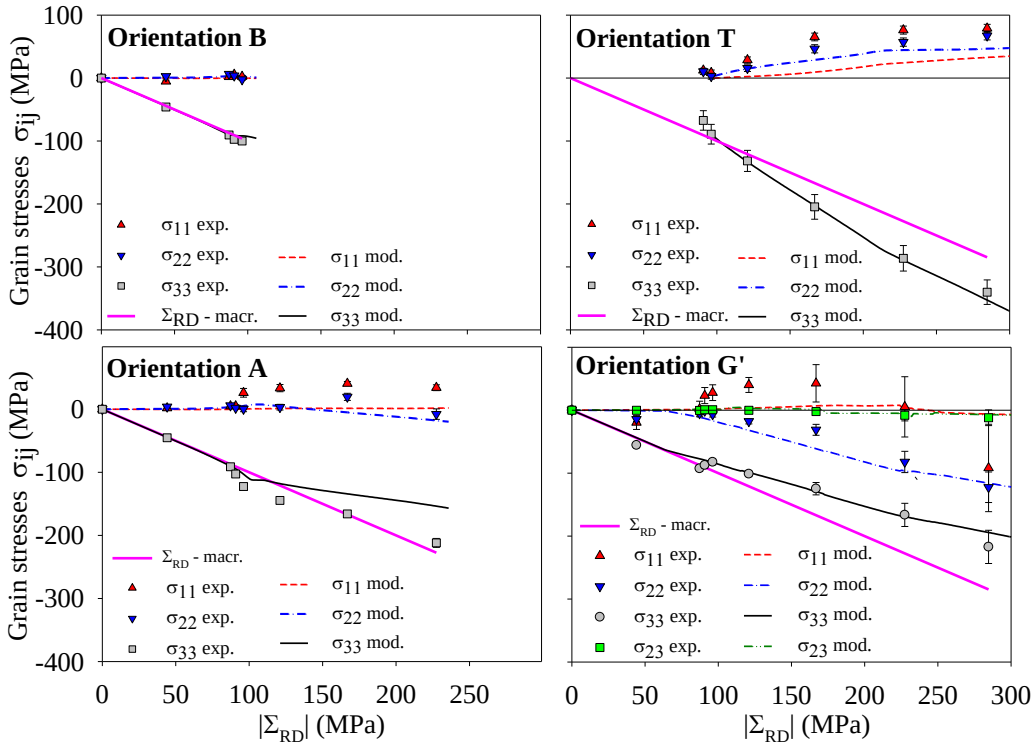

Fig. 6.9 Evolution of the grain stresses for orientations A, B, T and G' versus macrostress $|\Sigma_{RD}|$ during compression test performed along RD compared with model using threshold assumption. The grains having B orientation are transformed to twins (T-orientation) at approximately $|\Sigma_{RD}|$ = 90 MPa. The evolution of macroscopic stress $|\Sigma_{RD}|$ is drawn with a dotted line.

6.3.2. **Determination of CRSS for slip and twin systems**

Having determined evolution of the σ_{ij}^{CR} stresses during three different modes of deformation the resolved shear stresses (RSS) for different slip systems can be calculated. Then analysing the behaviour of chosen RSS for specific grain orientations during three different tests the CRSS values for these systems can be found. To do this, the following rules for finding an active slip system were applied:

- a potentially active slip system is the one for which RSS is the maximum among all symmetrically equivalent slip systems – this system is activated when its RSS reaches the CRSS value,
- when the system is activated the RSS on this system starts to grow slower or does not change significantly – the RSS value for the system which is activated is considered a CRSS value,
- if the evolution of RSS on more than one system indicates their activation at the same sample load, another test should be analysed to select the really activated system,
- the slip systems for which the Schmid factor calculated for the uniaxial macroscopic stress is equal to zero, are excluded and treated as inactive, i.e. it is assumed that intergranular stresses are too low to activate the slips by themselves (however, the values of intergranular stresses are taken into account in the calculation of RSS and CRSS from the measured tensor σ_{ij}^{CR}).

Using the above rules, the analysis of the measurement results was carried out considering the potential possibility of activating the slip and twinning systems during the three conducted experiments.

In the case of tensile test performed in RD, the basal slip system cannot be activated in the grains having A and B orientations, because the load applied to the sample is parallel to the basal plane, leading to zero value of Schmid factor for macrostress Σ_{RD}. The RSS on tensile twinning system is negative therefore twinning cannot occur. The other slip systems can be active for such grain orientations. On the other hand, the basal system and all other systems can be activated for C orientation.

During compression test in ND, the only potentially active system for the orientation A and B are the pyramidal <c+a> systems for which the Schmid factor is not equal to zero. The tensile twinning system is inactive because of negative RSS value. The other systems are not activated due to zero value of the Schmid factor when uniaxial Σ_{ND} stress is perpendicular to the slip plane (as for basal system), parallel to the slip plane (as for prismatic system) or perpendicular to slip direction (as for basal, prismatic and

pyramidal <a> systems). For the D, F and G orientations, all slip systems including the basal system, can be active.

In the compression test along RD, the RSS on tensile twinning system is positive and significant for the orientations A and B. This is a chance to find out the value of CRSS for twinning process. The RSS evolution for G' orientations are also considered and, in this case, all slip systems can be active. Moreover, for the tensile twins (T-orientation) the Schmid factor calculated for the Σ_{RD} stress is close to zero for the basal, prismatic, pyramidal <a> systems, while for tensile twin system RSS is negative. Therefore, only the pyramidal <c+a> systems can be activated in the grains having orientation T. It should be emphasised, that only the first order tensile twinning systems were considered in this work, because only this type of twinning is significant in the analysed samples and deformation modes, as was observed in EBSD and texture measurements, discussed in section 7.3.

Considering the above remarks at first the evolution of the maximum RSS (among all symmetrically equivalent systems) for the basal system in the tilted orientations were analysed. The tilted orientations are those for which the <c> axes is not perpendicular to one of the directions RD, TD or ND and Schmid factor is not zero for basal system. A common feature of such orientations is that the basal system can be activated, while for the A, B and T orientations it is inactive due to zero value of Schmid factor. It was found that the grain stress for the tilted orientations is always lower than the macroscopic value, i.e. these grains are softer than e.g., A, B and T orientations (cf. Fig. 6.7-Fig. 6.9). The conclusion is that CRSS and work hardening are the lowest for the basal system compared to other systems. The evolution of the maximum RSS for basal system was shown in Fig. 6.10 for the tilted orientations F and G during the compression test in ND. It is clearly visible that after the linear increase in the maximum RSS during elastic deformation, the value of RSS stabilizes and does not change for a certain range of deformation (or even slightly decreases). The CRSS is equal to the RSS value where the trend of the plot has radically changed, and it is determined as the average of the points closest to the trend change. The uncertainty of CRSS is estimated based on experimental uncertainty of these points. In the case of the compression test performed along the ND, the mean CRSS value for the base system is 28 MPa (calculated for the D and F orientations) and this value was used in further analysis (see Table 6.1). In the other two experiments, the CRSS values are more difficult to determine, and they are ambiguous, but they confirm the value determined from the compression test performed in ND, as shown in section 7.2.

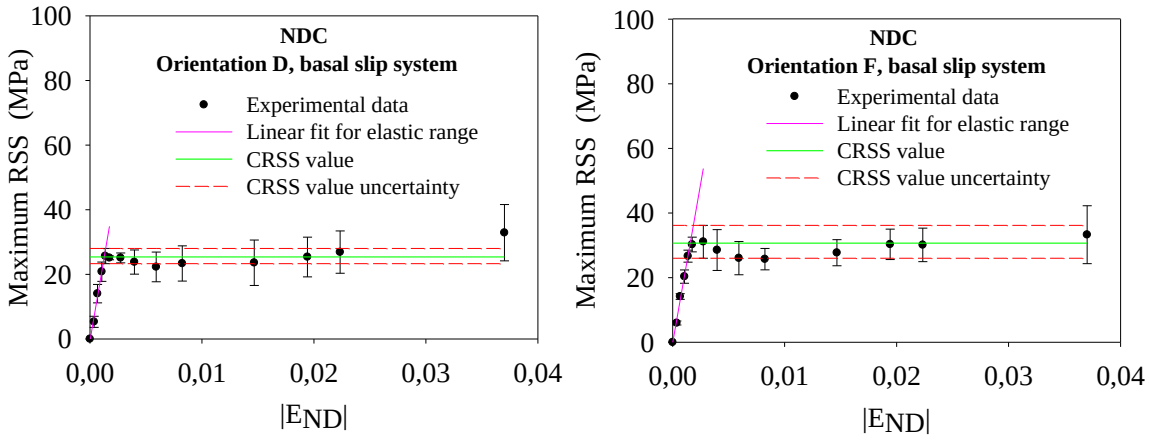

Fig. 6.10 Evolution of the RSS for basal system (activated in grains having orientations D and F) versus sample strain $|\mathbf{E}_{ND}|$ during compression test performed along ND. Determined CRSS values and their uncertainties are marked with horizontal lines.

Also, the values of CRSS for pyramidal systems <c+a> can be determined from the compression test in ND. In this case the evolution of maximum RSS on these systems in the grains with orientations A and B were considered. For such orientations only pyramidal systems <c+a> exhibit nonzero Schmid factors. As shown in Fig. 6.11a-d, a linear dependence of the maximum RSS versus $|\Sigma_{ND}|$ during elastic deformation of the sample occurred. Then the RSS increases faster due to the load transfer to those grains from the grains with tilted orientations in which the basal system is activated. Eventually, the upward trend in RSS value suddenly slows down and stabilizes, which means activation of pyramidal <c+a> systems (cf. Fig. 6.11 a-d). Therefore, the intersection of the regression lines fitted below and above the trend change can be identified as the point at which the RSS value equals to the CRSS value. Also, the uncertainty of the CRSS value obtained in this way can be estimated by considering the maximum difference between the intersections of the extreme lines corresponding to the uncertainty range for both fitted lines. The values of CRSS with their uncertainties for the first and the second order the pyramidal <c+a> systems activated in grains A and B during NDC experiment are given in Table 6.2. It is worth noting, that we cannot distinguish which of the two systems (first or second order) is activated, it is also possible that they are activated together.

Similar analysis of the pyramidal <c+a> systems activation can be performed considering the twin grains (T-oriented) during RCD test. Except for intergranular stresses, the stress state of the T-oriented grains in the RDC test is similar to the A and B-oriented grains in the NDC test, i.e. the load is parallel to the <c> axis. Based on the analysis of the maximum RSS values on the <c+a> systems, it was found that the CRSS values are different for the T-oriented grains (Fig. 6.11e, f), compared to the A and B-oriented grains (Fig. 6.11a-d), i.e. twins show a higher CRSS value than the grains in the initial

(undeformed) sample (Table 6.2). It should be emphasized that due to the small number of experimental points and their significant uncertainty, the uncertainty of the CRSS value for twins cannot be accurately estimated. Therefore, a measure of this uncertainty is defined by the points that are closest to the point where the curve changes its trend (see Fig. 6.11e, f and Table 6.2).

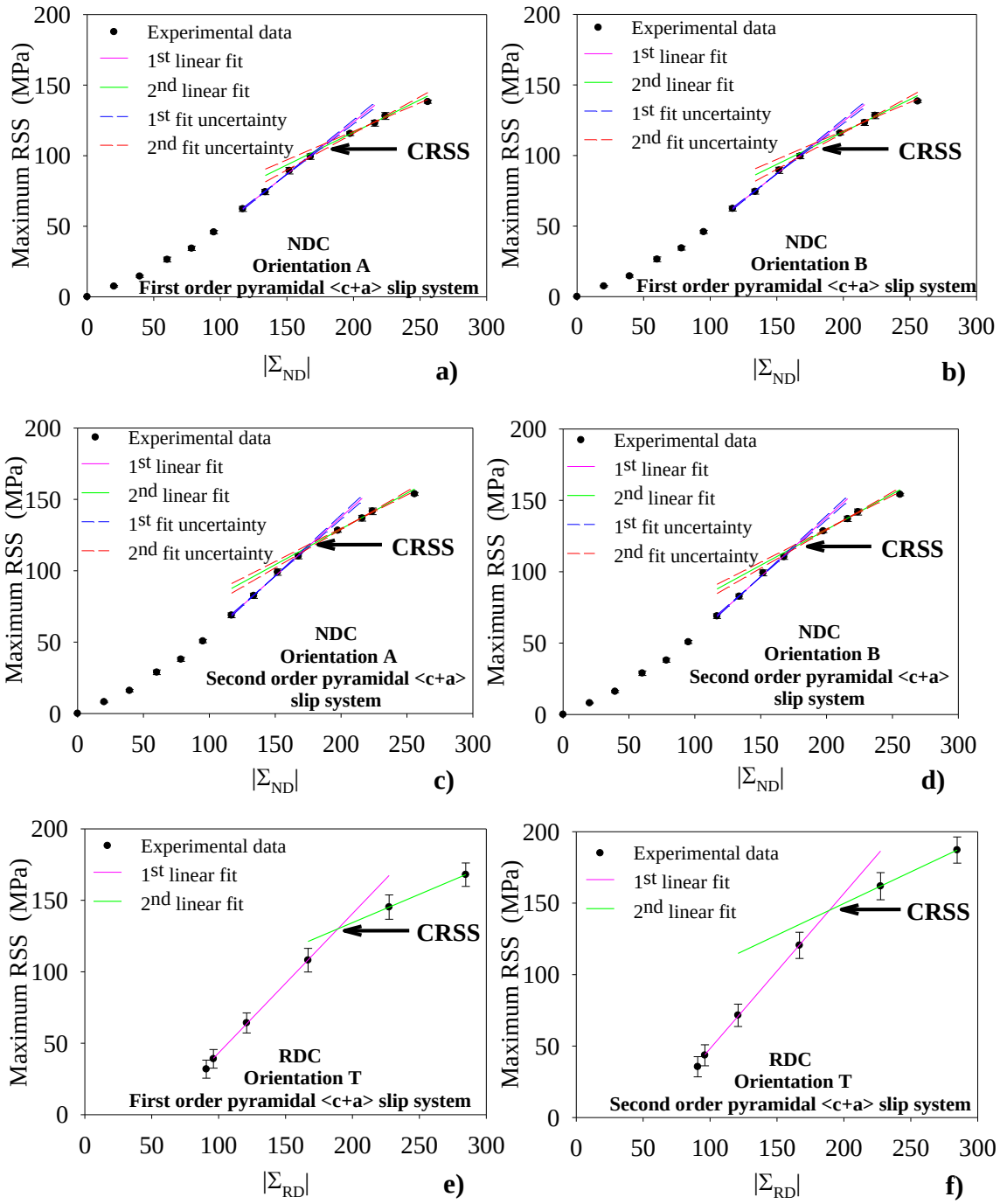

Fig. 6.11 Evolution of the RSS for the pyramidal <c+a> systems in the grains with A and B versus sample stress $|\Sigma_{ND}|$ during compression test performed along ND (a-d). Corresponding results, but for T-oriented grains (twins) are shown versus sample stress $|\Sigma_{RD}|$ during compression test performed along RD (e, f). The intersection points identified as CRSS values are indicated by arrows.

The values of CRSS for pyramidal system <a> and prismatic system can be determined analysing the behaviour of RSS in the grains A and B during tensile test in RD. In the previous work (cf. [40]), it was found that from the RDT experiment it is possible to estimate the CRSS for the base system, however in the case of non-planar systems it could be concluded that they are activated for RSS in the range 62-85 MPa. It was not been possible to determine which system among the pyramidal <a>, prismatic and pyramidal <c+a> systems is responsible for the initiation of plastic deformation for A and B - oriented grains, because they all show non-zero values of RSS for the load applied along RD. The NDC experiment then demonstrated that the determined CRSS values for pyramidal <c+a> systems are significantly higher than RSS value on these systems during RDT testing (compare Table 6.2 and Fig. 6.11). Therefore, pyramidal <c+a> systems cannot be activated, and activation of pyramidal <a> and/or prismatic systems must be responsible for changing the trend of RSS vs. $|E_{RD}|$ dependence during RDT test. The beginning of the change in the curve trend enabled to determine CRSS value which is equal to RSS at this point. The uncertainty of CRSS was determined on the basis of experimental uncertainties of the closes measurement points. The so determined CRSS values for pyramidal <a> system and prismatic system are given in Table 6.2 and shown in Fig. 6.12. As expected, these values are smaller when compared to CRSS values for the pyramidal <c+a> systems. For this reason, the macroscopic stress-strain curve is significantly lower in the RDT test compared to the NDC test. It is impossible to distinguish which of the systems or both systems: pyramid <a> and prismatic are activated, but it is worth noting that both systems have the same slip direction <a>.

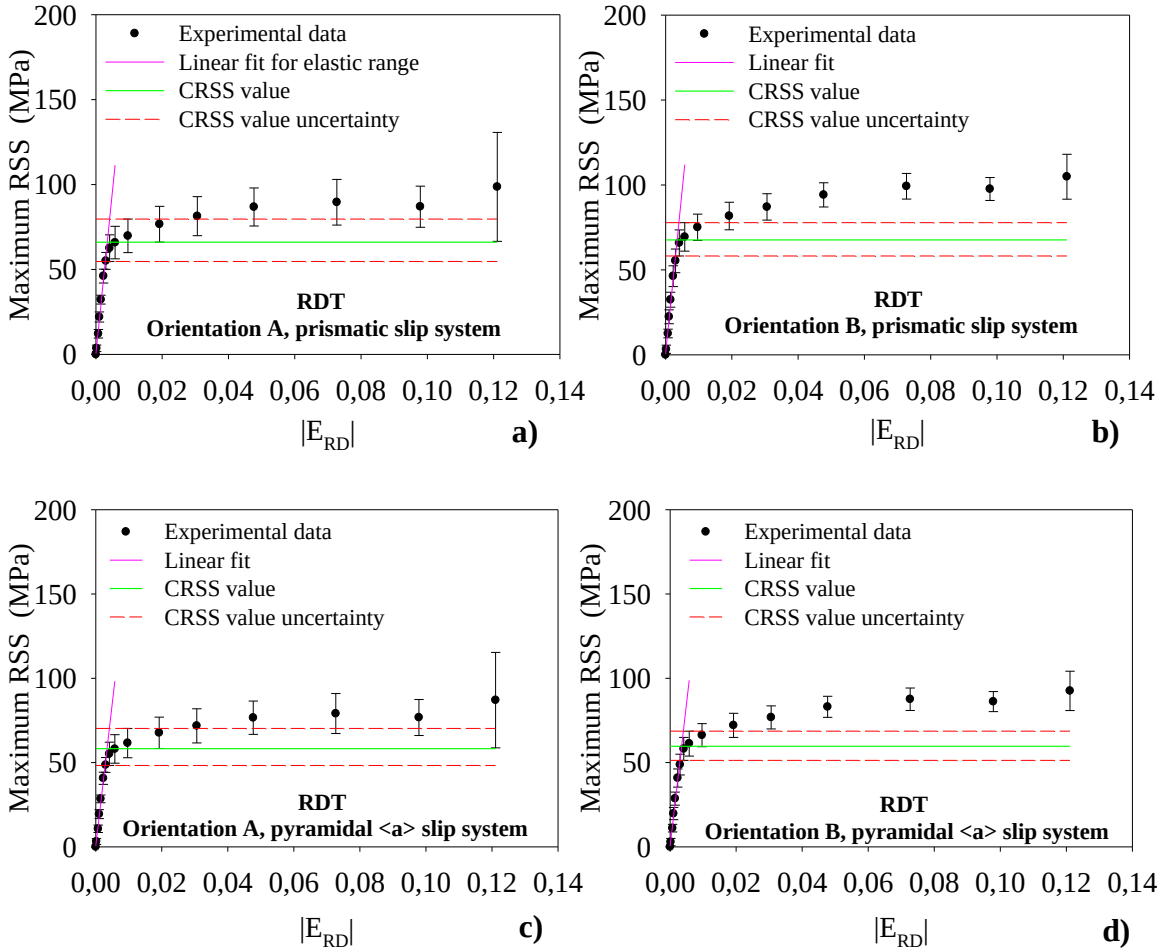

Fig. 6.12 Evolution of the RSS for prismatic system and pyramidal <a> system (activated in grains having orientations A and B) versus sample strain $|E_{RD}|$ during tensile test performed along RD. Determined CRSS values and their uncertainties are marked with horizontal lines.

Finally the CRSS for the twinning system can be determined from the RSS evolution occurring during compression along RD. In this case, the orientation B is taken into account because the Schmid factor for the twinning system in this orientation is the highest among all the other orientations considered. As shown in Fig. 6.13, the maximum RSS value for the twin system increases linearly and saturates suddenly until the plot finally ends as the B-grains disappear. The CRSS value and its uncertainty for the tensile twin system can be easily determined as the average of three points for the horizontal part of the graph (Fig. 6.13).

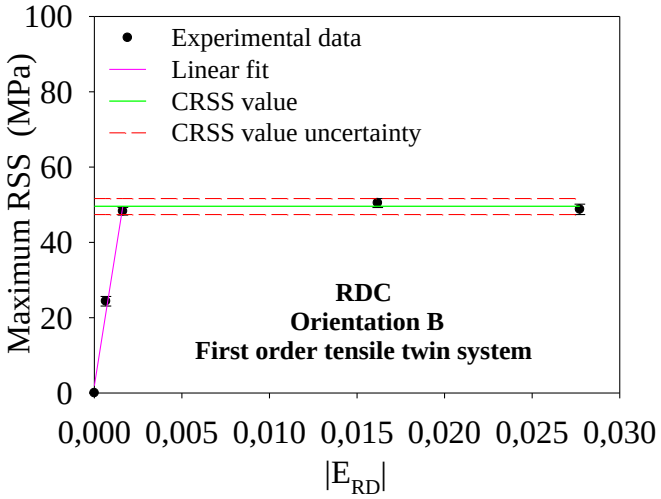

Fig. 6.13 Evolution of the RSS for tensile twin system (activated in grains having orientations B) versus sample strain $|E_{RD}|$ during compression test performed along RD. Determined CRSS value and its uncertainty is marked with horizontal lines.

The values of CRSS determined in this work are given in Table 6.2 and compared with these obtained in [40]. As shown in this table the previously determined CRSS are close to the values obtained in this work excluding the values obtained for pyramidal <c+a> systems. Previously it was found that CRSS for all systems, excluding the basal system, are between 62-85 MPa, while in this work it was shown that the pyramidal <c+a> systems exhibit CRSS higher than 100 MPa. In the new analysis, taking into account compression tests in ND and RD, the CRSS for all slip systems and tensile twinning system were determined. However, as mentioned above it is not possible to find out which system pyramidal <a> or prismatic or both together are active, and the same concerns the first and second order pyramidal <c+a> systems.

Table 6.2 CRSS values determined from experiment and parameters of Voce law used in the modified EPSC model.

		Publication [40]	Present work	
Slip system		CRSS from experiment τ_0 (MPa)	CRSS from experiment τ_0 (MPa)	Parameters of Voce law used in modified EPSC model (in chapter 7) (MPa)
Basal B: $\{0001\}\langle 11\bar{2}0\rangle$ (initial sample)		35	28,0 (3,1)	τ_0=28, $\tau_1\rightarrow 0$ $\theta_0\rightarrow 0$, $\theta_1\rightarrow 0$
Prismatic P: $\{1\bar{1}00\}\langle 11\bar{2}0\rangle$ (initial sample)		62-85	67,7 (7,9)	τ_0=68, τ_1=20 θ_0=180, θ_1=50
Pyramidal <a>: $\{1\bar{1}01\}\langle 11\bar{2}0\rangle$ (initial sample)			59,7 (6,9)	τ_0=60, τ_1=20 θ_0=180, θ_1=50
First order pyramidal <c+a> : $\{1\bar{1}01\}\langle\bar{1}2\bar{1}3\rangle$ (initial sample)			104,4 (5,6)	τ_0=104, τ_1=110 θ_0=1000, θ_1=80
Second order pyramidal <c+a>: $\{1\bar{2}12\}\langle\bar{1}2\bar{1}3\rangle$ (initial sample)			116,6 (3,5)	τ_0=114, τ_1=110 θ_0=1000, θ_1=80
First order tensile twin: $\{1\bar{1}02\}\langle\bar{1}101\rangle$ (initial sample)	Continuous approach	-	49,1 (2,5)	τ_0=45 θ_0=2000
	Threshold approach $\gamma_{thres}^{T} = 0{,}0325$ (w^T=0,25)			τ_0=47 θ_0=750
First order pyramidal <c+a>: $\{1\bar{1}01\}\langle\bar{1}2\bar{1}3\rangle$ (in the twin)		-	130 (between 108 and 145)	τ_0=134, τ_1=110 θ_0=1000, θ_1=80
Second order pyramidal <c+a>: $\{1\bar{2}12\}\langle\bar{1}2\bar{1}3\rangle$ (in the twin)		-	144 (between 120 and 161)	τ_0=144, τ_1=110 θ_0=1000, θ_1=80

6.4. Summary

The most important goal of the work presented in this chapter is to introduce the crystallite group method to the *in situ* study of the textured materials subjected to the mechanical loading. This method was especially convenient to analyse the stress state for groups of grains having particular orientations. For the first time, the stress tensor components were determined for selected grain orientations directly from the lattice strain measured *in situ* during three different test. Knowing the grain stress the load partitioning at the scale of grains was described. It was found that for individual modes of sample deformation, the orientations can be divided into soft, intermediate, hard and those in which the twinning phenomenon occurs. The soft are these grains in which the basal slip system can be activated, in intermediate grains the prismatic or pyramidal <a> systems are active, while in for the hard orientations only the pyramidal <c+a> systems are potentially active. Hard grains bear the highest loads, and soft grains and those in which the twinning process occurs are the least loaded.

It was found that the load partitioning plays a key role in macroscopic deformation and explains significant difference between macroscopic stress-strain curves for different deformation modes. In the case of compression test in ND, plastic deformation in hard grains requires activation of the pyramidal <c+a> systems, which leads to much higher macroscopic stress compared to tensile test in RD, where the prismatic and/or pyramidal <a> systems are activated. Significant influence of twinning phenomenon on the macroscopic behaviour of the sample was observed during compression test in RD. In the beginning of deformation, the twinning leads to perfect plasticity for which the load on all grains is similar and the sample deformation occurs for almost constant stress, while the significant sample strengthening was found when the volume fraction of twins increased. The orientations of the twins are very hard because the deformation of this grains require activation of the pyramidal <c+a> systems.

A very important achievement of this work is that the CRSS values and their uncertainties were determined directly from experiment, without help of model as in the previous works [15,16,23,26,158,162–166]. This has been done analysing the evolution of the RSS on the slip systems and twin system for particular orientations.

7. Plastic deformation of AZ31 alloy study using EPSC model and experimental data

7.1. Model calculations of the stress partitioning compared to experiment

The CRSS for the slip systems and tensile twinning system were determined directly from experiment, as described in the previous sections. However, the other parameters of the Voce law (equation (3.13)) cannot be found out without help of crystallographic model. Therefore, the experimental CRSS values (or values close to them within the uncertainty range) were used as input data for the EPSC calculations, while the hardening parameters of Voce law were adjusted in order to fit the model lattice strains to the experimental ones (measured in the direction of the applied load) and macroscopic stress-strain curves, simultaneously.

It should be emphasised that the same set of parameters of Voce law was applied for the three tests analysed in this work (Table 6.2). It was found that to fit the model values to the experimental ones the interaction of grains represented by interaction tensor T^{gg} (equation (3.35)) should be multiplied by the factor $\alpha = 1{,}2$, i.e.:

$$T_{ijkl}^{gg,\alpha} = \alpha\, T_{ijkl}^{gg} \tag{7.1}$$

where $T_{ijkl}^{gg,\alpha}$ is the modified tensor used to calculate the localisation tensor A_{ijkl} (cf. equation (3.35)) and the T_{ijkl}^{gg} tensor is calculated for the Eshelby spherical inclusion embedded into homogeneous medium characterised by macroscopic tangent modulus tensor L_{ijkl}.

This means that the differences in the strains between grains are enlarged in comparison to these calculated for the spherical Eshelby inclusion by factor α, i.e. in some assumption:

$$A^g = (I - \alpha T^{gg} \Delta l^g)^{-1} \approx (I + \alpha T^{gg} \Delta l^g) \quad (7.2)$$

Therefore, the interactions between grains in the modified model are shifted from those obtained by the self-consistent model towards the Sachs approach (assumption of homogeneous stresses and free strains). It should be emphasised, that the above assumption is necessary to modify the properties of the grains interaction in order to fit the model to experiment because the original EPSC model does not predict correctly processes occurring during elastoplastic deformation of the studied textured Mg alloy.

In the used modified EPSC model the twinning process is predicted continuously and starts when the RSS on the twin plane reaches the CRSS value. It was assumed that single twin orientation is created in the parent for this twin system for which the Schmid factor is maximum.

The twinning phenomena can be included into the model in various ways. In this work, twinning is predicted using two different approaches:

- "Continuous assumption" means that when RSS reaches the CRSS value, a twin grain is formed with the stress state and CRSS the same as the parent grain shows, but with a new crystal lattice orientation, calculated using equation (3.16). The twin grain then grows with increasing shear strain on the twin system reducing the parent grain volume as described by equations (3.17) and (3.18).
- In the case of "threshold assumption", when the RSS reaches the CRSS value, the twin system is activated, but no twin is formed yet. The parent grain is subjected to deformation in the same way as in the case of crystallographic slips, i.e. the state of stresses for the parent grain and CRSS on its slip systems changes. Twin grain is formed after exceeding the assumed shear strain value on the twinning system (γ^T_{thres}) and then the grain orientation changes. The volume of twin grain is proportional to the total shear strain on the twinning system (equations (3.17)), counted from the moment of twin system activation.

The assumption introduced for the parent grains is that $l_{ijkl} \rightarrow 0$. This means that during twinning, which is approximated by a crystallographic slip on the twin system, the parent grain is perfectly plastic. In this case, the grain adjusts completely to the surrounding matrix without causing mismatch stresses, i.e. the stress for the grain is equal to the uniaxial macroscopic stress (as in the Sachs model). The self-hardening for the twin system is equal to zero, while the twin slip causes the linear hardening of other systems in the parent grain (hardening is described by one parameter of Voce law, i.e. θ_0 given in Table 6.2)

The comparison of the model prediction with the experimental results obtained for three different tests are shown in Fig. 7.1-Fig. 7.3. It is well seen that both the elastic lattice strains measured in the direction of applied load and the macroscopic stress-strain curves

are well predicted by the modified EPSC model in which the Voce parameters given in Table 6.2 are used. In Fig. 7.1-Fig. 7.3 two types of the macroscopic stress-strain curves are shown: the upper line corresponds to the stress during incising sample load and the lower line shows the macrostress after relaxation at constant strain. It should be emphasized that the results of the diffraction measurement of lattice deformations correspond to the sample load at the level of the lower curve at which they were carried out. Also, the model of elastic-plastic deformation should be adjusted to the lower curve.

Some disagreement between predicted and experimental lattice strains is observed in the case of tensile test in RD (Fig. 7.1), i.e. the qualitative agreement occur, but the difference between lattice strains measured using different hkl reflection is greater than the model values. This means that the shift to the Sachs model is possibly greater that it was assumed in the modified model with $\alpha = 1{,}2$ (this was also suggested in the paper [40]). In the case of compression test in ND (Fig. 7.2) a very good agreement between experimental and predicted lattice strains as well as for the macroscopic stress-strain curve was found.

The above-described assumptions (continuous and threshold) were used to predict twinning process. For both approaches, the model results were well adjusted to the experimental results but with different values of the work hardening parameter θ_0 and slightly different CRSS values (τ_0), which are 1-3 MPa lower than the experimental one. It was found that in the case of 002 reflection, which represents lattice strains in the twins, better agreement between model and experiment was found for the threshold assumption.

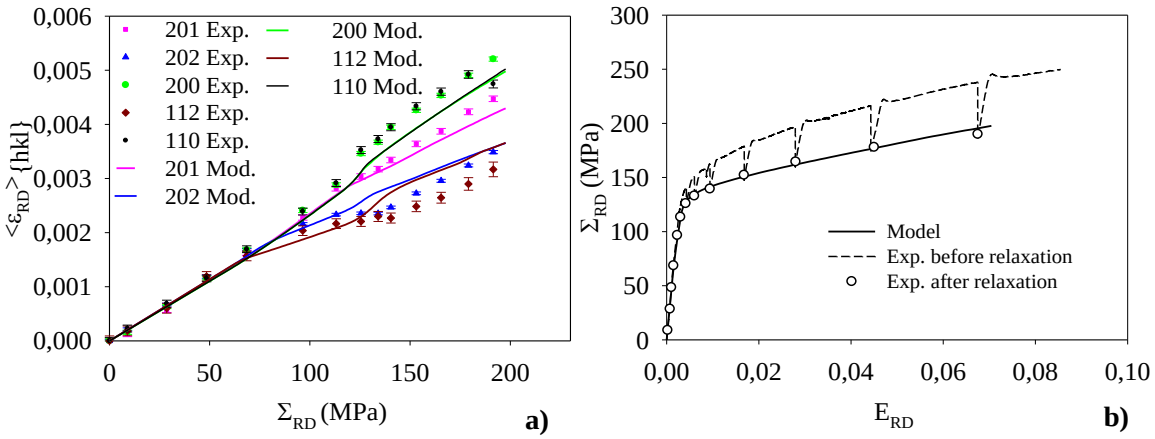

Fig. 7.1 Lattice strains measured in the direction of applied load and macroscopic stress-strain plot compared with model calculation (threshold assumption) for the tensile test in RD.

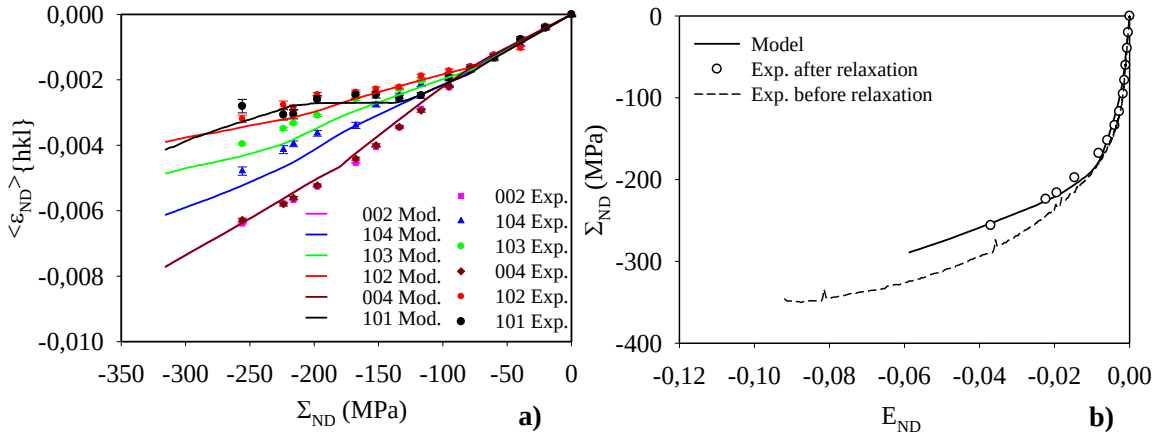

Fig. 7.2 Lattice strains measured in the direction of applied load and macroscopic stress-strain plot compared with model calculation (threshold assumption) for the compression test in ND.

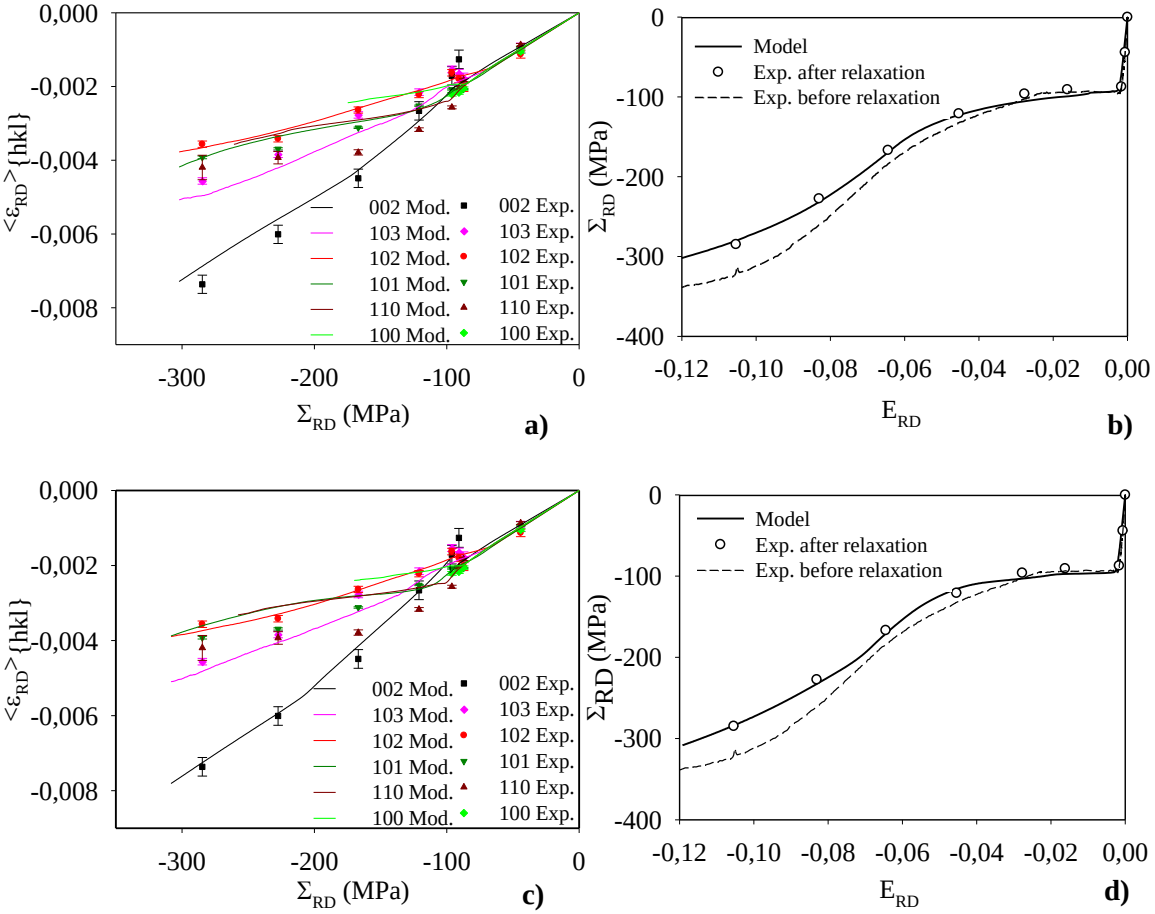

Fig. 7.3 Lattice strains measured in the direction of applied load and macroscopic stress-strain plot compared with model calculation for the compression test in RD with continuous assumption (a, b) and threshold assumption (c, d).

When the model parameters are established, the stress evolution for different grains can be calculated and compared with the experimental results. Such comparison is shown in Fig. 6.7-Fig. 6.9 where the threshold assumption was used in twinning prediction. The results of the compression test in RD direction are shown in Appendix 3 (Fig. A3.1). It was found that the choice of the type of assumption for twinning prediction is insignificant in the case of tensile test in RD and compression test in ND, because the volume fraction of the twins is negligible (see section 7.3). However, in the case of the compression test in RD, a better agreement between the model and the experimental stress localised at the twin grain was found for the threshold assumption (cf. Fig. 6.9).

In general, a very good agreement of the experimental and model components of the grain stress tensor was found for the three tests and different grain orientations. A significant disagreement was found only for the stress σ_{33}^{C} (C orientation) during tensile test in RD and for σ_{33}^{A} (A orientation) during compression test in RD. It should be emphasized that in the above comparison, the experimental data were determined for grain groups (using CGM), while the model results were calculated for a given (single) crystal lattice orientation. Thus, the agreement between the experiment and the model prediction, obtained in most cases, means that the stress tensors determined by the CGM method well represent the grain stress for a given lattice orientation.

To discuss the partitioning of the load between grains, the evolution of the grain stresses in the direction of loading together with the macroscopic stress are shown in Fig. 7.4- Fig. 7.6 (the absolute values of stresses and sample strain are shown). The evolutions of these stresses in function of the macroscopic stress $|\Sigma_{ND}|$ (or $|\Sigma_{RD}|$) and strain $|E_{ND}|$ (or $|E_{RD}|$) are presented. As shown in Fig. 7.4 during tensile test along RD, the grains having orientations A and B (let's call them "intermediate grains") are more loaded than the grains with orientations C and D ("soft grains"). This is certainly because the basal system, with the lowest value of CRSS can only be activated for soft grains having the <c> axis deviated from the ND direction. The yield stress for the intermediate grains depends on the CRSS of the prismatic and/or pyramidal <a> systems, which are higher than CRSS for the basal system but lower that for pyramidal <c+a> systems. It was found that the value of macroscopic stress is between the stresses localized at intermediate and soft grains. As shown in Fig. 7.4, the macroscopic curve obtained from the model is well fitted to the experimental data, and the qualitative agreement between the experiment and the model was obtained for orientation A and the arithmetic mean for orientations C and D. As mentioned above, the quantitative discrepancy indicates that the difference between the loading of hard and soft grains is greater in the real sample compared to the calculations of the modified EPSC model.

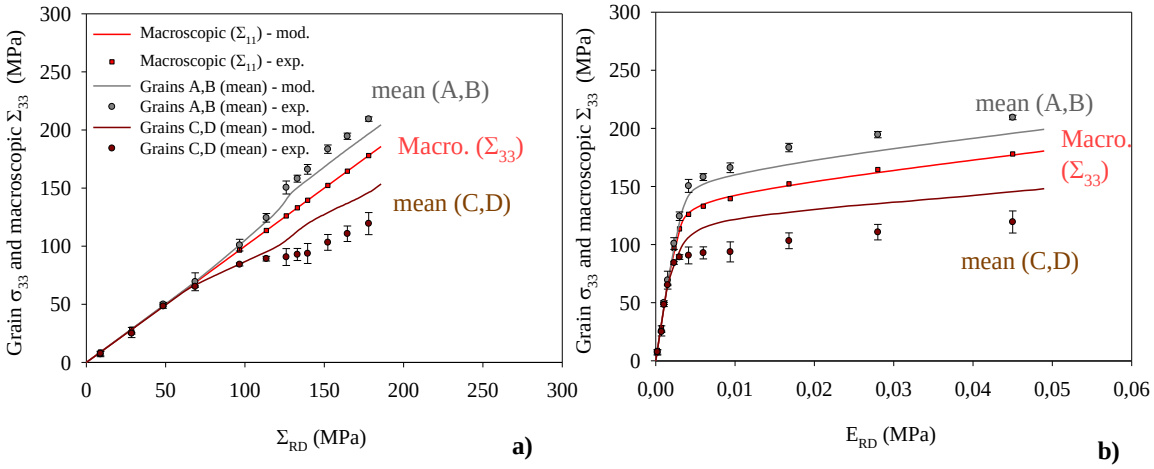

Fig. 7.4 Partitioning of the macroscopic stress $\Sigma_{33} = \Sigma_{RD}$ between soft (mean for C and D) and intermediate (A, B) grains during tensile test in RD. Model prediction are compared with experimental results.

The load partitioning between grains during compression along ND is presented in Fig. 7.5. In this test, the highest load is localised at "hard grains" having orientations A and B. For these grains plastic deformation occurs as a result of slips on pyramidal systems <c+a>, for which CRSS is the highest of all slip systems (Table 6.2). Therefore, the stress localised at hard grains as well as macroscopic stress for the sample are greater in the case of compression in ND compared to tensile in RD (cf. Fig. 7.4 and Fig. 7.5). Due to the large difference between the loading of the grains, the yield points for soft grains (mean for D, F, G orientations) and hard grains (mean A and B) are clearly visible in Fig. 7.5, as changes in the curve trends at $|\Sigma_{ND}| \approx 70$ MPa ($|E_{ND}| \approx 0{,}0015$) and $|\Sigma_{ND}| \approx 170$ MPa ($|E_{ND}| \approx 0{,}008$), respectively.

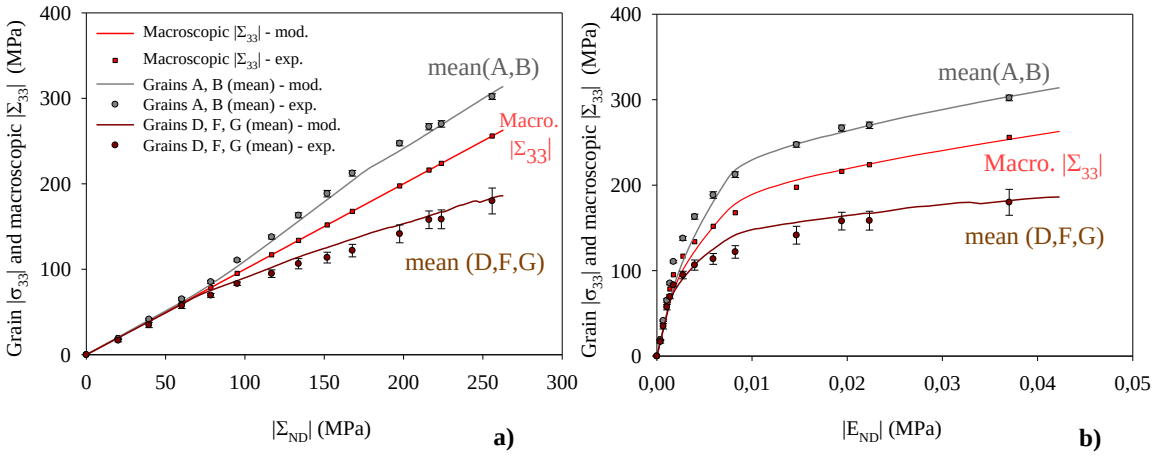

Fig. 7.5 Partitioning of the macroscopic stress $\Sigma_{ND} = \Sigma_{ND}$ between soft (mean D, F and G) and hard (mean A, B) grains during compression test in ND. Model prediction are compared with experimental results.

The load partitioning between grains having different orientations during compression test in RD direction is more complex due to the twinning phenomenon. As shown in Fig. 7.6 all grains are almost equally loaded up to the stress at which the twinning is activated at about $|\Sigma_{RD}| \approx 90$ MPa. The basal system in the soft grain with orientation G' is also activated about this load. As expected the stress $|\sigma_{33}^{G'}|$ for this grain is the lowest compared to all other grains. The B-oriented grains transform to twins (T-oriented) and during this transition the macroscopic stress $|\Sigma_{RD}|$ practically remains constants, cf. Fig. 7.6b, d. This is why in the model perfect plasticity of parent grains (B and A – oriented) was assumed, which leads to very small increase of macroscopic stress up to $|E_{RD}| \approx 0{,}03$ (cf. Fig. 7.6b, d) as seen in the experimental macroscopic curve. The created twins (T-oriented) exhibit a smaller stress $|\sigma_{33}^{T'}|$ compared to other grains, due to back stress generated during twinning (arrow in Fig. 7.6b, d). It should be however emphasised that the effect of back stress is much smaller than reported in [16]. Because in this version of the model the back stress is not taken into account (the twin grain initially has the same stress state as the parent) the model overestimates the stress for T-oriented grain compared to experimental result at the beginning of twinning process. However, it is worth noting that in the case of threshold assumption (cf. Fig. 7.6a, b) the stress localised at the twin grain is much lower than in the case of continuous assumption (cf. Fig. 7.6c, d), because of relaxation of the stresses in the parent grain occurring before the twin is created at the threshold. For the greater load the model stress at the twin $|\sigma_{33}^{T}|$ approaches the experimental value, and at the end of the test the agreement between experiment and model is very good, and again better accordance was found in the case of the threshold assumption. In the case of A-oriented grains the stress calculated by the model is lower than the experimental one, but the tendency of the experimental and model plots agree qualitatively. These grains also transform into twins but stay longer in the sample, i.e. over $|\Sigma_{RD}| = 200$ MPa. It should be emphasised, that interesting interplay between the grain stresses occurs giving the macroscopic sample stress, which is an average over all grain stresses. The macroscopic plot obtained by the model is perfectly fitted to the experimental points, and the stress distribution between grains of different orientations is also well predicted by the model (at last qualitatively in the case of orientation A).

In Fig. 7.6e, f the grain stresses $|\sigma_{33}^{B}|$ and $|\sigma_{33}^{T}|$ are shown together with the macroscopic stress. It is worth noting that the $|\sigma_{33}^{B}|$ stress remains constant over the plateau range. i.e. no change in intergranular stress appears in the parent grains during the twinning process and the localized stress remains constant. Due to the lack of initial T-oriented grains in the undeformed sample ($< d >_{hkl}^{0}$ value was estimated by interpolation as shown in Appendix 1), it is important to verify that the stresses localized at the twin grains are correctly determined. Therefore, in Fig. 7.6e, f two components of the $|\sigma_{33}^{T}|$ stress uncertainty are shown by error bars (statistical uncertainty) and uncertainty corridor

(possible systematic error). The systematic error in the case of twins can be caused by the uncertainty of the value $< d >^0_{hkl}$ which is estimated on the basis of interpolation in Appendix 1. This error is important in the performed stress analysis because it influences all lattice strains calculated from equation (6.1). As shown in Fig. 7.6e, f both systematic and statistic uncertainties of the stress $|\sigma^T_{33}|$ are not significant. It is worth noting that, the new T-oriented grains significantly affect the macroscopic behaviour of the sample. As shown in Fig. 7.6e, f the shape of the plot $|\Sigma_{RD}|$ versus $|E_{RD}|$ is enforced by the $|\sigma^T_{33}|$ stress evolution, and high macrostress value at the end of the test is due to the high stress localised at twins. As shown in section 7.3, the volume fraction of twins is very significant at the end of the test. Thus, the twins exhibiting a high yield stress, can be considered as the reinforcing phase for the studied sample. As discussed above, in the case of grains with T orientation, only the pyramidal <c+a> systems with the highest CRSS can be activated, because the applied stress is nearly parallel to the axis <c>.

In conclusion, it can be emphasized that the role of different grain orientation in the mechanical behaviour of the tested sample was explained both experimentally and with a modified EPSC model. This can be summarized as follows:

- In all tests carried out, the lowest load is always found at tilted soft grains in which the basal system is activated. These grains soften the sample and reduce macrostresses.
- The significant difference between the macroscopic stress-strain curves obtained during the tensile test in RD and compression test in ND is due to the difference in CRSS between slip systems activated in the intermediate and hard grains having preferred A and B orientations. The CRSS for pyramidal <a> and prismatic systems activated during tensile test in RD are significantly smaller than the CRSS for pyramidal <c+a> systems activated during compression test in ND. This leads to a lower macroscopic stress-strain curve obtained for the tensile test in RD compared to that obtained for the compression test in ND.
- The shape of the macroscopic stress-strain curve is significantly affected by the twinning phenomena. When twinning occurs for majority of grains (A and B – oriented) the sample is very soft and initially there is a plateau in the macroscopic stress-strain curve. When the fraction of the twins is significant and the fraction of parents is small, the macroscopic stress increases significantly, because the twins with the T orientation are very hard and they play the role of reinforcement. Localization of the stresses at the T-oriented grains (twins) is better predicted by the modified EPSC model with threshold assumption compared to the continuous assumption.

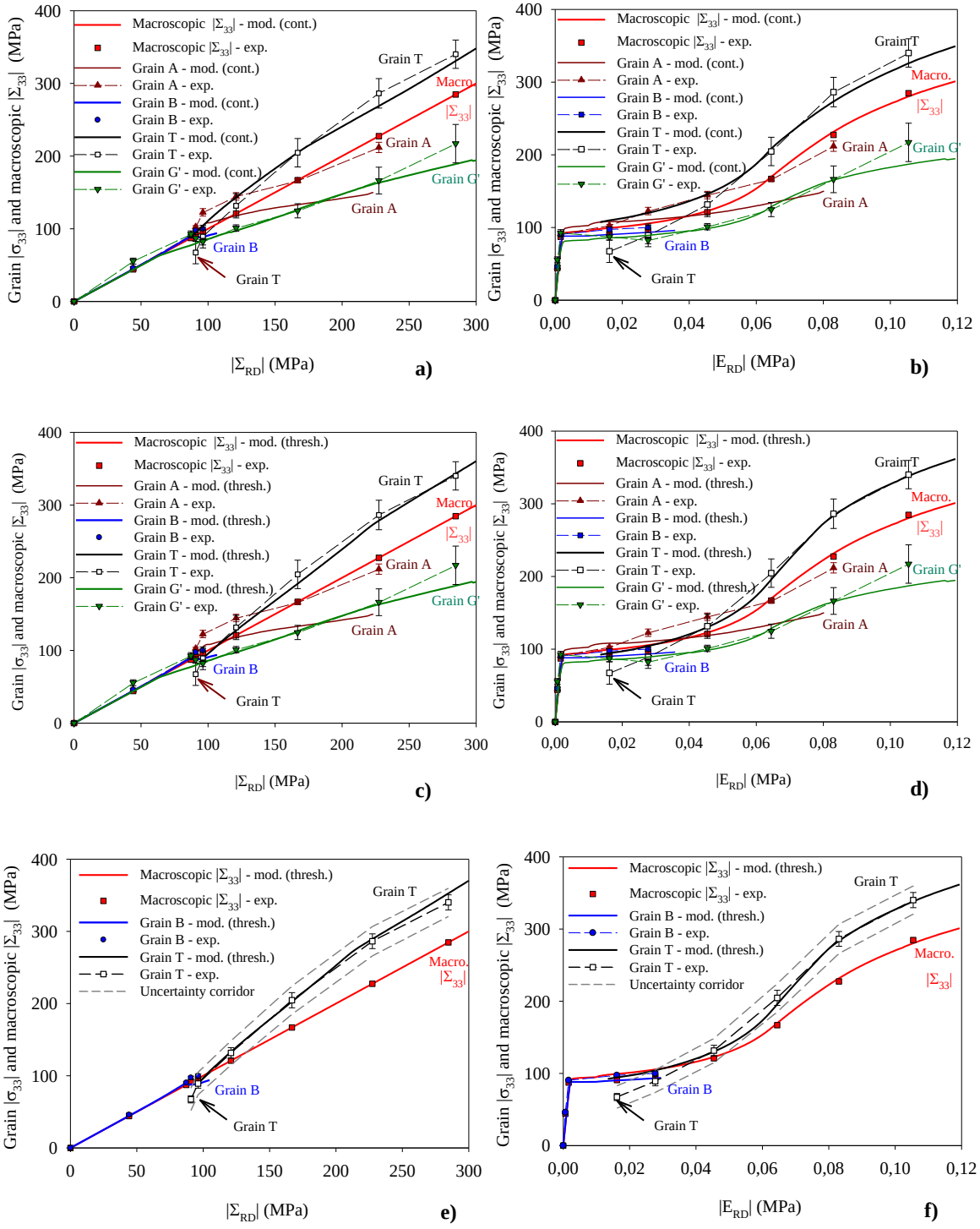

Fig. 7.6 Partitioning of the macroscopic stress $\boldsymbol{\Sigma_{33} = \Sigma_{RD}}$ between soft (G') and hard (A) grains during compression test in RD. Two versions of model prediction: with continuous assumption (a, b) and with threshold assumption (c-f) are compared with experimental results. In figures (e, f) the evolution of the stresses $|\sigma_{33}^{B}|$ and $|\sigma_{33}^{T}|$ are shown together with macroscopic stress. In the case of $|\sigma_{33}^{T}|$ the uncertainty due to statistical error (bars) and systematic errors (corridor) are presented.

7.2. CRSS and RSS evolutions predicted by model

To verify the experimentally determined CRSS and their evolution predicted by the modified EPSC model the calculated RSS and CRSS were compared with the RSS measured for different macrostresses $|\Sigma_{ND}|$ and sample strains $|E_{ND}|$. The activations of the basal system in the soft grains during three performed test are shown in Fig. 7.7. For all grains (D, F, G) the model predicted evolution of RSS versus macrostress $|\Sigma_{ND}|$ perfectly agrees with the experimentally determined one. It is worth noting that, the activation of the basal system is clearly seen when the model CRSS are compared with the RSS evolution: during elastic deformation of the grain the CRSS value is constant and higher than RSS, but when the RSS reaches the CRSS value it stops growing and remains constant, equal or slightly higher than CRSS. This means that the basal system is active and the self-hardening of the basal system is negligible (parameters of work hardening for basal system tends to zero, c.f. Table 6.2). It should be emphasised, that only the basal system is activated for the soft grains (D, F, G) at least at the beginning of sample loading. It was verified (see Fig. A4.2 in Appendix 4.a) that for other slip systems as well as for the tensile twin system the values of CRSS exceeds significantly maximum values of RSS. In Fig. 7.7 additionally the evolutions of RSS and CRSS in two examples of soft grains are shown. These results confirm low and stable value of CRSS for basal slip system at least for small and intermediate loads.

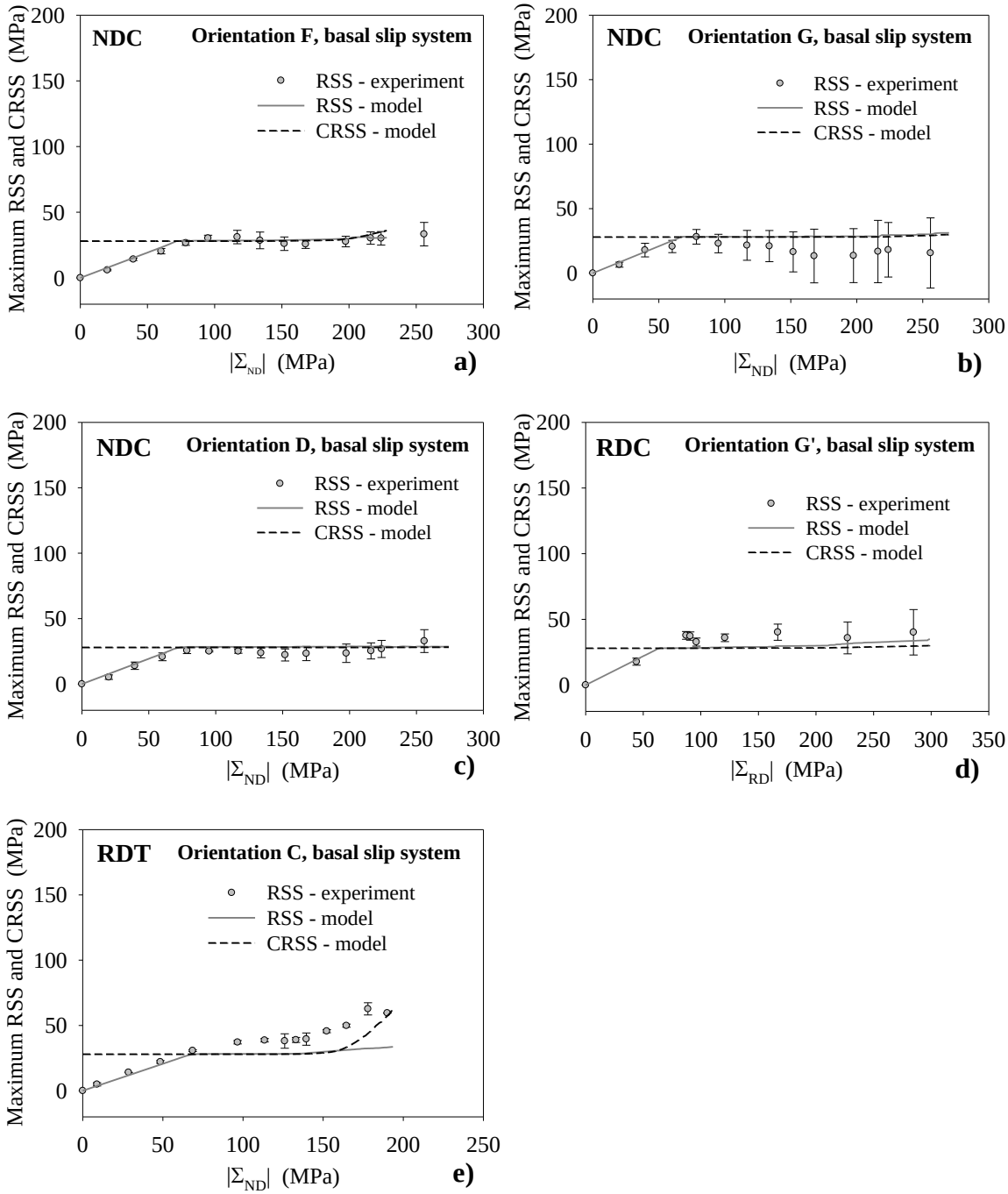

Fig. 7.7 Evolution of CRSS and maximum RSS on basal system in soft grains versus $|\boldsymbol{\Sigma_{ND}}|$, during compression test in ND (a, b, c), compression test in RD (d) and tensile test in RD (e). Model predicted maximum RSS and CRSS are compared with experimental maximum RSS. The modified EPSC model with threshold assumption was used.

Next, the analysis of slip system activation was done for the pyramidal <c+a> systems on the basis of RSS and CRSS evolution for the hard grains (A orientation) during compression test in ND. As shown in Fig. 7.8 the model predicted evolution of RSS agree with the experimental one, showing the same changes of the curve trends. Similarly, as in the case of basal system, the activation of <c+a> pyramidal systems is seen as slowdown

in RSS increase, after it reaches CRSS value. However, for the <a + c> pyramid systems, the increase in RSS remains when the system is active. It can be noticed that the RSS values are slightly above the CRSS for the first order and slightly below the CRSS for the second order ones. This suggests that the first order pyramidal <c+a> systems is active during whole loading, while the second order one is active only in the beginning of the test. However, the latter conclusion is based on the small differences of a few MPa, therefore it is not sure which type of the pyramidal <c+a> systems is really active, or maybe they are both active for different ranges of sample loading. The increase in the CRSS versus $|E_{ND}|$, after activation of the slip, determines the significant work hardening of the <c+a> pyramid systems described by Voce law, cf. Table 6.2. It should be emphasised that, the activation of the pyramidal <c+a> system can be analysed for A-oriented grains, because the other systems cannot be activated in these grains. Indeed, the CRSS values for all systems, excluding the pyramidal <c+a>, are higher than RSS during whole compression test in ND, as shown in Fig. A4.1 in Appendix 4.a.

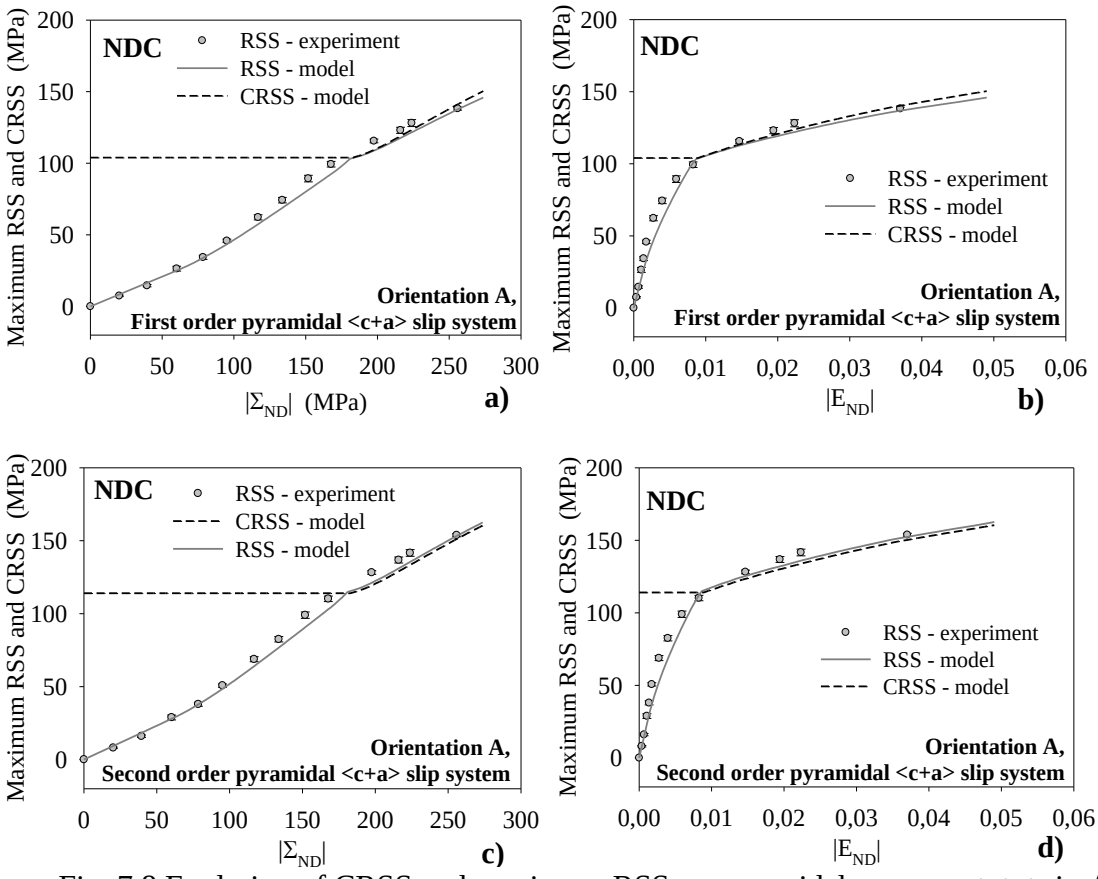

Fig. 7.8 Evolution of CRSS and maximum RSS on pyramidal systems <c+a> in A-oriented grains versus $|\Sigma_{ND}|$ and $|E_{ND}|$, during compression test in ND. Model predicted maximum RSS and CRSS are compared with experimental maximum RSS for the first order (a, b) and the second order (c, d) pyramidal systems <c+a> . The modified EPSC model with threshold assumption was used.

The evolutions of RSS and CRSS for the pyramidal <a> and prismatic systems in A-oriented grains during tensile test in RD is presented in Fig. 7.9. The model evolutions of RSS agree very well with experiment and the change in the plot trends is well seen when RSS riches value of CRSS (it is better visible on the plots drawn with respect to sample strain E_{RD}). Then, the values of CRSS and RSS are almost equal to each other and they increase with applied load. It cannot be distinguish which system actually operates and the increase of the CRSS versus E_{RD} determines hardening of the active system. The same hardening, smaller as compared to the pyramidal <c+a> system is assumed for both systems pyramidal and prismatic having the same slip direction <a> (cf. Table 6.2). In Appendix 4.b (Fig. A4.3) it is shown that the first order tensile twin system and all slip systems, excluding pyramidal <a> and prismatic systems, cannot be activated in the A-oriented grains, because the CRSS exceeds significantly the RSS values.

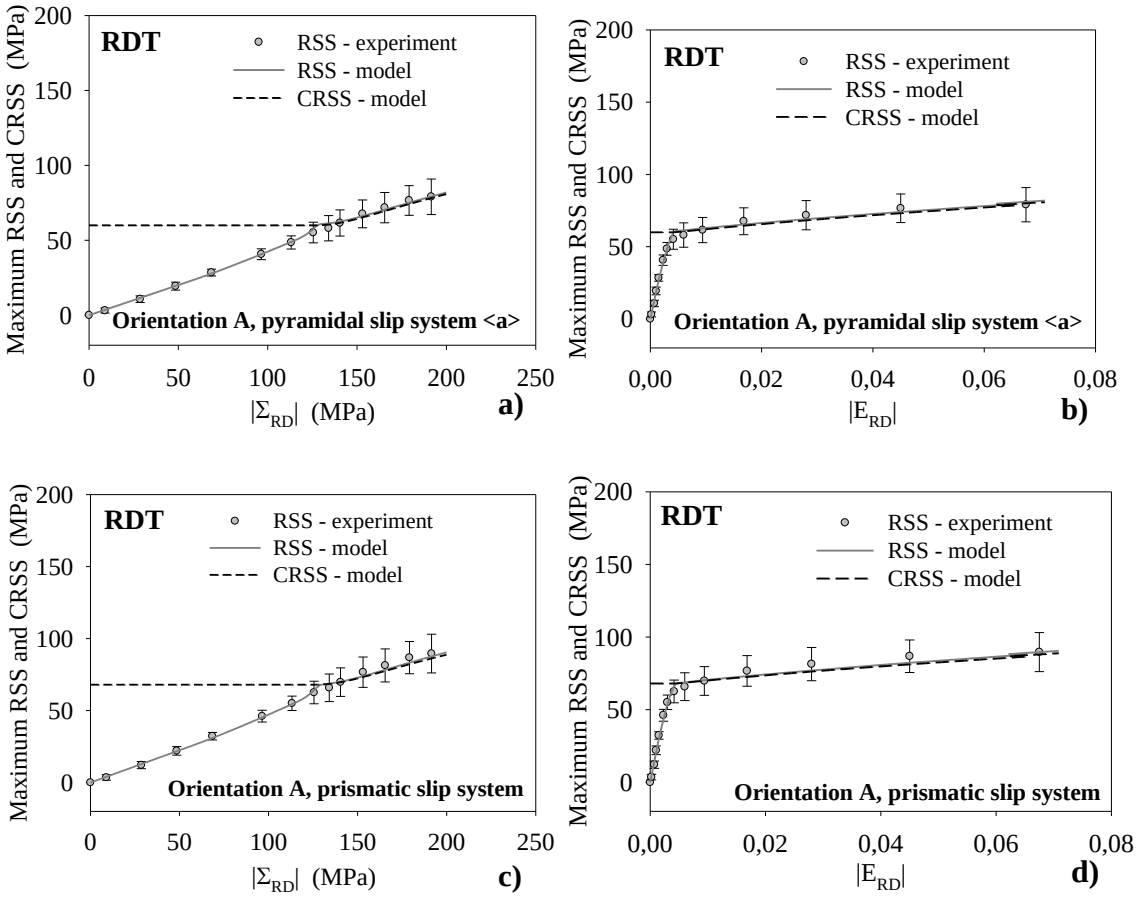

Fig. 7.9 Evolution of CRSS and maximum RSS on pyramidal <a> systems (a, b) and prismatic system (c, d) in A-oriented grains versus Σ_{RD} and E_{RD}, during tensile test in RD. Model predicted maximum RSS and CRSS are compared with experimental results. The modified EPSC model with threshold assumption was used.

To determine the RSS and CRSS evolution for tensile twin system the orientation B during compression test in RD should be analysed (Fig. 7.10a, b). The grains having this orientation as the first ones transform to twins and completely disappear at $E_{RD} = 0{,}03$, because of the highest value of Schmid factor for tensile twining slip system. As seen in Fig. 7.10a, b the experimental and model evolution of RSS perfectly coincides and the activation of this system is clearly seen. It is worth noting that the self-hardening of the twin system is negligible. In Fig. A4.4 (Appendix 4.c) it was shown that during twinning only the twin system operates, while the other ones are inactive because the RSS values for these systems are significantly smaller than CRSS values. Additionally, in Fig. 7.10c, d the evolutions of the RSS and CRSS values are shown for tensile slip in the case of A-oriented grains. It is seen that the value of RSS in the beginning is smaller than CRSS but during sample loading the RSS exceeds CRSS, leading to transformation of these grains to twins. This is why the twinning process occurs slower for A-oriented grains compared to the B-oriented. The agreement between model and experiment is much worse for the A-oriented grains comparing to the other results presented in this section.

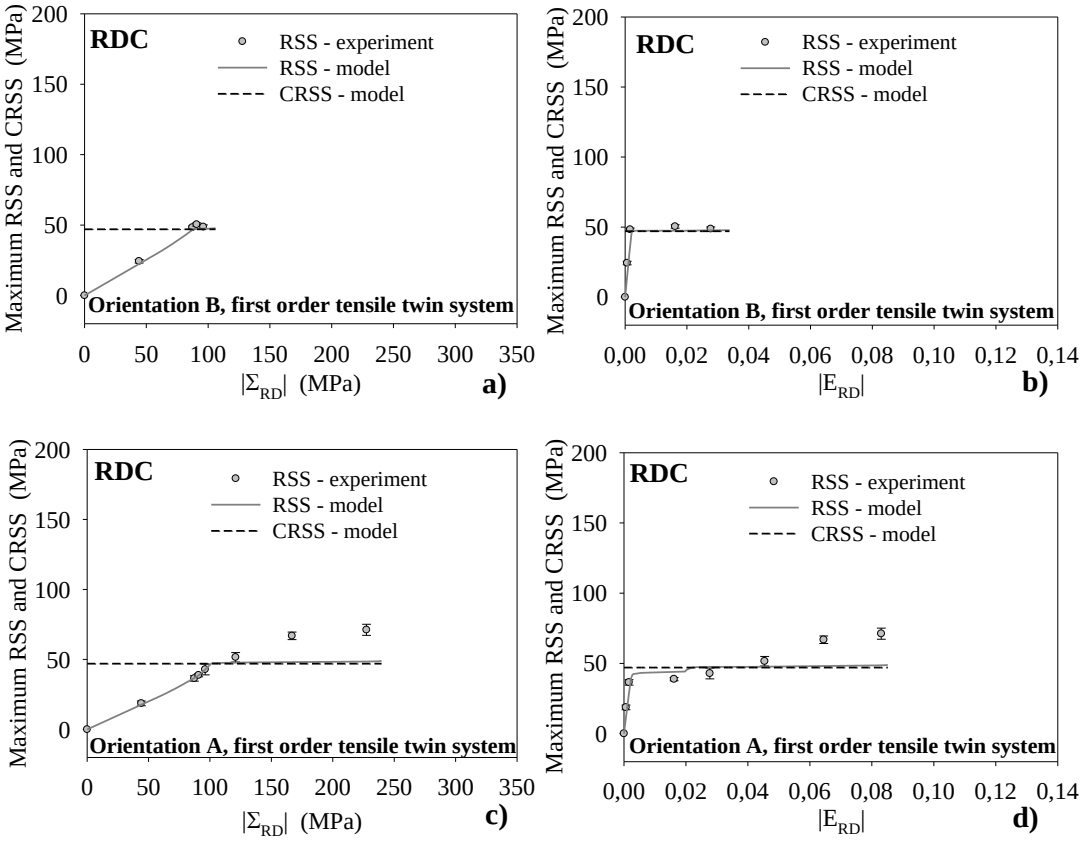

Fig. 7.10 Evolution of CRSS and maximum RSS on tensile twin system in B-oriented grains (a, b) and A-oriented grains (c, d), versus $|\Sigma_{RD}|$ and $|E_{RD}|$, during compression test in RD. Model predicted maximum RSS and CRSS are compared with experimental results. The modified EPSC model with threshold assumption was used.

Finally, the activation and hardening of the pyramidal systems <c+a> in the T-oriented grains (twins) during compression test in RD was studied (cf. Fig. 7.11). Because for these grains the load is nearly parallel to <c> axis, therefore the only systems which can be activated are the pyramidal systems <c+a> (similarly as for the A-oriented grains in compression test in ND). As shown in Appendix 4.c(Fig. A4.5) the other systems cannot be activated, because the CRSS is much higher than RSS. Fig. 7.11confirms that the values of the CRSS well agree with the change in the trend of the presented RSS evolutions for the pyramidal <c+a> systems. Therefore, it is shown that the CRSS values for these systems in twin grains are higher compared to those determined for A orientations in the initial sample (see Table 6.2). In the presented model, it was assumed that before transforming into a twin system, the slip systems undergo significant hardening during slips on the twin system. Then the transformation does not change the CRSS value for the created twin, which is initially equal to the CRSS in the parent. However, it is also possible that the hardening of the system occurs immediately after transformation and this assumption will lead to the same results obtained in the analysis of the experimental data compared to model prediction.

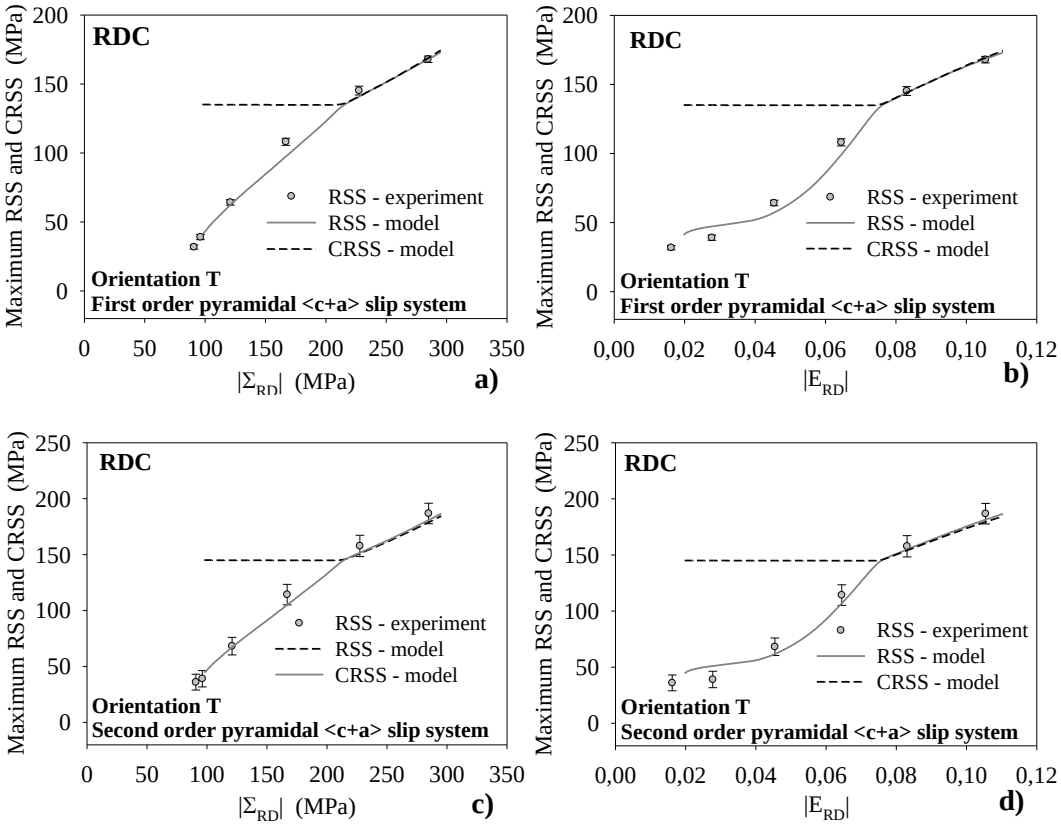

Fig. 7.11 Evolution of CRSS and maximum RSS on pyramidal systems <c+a> in T-oriented grains versus $|\Sigma_{RD}|$ and $|E_{RD}|$, during compression test in RD. Model predicted maximum RSS and CRSS are compared with experimental maximum RSS for the first order (a, b) and the second order (c, d) pyramidal systems <c+a> . The modified EPSC model with threshold assumption was used.

Summarizing this section it can be emphasised that the RSS values for different grain orientations are correctly predicted by the modified EPSC model in which experimentally determined CRSS (or values very close to the measured ones) are used. It was found that changes in RSS evolution trends are well correlated with the CRSS values used in the model for both the slip and twin systems, which confirms their proper choice. It is also observed that the CRSS evolution coincides with the evolution of RSS when the system is activated, that means that the other parameters of Voce law (describing hardening of the systems) are also correctly adjusted. The most difficult problem in the conducted analysis concerns hardening related to the twin systems. Two approaches were considered in this work. In the first one the transformation of the parent grains into twins occurring continuously, from the beginning and the twin grains obtain the same stress state and CRSS as the parent. In the second approach, the twin system is initially active, but it does not produce a twin, up to the given threshold. In this case the hardening of the parent grain occurs, and the twin grain created after threshold is much harder. Moreover, the stress at the parent grain relaxes due to plasticity occurring during twin slips before creation of the twin. The so called threshold assumption shows much better agreement with the experimental results compared to continuous assumption, and explains significant initial hardness of the twin grains, which play role of the reinforcement during advanced sample deformation. The threshold is physically explained by some energy barrier that must be overcome to form a twin and has also been used in previous works, e.g., [16]. In this model the twin is suddenly created when its relative volume calculated from equation (3.17) reaches 25%. The stress and the CRSS values for the created twin are the same as for the parent at this stage.

7.3. Evolution of texture and twin fraction

The mechanical behaviour of the grains was described in the previous sections. However, it should be emphasised that the macroscopic properties of the sample depend not only on the properties of grains but also on the interaction between them as well as on the number of grains having specific orientations (characterised by texture). As mentioned, the interaction between grains is well described by the modified EPSC model. Therefore, in this section the changes in texture (ODF) and volume fraction of twin grains will be described.

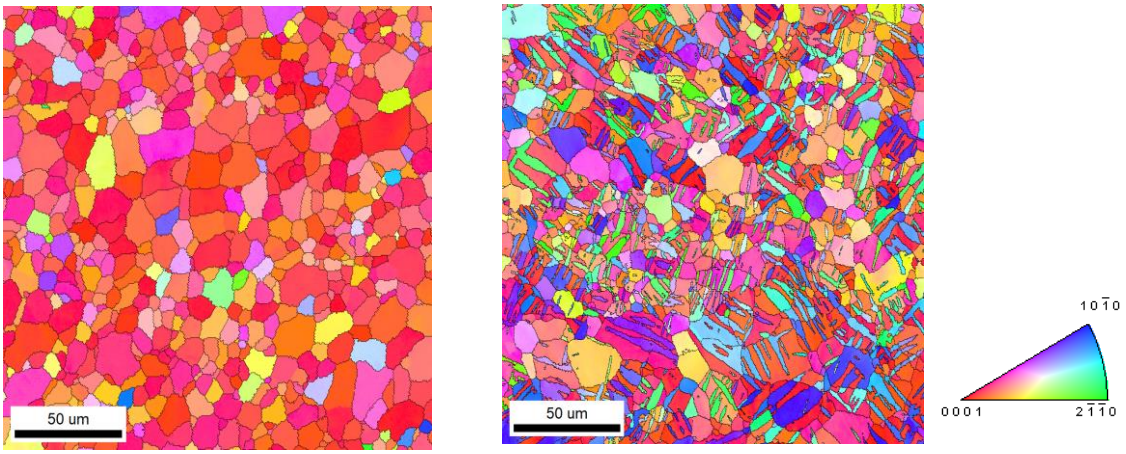

a) Non-deformed

b) $E_{ND} = -2\%$

c) $E_{RD} = 2\%$

d) $E_{RD} = -2\%$

e) $E_{RD} = -3\%$

f) $E_{RD} = -4\%$

Fig. 7.12 EBSD orientation maps obtained for a) initial sample, b) sample compressed to - 2% in ND, c) sample stretched to 2% in rolling direction; and samples compressed in rolling direction to: d) - 2% , e) - 3% and f) to - 4%.

The ODF was determined from EBSD for the samples subjected to different tests (see Fig. 7.12). The ODF for the initial undeformed sample is shown in Fig. 7.13 and the grain orientations that are tested in this work are marked. The changes of the texture are considered in model calculations, and they can be compared with the experimental ones.

In Fig. 7.14 the model and experimental ODFs after tensile test in RD up to $E_{RD} = 3\%$ are shown. It is observed that both model and experiment show an increase in ODF value for B orientation and a decrease for the A orientation. These changes do not influence significantly macroscopic properties of the sample as well as the properties of grains because insignificant difference was found in the behaviour of A and B – oriented grains (similar grain stresses were measured for A and B orientations during tensile test in RD, c.f. Fig. 6.7).

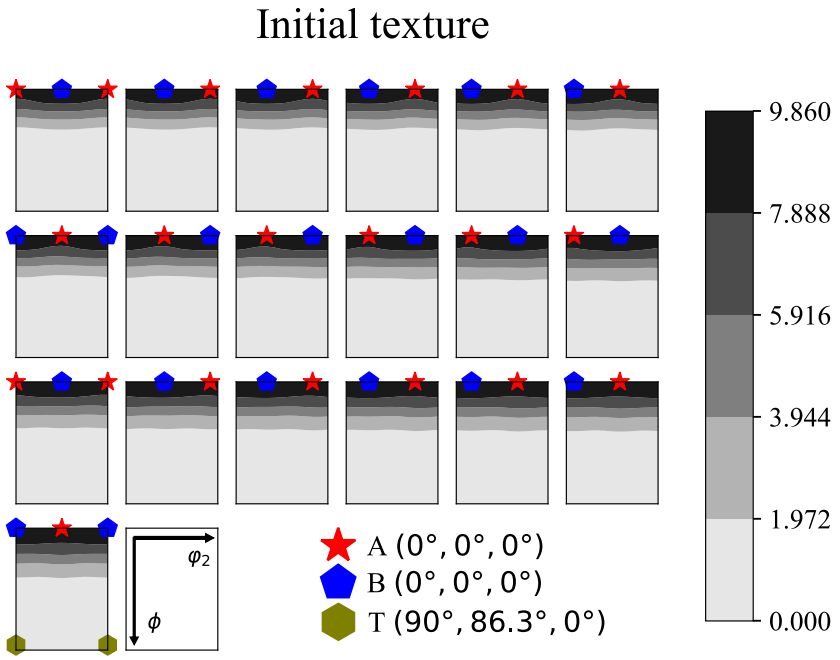

Fig. 7.13 Experimental texture measured using EBSD method for the initial sample. The sections through reduced Euler space ($0° \leq \varphi_1 \leq 90°$, $0° \leq \Phi \leq 90°$ and $0° \leq \varphi_2 \leq 60°$) along the φ_1 axis with step of 5º are presented. Moreover, the preferred orientations A and B, as well as the twin orientation (not present in the initial sample) are marked.

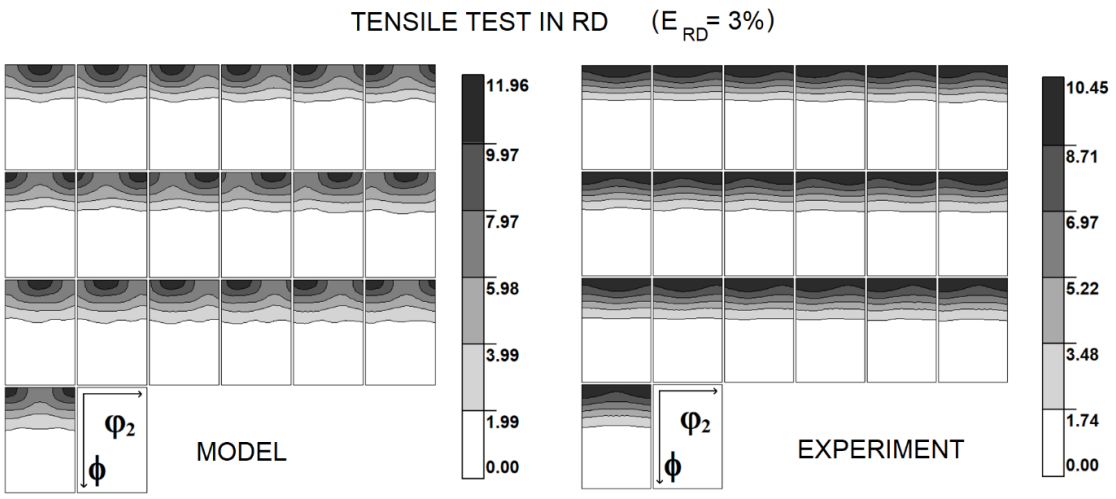

Fig. 7.14 Model predicted and experimental texture after tensile test in RD up to $E_{RD} = 3\%$. The modified EPSC model with either continuous or threshold assumption give practically the same results.

In the case of compression test in ND the changes in the ODF are not significant after deformations up to $|E_{ND}| = 4\%$ (c.f. Fig. 7.15). Both experiment and model show only small rearrangement of the preferred orientations which does not significantly change the mechanical properties of the sample and the individual grains.

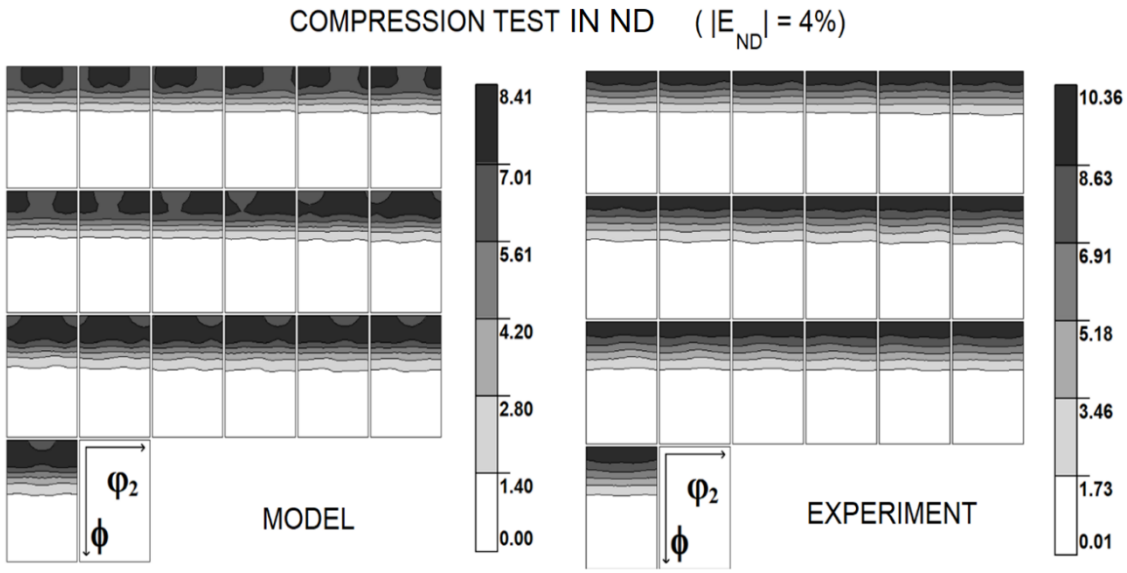

Fig. 7.15 Model predicted and experimental texture after compression test in ND up to $E_{ND} = 4\%$. The modified EPSC model with either continuous or threshold assumption give practically the same result.

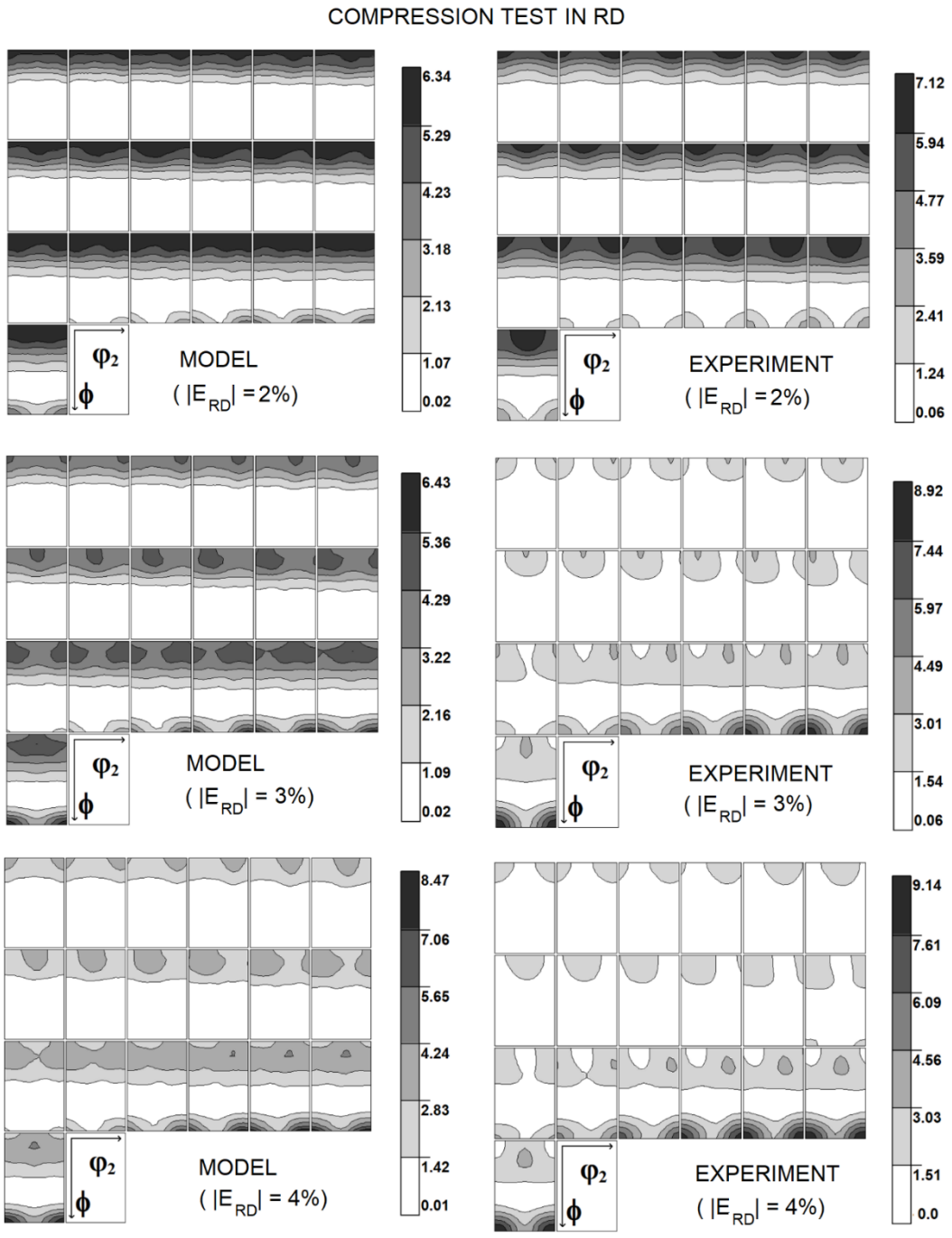

Fig. 7.16 Model predicted and experimental texture after compression test in RD up to $|E_{RD}| = 2\%, 3\%$ and 4%. The modified EPSC model with continuous assumption of twin process was used.

Certainly, the most important changes in ODF occur during compression test in the RD due to twinning process. As described above at first the softening of the sample is caused by twinning, but then the created twins reinforce the sample. The experimental ODFs for the deformations $|E_{RD}| = 2\%, 3\,\%$ and 4% are compared with the modified EPSC model with either continuous or threshold assumptions of twins creation in Fig. 7.16

and Fig. 7.17, respectively. It was found that model qualitatively predicts the texture evolution and better agreement between model and experimental result are obtained for the calculations with continuous assumptions. It is worth noting that experimental and model results show a significant increase of twins during the compression test performed in RD (compare Fig. 7.16 with Fig. 7.13, where the twin orientation is marked).

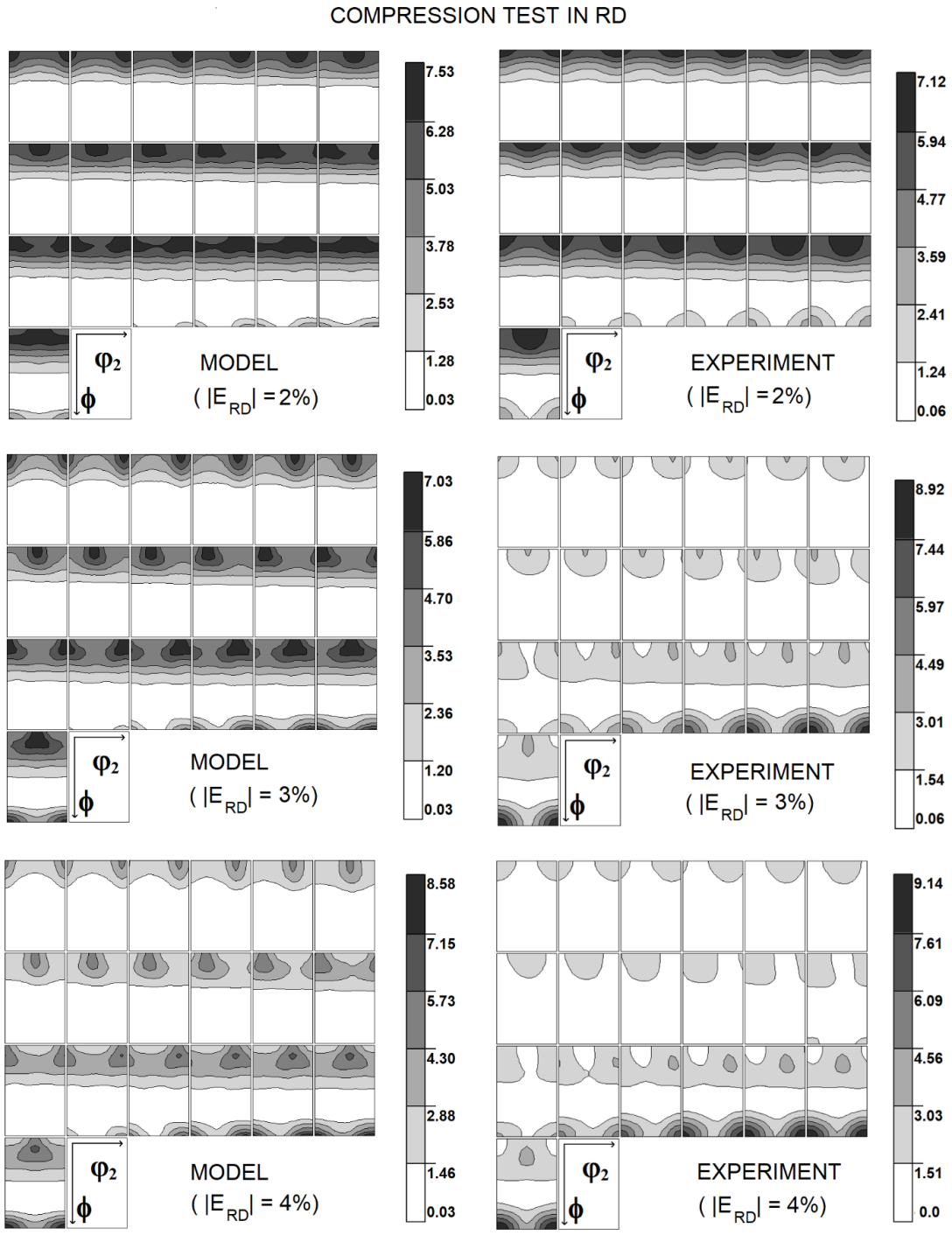

Fig. 7.17 Model predicted and experimental texture after compression test in RD up to $|E_{RD}| = 2\%, 3\%$ and 4%. The modified EPSC model with threshold assumption of twin process was used.

Knowing the evolution of texture the changes in the volume fraction of twins can be determined. This has been done using model, in which the number of twins is strictly determined. It was found that insignificant fraction of grains is created during tensile test in RD (Fig. 7.18a) and compression test in ND (Fig. 7.18b), and this result is confirmed by EBSD measurements in which the twins were not observed (see Fig. 7.12 and ODF presented in Fig. 7.15 and Fig. 7.16).

In the case of compression test in RD model calculation show significant increase of the twin fraction, what is confirmed by the EBSD measurements, as well as the increase in the intensity of the diffraction peak 002 measured in the RD (Fig. 7.18c, d). The EBSD estimation of the twin fraction is based on the measured ODF function for which the twin fraction was related to the ODF intensity integrated around the twin orientation within the cube with the edge of 27º (this volume in the Euler space is representative for the twins' fraction as it was checked by the model in which the number of twins is known). The evolution of measured relative peak intensity brings only qualitative information because it is calculated with respect to the final experimental results for which the twin fraction is unknown. Therefore, the presented function of relative peak intensity was calibrated using the values obtained from EBSD for $|\mathrm{E}_{RD}| = 2\%, 3\ \%$ and 4% . In spite of possible error in such calibration using only beginning of the plot, the trend of changes is presented, especially because of a good accordance with EBSD results and good agreement with the model results for deformations over $|\mathrm{E}_{RD}| = 8\%$ (c.f. Fig. 7.15c, d).

Analysing the results of the experiment performed during compression test in RD, it can be concluded that in the beginning of deformation $|\mathrm{E}_{RD}| < 2\%$ the volume of twins increases slowly, as seen in Fig. 7.18, and also proved by texture development shown in Fig. 7.16 and Fig. 7.17. Then in the range $|\mathrm{E}_{RD}| \approx 2\% - 6\%$ a very significant increase of twins' fraction occurs, especially at the beginning of this range. Finally, for $|\mathrm{E}_{RD}| > 6\%$, the saturation in twin fraction is seen. At the end of performed test ($|\mathrm{E}_{RD}| \approx 10{,}5\%$) the volume fraction reaches value of 70%.

The behaviour of the experimentally determined evolution of twin fraction confirms the delay in the twins formation in the beginning of deformation, which agrees with the threshold assumption, however, both model assumptions (continuous and threshold) underestimates the twin fraction during its significant increase in the range $|\mathrm{E}_{RD}| \approx 2\% - 6\%$. In this range slightly better prediction was obtained using continuous assumption. Finally, the model results approach the experimental points despite the assumption concerning twin formation.

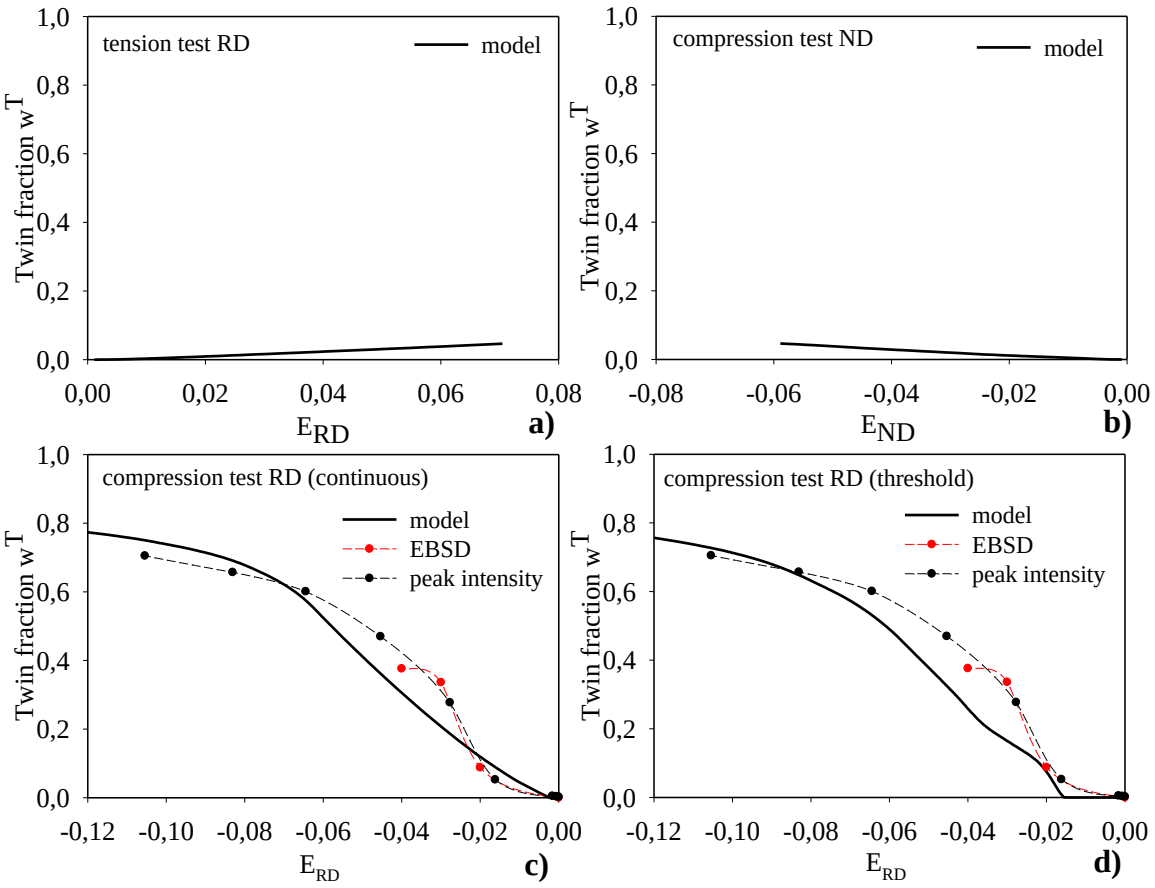

Fig. 7.18 Evolution of volume twin fraction during tensile test in RD (a), compression test in ND (b) and compression test in RD (c, d). In the case of the latter test the experimental results (from EBSD measurements and analysing intensity of diffraction peak 002 measured in the RD) are compared with the model results obtained using modified EPSC model with continuous assumption (c) and threshold assumption (d).

7.4. Compression tests performed in different directions

The last experiment confirming the values of CRSS and the work hardening parameters (from Voce law) was performed for the samples cut in this way that the compression load is inclined from the ND towards RD directions, as shown in Fig. 7.19

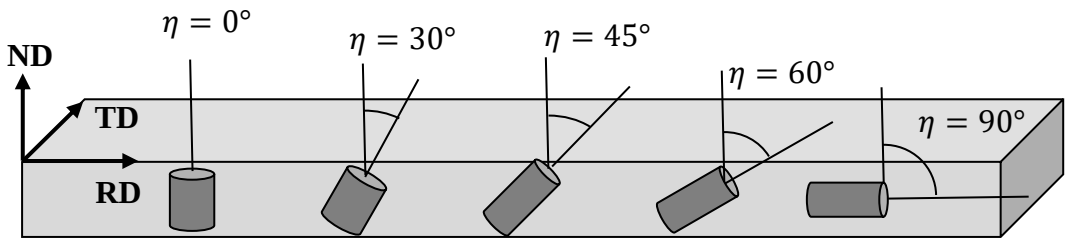

Fig. 7.19 Orientations of the samples with respect to the compressive force. The angle between direction of the load and ND is marked by η.

In Fig. 7.20 the macroscopic stress-strain plots obtained from the compression test conducted with the force direction deviated from the ND by angle η are compared with modified EPSC model predictions for the continuous and threshold assumption, respectively. The model parameters presented in Table 6.2 were used in the model calculations. Moreover, the macroscopic stresses after stabilization (partial relaxation at given strain) available from the NDC and RDC experiments for $\eta = 0°$ and $\eta = 90°$ are also shown for comparison. These stresses better correspond to the states predicted by the time-independent EPSC model. The comparison of the experimental and model results shows quite good agreement which is slightly better in the case of the continuous assumption. The interplay between activation of different slip and twin systems is clearly seen from the curves presented for different angles η. In addition, the evolutions of the calculated twin fraction are shown in Fig. 7.20.

When the compressive load is applied in ND ($\eta = 0°$) a high value of the yield stress and significant hardening of the sample is observed. As explained above, it is caused by a high value of CRSS and significant hardening of the pyramidal <c+a> slip systems, the only systems which can be activated for the majority of preferred grain orientations (i.e. orientations A and B). The model prediction much better agree with the stresses after sample stabilisation comparing to continuous loading of the sample with a strain rate of $5{,}8 \cdot 10^{-5}\mathrm{s}^{-1}$.

When the compressive load is inclined from ND by $\eta = 30°$ significant decrease in yield stress and work hardening is observed but the plateau characteristic for twin formation is not seen in the experimental stress-strain plot. This means that the softening of the sample is caused by the activation of other slip systems for most grains, from which the softest basal system is the most important. The twin fraction is still small, i.e. the twinning process is not the most significant during sample deformation. It is wort noting that the effect of slip systems activation is well predicted by model.

For greater values of inclination angle $\eta = 45°$ and $60°$ the formation of the plateau in the beginning of sample deformation is seen. Thus, the twinning begins play a significant role in plastic deformation. Indeed, the volume fraction of twins increases significantly. Again, the model predicts this effect correctly (however the effect of plateau is too large in the case of threshold assumption).

Finally, for the angle $\eta = 90°$ the compressive force is parallel to RD, and this case was widely described in this work. The plateau is observed, i.e. the twinning process is the most significant especially in the beginning of deformation, while when the fraction of twins significantly increases a significant hardening of the sample occurs. The model data better agree with the stabilised stress, after partial relaxation at given sample strain.

It can be concluded that the latter experiment fully confirms the CRSS values and hardening parameters found in this work. The mechanical tests performed for different angles η shows the competition between the basal and tensile twinning systems exhibiting low values of the CRSS, which was previously shown in [176] using acoustic emission method. Further neutron diffraction experiments for the samples compressed by a force inclined from ND are in preparation. Especially interesting is the experiment for $\eta = 30°$, in which a significant value of RSS will be generated on the based slip system in grains with preferred texture orientations. This experiment, performed using CGM, will provide more reasonable data for CRSS verification for the basal slip system compared to the data obtained from the NDC, RDC and RDT experiments.

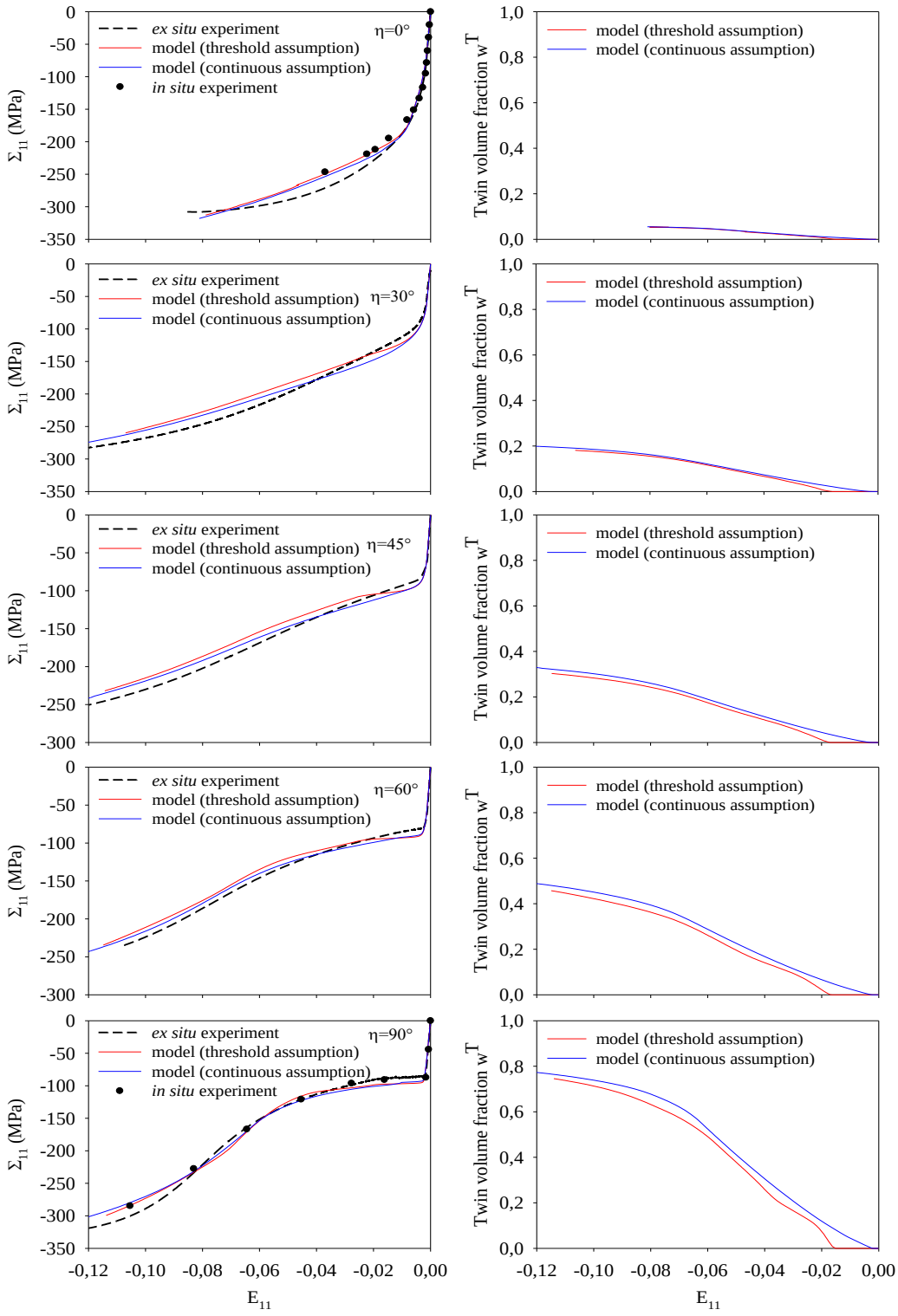

Fig. 7.20 Macroscopic stress-strain experimental curves compared with modified EPSC model results (with continuous or threshold assumption) for different inclination angles η. The macroscopic stresses after stabilization (partial relaxation at given strain) available from the *in situ* NDC and NTD experiments for $\eta = 0°$ and $\eta = 90°$ are also shown (points). The corresponding model predicted volume fraction of twins is shown on the right.

7.5. Summary

The experimentally determined CRSS values were used in the calculations using the EPSC model, in which the grains interactions were modified (towards Sachs model). The so obtained modified EPSC was applied to predict lattice strains and macroscopic stress-strain plots for three tests studied in this work. As a result, such a set of hardening parameters (Voce's laws) was found for which the predicted lattice strains and macroscopic stress-strain plots are closest to the experimental ones, simultaneously for all tests.

After determining all the parameters characterizing the slip systems and the twin system, the evolution of the model RSS was compared with those obtained directly from the experiment, obtaining an excellent agreement. Moreover, the experimental values of CRSS were confirmed by model calculations as values for which the model RSS exceeds the CRSS values. When the systems are active, the RSS and CRSS values show the same evolution, with RSS slightly exceeding CRSS. The model also showed which systems are not activated for the given grain orientation - this result confirms the assumptions made during the determination of the experimental CRSS values.

The evolution of the crystallographic texture and volume fraction of the twins was also studied comparing model and experimental data. The qualitative agreement between model and experimental texture was found. In the case of twin volume fraction model prediction is underestimated in the beginning of the compression test in RD and approaches to the experiment for increasing load. The model and experiment show insignificant twin fraction in the case of tensile test in RD and compression in ND.

The main problem of this work was the prediction of the twinning phenomena in model calculations. To do this, two assumptions concerning twin creation were proposed (continuous and threshold assumption), but in both cases the results are not well fitted to experiment. For example, the stress localisation at the twins is much better predicted by the model with threshold assumption, while the calculations with the continuous assumption show the texture and twin fraction evolutions closest to the experiment.

Finally, the experiment confirming the determined parameters characterising activation and hardening of slip systems and twin system was performed. In this experiment the compressive load was applied in the direction inclined from ND towards RD and macroscopic stress-strain plots were measured. Then the model calculations in which the set of CRSS and Voce law parameters were done, and the results were compared with experiment. A very good agreement between measured and calculated macroscopic stress-strains curves confirm the correctness of the parameters used in models. Moreover, the changes in evolution of these plots was explained by the activation of different slip systems and finally by twinning process.

8. General conclusions and summary

The main purpose of this work was to develop experimental methods for investigating the micromechanical properties of polycrystalline materials, which enable direct determination of stresses for groups of grains and grains belonging to different phases. The proposed methodology is based on neutron measurements performed for a large representative volume in the sample, and the analysis of the obtained results uses the selective feature of diffraction method. The experimental methods developed in the study showed that the components of the stress tensor can be determined for groups of grains when the lattice strains are determined in many directions. The TOF technique used in this work is particularly advantageous because it enables measurements of lattice deformations with many *hkl* reflections for each direction in which the measurement is performed.

Having developed experimental methods, the measurements were carried out *in situ* for various loads applied to the samples. The experimental studies concerned the behaviour of polycrystalline grains during elastic-plastic deformation, in particular such phenomena as slips on crystallographic planes, the phenomenon of twinning, stress localization in individual grains and changes in the crystallographic texture during plastic deformation. The developed methods were used to determine the micromechanical properties of grains having different orientations in hot-rolled AZ31 magnesium alloy and the evolution of phase stresses (for both constituents) in the Al/SiC_p composite.

In the first part of the work, *in situ* diffraction measurements were performed for the Al/SiC_p composite subjected to thermal treatment and compression test. The source of the residual stresses in individual phases in the cooled material was explained by a significant difference in the thermal expansion coefficients of the components. SiC_p reinforcement, having nearly nine times lower coefficient of thermal expansion compared to aluminium, shrinks much slower than the aluminium matrix in which it is contained. This causes the accumulation of high compressive hydrostatic stresses in the SiC_p reinforcement. Thermally induced phase stresses were correctly predicted by the thermomechanical self-consistent model (TMSC).

Then, the evolution of mean phase stresses caused by plastic strain (deviatoric character) and relaxation of thermal stresses (hydrostatic character) during the compression test were determined. These studies were aimed at determining the stresses in both phases of the composite, as well as explaining the phenomenon of thermally induced stress relaxation using the newly developed thermomechanical self-consistent (DTMSC) model. This model takes into account the stresses resulting from the thermal mismatch between the SiC particle and the plastically deformed soft matrix. The softening of the matrix leads to a relaxation of thermally induced phase stresses which are in good agreement with that measured experimentally. It should be emphasized that the relaxation of thermal stresses can also be caused by such phenomena as microdamage processes causing the decoupling of SiC particles from the aluminum alloy matrix. However, these effects cannot be predicted using continuum mechanics models such as those used in this work.

The second tested sample was hot rolled AZ31 magnesium alloy. It is a material which, despite its almost isotropic elastic properties, shows a strongly anisotropic response to an applied external load caused by a significant crystallographic texture. In the research carried out on this sample, an attempt was made to explain this phenomenon by examining the nature of the plastic response of polycrystalline grains to loads applied in two different directions. Diffraction measurements were carried out *in situ* during the compression of the sample using the crystallite group (CGM) methods to determine the stresses for selected groups of crystallites.

Thanks to the stress evolution measurements for different grain groups, it was possible to determine the stress distribution between crystallites having different lattice orientation with respect to the applied load. There are four characteristic groups of grains: hard, intermediate, soft and those for which twinning phenomenon occurs. Hard grains are those for which the plastic process takes place much later, by activation of the pyramidal slip systems <c+a> showing the highest CRSS value, while the other slips and twinning cannot be activated due to the nearly zero and negative RSS values. Soft grains are those grains in which the basal slip with the lowest CRSS value is activated, while the intermediate grains are those for which the prismatic <a> and / or the pyramidal <a> system is activated, and the other slips and twinning remain inactive. In the fourth group of grains, twinning phenomena can occur, leading to saturation of localized stress regardless of the slip systems activity.

The partitioning of stresses between the grains plays a key role in the macroscopic response of the sample depending on the combination of the type and direction of the applied load with a sharp crystallographic texture. Due to the different types (compressive or tensile) and orientations of the applied load, most grains with the preferred texture orientations exhibit very different plastic behaviour leading to macroscopic anisotropy of the sample. As shown in this work, the greatest macroscopic stresses can be achieved when for most crystallites the applied compressive force is parallel to the c-axis, i.e. when the

load is parallel to ND. Due to such geometrical relationships, the value of RSS greater than zero can be achieved only for pyramidal slip systems <c+a>, what can be easily calculated from Schmid's law. Therefore the majority of the grains is hard and the sample is hard as well. Different situations take place during the tensile test in RD, when for the preferred orientations the twinning systems remain inactive (RSS is less than zero), the basic system is also inactive (RSS is equal to zero), and the prismatic <a> or/and pyramidal <a> systems activate for majority of the grains at an intermediate level of the applied load (much lower than when the compressive load was parallel to ND). Due to the low value of the stress applied to the sample, also the RSS values on the <c+a> slip systems are too low to activate them. This is an intermediate sample response. In the third experiment (compression in RD) the most complex sample response was observed, i.e. for a small value of the applied load, the twinning process occurred for the preferred texture orientations leading to saturation of the macroscopic stress-strain curve, i.e. plastic deformation took place without visible hardening. However, as most of the grains jumped to the twin orientations, significant sample hardening occurred as the twin orientation exhibited a c-axis parallel to the tensile load applied along RD. This means that the orientations of the twin are hard, and the twins can carry the greatest load compared to other grains.

A very important achievement of this work is the determination of the values of resolved shear stresses (RSS) and critical distributed shear stresses (CRSS) for various slip systems and twinning, directly from the experiment. For this purpose, no model assumptions were used, and the CRSS values were determined directly on the basis of the analysed trends in the evolution of experimental RSS as a function of macrostress and/or macrostrain values. The values determined from the experiment were obtained with their uncertainties, excluding the CRSS for the <c+a> pyramidal systems for the twin orientation (in the latter case, due to an insufficient number of measuring points, the uncertainty was estimated only roughly). It should be emphasized that the uncertainties of the determined CRSS values were calculated for the first time. In previous works, uncertainty analysis was not possible when CRSS were estimated by comparing the evolution of the model strains with those measured in two directions with respect to the sample. The second advantage of the new methodology presented in this paper is that the results are unambiguous and do not depend on the assumptions used in the model. Moreover, the experimentally determined CRSS can be used to validate the crystallographic model.

In order to check the agreement of the EPSC model with the obtained experimental results, the CRSS parameters were entered into the calculations as input data. After adjusting the model to the experimental data by changing its other parameters (hardening parameters used in Voce's law), full qualitative agreement was achieved in terms of the evolution of lattice strains, stresses localized at particular grains and macroscopic stresses. It should be emphasized that to achieve a very good agreement between the three experiments and the corresponding model calculations, the assumption of the

self-consistent model was slightly modified by shifting the type of intergranular interaction towards the Sachs assumption. It has been found that during plastic deformation the total incompatibility strains are about 20% greater than those predicted by the self-consistent approach, i.e. weaker intergranular interaction takes place comparing to self-consistent Eshelby type model. In addition, two different approximations concerning the formation of twins were tested, i.e. the so-called "threshold assumption" and "continuous assumption ". It has been found that the localization of stress in “newborn” twins is slightly better predicted using the threshold assumption, while the twins fraction and texture evolution are better estimated using the continuous assumption. It is worth noting that the twins phenomenon and the stress values of the newly formed twins have not been accurately predicted using the model used in this work. Therefore other methods for simulation of twins formation process should be tested using the experimental results obtained in this work.

Finally, the experimental CRSS values and a set of other model parameters (determined on the basis of three conducted experiments) were used to predict the macroscopic behaviour of the sample for a compressive load tilted from the ND by a given angle. The model results were then compared with the experimental results and a very good agreement was obtained. This is a confirmation that the parameters describing the plastic deformation of the tested material AZ31 are correctly determined. Further neutron diffraction experiments with a compressive load tilted from ND are in preparation. These measurements, using the crystallite group (CGM) method, will show the stress partitioning between grains for the sample in which the basal slip system is activated for the majority of crystallites. This will allow us to determine the CRSS value for the basal system more unambiguously than in the experiments carried out in this paper, in which this system was activated for non-preferred texture orientations.

Appendix 1. Determination of the interplanar spacings for reflections absent in the initial sample

In the study of AZ31 alloy the lattice strains were determined on the basis of equation (6.1) in which the difference between interplanar spacing in the sample under load ($< d >_{hkl}$) and these in initial sample were calculated ($< d >^{0}_{hkl}$). This minimises the possible systematic errors in peak position determining. However, in the case of the twin grains arising during compression in RD the grains with orientations corresponding to the twins were not present in the initial sample, therefore the necessary interplanar spacings $< d >^{0}_{hkl}$ were not available. This especially concerns the absence of diffraction peaks for 002 and 004 reflections in the detector L2 measuring the interplanar spacings in the direction of the load applied along RD. Thus, the values of the $< d >^{0,L2}_{002}$ and $< d >^{0,L2}_{004}$ were found using interpolation method in which the available interplanar spacings $< d >^{0,L2}_{hkl}$ and $< d >^{0,L5}_{hkl}$ measured respectively by L2 and L5 detectors were used. To do this the ratios of interplanar spacings for the corresponding reflections hkl were calculated (except of reflections 002 and 004):

$$k_{hkl} = \frac{<d>^{0,L2}_{hkl}}{<d>^{0,L5}_{hkl}}. \qquad \text{(A1.1)}$$

Then, the linear regression was used to fit the straight lines assuming dependence:

$$k_{hkl} = A < d >^{0,L5}_{hkl} + B \qquad \text{(A1.2)}$$

The unknown k_{002} and k_{004} values were found from the fitted lines on the basis of measured $< d >^{0,L5}_{002}$ and $< d >^{0,L5}_{004}$ values as shown in Fig. A1.1. Finally the values :

$$< d >^{0,L2}_{002} = k_{002} < d >^{0,L5}_{002} \text{ and } < d >^{0,L2}_{004} = k_{004} < d >^{0,L5}_{004} \qquad \text{(A1.3)}$$

were found. The uncertainties of the determined interplanar spacings were calculated from the propagation of linear regression uncertainties. The same procedure was applied for the data obtained before ($\omega = 0°$) and after sample rotation about sample axis ($\omega = 90°$) (see Fig. A1.1), and the results are given in Table A1.1

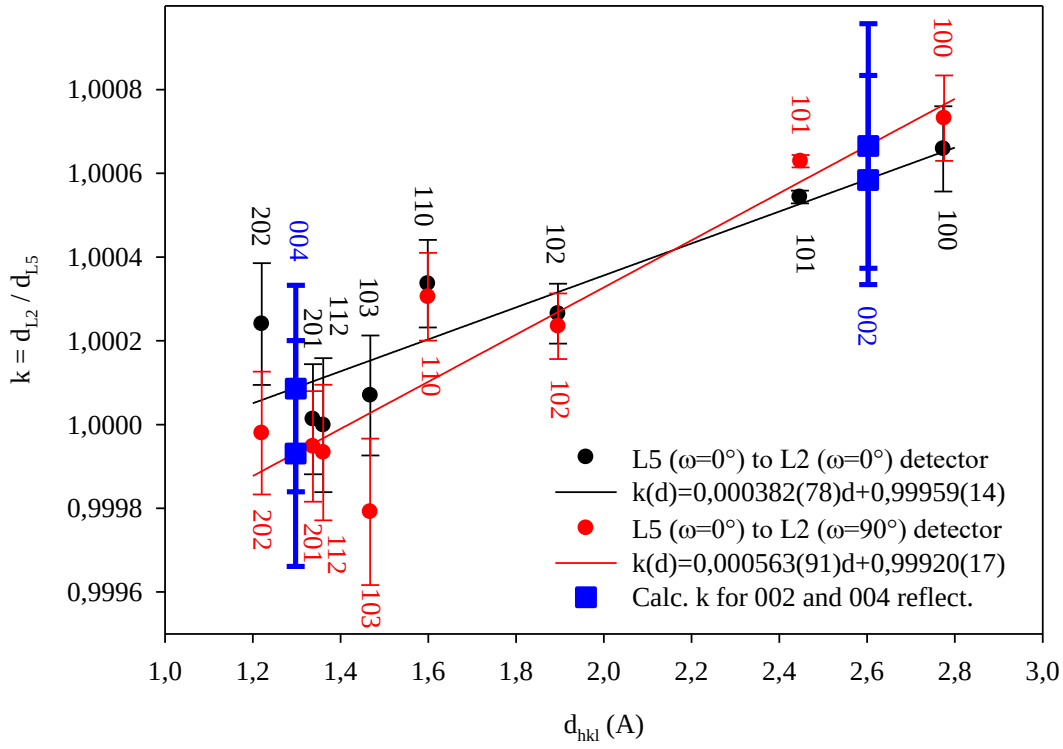

Fig. A1.1 The dependences of k_{hkl} vs. $< d >_{hkl}^{0,L5}$ fitted by straight lines on the basis of which the k_{002} and k_{004} values were interpolated for measured $< d >_{002}^{0,L5}$ and $< d >_{004}^{0,L5}$ values.

Table A1.1 Determined $< d >_{002}^{0,L2}$ and $< d >_{004}^{0,L2}$ interplanar spacings for sample rotation angle $\omega = 0°$ and $\omega = 90°$.

Reflection	$< d >_{hkl}^{0,L2}$ (Å)	$u(< d >_{hkl}^{0,L2})$ (Å)
002 ($\omega = 0°$)	2,60232	0,00065
004 ($\omega = 0°$)	1,29791	0,00032
002 ($\omega = 90°$)	2,60253	0,00076
004 ($\omega = 90°$)	1,29771	0,00035

Appendix 2. Sets of reflections used for stress determination by using crystallite group method

Table A2.1 Examined poles for crystal orientations A - G' of AZ31 magnesium during normal direction compression (NDC), rolling direction tensile (RDT) and rolling direction compression (RDC) tests. The orientations of the scattering vector (ψ and φ) used in the measurement are given. In the case of EPSILON-MSD, the orientations of the scattering vector closest to the selected poles are shown.

No.	$(hkil)$	ψ [°]	φ [°]	No.	$(hkil)$	ψ [°]	φ [°]
Orientation A, Experiment: RDT				**Orientation A, Experiment: RDC**			
1	$1\bar{2}10$	0,00	0,00	1	$1\bar{2}10$	0,00	0,00
2	$1\bar{1}00$	30,00	0,00	2	$10\bar{1}0$	90,00	0,00
3	$2\bar{1}\bar{1}0$	60,00	0,00	3	$\bar{1}010$	90,00	0,00
4	$10\bar{1}0$	90,00	0,00	4	$11\bar{2}2$	60,00	215,00
5	0001	90,00	90,00	5	$2\bar{1}\bar{1}2$	60,00	35,00
6	$1\bar{1}03$	62,70	72,70	6	0001	90,00	90,00
7	$10\bar{1}3$	90,00	58,00	7	$000\bar{1}$	90,00	270,00
8	$10\bar{1}1$	90,00	28,00	**Orientation B, Experiment: RDC**			
Orientation B, Experiment: RDT				1	$20\bar{2}\bar{1}$	14,81	97,47
1	$10\bar{1}0$	0,00	0,00	2	$20\bar{2}1$	14,81	262,53
2	$11\bar{2}0$	30,00	0,00	3	$10\bar{1}0$	0,00	0,00
3	$01\bar{1}0$	60,00	0,00	4	$1\bar{2}10$	90,00	0,00
4	$\bar{1}2\bar{1}0$	90,00	0,00	5	$\bar{1}2\bar{1}0$	90,00	180,00
5	0001	90,00	90,00	6	$1\bar{1}02$	71,30	136,00
6	$01\bar{1}3$	74,60	61,60	7	$1\bar{1}01$	60,00	215,00
7	$10\bar{1}3$	58,00	90,00	8	$1\bar{1}0\bar{2}$	71,30	226,00
Orientation C, Experiment: RDT				9	$0\bar{1}12$	71,30	316,00
1	$1\bar{2}12$	0,00	0,00	10	$0\bar{1}1\bar{2}$	71,30	46,00
2	$01\bar{1}3$	88,47	74,61	11	$0\bar{1}11$	60,00	35,00
3	0001	60,00	90,00	12	0001	90,00	90,00
4	$20\bar{2}1$	82,60	13,00	13	$000\bar{1}$	90,00	270,00
5	$10\bar{1}1$	76,36	24,77	**Orientation D, Experiment: RDC**			
Orientation D, Experiment: RDT				1	$10\bar{1}1$	0,00	0,00
1	$\bar{1}013$	90,00	90,00	2	$10\bar{1}2$	14,80	97,00
2	$10\bar{1}1$	0,00	0,00	3	$0\bar{1}1\bar{3}$	47,20	116,00

Orientation A, Experiment: NDC			
1	0001	0,00	0,00
2	$1\bar{2}10$	90,00	90,00
3	$1\bar{1}02$	46,00	125,00
4	$\bar{1}010$	90,00	180,00
5	$0\bar{1}1\bar{2}$	46,00	244,08
6	$\bar{1}2\bar{1}0$	90,00	270,00
7	$1\bar{1}0\bar{2}$	46,00	295,92
8	$10\bar{1}0$	90,00	0,00
9	$0\bar{1}12$	46,00	64,08
Orientation B, Experiment: NDC			
1	0001	0,00	0,00
2	$1\bar{2}10$	90,00	0,00
3	$1\bar{1}02$	46,00	35,00
4	$\bar{1}010$	90,00	90,00
5	$0\bar{1}1\bar{2}$	46,00	154,08
6	$\bar{1}2\bar{1}0$	90,00	180,00
7	$1\bar{1}0\bar{2}$	46,00	205,92
8	$10\bar{1}0$	90,00	270,00
9	$0\bar{1}12$	46,00	334,08
Orientation D, Experiment: NDC			
1	$1\bar{1}0\bar{2}$	14,81	262,53
2	$1\bar{1}03$	0,00	0,00
3	$10\bar{1}3$	60,00	125,26
4	$2\bar{1}\bar{1}0$	60,00	305,26
5	$0\bar{1}13$	60,00	55,00
6	$1\bar{2}10$	60,00	235,00
7	$1\bar{1}01$	90,00	270,00
8	$1\bar{1}01$	90,00	90,00
9	$11\bar{2}0$	90,00	0,00
10	$\bar{1}\bar{1}20$	90,00	180,00
Orientation F, Experiment: NDC			
1	$2\bar{2}0\bar{1}$	14,81	262,53
2	$1\bar{1}0\bar{1}$	0,00	0,00
3	$1\bar{1}0\bar{2}$	14,81	97,47
4	$10\bar{1}\bar{1}$	47,22	25,92
4	$0\bar{1}14$	47,20	116,00
5	$0\bar{1}13$	60,00	125,00
6	$10\bar{1}3$	90,00	270,00
7	$1\bar{1}03$	47,20	63,00
8	$1\bar{1}04$	47,20	63,00
9	$10\bar{1}3$	90,00	270,00
10	$10\bar{1}3$	90,00	90,00
Orientation F, Experiment: RDC			
1	$10\bar{1}3$	0,00	0,00
2	$10\bar{1}2$	14,81	262,53
3	$1\bar{1}04$	47,20	116,00
4	$1\bar{1}0\bar{3}$	60,00	125,00
5	$1\bar{2}10$	90,00	180,00
6	$10\bar{1}\bar{1}$	90,00	270,00
7	$\bar{1}2\bar{1}0$	90,00	0,00
Orientation G', Experiment: RDC			
1	$10\bar{1}2$	0,00	0,00
2	$10\bar{1}1$	14,81	262,53
3	$10\bar{1}3$	14,81	97,00
4	$10\bar{1}4$	14,81	97,00
5	$1\bar{1}0\bar{3}$	60,00	125,00
6	$1\bar{1}0\bar{4}$	60,00	125,00
7	$10\bar{1}\bar{2}$	90,00	270,00
8	$0\bar{1}13$	60,00	55,00
9	$0\bar{1}14$	60,00	55,00
10	$10\bar{1}\bar{2}$	90,00	90,00
Orientation T, Experiment: RDC			
1	0004	0,00	0,00
2	$11\bar{2}2$	125,00	60
3	$1\bar{2}10$	0,00	90,00
4	0002	0,00	0,00
5	$2\bar{2}0\bar{2}$	35,00	60,00
6	$1\bar{1}0\bar{1}$	35,00	60,00
7	$10\bar{1}0$	270,00	90,00
8	$\bar{1}\bar{1}22$	305,00	60,00
9	$\bar{1}2\bar{1}0$	180,00	90,00

5	$0\bar{1}1\bar{1}$	47,22	154,00	10	$2\bar{2}0\bar{2}$	215,00	60,00
6	$10\bar{1}1$	71,29	315,81	11	$1\bar{1}0\bar{1}$	215,00	60,00
7	$0\bar{1}11$	71,29	225,81	12	$\bar{1}010$	90,00	90,00
8	$11\bar{2}0$	90,00	0,00				
9	$\bar{1}\bar{1}20$	90,00	180,00				
Orientation G, Experiment: NDC							
1	$1\bar{1}0\bar{2}$	0,00	0,00				
2	$1\bar{1}0\bar{1}$	14,80	277,47				
3	$11\bar{2}0$	90,00	0,00				
4	$\bar{1}\bar{1}20$	90,00	180,00				
5	$10\bar{1}2$	71,29	135,81				
6	$0\bar{1}12$	71,00	44,00				
7	$10\bar{1}3$	60,00	125,26				
8	$1\bar{2}12$	88,10	255,31				

Appendix 3. Grain stresses predicted for RDC experiment by modified EPSC model with continuous assumption

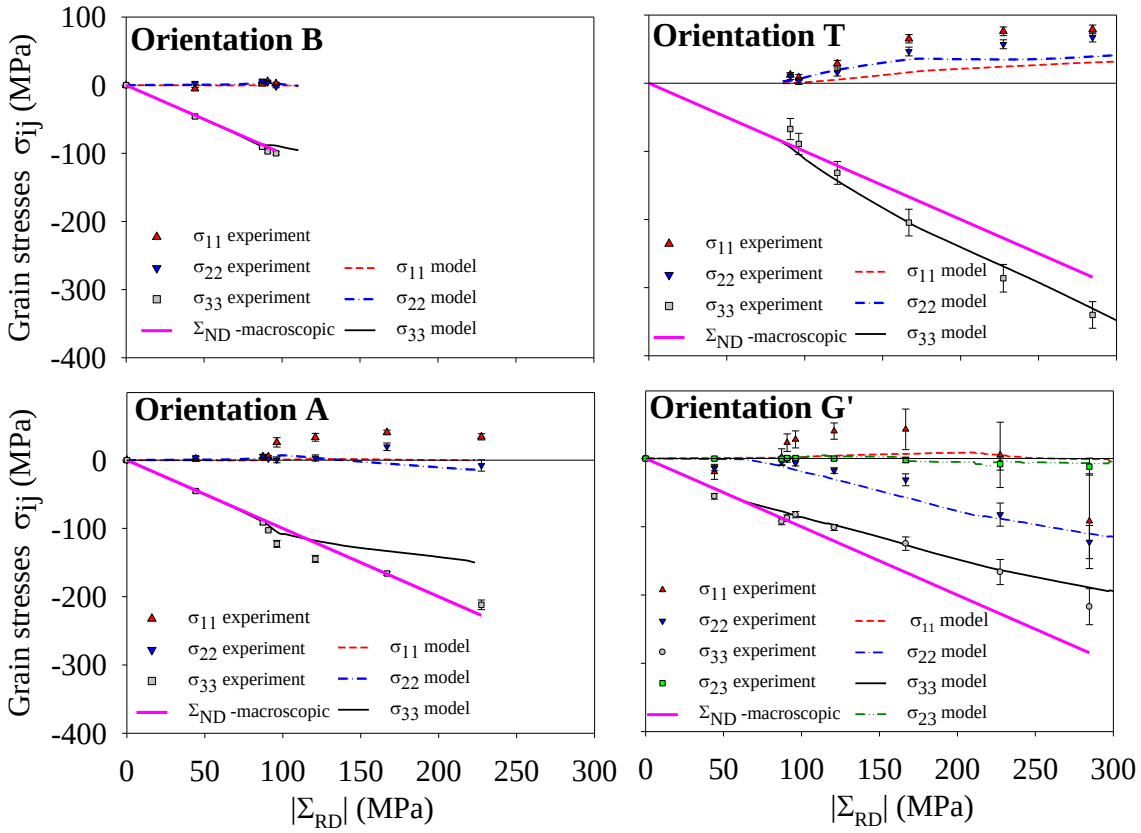

Fig. A3.1 Evolution of the grain stresses for orientations A,B,T and G' versus macrostress $|\Sigma_{RD}|$ during compression test performed along RD compared with model using continuous assumption. The grains having B orientation are transformed to twins (T-orientation) at approximately $|\Sigma_{RD}|$=90 MPa. The evolution of macroscopic stress $|\Sigma_{RD}|$ is drawn with a solid orange line.

Appendix 4. Comparison of experimental and model evolutions of RSS and CRSS for inactive systems.

In this appendix the evolution of RSS (experimental and predicted) and CRSS versus $|\Sigma_{ND}|$ or $|E_{ND}|$ are presented for slip and twinning systems, which are not activated for given grain orientations in three studied deformation modes. In all figures model predicted maximum RSS and CRSS are compared with experimental maximum RSS.

a. NDC experiment

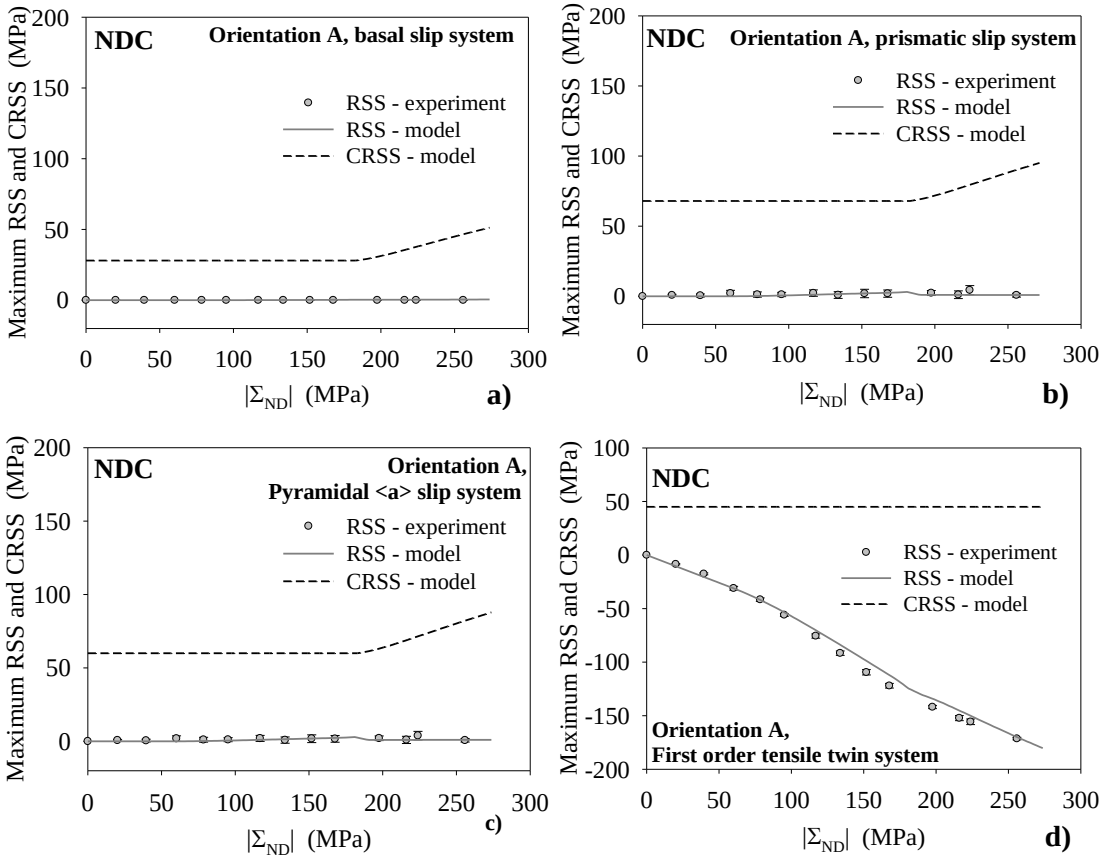

Fig. A4.1 Evolution of CRSS and maximum RSS on basal (a), prismatic (b), pyramidal <a> (c) slip systems and first order tensile twin system (d) in A-oriented grains versus $|\Sigma_{ND}|$, during compression test in ND.

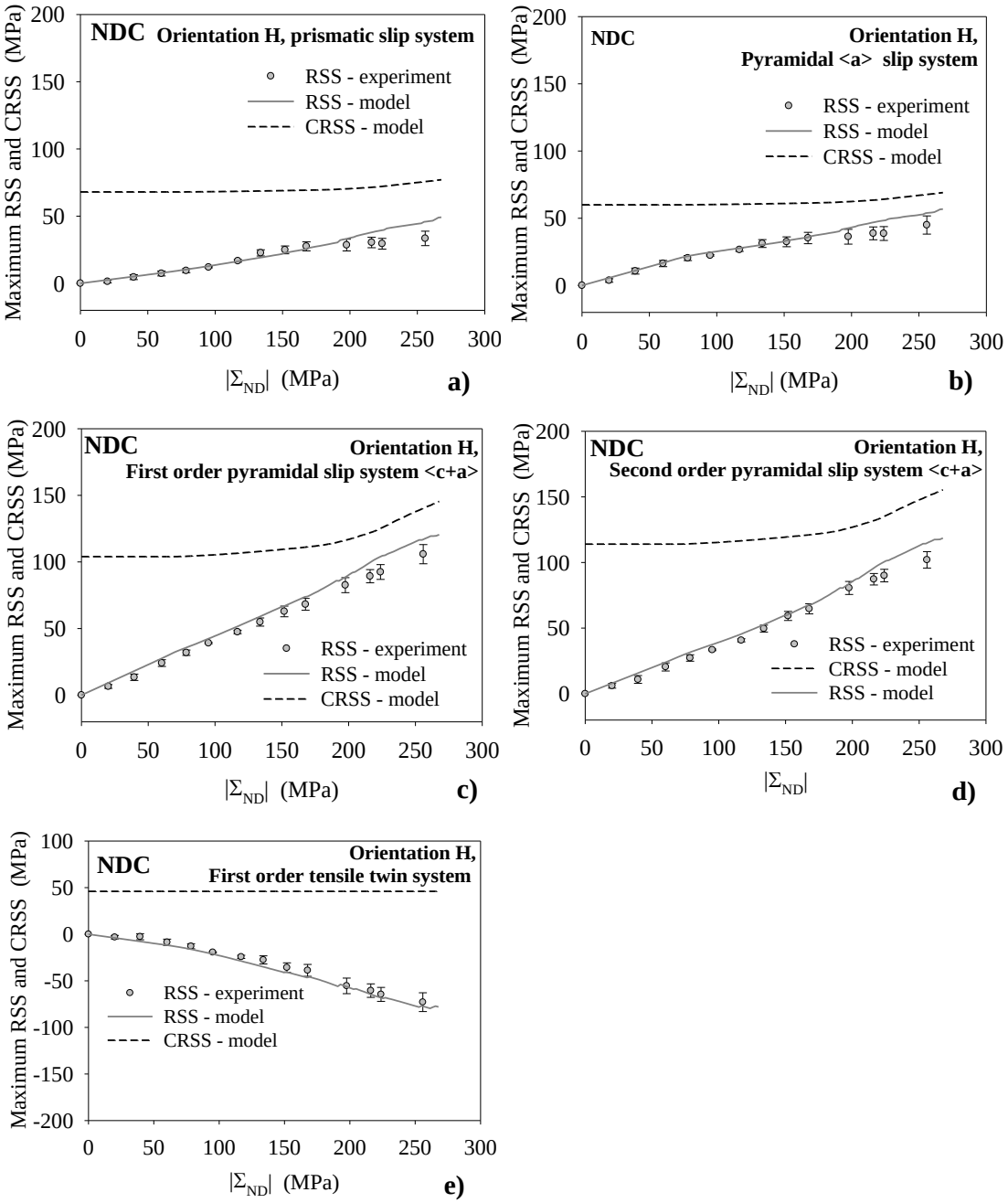

Fig. A4.2 Evolution of CRSS and maximum RSS on prismatic (a), pyramidal <a> (b), first (c) and second (d) order pyramidal <c+a> slip systems and first order tensile twin system (e) in soft grains versus $|\Sigma_{ND}|$, during compression test in ND. Model predicted maximum RSS and CRSS are compared with experimental maximum RSS.

b. RDT experiment

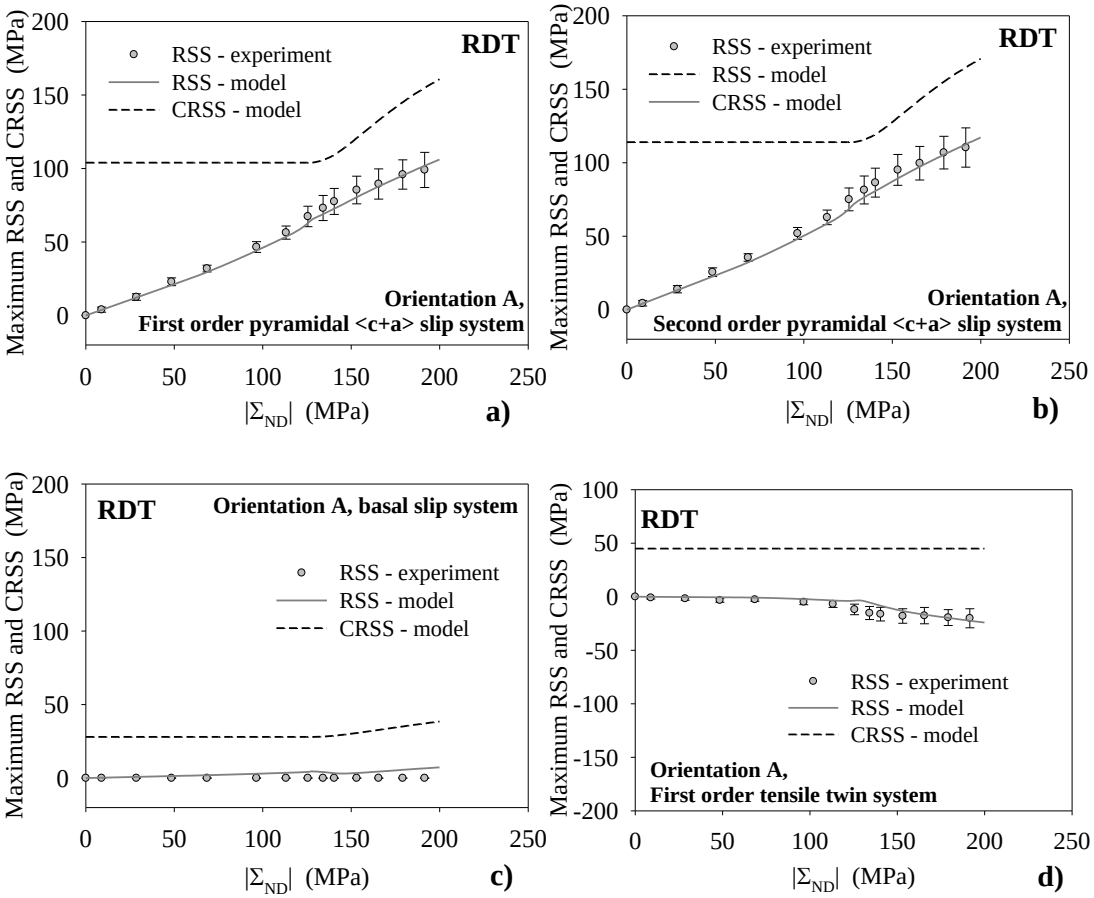

Fig. A4.3 Evolution of CRSS and maximum RSS on the fist (a), second (b) pyramidal <c+a>, basal (c) slip systems and first order tensile twin system (d) in A-oriented grains versus $|\Sigma_{RD}|$, during tensile test in RD.

c. RDC experiment

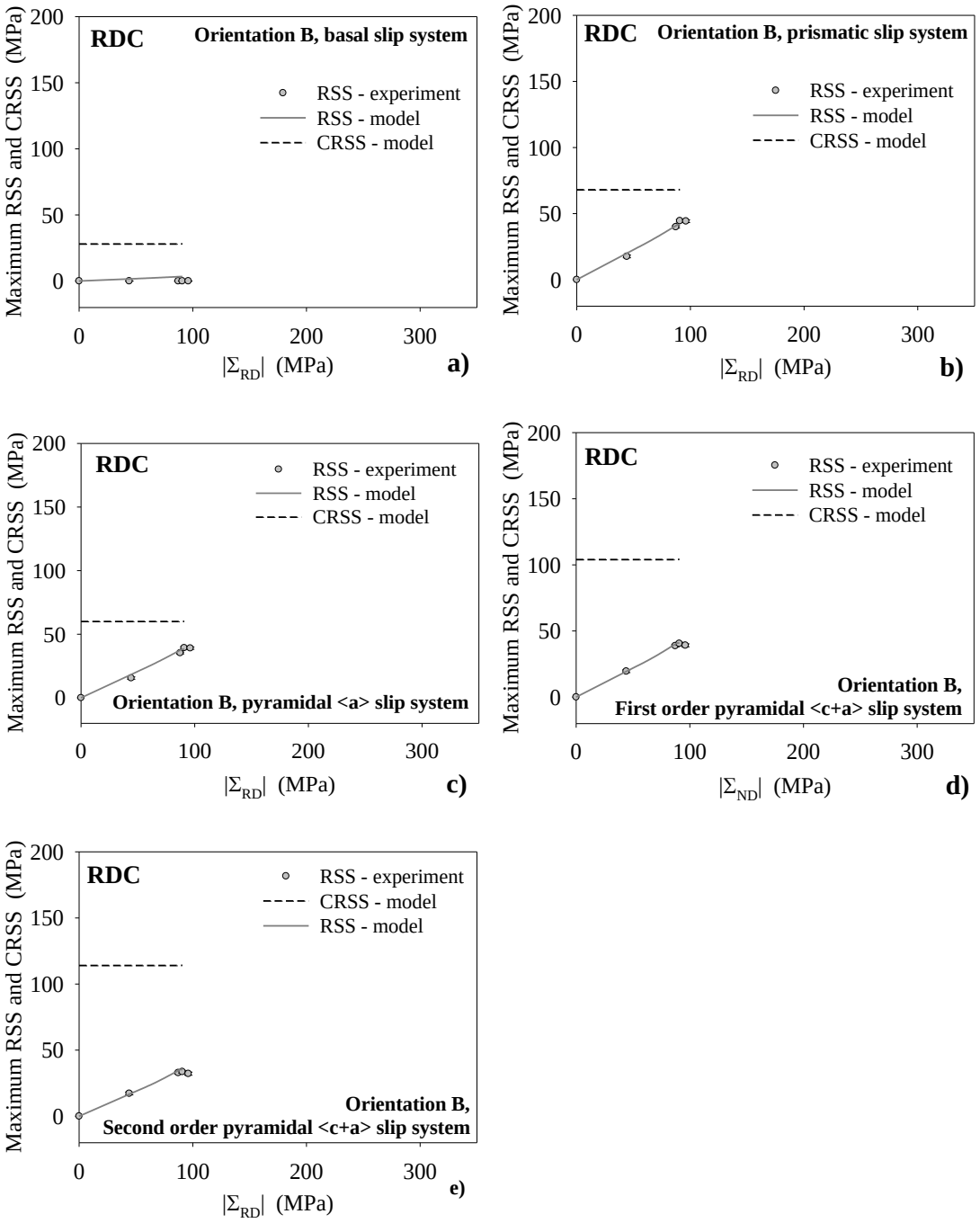

Fig. A4.4 Evolution of CRSS and maximum RSS on basal (a), prismatic (b), pyramidal <a> (c), first order (d) and second order (e) pyramidal <c+a> slip systems in B-oriented grains versus $|\Sigma_{RD}|$, during compression test in RD. Twin during rolling direction compression experiment

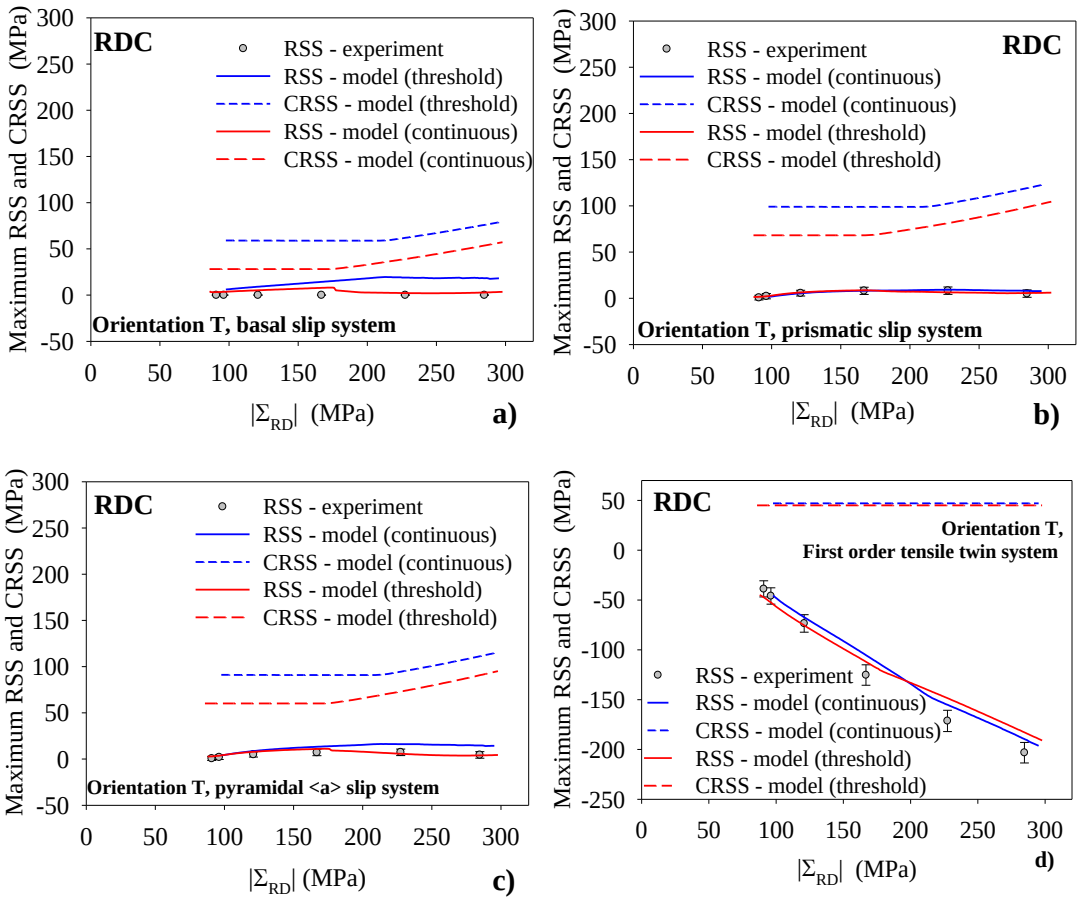

Fig. A4.5 Evolution of CRSS and maximum RSS on basal (a), prismatic (b), pyramidal <a> (c) slip systems and first order tensile twin system (d) in twin grains versus $|\Sigma_{RD}|$, during compression test in RD. The results of modified EPSC models with continuous and threshold assumptions are shown.

List of publications published by author

1) Neutron Diffraction Study of Phase Stresses Evolution in Two Phase polycrystalline Al/SiC Composite During Elastoplastic Deformation,
A. Baczmański, E. Gadalińska, S. Wroński, P. Kot, M. Wroński, M. Wróbel,
Ch. Scheffzuek, G. Bokuchava, K. Wierzbanowski,
International conference on Electron, Positron, Neutron and X-ray scattering under External Influence, Institute of Applied problems of Physics 2019 p.114-129 ISBN 978-9939-1-1046-2

2) Neutron measurements of stresses in Al/SiC$_p$ composite during mechanical loading,
A. Baczmański, P. Kot, E. Gadalińska, S. Wroński, M. Wroński, M. Wróbel,
Ch. Scheffzuek, G. Bokuchava, K. Wierzbanowski,
Processing and fabrication of advanced materials-XXVII : 27–29 May 2019,
p. 295-305 ISBN: 978-91-87289-44-6,
DOI: http://doi.org/10.13140/RG.2.2.14672.25603

3) Neutron diffraction study of phase stresses in Al/SiCp composite during tensile test,
E. Gadalińska, A. Baczmański, S. Wroński, P. Kot, M. Wroński, M. Wróbel,
Ch. Scheffzük, G. Bokuchava, K. Wierzbanowski,
Metals and Materials International 2019 vol. 25 iss. 3, p. 657-668 ISSN 1598-9623

4) Evolution of phase stresses in Al/SiC$_p$ composite during thermal cycling and compression test studied using diffraction and self-consistent models,
P. Kot, A. Baczmański, E. Gadalińska, S. Wroński, M. Wroński, M. Wróbel,
G. Bokuchava, Ch. Scheffzük, K. Wierzbanowski,
Journal of Materials Science & Technology 2019, ISSN 1005-0302
DOI: https://doi.org/10.1016/j.jmst.2019.03.046

5) Direct diffraction measurement of critical resolved shear stresses and stress localisation in magnesium alloy,
A. Baczmański, P. Kot, S. Wroński, M. Wróbel, M. Wroński, J. Pilch, M. Muzyka,
K. Wierzbanowski, Y. Zhao, L. Le Joncour, M. François, B. Panicaud,
Materials Science & Engineering A 2021 vol. 801, ISSN: 0921-5093,
DOI: https://doi.org/10.1016/j.msea.2020.140400

6) The role of basal slip in the generation of intergranular stresses in magnesium alloy studied using X-ray diffraction and modelling,
A. Baczmański, M. Wroński, P. Kot, S. Wroński, A. Łabaza, K. Wierzbanowski, A. Ludwik, M. Marciszko-Wiąckowska,
Materials & Design 2021 vol 202, ISSN: 0264-1275,
DOI: https://doi.org/10.1016/j.matdes.2021.109543

List of conferences attended by author

1) Pomiary neutronowe naprężeń w kompozycie Al/SiC_p oraz w materiałach dwufazowych przy obciążeniu mechanicznym
[Neutron diffraction study of stress partitioning between phases in Al/SiC_p composite during heat treatment followed by tensile test]
XI Ogólnopolska Konferencja "Rozpraszanie Neutronów i Metody Komplementarne w Badaniach Fazy Skondensowanej", June 15-20, 2019, Chlewiska k/Siedlec, Poland (report)

2) Neutron diffraction and elastic-plastic models used to study evolution of phase stresses in Al/SiC_p composite during thermal cycling and mechanical loading,
International conference on Electron, Positron, Neutron and X-ray scattering under External Influence, October 21-26, 2019, Yerevan, Armenia, (poster)

3) Investigation of microstress evolution in Mg-alloy using TOF neutron diffraction
International Conference Condensed Matter Research at the IBR-2, October 12-16, 2020, online, (oral)

4) Selective investigation of microstresses for different grain orientations and different phases using TOF neutron diffraction
The 19th International Conference on Textures of Materials (ICOTOM 19), March 1-4, 2021, online, (oral)

5) Mechanisms of elastic-plastic deformation in magnesium alloy studied using neutron diffraction and crystallite group method
XXV General Assembly and Congress of the International Union of Crystallography - IUCr 2021, August 14-22, 2021, Prague, Czech Republic, (oral)

6) Diffraction measurement of stress evolution for selected groups of grains in textured polycrystalline materials
ICRS 11 – The 11th International Conference on Residual Stresses, March 27-30, 2022, Nancy, France, (oral)

Bibliography

[1] M.R. Daymond, M.E. Fitzpatrick, Effect of cyclic plasticity on internal stresses in a metal matrix composite, Metallurgical and Materials Transactions A: Physical Metallurgy and Materials Science. 37 (2006) 1977–1986. https://doi.org/10.1007/s11661-006-0140-9.

[2] S. Cabeza, T. Mishurova, G. Garcés, I. Sevostianov, G. Requena, G. Bruno, Stress-induced damage evolution in cast AlSi12CuMgNi alloy with one- and two-ceramic reinforcements, Journal of Materials Science. 52 (2017) 10198–10216. https://doi.org/10.1007/s10853-017-1182-7.

[3] M.E. Fitzpatrick, M. Dutta, L. Edwards, Determination by neutron diffraction of effect of plasticity on crack tip strains in a metal matrix composite, Materials Science and Technology. 14 (1998) 980–986.

[4] R. Levy-Tubiana, A. Baczmanski, A. Lodini, Relaxation of thermal mismatch stress due to plastic deformation in an Al/SiCp metal matrix composite, Materials Science and Engineering A. (2003). https://doi.org/10.1016/S0921-5093(02)00204-6.

[5] G. Bruno, M. Ceretti, E. Girardin, A. Giuliani, A. Manescu, Relaxation of residual stress in mmc after combined plastic deformation and heat treatment, Scripta Materialia. 51 (2004) 999–1004. https://doi.org/10.1016/j.scriptamat.2004.07.016.

[6] A.J. Allen, M.A.M. Bourke, S. Dawes, M.T. Hutchings, P.J. Withers, The analysis of internal strains measured by neutron diffraction in Al/SiC metal matrix composites, Acta Metallurgica et Materialia. 40 (1992) 2361–2373. https://doi.org/10.1016/0956-7151(92)90155-8.

[7] A.J.J. Allen, M.A.M.A.M. Bourke, S. Dawes, M.T.T. Hutchings, P.J.J. Withers, The analysis of internal strains measured by neutron diffraction in Al/SiC metal matrix composites, Acta Metallurgica et Materialia. 40 (1992) 2361–2373. https://doi.org/10.1016/0956-7151(92)90155-8.

[8] B. Clausen, T. Lorentzen, T. Leffers, Self-consistent modelling of the plastic deformation of F.C.C. polycrstals and its implications for diffraction measurements of internal stresses, Acta Materialia. 46 (1998) 3087–3098. https://doi.org/10.1016/S1359-6454(98)00014-7.

[9] M.R. Daymond, H.G. Priesmeyer, Elastoplastic deformation of ferritic steel and cementite studied by neutron diffraction and self-consistent modelling, Acta Materialia. 50 (2002) 1613–1626. https://doi.org/10.1016/S1359-6454(02)00026-5.

[10] A. Baczmanski, C. Braham, Elastoplastic properties of duplex steel determined using neutron diffraction and self-consistent model, Acta Materialia. 52 (2004) 1133–1142. https://doi.org/10.1016/j.actamat.2003.10.046.

[11] S. Cai, M.R. Daymond, R.A. Holt, Deformation of high β-phase fraction Zr-Nb alloys at room temperature, Acta Materialia. 60 (2012) 3355–3369. https://doi.org/10.1016/j.actamat.2012.02.040.

[12] N. Jia, Z.H. Cong, X. Sun, S. Cheng, Z.H. Nie, Y. Ren, P.K. Liaw, Y.D. Wang, An in situ high-energy X-ray diffraction study of micromechanical behavior of multiple phases in advanced high-strength steels, Acta Materialia. 57 (2009) 3965–3977. https://doi.org/10.1016/j.actamat.2009.05.002.

[13] J. Čapek, J. Stráská, B. Clausen, K. Máthis, Twinning evolution as a function of loading direction in magnesium, in: Acta Physica Polonica A, 2015: pp. 762–764. https://doi.org/10.12693/APhysPolA.128.762.

[14] S.R. Agnew, A. Singh, C.A. Calhoun, R.P. Mulay, J.J. Bhattacharyya, H. Somekawa, T. Mukai, B. Clausen, P.D. Wu, In-situ neutron diffraction of a quasicrystal-containing Mg alloy interpreted using a new polycrystal plasticity model of hardening due to 10.2 tensile twinning, International Journal of Plasticity. 100 (2018) 34–51. https://doi.org/10.1016/j.ijplas.2017.09.005.

[15] H. Wang, B. Clausen, L. Capolungo, I.J. Beyerlein, J. Wang, C.N. Tomé, Stress and strain relaxation in magnesium AZ31 rolled plate: In-situ neutron measurement and elastic viscoplastic polycrystal modeling, International Journal of Plasticity. 79 (2016) 275–292. https://doi.org/10.1016/j.ijplas.2015.07.004.

[16] B. Clausen, C.N.N. Tomé, D.W.W. Brown, S.R.R. Agnew, Reorientation and stress relaxation due to twinning: Modeling and experimental characterization for Mg, Acta Materialia. 56 (2008) 2456–2468. https://doi.org/10.1016/j.actamat.2008.01.057.

[17] D. Sun, M. Ponga, K. Bhattacharya, M. Ortiz, Proliferation of twinning in hexagonal close-packed metals: Application to magnesium, Journal of the Mechanics and Physics of Solids. 112 (2018) 368–384. https://doi.org/10.1016/j.jmps.2017.12.009.

[18] H. Wang, P.D. Wu, C.N. Tomé, J. Wang, Study of lattice strains in magnesium alloy AZ31 based on a large strain elastic-viscoplastic self-consistent polycrystal model, International Journal of Solids and Structures. 49 (2012) 2155–2167. https://doi.org/10.1016/j.ijsolstr.2012.04.026.

[19] O. Muránsky, D.G. Carr, M.R. Barnett, E.C. Oliver, P. Šittner, Investigation of deformation mechanisms involved in the plasticity of AZ31 Mg alloy: In situ neutron diffraction and EPSC modelling, Materials Science and Engineering A. 496 (2008) 14–24. https://doi.org/10.1016/j.msea.2008.07.031.

[20] M.L. Young, J.D. Almer, M.R. Daymond, D.R. Haeffner, D.C. Dunand, Load partitioning between ferrite and cementite during elasto-plastic deformation of an ultrahigh-carbon steel, Acta Materialia. 55 (2007) 1999–2011. https://doi.org/10.1016/j.actamat.2006.11.004.

[21] A. Baczmański, Y. Zhao, E. Gadalińska, L. le Joncour, S. Wroński, C. Braham, B. Panicaud, M. François, T. Buslaps, K. Soloducha, Elastoplastic deformation and damage process in duplex stainless steels studied using synchrotron and neutron diffractions in comparison with a self-consistent model, International Journal of Plasticity. 81 (2016) 102–122. https://doi.org/10.1016/j.ijplas.2016.01.018.

[22] L. Wang, Z. Zheng, H. Phukan, P. Kenesei, J.-S. Park, J. Lind, R.M. Suter, T.R. Bieler, Direct measurement of critical resolved shear stress of prismatic and basal slip in polycrystalline Ti using high energy X-ray diffraction microscopy, Acta Materialia. 132 (2017) 598–610. https://doi.org/10.1016/j.actamat.2017.05.015.

[23] S. Kaboli, P.C. Burnley, In-situ synchrotron X-ray diffraction deformation and EPSC modeling of AZ31 Mg alloy, Materials Science and Engineering: A. 739 (2019) 99–104. https://doi.org/10.1016/j.msea.2018.10.008.

[24] E. Gadalińska, A. Baczmański, C. Braham, G. Gonzalez, H. Sidhom, S. Wroński, T. Buslaps, K. Wierzbanowski, Stress localisation in lamellar cementite and ferrite during elastoplastic deformation of pearlitic steel studied using diffraction and modelling, International Journal of Plasticity. 127 (2020) 102651. https://doi.org/10.1016/j.ijplas.2019.102651.

[25] E. Gadalińska, A. Baczmański, S. Wroński, L. le Joncour, C. Braham, M. François, B. Panicaud, K. Wierzbanowski, Direct determination of phase stress evolution in duplex steel using synchrotron diffraction, Materials Science and Engineering A. 801 (2021) 140400. https://doi.org/10.1016/j.msea.2020.140355.

[26] Q. Chen, L. Hu, L. Shi, T. Zhou, M. Yang, J. Tu, Assessment in predictability of visco-plastic self-consistent model with a minimum parameter approach: Numerical investigation of plastic deformation behavior of AZ31 magnesium alloy for various loading conditions, Materials Science and Engineering A. 774 (2020) 138912. https://doi.org/10.1016/j.msea.2020.138912.

[27] V.S. Vakhrusheva, N. v. Hruzin, I.A. Tiutieriev, O.D. Malysh, Influence of texture on mechanical properties of titanium alloy tubes, Physical Metallurgy and Heat Treatment of Metals. 0 (2019) 16–21. https://doi.org/10.30838/J.PMHTM.2413.241219.16.596.

[28] J. Peng, Z. Zhang, Z. Liu, Y. Li, P. Guo, W. Zhou, Y. Wu, The effect of texture and grain size on improving the mechanical properties of Mg-Al-Zn alloys by friction stir processing, Scientific Reports. 8 (2018) 4196. https://doi.org/10.1038/s41598-018-22344-3.

[29] A. Baczmański, M. Wroński, P. Kot, S. Wroński, A. Łabaza, K. Wierzbanowski, A. Ludwik, M. Marciszko-Wiąckowska, The role of basal slip in the generation of intergranular stresses in magnesium alloy studied using X-ray diffraction and modelling, Materials and Design. 202 (2021) 109543. https://doi.org/10.1016/j.matdes.2021.109543.

[30] H.-J. Bunge, Texture Analysis in Materials Science: Mathematical Methods, Elsevier, London, 1982. https://doi.org/10.1016/C2013-0-11769-2.

[31] S. Kurukuri, M.J. Worswick, D. Ghaffari Tari, R.K. Mishra, J.T. Carter, Rate sensitivity and tension–compression asymmetry in AZ31B magnesium alloy sheet, Philosophical Transactions of the Royal Society A: Mathematical, Physical and Engineering Sciences. 372 (2014) 20130216. https://doi.org/10.1098/rsta.2013.0216.

[32] S. You, Y. Huang, K.U. Kainer, N. Hort, Recent research and developments on wrought magnesium alloys, Journal of Magnesium and Alloys. 5 (2017) 239–253. https://doi.org/10.1016/j.jma.2017.09.001.

[33] S. Li, X. Yang, J. Hou, W. Du, A review on thermal conductivity of magnesium and its alloys, Journal of Magnesium and Alloys. 8 (2020) 78–90. https://doi.org/10.1016/j.jma.2019.08.002.

[34] B.L. Mordike, T. Ebert, Magnesium Properties - applications - potential, Materials Science and Engineering A. 302 (2001) 37–45. https://doi.org/10.1016/S0921-5093(00)01351-4.

[35] M.K. Kulekci, Magnesium and its alloys applications in automotive industry, International Journal of Advanced Manufacturing Technology. (2008). https://doi.org/10.1007/s00170-007-1279-2.

[36] M. Easton, A. Beer, M. Barnett, C. Davies, G. Dunlop, Y. Durandet, S. Blacket, T. Hilditch, P. Beggs, Magnesium alloy applications in automative structures, Jom. 60 (2008) 57–62. https://doi.org/10.1007/s11837-008-0150-8.

[37] C.S. Jawalkar, S. Kant, A Review on use of Aluminium Alloys in Aircraft Components, I-Manager's Journal on Material Science. 3 (2015) 33–38. https://doi.org/10.26634/jms.3.3.3673.

[38] Q. Luo, J. Li, B. Li, B. Liu, H. Shao, Q. Li, Kinetics in Mg-based hydrogen storage materials: Enhancement and mechanism, Journal of Magnesium and Alloys. 7 (2019) 58–71. https://doi.org/10.1016/j.jma.2018.12.001.

[39] V. Bazhenov, A. Koltygin, A. Komissarov, A. Li, V. Bautin, R. Khasenova, A. Anishchenko, A. Seferyan, J. Komissarova, Y. Estrin, Gallium-containing magnesium alloy for potential use as temporary implants in osteosynthesis, Journal of Magnesium and Alloys. 8 (2020) 352–363. https://doi.org/10.1016/j.jma.2020.02.009.

[40] A. Baczmański, P. Kot, S. Wroński, M. Wróbel, M. Wroński, J. Pilch, M. Muzyka, K. Wierzbanowski, Y. Zhao, L. le Joncour, M. François, B. Panicaud, Direct diffraction measurement of critical resolved shear stresses and stress localisation in magnesium alloy, Materials Science and Engineering A. 801 (2021) 140400. https://doi.org/10.1016/j.msea.2020.140400.

[41] J. Čapek, K. Máthis, B. Clausen, J. Stráská, P. Beran, P. Lukáš, Study of the loading mode dependence of the twinning in random textured cast magnesium by acoustic emission and neutron diffraction methods, Materials Science and Engineering A. 602 (2014) 25–32. https://doi.org/10.1016/j.msea.2014.02.051.

[42] P.F. Willemse, B.P. Naughton, C.A. Verbraak, X-ray residual stress measurements on cold-drawn steel wire, Materials Science and Engineering. 56 (1982) 25–37. https://doi.org/10.1016/0025-5416(82)90179-3.

[43] V. Hauk, Structural and Residual Stress Analysis by Nondestructive Methods, 1997. https://doi.org/10.1016/b978-0-444-82476-9.50022-0.

[44] B. Ortner, On the selection of measurement directions in second-rank tensor (e . g . elastic strain) determination of single crystals , Journal of Applied Crystallography. 22 (1989) 216–221. https://doi.org/10.1107/s0021889888014141.

[45] U. Welzel, J. Ligot, P. Lamparter, A.C. Vermeulen, E.J. Mittemeijer, Stress analysis of polycrystalline thin films and surface regions by X-ray diffraction, Journal of Applied Crystallography. 38 (2005) 1–29. https://doi.org/10.1107/S0021889804029516.

[46] R. Dakhlaoui, V. Klosek, M.H. Mathon, B. Marini, Orientation stress field analysis in polycrystalline bcc steel using neutron diffraction, Acta Materialia. 58 (2010) 499–509. https://doi.org/10.1016/j.actamat.2009.09.028.

[47] D. Munz, T. Fett, Ceramics, Springer Berlin Heidelberg, Berlin, Heidelberg, 1999. https://doi.org/10.1007/978-3-642-58407-7.

[48] B. Basu, K. Balani, Advanced Structural Ceramics, John Wiley & Sons, Inc., Hoboken, NJ, USA, 2011. https://doi.org/10.1002/9781118037300.

[49] A. Mortensen, J. Llorca, Metal Matrix Composites, Annual Review of Materials Research. 40 (2010) 243–270. https://doi.org/10.1146/annurev-matsci-070909-104511.

[50] N. Chawla, K.K. Chawla, Metal Matrix Composites, Springer New York, New York, NY, 2013. https://doi.org/10.1007/978-1-4614-9548-2.

[51] T.W. Clyne, P.J. Withers, An Introduction to Metal Matrix Composites, Cambridge University Press, Cambridge, 1993.

[52] F. Nturanabo, L. Masu, J. Baptist Kirabira, Novel Applications of Aluminium Metal Matrix Composites, in: Aluminium Alloys and Composites, IntechOpen, 2020. https://doi.org/10.5772/intechopen.86225.

[53] B. v Ramnath, C. Elanchezhian, R.M. Annamalai, S. Aravind, T.S.A. Atreya, V. Vignesh, C. Subramanian, Aluminium metal matrix composites - A review, Rev. Adv. Mater. Sci. 38 (2014) 55–60.

[54] V.M. Kumar, C. v Venkatesh, A comprehensive review on material selection, processing, characterization and applications of aluminium metal matrix composites, Materials Research Express. 6 (2019) 072001. https://doi.org/10.1088/2053-1591/ab0ee3.

[55] M.D. Hayat, H. Singh, Z. He, P. Cao, Titanium metal matrix composites: An overview, Composites Part A: Applied Science and Manufacturing. 121 (2019) 418–438. https://doi.org/10.1016/j.compositesa.2019.04.005.

[56] J. Shi, Y. Wang, Development of metal matrix composites by laser-assisted additive manufacturing technologies: a review, Journal of Materials Science. 55 (2020) 9883–9917. https://doi.org/10.1007/s10853-020-04730-3.

[57] S. Tang, R. Ummethala, C. Suryanarayana, J. Eckert, K.G. Prashanth, Z. Wang, Additive Manufacturing of Aluminum-Based Metal Matrix Composites—A Review, Advanced Engineering Materials. 23 (2021) 2100053. https://doi.org/10.1002/adem.202100053.

[58] M.O. Bodunrin, K.K. Alaneme, L.H. Chown, Aluminium matrix hybrid composites: a review of reinforcement philosophies; mechanical, corrosion and tribological characteristics, Journal of Materials Research and Technology. 4 (2015) 434–445. https://doi.org/10.1016/j.jmrt.2015.05.003.

[59] S. Soleymani Shishvan, A.-H. Asghari, Particle size effect in metal matrix composites: A study by the continuum theory of stress gradient plasticity, Journal of Composite Materials. 50 (2016) 1717–1723. https://doi.org/10.1177/0021998315595708.

[60] N.K. Bhoi, H. Singh, S. Pratap, Developments in the aluminum metal matrix composites reinforced by micro/nano particles – A review, Journal of Composite Materials. 54 (2020) 813–833. https://doi.org/10.1177/0021998319865307.

[61] M. Kouzeli, A. Mortensen, Size dependent strengthening in particle reinforced aluminium, Acta Materialia. 50 (2002) 39–51. https://doi.org/10.1016/S1359-6454(01)00327-5.

[62] M.L. Young, R. Rao, J.D. Almer, D.R. Haeffner, J.A. Lewis, D.C. Dunand, Load partitioning in Al2O3–Al composites with three-dimensional periodic architecture, Acta Materialia. 57 (2009) 2362–2375. https://doi.org/10.1016/j.actamat.2009.01.019.

[63] M.E. Fitzpatrick, P.J. Withers, A. Baczmanski, M.T. Hutchings, R. Levy, M. Ceretti, A. Lodini, Changes in the misfit stresses in an Al/SiCpmetal matrix composite under plastic strain, Acta Materialia. 50 (2002) 1031–1040. https://doi.org/10.1016/S1359-6454(01)00401-3.

[64] A. Baczmański, R. Levy-Tubiana, M.E. Fitzpatrick, A. Lodini, Elastoplastic deformation of Al/SiCp metal–matrix composite studied by self-consistent modelling and neutron diffraction, Acta Materialia. 52 (2004) 1565–1577. https://doi.org/10.1016/j.actamat.2003.12.002.

[65] E. Gadalińska, A. Baczmański, S. Wroński, P. Kot, M. Wroński, M. Wróbel, C. Scheffzük, G. Bokuchava, K. Wierzbanowski, Neutron Diffraction Study of Phase Stresses in Al/SiCp Composite During Tensile Test, Metals and Materials International. 25 (2019) 657–668. https://doi.org/10.1007/s12540-018-00218-7.

[66] P. Kot, A. Baczmański, E. Gadalińska, S. Wroński, M. Wroński, M. Wróbel, G. Bokuchava, C. Scheffzük, K. Wierzbanowski, Evolution of phase stresses in Al/SiCp composite during thermal cycling and compression test studied using diffraction and self-consistent models, Journal of Materials Science & Technology. 36 (2020) 176–189. https://doi.org/10.1016/j.jmst.2019.03.046.

[67] C.N. Reid, Deformation Geometry for Materials Scientists, Elsevier, 1973. https://doi.org/10.1016/C2013-0-02546-7.

[68] J.F. Nye, Physical Properties of Crystals. Their representation by tensors and matrices., Claredon Press Oxford, 1957.

[69] K. Pawlik, J. Pospiech, K. Lücke, The ODF Approximation From Pole Figures With the Aid of the ADC Method, Textures and Microstructures. 14 (1991) 25–30. https://doi.org/10.1155/TSM.14-18.25.

[70] S. Matthies, H.-R. Wenk, G.W. Vinel, Some basic concepts of texture analysis and comparison of three methods to calculate orientation distributions from pole figures, Journal of Applied Crystallography. 21 (1988) 285–304. https://doi.org/10.1107/S0021889888000275.

[71] I.C. Noyan, J.B. Cohen, Residual Stress. Measurement by Diffraction and Interpretation, Springer New York, 1987.

[72] A. Baczmański, Stress fields in polycrystalline materials studied using diffraction and self-consistent modeling, AGH - University of Science and Technology, 2005.

[73] A. Baczmanski, P. Lipinski, A. Tidu, K. Wierzbanowski, B. Pathiraj, Quantitative estimation of incompatibility stresses and elastic energy stored in ferritic steel, Journal of Applied Crystallography. 41 (2008) 854–867. https://doi.org/10.1107/S0021889808023911.

[74] A. Reuss, Berechnung der Fließgrenze von Mischkristallen auf Grund der Plastizitätsbedingung für Einkristalle ., ZAMM - Journal of Applied Mathematics and Mechanics / Zeitschrift Für Angewandte Mathematik Und Mechanik. 9 (1929) 49–58. https://doi.org/10.1002/zamm.19290090104.

[75] W. Voigt, Lehrbuch der Kristallphysik, 1928. https://doi.org/10.1007/978-3-663-15884-4.

[76] R. Hill, The Elastic Behaviour of a Crystalline Aggregate, Proceedings of the Physical Society. Section A. 65 (1952) 349–354. https://doi.org/10.1088/0370-1298/65/5/307.

[77] A. Morawiec, Calculation of Polycrystal Elastic Constants from Single-Crystal Data, Physica Status Solidi (b). 154 (1989) 535–541. https://doi.org/10.1002/pssb.2221540213.

[78] J.D. Eshelby, The determination of the elastic field of an ellipsoidal inclusion, and related problems, Proceedings of the Royal Society of London. Series A. Mathematical and Physical Sciences. 241 (1957) 376–396. https://doi.org/10.1098/rspa.1957.0133.

[79] E. Kröner, Berechnung der elastischen Konstanten des Vielkristalls aus den Konstanten des Einkristalls, Zeitschrift Für Physik. 151 (1958) 504–518. https://doi.org/10.1007/BF01337948.

[80] P. Lipinski, M. Berveiller, Elastoplasticity of micro-inhomogeneous metals at large strains, International Journal of Plasticity. 5 (1989) 149–172. https://doi.org/10.1016/0749-6419(89)90027-2.

[81] P. Franciosi, M. Berveiller, A. Zaoui, Latent hardening in copper and aluminium single crystals, Acta Metallurgica. 28 (1980) 273–283. https://doi.org/10.1016/0001-6160(80)90162-5.

[82] C.J. Neil, J.A. Wollmershauser, B. Clausen, C.N. Tomé, S.R. Agnew, Modeling lattice strain evolution at finite strains and experimental verification for copper and stainless steel using in situ neutron diffraction, International Journal of Plasticity. 26 (2010) 1772–1791. https://doi.org/10.1016/j.ijplas.2010.03.005.

[83] C. Tome, G.R. Canova, U.F. Kocks, N. Christodoulou, J.J. Jonas, The relation between macroscopic and microscopic strain hardening in F.C.C. polycrystals, Acta Metallurgica. 32 (1984) 1637–1653. https://doi.org/10.1016/0001-6160(84)90222-0.

[84] N. Jia, R. Lin Peng, Y.D. Wang, S. Johansson, P.K. Liaw, Micromechanical behavior and texture evolution of duplex stainless steel studied by neutron diffraction and self-consistent modeling, Acta Materialia. 56 (2008) 782–793. https://doi.org/10.1016/j.actamat.2007.10.040.

[85] S. Pfeiffer, M.F.-X. Wagner, Elastic deformation of twinned microstructures, Proceedings of the Royal Society A: Mathematical, Physical and Engineering Sciences. 473 (2017). https://doi.org/10.1098/rspa.2017.0330.

[86] H. Schuman, Kristallgeometrie : Einführung in die Theorie der Gittertransformationen metallischer Werkstoffe., Leipzig : VEB Deutscher Verlag für Grundstoffindustrie, 1979.

[87] P.G. Partridge, The crystallography and deformation modes of hexagonal close-packed metals, Metallurgical Reviews. 12 (1967) 169–194. https://doi.org/10.1179/mtlr.1967.12.1.169.

[88] C.N. Tomé, R.A. Lebensohn, U.F. Kocks, A model for texture development dominated by deformation twinning: Application to zirconium alloys, Acta Metallurgica et Materialia. 39 (1991) 2667–2680. https://doi.org/10.1016/0956-7151(91)90083-D.

[89] Y. Jeong, C.N. Tomé, Extension of the visco-plastic self-consistent model to account for elasto-visco-plastic behavior using a perturbed visco-plastic approach, Modelling and Simulation in Materials Science and Engineering. 27 (2019) 85013. https://doi.org/10.1088/1361-651x/ab4b66.

[90] A. Jain, S.R. Agnew, The Temperature Dependent Role of Twinning in the Ductility of Magnesium Alloy Sheet, in: Proceedings of the TMS 2006 Annual Meeting – Magnesium Technology, San Antonio, TX, 2006: pp. 219–224.

[91] G.I. Taylor, Plastic strain in metals, Journal of the Institute of Metals. 62 (1938) 307–324. https://doi.org/not found.

[92] G. Sachs, Zur Ableitung einer Fliessbedinung, Zeitschrift Des VDI. 72 (1928) 734–736.

[93] J.G. de Mey, P.M. Vanhoutte, Heterogeneous behavior of the canine arterial and venous wall. Importance of the endothelium., Circulation Research. 51 (1982) 439–447. https://doi.org/10.1161/01.RES.51.4.439.

[94] E. Kröner, Zur plastischen verformung des vielkristalls, Acta Metallurgica. 9 (1961) 155–161.

[95] R. Hill, A self-consistent mechanics of composite materials, Journal of the Mechanics and Physics of Solids. 13 (1965) 213–222. https://doi.org/10.1016/0022-5096(65)90010-4.

[96] P.A. Turner, C.N. Tomé, A study of residual stresses in Zircaloy-2 with rod texture, Acta Metallurgica Et Materialia. 42 (1994) 4143–4153. https://doi.org/10.1016/0956-7151(94)90191-0.

[97] I.J. Beyerlein, C.N. Tomé, A dislocation-based constitutive law for pure Zr including temperature effects, International Journal of Plasticity. 24 (2008) 867–895. https://doi.org/10.1016/j.ijplas.2007.07.017.

[98] R.A. Lebensohn, A.K. Kanjarla, P. Eisenlohr, An elasto-viscoplastic formulation based on fast Fourier transforms for the prediction of micromechanical fields in polycrystalline materials, International Journal of Plasticity. 32–33 (2012) 59–69. https://doi.org/10.1016/j.ijplas.2011.12.005.

[99] M. v Upadhyay, A. Patra, W. Wen, T. Panzner, S. van Petegem, C.N. Tomé, R.A. Lebensohn, H. van Swygenhoven, Mechanical response of stainless steel subjected to biaxial load path changes: Cruciform experiments and multi-scale modeling, International Journal of Plasticity. 108 (2018) 144–168. https://doi.org/10.1016/j.ijplas.2018.05.003.

[100] I. Chelladurai, D. Adams, D.T. Fullwood, M.P. Miles, S. Niezgoda, I.J. Beyerlein, M. Knezevic, Modeling of trans-grain twin transmission in AZ31 via a neighborhood-based viscoplastic self-consistent model, International Journal of Plasticity. 117 (2019) 21–32. https://doi.org/10.1016/j.ijplas.2018.03.012.

[101] N. Bonfoh, P. Lipinski, A. Carmasol, S. Tiem, Micromechanical modeling of ductile damage of polycrystalline materials with heterogeneous particles, International Journal of Plasticity. 20 (2004) 85–106. https://doi.org/10.1016/S0749-6419(03)00017-2.

[102] G. Franz, F. Abed-Meraim, M. Berveiller, Strain localization analysis for single crystals and polycrystals: Towards microstructure-ductility linkage, International Journal of Plasticity. 48 (2013) 1–33. https://doi.org/10.1016/j.ijplas.2013.02.001.

[103] P. Lipinski, M. Berveiller, E. Reubrez, J. Morreale, Transition theories of elastic-plastic deformation of metallic polycrystals, Archive of Applied Mechanics. 65 (1995) 291–311. https://doi.org/10.1007/BF00789222.

[104] J. Fajoui, D. Gloaguen, V. Legrand, G. Oum, J. Kelleher, W. Kockelmann, Bauschinger Effect in an Austenitic Steel: Neutron Diffraction and a Multiscale Approach, Metallurgical and Materials Transactions A: Physical Metallurgy and Materials Science. 47 (2016) 2024–2036. https://doi.org/10.1007/s11661-016-3362-5.

[105] E. Gadalińska, A. Baczmański, S. Wroński, M. Wróbel, C. Scheffzük, The hardening in alloys and composites and its examination with a diffraction and self-consistent model, Fatigue of Aircraft Structures. 2018 (2018) 31–46. https://doi.org/10.2478/fas-2018-0003.

[106] D. Gloaguen, J. Fajoui, B. Girault, Residual stress fields analysis in rolled Zircaloy-4 plates: Grazing incidence diffraction and elastoplastic self-consistent model, Acta Materialia. 71 (2014) 136–144. https://doi.org/10.1016/j.actamat.2014.02.031.

[107] V. Hounkpati, S. Fréour, D. Gloaguen, V. Legrand, J. Kelleher, W. Kockelmann, S. Kabra, In situ neutron measurements and modelling of the intergranular strains in the near-β titanium alloy Ti-β21S, Acta Materialia. 109 (2016) 341–352. https://doi.org/10.1016/j.actamat.2016.02.065.

[108] J. Tarasiuk, K. Wierzbanowski, A. Baczmanski, Application of the Method for Non-Destructive Evaluation of Texture Heterogeneity, Materials Science Forum. 157–162 (1994) 213–220. https://doi.org/10.4028/www.scientific.net/MSF.157-162.213.

[109] K. Wierzbanowski, J. Jura, W.G. Haije, R.B. Helmholdt, F.C.C. Rolling Texture Transitions in Relation to Constraint Relaxation, Crystal Research and Technology. 27 (1992) 513–522. https://doi.org/10.1002/crat.2170270417.

[110] Typical X-ray Spectra by Anode Material, (n.d.). https://xray.oxinst.com/learning/view/article/typical-x-ray-spectra-by-anode-material (accessed October 22, 2021).

[111] Strain Diffractometer (TKSN-400) - instrumenta parameters and equipment, (n.d.). http://www.ujf.cas.cz/en/departments/department-of-neutron-physics/instruments/lvr15/hk9/ (accessed February 7, 2022).

[112] Frank Laboratory for Nuclear Physics JINR Dubna, (n.d.). http://flnph.jinr.ru/en/ (accessed February 7, 2022).

[113] C. Kittel, Introduction to Solid State Physics, 8th edition, Wiley & Sons, New York, NY. (2004).

[114] R.A. Young, The Rietveld Method, Oxford University Press, 1993.

[115] Rietveld Refinement in the Characterization of Crystalline Materials, MDPI, 2019. https://doi.org/10.3390/books978-3-03897-528-1.

[116] J. Rodríguez-Carvajal, An Introduction to the program FullProf 2000, 2001.

[117] Z. Bojarski, Rentgenowska analiza strukturalna, Wydaw. Uniwersytetu Śląskiego, , 1995.

[118] B.D. Cullity, Elements of X-ray Diffraction, Addison-Wesley Publishing Company, 1978.

[119] E. Macherauch, H. Wohlfahrt, U. Wolfstieg, Practical sefinition of residual stresses, Harterei Tech. Mitt. 28 (1973) 201–211.

[120] M. Marciszko-Wiąckowska, A. Oponowicz, A. Baczmański, Ch. Braham, M. Wątroba, M. Wróbel, M. Klaus, Ch. Genzel, A novel approach for nondestructive depth-resolved analysis of residual stress and grain interaction in the near-surface zone applied to an austenitic stainless steel sample subjected to mechanical polishing, Measurement. 194 (2022) 111016. https://doi.org/10.1016/j.measurement.2022.111016.

[121] S. Takahashi, Measurement of third-order elastic constants and stress dependent coefficients for steels, Mechanics of Advanced Materials and Modern Processes. 4 (2018) 2. https://doi.org/10.1186/s40759-018-0035-7.

[122] S.-J. Wu, P.-C. Chin, H. Liu, Measurement of Elastic Properties of Brittle Materials by Ultrasonic and Indentation Methods, Applied Sciences. 9 (2019) 2067. https://doi.org/10.3390/app9102067.

[123] E. Hu, W. Wang, The Elastic Constants Measurement of Metal Alloy by Using Ultrasonic Nondestructive Method at Different Temperature, Mathematical Problems in Engineering. 2016 (2016) 1–7. https://doi.org/10.1155/2016/6762076.

[124] H. Dölle, J.B. Cohen, Evaluation of (residual) stresses in textured cubic metals, Metallurgical Transactions A. 11 (1980). https://doi.org/10.1007/BF02661212.

[125] M. Barral, J.L. Lebrun, J.M. Sprauel, G. Maeder, X-ray macrostress determination on textured material; use of the ODF for calculating the X-ray compliances, Metallurgical Transactions A. 18 (1987) 1229–1238. https://doi.org/10.1007/BF02647192.

[126] C.M. Brakman, The Voigt model case, Philosophical Magazine A. 55 (1987) 39–58. https://doi.org/10.1080/01418618708209799.

[127] A. Baczmański, K. Wierzbanowski, W.G. Haije, R.B. Helmholdt, G. Ekambaranathan, B. Pathiraj, Diffraction Elastic Constants for Textured Materials — Different Methods of Calculation, Crystal Research and Technology. 28 (1993) 229–243. https://doi.org/10.1002/crat.2170280217.

[128] S. Fréour, J. Fajoui, Eshelby-Kröner self-consistent elastic model: the geometric mean versus the arithmetic mean - A numerical investigation, ZAMM - Journal of Applied Mathematics and Mechanics / Zeitschrift Für Angewandte Mathematik Und Mechanik. 92 (2012) 329–338. https://doi.org/10.1002/zamm.201100135.

[129] A. Baczmański, K. Wierzbanowski, P. Lipiński, R.B. Helmholdt, G. Ekambaranathan, B. Pathiraj, Examination of the residual stress field in plastically deformed polycrystalline material, Philosophical Magazine A: Physics of Condensed Matter, Structure, Defects and Mechanical Properties. 69 (1994) 437–449. https://doi.org/10.1080/01418619408242223.

[130] S. Wroński, A. Baczmański, R. Dakhlaoui, C. Braham, K. Wierzbanowski, E.C. Oliver, Determination of the stress field in textured duplex steel using the TOF neutron diffraction method, Acta Materialia. 55 (2007) 6219–6233. https://doi.org/10.1016/j.actamat.2007.07.044.

[131] R. Wawszczak, A. Baczmański, C. Braham, W. Seiler, M. Wróbel, K. Wierzbanowski, A. Lodini, Residual stress field in steel samples during plastic deformation and recovery processes, Philosophical Magazine. 91 (2011) 2263–2290. https://doi.org/10.1080/14786435.2011.557401.

[132] A. Ostapovets, P. Molnár, A. Jäger, P. Lejček, ANALYSIS OF NEAR-COINCIDENCE SITE LATTICE BOUNDARY FREQUENCY IN AZ31 MAGNESIUM ALLOY, in: 21st International Conference on Metallurgy and Materials METAL 2012, Brno, Czech Republic, 2012.

[133] W. Reimers, H. Clemens, A. Schreyer, A.R. Kaysser-Pyzalla, Neutrons and Synchrotron Radiation in Engineering Materials Science, Wiley, 2008. https://doi.org/10.1002/9783527621927.

[134] M. Marciszko-Wiackowska, A. Oponowicz, A. Baczmański, M. Wróbel, C. Braham, R. Wawszczak, Multireflection grazing-incidence X-ray diffraction: A new approach to experimental data analysis, Journal of Applied Crystallography. 52 (2019) 1409–1421. https://doi.org/10.1107/S1600576719013876.

[135] A. Iserles, Numerical recipes in C—the art of scientific computing, by W. H. Press, B. P. Flannery, S. A. Teukolsky and W. T. Vetterling. Pp 735. £27·50. 1988. ISBN 0-521-35465-X (Cambridge University Press), The Mathematical Gazette. 73 (1989) 167–170. https://doi.org/10.2307/3619708.

[136] G. Requena, D.C. Yubero, J. Corrochano, J. Repper, G. Garcés, Stress relaxation during thermal cycling of particle reinforced aluminium matrix composites,

Composites Part A: Applied Science and Manufacturing. 43 (2012) 1981–1988. https://doi.org/10.1016/j.compositesa.2012.07.004.

[137] P. Fernández-Castrillo, G. Bruno, G. González-Doncel, Neutron and synchrotron radiation diffraction study of the matrix residual stress evolution with plastic deformation in aluminum alloys and composites, Materials Science and Engineering A. 487 (2008) 26–32. https://doi.org/10.1016/j.msea.2007.09.067.

[138] M. Dutta, G. Bruno, L. Edwards, M.E. Fitzpatrick, Neutron diffraction measurement of the internal stresses following heat treatment of a plastically deformed Al/SiC particulate metal-matrix composite, Acta Materialia. 52 (2004) 3881–3888. https://doi.org/10.1016/j.actamat.2004.05.002.

[139] S. Cabeza, T. Mishurova, G. Bruno, G. Garcés, G. Requena, The role of reinforcement orientation on the damage evolution of AlSi12CuMgNi + 15% Al2O3 under compression, Scripta Materialia. 122 (2016) 115–118. https://doi.org/10.1016/j.scriptamat.2016.05.023.

[140] S. Sarkar, A. Singh, Studies on Aluminum-Iron Ore in-Situ Particulate Composite, Open Journal of Composite Materials. 02 (2012) 22–30. https://doi.org/10.4236/ojcm.2012.21004.

[141] K. Suryanarayanan, R. Praveen, S. Raghuraman, Silicon Carbide Reinforced Aluminium Metal Matrix Composites for Aerospace Applications : A Literature Review, International Journal of Innovative Research in Science, Engineering and Technology. 2 (2013) 6336–6344.

[142] V.C. Kale, Aluminium Based Metal Matrix Composites for Aerospace Application: A Literature Review, IOSR Journal of Mechanical and Civil Engineering. 12 (2015) 1684–2278. https://doi.org/10.9790/1684-12653136.

[143] P.P. Castañeda, P. Suquet, Nonlinear Composites, Advances in Applied Mechanics. 34 (1997) 171–302. https://doi.org/10.1016/S0065-2156(08)70321-1.

[144] C. González, J. Llorca, Self-consistent approach to the elasto-plastic behaviour of two-phase materials including damage, Journal of the Mechanics and Physics of Solids. 48 (2000) 675–692. https://doi.org/10.1016/S0022-5096(99)00057-5.

[145] C. González, J. Segurado, J. LLorca, Numerical simulation of elasto-plastic deformation of composites: Evolution of stress microfields and implications for homogenization models, Journal of the Mechanics and Physics of Solids. (2004). https://doi.org/10.1016/j.jmps.2004.01.002.

[146] P. Gilormini, Insuffisance de l'extension classique du modele auto-coherent au comportement non lineaire, C. R. Acad. Sci. Paris. 320 (1995) 115–122.

[147] O. Pierard, C. González, J. Segurado, J. LLorca, I. Doghri, Micromechanics of elasto-plastic materials reinforced with ellipsoidal inclusions, International Journal of Solids and Structures. 44 (2007) 6945–6962. https://doi.org/10.1016/j.ijsolstr.2007.03.019.

[148] M. Kursa, K. Kowalczyk-Gajewska, M.J. Lewandowski, H. Petryk, Elastic-plastic properties of metal matrix composites: Validation of mean-field approaches, European Journal of Mechanics, A/Solids. 68 (2018) 53–66. https://doi.org/10.1016/j.euromechsol.2017.11.001.

[149] E. Gadalińska, Micromechanical properties and stresses in two-phase polycrystalline materials studied using diffraction and self-consistent model, AGH-University of Science and Technology, Kraków, 2018. files/2320/Gadalińska.

[150] P. Kot, Development of methods and software for the interpretation of diffraction measurements of crystal lattice deformation, MSc thesis, only in Polish, AGH University of Science and Technology, 2018.

[151] ASM-Handbook, Properties of Wrought Aluminum and Aluminum Alloys, in: Handbook ASM, Volume 2: Properties and Selection: Nonferrous Alloys and Special-Purpose Materials, ASM International, 1990: pp. 62–122.

[152] L.L. Snead, T. Nozawa, Y. Katoh, T.S. Byun, S. Kondo, D.A. Petti, Handbook of SiC properties for fuel performance modeling, Journal of Nuclear Materials. 371 (2007) 329–377. https://doi.org/10.1016/j.jnucmat.2007.05.016.

[153] F. Corvasce, P. Lipinski, M. Berveiller, Thermomechanical Behaviour of Metal Matrix Composites, in: P. Höller, V. Hauk, G. Dobmann, O. Ruud C, E. Green R (Eds.), Nondestructive Characterization of Materials, Springer, Berlin, Heidelberg, 1989: pp. 194–203.

[154] F. Corvasce, P. Lipinski, M. Berveiller, The Effects of thermal, Plastic and elastic Stress Concentration on the Overall Behavior of Metal matrix Composites, in: J. Dvorak G (Ed.), Inelastic Deformation of Composite Materials, IUTAM Symposium 1990, Springer-Verlag, Troy, New York, 1991: pp. 389–408.

[155] M.E. Fitzpatrick, A study of the effects of a quench residual stress field on fatigue in an Al/SiCp metal matrix composite, Ph.D., University of Cambridge, 1995.

[156] C. Badini, F. Marino, E. Verné, Calorimetric study on precipitation path in 2024 alloy and its SiC composite, Materials Science and Engineering A. 191 (1995) 185–191. https://doi.org/10.1016/0921-5093(94)09637-C.

[157] G. Simmons, H. Wang, Single Crystal Elastic Constants and Calculated Aggregate Properties:A Handbook, The MIT Press, Cambridge, London, 1971.

[158] M.H. Yoo, Slip, twinning, and fracture in hexagonal close-packed metals, Metallurgical Transactions A. 12 (1981) 409–418. https://doi.org/10.1007/BF02648537.

[159] S.R. Agnew, Ö. Duygulu, Plastic anisotropy and the role of non-basal slip in magnesium alloy AZ31B, in: International Journal of Plasticity, 2005: pp. 1161–1193. https://doi.org/10.1016/j.ijplas.2004.05.018.

[160] M. Zecevic, I.J. Beyerlein, M. Knezevic, Activity of pyramidal I and II <c+a> slip in Mg alloys as revealed by texture development, Journal of the Mechanics and Physics of Solids. 111 (2018) 290–307. https://doi.org/10.1016/j.jmps.2017.11.004.

[161] A. Staroselsky, L. Anand, A constitutive model for hcp materials deforming by slip and twinning: Application to magnesium alloy AZ31B, International Journal of Plasticity. 19 (2003) 1843–1864. https://doi.org/10.1016/S0749-6419(03)00039-1.

[162] W. Wen, M. Borodachenkova, C.N. Tomé, G. Vincze, E.F. Rauch, F. Barlat, J.J. Grácio, Mechanical behavior of Mg subjected to strain path changes: Experiments and modeling, International Journal of Plasticity. 73 (2015) 171–183. https://doi.org/10.1016/j.ijplas.2014.10.009.

[163] K.J. Tam, M.W. Vaughan, L. Shen, M. Knezevic, I. Karaman, G. Proust, Modelling the temperature and texture effects on the deformation mechanisms of magnesium alloy AZ31, International Journal of Mechanical Sciences. 182 (2020) 105727. https://doi.org/10.1016/j.ijmecsci.2020.105727.

[164] H. Wang, P.D. Wu, C.N. Tomé, J. Wang, A constitutive model of twinning and detwinning for hexagonal close packed polycrystals, Materials Science and Engineering: A. 555 (2012) 93–98. https://doi.org/10.1016/j.msea.2012.06.038.

[165] B. Zhou, L. Wang, P. Jin, H. Jia, H.J. Roven, X. Zeng, Y. Li, Revealing slip-induced extension twinning behaviors dominated by micro deformation in a magnesium alloy, International Journal of Plasticity. 128 (2020) 102669. https://doi.org/10.1016/j.ijplas.2020.102669.

[166] J. Wang, M.R.G. Ferdowsi, S.R. Kada, P.A. Lynch, Z. Wang, J.A. Kimpton, M.R. Barnett, Stress relaxations during cyclic loading-unloading in precipitation hardened Mg-4.5Zn, Acta Materialia. 205 (2021) 116531. https://doi.org/10.1016/j.actamat.2020.116531.

[167] Y. Zhao, S. Wroński, A. Baczmański, L. le Joncour, M. Marciszko, T. Tokarski, M. Wróbel, M. François, B. Panicaud, Micromechanical behaviour of a two-phase Ti alloy studied using grazing incidence diffraction and a self-consistent model, Acta Materialia. 136 (2017) 402–414. https://doi.org/10.1016/j.actamat.2017.06.022.

[168] H. Fan, J.A. El-Awady, Molecular Dynamics Simulations of Orientation Effects During Tension, Compression, and Bending Deformations of Magnesium Nanocrystals, Journal of Applied Mechanics. 82 (2015). https://doi.org/10.1115/1.4030930.

[169] Md.S. Hasan, R. Lee, W. Xu, Deformation nanomechanics and dislocation quantification at the atomic scale in nanocrystalline magnesium, Journal of Magnesium and Alloys. 8 (2020) 1296–1303. https://doi.org/10.1016/j.jma.2020.08.014.

[170] Z.H. Aitken, H. Fan, J.A. El-Awady, J.R. Greer, The effect of size, orientation and alloying on the deformation of AZ31 nanopillars, Journal of the Mechanics and Physics of Solids. 76 (2015) 208–223. https://doi.org/10.1016/j.jmps.2014.11.014.

[171] Q. Yu, L. Qi, K. Chen, R.K. Mishra, J. Li, A.M. Minor, The Nanostructured Origin of Deformation Twinning, Nano Letters. 12 (2012) 887–892. https://doi.org/10.1021/nl203937t.

[172] K.E. Prasad, K. Rajesh, U. Ramamurty, Micropillar and macropillar compression responses of magnesium single crystals oriented for single slip or extension twinning, Acta Materialia. 65 (2014) 316–325. https://doi.org/10.1016/j.actamat.2013.10.073.

[173] K. Máthis, P. Beran, J. Čapek, P. Lukáš, In-situ neutron diffraction and acoustic emission investigation of twinning activity in magnesium, Journal of Physics: Conference Series. 340 (2012) 012096. https://doi.org/10.1088/1742-6596/340/1/012096.

[174] M.A. Lebyodkin, I. v. Shashkov, T.A. Lebedkina, K. Mathis, P. Dobron, F. Chmelik, Role of superposition of dislocation avalanches in the statistics of

acoustic emission during plastic deformation, Physical Review E. 88 (2013) 042402. https://doi.org/10.1103/PhysRevE.88.042402.

[175] K. Máthis, G. Csiszár, J. Čapek, J. Gubicza, B. Clausen, P. Lukáš, A. Vinogradov, S.R. Agnew, Effect of the loading mode on the evolution of the deformation mechanisms in randomly textured magnesium polycrystals – Comparison of experimental and modeling results, International Journal of Plasticity. 72 (2015) 127–150. https://doi.org/10.1016/j.ijplas.2015.05.009.

[176] J. Čapek, M. Knapek, P. Minárik, J. Dittrich, K. Máthis, Characterization of Deformation Mechanisms in Mg Alloys by Advanced Acoustic Emission Methods, Metals (Basel). 8 (2018) 644. https://doi.org/10.3390/met8080644.

[177] C.R. Heiple, S.H. Carpenter, Acoustic emission produced by deformation of metals and alloys - A review: Part II, Journal of Acoustic Emission, 1987.

[178] C.R. Heiple, S.H. Carpenter, Acoustic emission produced by deformation of metals and alloys - A review: Part I, Journal of Acoustic Emission, 1987.